



Doctoral School in Civil, Environmental and Mechanical Engineering

Curriculum “Modeling and Simulation” - XXX cycle - 2014/2017

Doctoral Thesis – October 2018

Vincenzo La Salandra

**Seismic risk mitigation of “special risk” process plants
through enhanced concepts and subplant hybrid
simulation**

Supervisor

Prof. Oreste S. Bursi, University of Trento, Italy

To my family

There is no favourable wind for the sailor who doesn't know where to go

Seneca

ACKNOWLEDGMENTS

First and foremost, I wish to express my deepest and most sincere gratitude to my family and to Francesca. I would never successfully complete my study without their enormous support, precious advices, and infinite patience and love. I wish also to thank my supervisor, Professors Oreste S. Bursi. His great knowledge and guidance benefited me enormously. Many thanks also to Dr. Giuseppe Abbiati for numerous fruitful discussions we had, and to Professor Luca Caracoglia for his cooperation in publishing scientific papers. The financial contribution of INDUSE-2-SAFETY project is also acknowledged and the scientific support of all those who cooperated with me in these years of doctorate. Last but not least, my gratitude goes to all beautiful people that I had the fortune to meet in Trento as colleagues, but most importantly as friends, among whom Angela, Roberto, Rocco, Narges, Istiak, and Camilo.

ABSTRACT

This doctoral thesis focuses on the seismic risk mitigation of “special risk” industrial facilities, like chemical, petrochemical and process industries. It is known that the impact of natural hazards, such as earthquakes, on this type of structures may cause significant accidents leading to severe consequences to both the environment and human lives; see, among others, Lanzano et al., (2015) and Krausmann et. al (2010).

In particular, the most critical components in a petrochemical plant are fluid-filled storage tanks; they can experience severe damages and trigger cascading effects in neighbouring tanks due to large vibrations induced by strong earthquakes, indeed. In order to reduce these tank vibrations, an innovative type of foundation based on metamaterial concepts is investigated. Metamaterials are generally regarded as manmade structures that exhibit unusual responses not readily observed in natural materials. Due to their exceptional properties and advancements in recent years, metamaterials have entered the field of seismic engineering, and therefore, offer a novel approach to design seismic shields. As a result, an encouraging and practicable strategy for the seismic protection of liquid storage tanks is presented and validated.

On the other hand, the outcomes of this research study also aim to improve seismic risk assessment of “special risk” facilities mainly through experimental dynamic analysis. In view of performing a dynamic analysis of these complex components, necessary for the global seismic risk assessment procedure, online hybrid (numerical/physical) dynamic substructuring simulations have shown their potential in enabling realistic dynamic analysis of almost any type of nonlinear structural system. At the same time, owing to faster and more accurate testing equipment, a number of different offline experimental substructuring methods, operating both in time and frequency domains, have been employed in mechanical engineering to examine dynamic substructure coupling. The scope of the study is the exploitation of different Experimental Dynamic Substructuring (EDS) methods in a complementary way to expedite a hybrid experiment/numerical simulation and, consequently, the comprehensive dynamic analysis. From this perspective, after a comparative uncertainty propagation analysis of three EDS algorithms, a new Composite-EDS (C-EDS) method is proposed and numerically validated. To the best of the author’s knowledge, this research study presents the first algorithm used to fuse both online and

offline algorithms into a unique simulator with significant advantages in terms of dynamic analysis and seismic risk assessment of industrial plants.

Finally, the research activity is supported by the results from different experimental testing campaigns with the main purpose to investigate the complex behaviour of critical industrial components, such as Tee joints and Bolted Flanged Joints (BFJs), with particular regard to the leakage phenomena resistance. In this respect, a reliable and innovative model capable of predicting the leakage force for a generic BFJ, including the interaction between axial and shear load, is proposed and validated.

PUBLICATIONS

As a result of the work conducted by the author during his years of doctorate, the following publications have been produced:

Journal publications

- **La Salandra, V.**; Wenzel, M.; Bursi, O. S.; Carta, G.; Movchan, A. B., "*Conception of a 3D Metamaterial-Based Foundation for Static and Seismic Protection of Fuel Storage Tanks*" in FRONTIERS IN MATERIALS, v. 4, (2017). - DOI: 10.3389/fmats.2017.00030.
- Abbiati, G.; **La Salandra, V.**; Bursi, O. S.; Caracoglia, L., "*A composite experimental dynamic substructuring method based on partitioned algorithms and localized Lagrange multipliers*" in MECHANICAL SYSTEMS AND SIGNAL PROCESSING, v. 100, (2018), p. 85-112. - DOI: 10.1016/j.ymssp.2017.07.020.
- Bursi, O. S.; di Filippo, R.; **La Salandra, V.**; Pedot, M.; Reza, Md S., "*Probabilistic seismic analysis of an LNG subplant*" in JOURNAL OF LOSS PREVENTION IN THE PROCESS INDUSTRIES, v. 2017, (2017). - DOI: 10.1016/j.jlp.2017.10.009.

Conference proceeding publications

- **La Salandra, V.**; Di Filippo, R.; Bursi, O. S.; Paolacci, F.; Alessandri, S., "*Cyclic Response of Enhanced Bolted Flange Joints for Piping Systems*" in Proceedings of the ASME 2016 Pressure Vessels & Piping Conference PVP, New York, USA: ASME, 2016. Proceedings of: PVP2016, Vancouver, British Columbia, Canada, July 17-21, 2016.
- Bursi, O. S.; **La Salandra, V.**; Abbiati, G.; Caracoglia, L., "*A comparison of online and offline experimental substructuring methods for the simulation of complex linear dynamic systems*" in 6 th European Conference on Structural Control, Sheffield, England: EACS, 2016. Proceedings of: EACS 2016, Sheffield, England, 11-13 July 2016.

- Abbiati, G.; Bursi, O. S.; **La Salandra, V.**; Marelli, S.; Stojadinovic, B., "*Uncertainty propagation and global sensitivity analysis in hybrid simulation using polynomial chaos expansion*" in CIVIL-SOFT-COMP 2015 The Fourth International Conference on Soft Computing Technology in Civil, Structural and Environmental Engineering Prague, Prague, Czech Republic: Civil-Comp Press, 2015. Proceedings of: CIVIL-SOFT-COMP 2015, Prague, Czech Republic, 1-4 September 2015.
- Bursi, O. S.; Abbiati, G.; Caracoglia, L.; **La Salandra, V.**; Di Filippo, R.; Reza, M.S., "*Dynamic Response of Coupled Tanks and Piping Systems under Seismic Loading*" in 2015 ASME Pressure Vessels & Piping Conference, USA: ASME, 2015. Proceedings of: ASME 2015, Boston, Massachusetts, USA, 19-23 July, 2015.
- Abbiati, G., Bursi, O. S., Cazzador, E., Molina, J., **La Salandra, V.**, 2014. "A *Model Updating Strategy for Hybrid Simulation of a Complex Bridge*" - Sixth World Conference on Structural Control and Monitoring, July 15-17, 2014, Barcelona, Spain.
- Abbiati, G.; Bursi, O. S.; Caracoglia, L.; Di Filippo, R.; **La Salandra, V.**, "*Probabilistic Seismic Response of Coupled Tank-Piping Systems*" in Proceedings of the ASME 2016 Pressure Vessels & Piping Conference, New York, USA: ASME, 2016. Proceedings of: PVP 2016, Vancouver, British Columbia, Canada, July 17-21, 2016.
- Caprinuzzi, S.; Ahmed, M.; Paolacci, F.; Bursi, O. S.; **La Salandra, V.**, "*Univariate Fragility Models for Seismic Vulnerability Assessment of Refinery Piping Systems*" in Proceedings of the ASME 2017 Pressure Vessels and Piping Conference PVP2017 July 16-20, 2017, Waikoloa, Hawaii, United States, New York, USA: American Society Mechanical Engineers, 2017, p. 1-10. - ISBN: 978-0-7918-5803-5. Proceedings of: Proceedings of the ASME 2017 Pressure Vessels and Piping Conference PVP2017, Waikoloa, Hawaii, United States, July 16-20, 2017. - DOI: 10.1115/PVP2017-65138.

Contents

Introduction	1
Chapter 1	8
1. Conception of a 3D Metamaterial-Based Foundation for Static and Seismic Protection of Fuel Storage Tanks	8
1.1 Introduction	9
1.2 Materials and Methods	10
1.3 Results	17
1.4 Discussion	27
Chapter 2	29
2. A Composite Experimental Dynamic Substructuring Method Based on Partitioned Algorithms and Localized Lagrange Multipliers	29
2.1 Introduction	29
2.2 A framework for composite online/offline experimental dynamic substructuring methods	32
2.3 Comparative uncertainty propagation analysis of the selected EDS methods	49
2.4 Application of the C-EDS method to a petrochemical prototype plant ...	61
2.5 Conclusions	72
2.A Additional research on real time/pseudo dynamic testing of piping systems with dynamic substructuring	74
Chapter 3	91
3. Probabilistic Seismic Analysis of an LNG Subplant	91
3.1 Introduction	92
3.2 Performance-based earthquake engineering procedure	94
3.3 LNG Plant	95
3.4 Critical components for leakage in the LNG plant	103
3.5 FE modelling of LNG plant components and preliminary analyses	111
3.6 Probabilistic Seismic Analysis	115
3.7 Conclusions	124

3.A Additional research on the cyclic Response of Enhanced Bolted Flange Joints for Piping Systems.....	125
Summary, conclusions and future perspectives	144
Bibliography.....	148

List of Figures

Figure 1.1 (a): broad tank on a standard foundation (b): broad tank on a smart foundation (c): broad tank on a smart foundation with optimized unit cells. 11

Figure 1.2 (a): Conception of a static system [Dimensions in mm]; (b): FE model of the foundation including the tank weight as a surface load [kN/m²]; (c): two unit cells on line supports including the weights of the rubber and inner concrete cubes as surf..... 13

Figure 1.3 (a): Top-section and cross-section of the optimized foundation; (b): Simplified model for shear-wave propagation; (c): 1D mass-resonator chain model. 16

Figure 1.4 (a): first impulsive mode at 4.15 Hz for a broad tank on a traditional foundation; (b): first impulsive mode of a broad tank on the proposed smart foundation at 3.95 Hz; (c): first impulsive mode at 2.4 Hz for a broad tank on the optimized found 18

Figure 1.5 (a): The unit cell and its Brillouin zone (dimensions in cm); (b): Dispersion analysis of the unit cell. 19

Figure 1.6 (a): compressive stresses in the walls at the ultimate limit state [N/mm²]; (b): line bending moments in slabs at the ultimate limit state [kNm/m]. 20

Figure 1.7 Summary of results for: (a): top slab above wall (top left); (b): the top slab in the field (top right); (c): intermediate slab above wall (bottom left); (d): intermediate slab in field (bottom right). 21

Figure 1.8 (a): acceleration response at the top of the foundation with a wall thickness of 20 cm; (b): acceleration response with a wall thickness of 10 cm. 22

Figure 1.9 (a): maximum acceleration response function of the tank wall for traditional and smart foundation; (b): acceleration responses for a tank with a reduced liquid height of 12 m. 22

Figure 1.10 The Northridge earthquake signal 23

Figure 1.11 Time histories of maximum absolute values of accelerations along the tank shell 23

Figure 1.12. Comparison of the snap-shots when the acceleration is maximum on the tank walls..... 24

Figure 1.13 (a): Frequency response function of the optimized foundation alone subjected to a base acceleration of 1 m/s²; (b): Tank response for a fully filled tank, on the optimized foundation, for a base acceleration of 1 m/s² [m/s²]; (c): Tank response 25

Figure 1.14 (a): Undamped frequency response function for 1, 5, and 25 layers of foundation for a base excitation of 1 m/s²; (b): Dispersion relations for the optimized unit cell; (c): Frequency response function of the analytical model for two layers and 3 layers. 26

Figure 1.15 (a): Position of cracks in the unit cell; (b): Crack modeled as a physical gap in the slabs due to static loads [dimensions in m]; (c): Dispersion analysis of the cracked foundation sector. 27

Figure 2.1 Three substructure coupling based on the LLM..... 35

Figure 2.2 Task sequence of: (a) the staggered GC method; (b) the parallel PM method... 37

Figure 2.3 The 5-DoF benchmark system: (a) linear; and (b) nonlinear variants 50

Figure 2.4 Empirical CDF of experimental data (“Data”) vs. theoretical CDF curves of several distribution models, used to examine an experimental hammer test (“hit”): (a) duration (D), (b) intensity (J).....	53
Figure 2.5 Truncated Gaussian PDF vs. experimental data (empirical histogram), normalized to unit area of experimental hammer tests: (a) Duration (D), (b) Intensity (J).....	53
Figure 2.6 Comparison between an experimental and a numerical hammer test (“hit”): (a) time domain, (b) frequency domain.	54
Figure 2.7 Convergence of error score statistical moments evaluated at interface Node #3 of the linear 5-DoF benchmark system considering the IBS method: (a) mean and (b) variance of NRMSE; (c) mean and (d) variance of NEE.....	57
Figure 2.8 Average displacement response histories of Node #3 and relevant 99% confidence intervals for the linear 5-DoF system with $\zeta = 0.01$ and $m_f = 0.5$: (a) IBS and REF; (b) RBS and REF; (c) HDS and REF.	58
Figure 2.9 Average displacement response histories of Node #3 and relevant 99% confidence intervals for the non-linear 5-DoF system with $\zeta = 0.01$ and $m_f = 0.5$: (a) IBS and REF; (b) HDS and REF.....	59
Figure 2.10 Average force-displacement hysteretic loops of the non-linear spring element and relevant 99% confidence intervals for the non-linear 5-DoF system with $\zeta = 0.01$ and $m_f = 0.5$: (a) IBS and REF; (b) HDS and REF.....	59
Figure 2.11 Petrochemical prototype plant case study with highlighted substructures.....	61
Figure 2.12 Substructuring schematics of the petrochemical prototype plant case study. ...	62
Figure 2.13 Piping system with main dimensions and locations of accelerometers for experimental modal analysis.	62
Figure 2.14 FE model and main characteristics of both piping system and temporary support frame.....	63
Figure 2.15 EDS of the piping system: (a) receptance function -Laplace domain- and (b) corresponding impulse response function -time domain- relevant to Node #301, dir. X....	64
Figure 2.16 Details of the CSB and test setup of the CSB array	65
Figure 2.17 Bilinear Mostaghel model: (a) S-DoF idealization; (b) Hysteretic loop.	66
Figure 2.18 Sliding liquid storage tank according to Malhotra et al. (2000); (a) schematic; (b) numerical model with mass DoF numbering	68
Figure 2.19 Partitioned model of the petrochemical prototype plant case study.....	70
Figure 2.20 Time history responses of Node 301: (a) displacement; (b) velocity and relevant zoomed views.	71
Figure 2.21 Dynamic response of the CSB array: (a) force time history; (b) displacement-force hysteretic loop and relevant zoomed views.....	72
Figure 2.A.1 Physical and numerical substructures for real-time/pseudodynamic tests	74
Figure 2.A.2 Selected storage tanks from the Case Study #1	75
Figure 2.A.3 Natural earthquake spectra that fit the Uniform Hazard Spectrum of Priolo Gargallo: RP = 475 years (left) and RP = 2475 years (right).	76
Figure 2.A.4 Sliding liquid storage tank according to Malhotra et al. (2000); (a) schematic; (b) numerical model with mass DoF numbering	76
Figure 2.A.5 Details of the CSB and test setup of the CSB array.	78

Figure 2.A.6 Bilinear Mostaghel model: (a) S-DoF idealization; (b) Hysteretic loop.	79
Figure 2.A.7 Physical substructure in the laboratory	80
Figure 2.A.8 Schematic of the FE model and relevant dimension of the piping system conceived as PS.....	81
Figure 2.A.9 Reduced model and location of accelerometers devoted to numerically evaluate.....	82
Figure 2.A.10 Comparison of displacement responses of the RM and CB reduced models at coupling interface DoF.....	83
Figure 2.A.11 Comparison of displacement responses of the RM and CB reduced models at coupling interface DoF.....	83
Figure 2.A.12 Particular of the strain gauges placement.....	84
Figure 2.A.13 ERA algorithm procedure	84
Figure 2.A.14 Hardware-Software architecture.....	85
Figure 2.A.15 (a) Selected slender tank and accelerogram, (b) experienced isolator displacement, (c) NS restoring force, (d) PS restoring force.....	86
Figure 2.A.16 (a) strain gauges placement, (b) strain on the elbows.	86
Figure 2.A.17 (a) Selected slender tank and accelerogram, (b) experienced isolator displacement, (c) NS restoring force, (d) PS restoring force.....	87
Figure 2.A.18 (a) strain gauges placement, (b) strain on the elbows.	88
Figure 2.A.19 (a) Selected slender tank and accelerogram, (b) experienced isolator displacement, (c) NS restoring force, (d) PS restoring force.....	89
Figure 2.A.20 (a) strain gauges placement, (b) strain on the elbows.	89
Figure 3.1 Refrigerated liquefied gas plant overview	94
Figure 3.2 LNG plant layout.....	96
Figure 3.3 Hazard Curve of the high-seismic site of Priolo Gargallo (Sicily, Italy).	96
Figure 3.4 Main tank layout.	97
Figure 3.5 Steel platform and position of the three pump columns.....	97
Figure 3.6 Concrete support structure	98
Figure 3.7 Knock-out drum process area.....	99
Figure 3.8 Pipelines layout on concrete support structure.....	99
Figure 3.9 Stress-strain curve for A312/TP304L at room temperature	100
Figure 3.10 Stress-strain curve for A312/TP304L at -80°C.....	101
Figure 3.11 BFJs connecting the pumps to the piping system	102
Figure 3.12 BFJ between the tank of the knock-out drum and the piping system.....	102
Figure 3.13 (a) BFJ setup. (b) Design 02 specimen, gasket, and a relevant bolt.....	104
Figure 3.14 Load-Displacement diagrams for 18 mm (Design 01) and 27 mm (Design 02) BFJs: (a) Monotonic loading and (b) Cyclic Loading.	105
Figure 3.15 Bolt, flange and gasket components and force balance in the mechanical model of a BFJ proposed in EN 1591-1 (2009).....	106
Figure 3.16 Comparison between axial and shear leakage forces from the predictive model and experimental results.	107
Figure 3.17 Axial deformation model for BFJs.....	108
Figure 3.18 (a) Mesh design for the outer tank; (b) FE model of the inner tank.....	111

Figure 3.19 ANSYS FE model: (a) steel platform; (b) concrete support structure.	112
Figure 3.20 (a) Experimental results for A312/TP304L steel (b) FE model of the piping layout.	113
Figure 3.21 FE model of Knock-out drum process area.	113
Figure 3.22 ANSYS complete FE model of the LNG plant.	114
Figure 3.23 Response spectra of the strongest components of natural records employed.	118
Figure 3.24 Seismic analysis results for: a) 6" BFJs; b) 18" BFJs.	120
Figure 3.25 Seismic analysis results and linear regression for EDP3 and PGA as IM.	121
Figure 3.26 Seismic analysis results and linear regression for EDP3 and Sa(T) as IM. ...	122
Figure 3.27 Fragility curves for EDP 3 and PGA as IM.	122
Figure 3.28 Fragility curves for EDP 3 and Sa(T) as IM.	123
Figure 3.A.1 A typical BFJ and two thick standard flanges.	125
Figure 3.A.2 Non-standard BFJ.	126
Figure 3.A.3 (a) Design 01 BFJ; (b) spiral wound gasket; (c) stud bolt.	128
Figure 3.A.4 Test set-up for combined loading tests.	128
Figure 3.A.5 Placement of the both axial and shear displacement transducers in the Design_02-BFJ: (a) frontal view; (b) bottom view.	129
Figure 3.A.6 Definition of the equivalent axial flange displacement.	130
Figure 3.A.7 Bi-linear and tri-linear approximations of a non-linear response after Bursi et al. (2002).	130
Figure 3.A.8 Load-displacement curves for monotonic tests and leakage force detection.	131
Figure 3.A.9 Load-displacement curves for cyclic tests and leakage force detection.	132
Figure 3.A.10 Details of the loss of containment through the joints: (a) Design 01 and (b) Design 02 BFJs.	132
Figure 3.A.11 Flange load-displacement curves in the transverse direction for monotonic tests.	133
Figure 3.A.12 Flange load-displacement curves in the axial direction for monotonic tests.	134
Figure 3.A.13 Detail of the displaced configuration of the tested BF_18_Mo BFJ specimen.	134
Figure 3.A.14 The BFJ model proposed by EN 1591-2009.	135
Figure 3.A.15 Comparison between the predicted axial force of ASML18 in Reza et al., 2014 and the experimental result.	138
Figure 3.A.16 Examples of the axial leakage force prediction for different BFJs.	139
Figure 3.A.17 Axial and shear leakage forces after Design 01 for the BFJ monotonic test.	140
Figure 3.A.18 Sketch of an inclined BFJ.	140
Figure 3.A.19 Sketch of an inclined BFJ.	141
Figure 3.A.20 Model for the joint axial stiffness evaluation.	142

List of Tables

Table 1.1 Mechanical properties of materials.	14
Table 1.2 First impulsive eigenfrequencies of broad-tank-foundation systems with various liquid heights.	18
Table 2.1 Main parameters and modal properties of the linear 5-DoF system.	51
Table 2.2. Main parameters of the non-linear 5-DoF system.	52
Table 2.3 Parameters of the reference ICP accelerometer – Model Number 393 C.	54
Table 2.4 Probabilistic characterization of experimental sources of uncertainty.	55
Table 2.5 Numerical simulation of the EDS methods for a single MC simulation.	55
Table 2.6 Comparison of error score statistics for the linear variant of the 5-DoFs benchmark system after MCS.	60
Table 2.7 Comparison of error score statistics for the non-linear variant of the 5-DoFs benchmark system after MCS.	60
Table 2.8 Parameters of the liquid storage tank model.	69
Table 2.9 Global parameters of the sloshing fluid model.	69
Table 2.A.1 Comparison between Nuclear and Italian standards.	75
Table 2.A.2 Parameters of the liquid storage tank model.	78
Table 2.A.3 Global parameters of the sloshing fluid model.	78
Table 2.A.4 Outcomes from the modal analysis of the entire PS.	81
Table 3.1 Properties of Knock-out drum C608 tank.	99
Table 3.2 Properties of Knock-out drum C608 tank.	100
Table 3.3 Leakage forces for the experimental tests	104
Table 3.4 Axial and shear stiffness and leakage forces of BFJs.	109
Table 3.5 Performance levels (after Vathi et al., 2015).	109
Table 3.6 Failure modes with relevant EDPs and limit states (after Vathi et al., 2015).	110
Table 3.7 Comparison between preliminary simulations.	115
Table 3.8 Natural records used for Cloud analysis.	117
Table 3.9 EDPs description	119
Table 3.10 EDPs leakage limit states	119
Table 3.11 Maximum and minimum absolute values of EDP3.	120
Table 3.12 Fragility function parameters	123
Table 3.A.1 Geometrical properties of non-standard BFJs (dimensions in mm).	127
Table 3.A.2 Average mechanical properties of pipes/flanges.	127
Table 3.A.3 Test program of non-standard BFJs.	129
Table 3.A.4 Main experimental forces after testing.	131
Table 3.A.5 Main experimental forces after testing.	133
Table 3.A.6 Prediction of the axial leakage force for ASML18 in Reza et al., 2014 and comparison with experimental result.	138
Table 3.A.7 Comparison between experimental and theoretical results at leakage after Design 02 test.	142

List of Abbreviations

<i>BFJ</i>	<i>Bolted flange joint</i>	<i>LOC</i>	<i>Loss of containment</i>
<i>C-EDS</i>	<i>Composite-EDS</i>	<i>MCSs</i>	<i>Monte Carlo simulations</i>
<i>CB</i>	<i>Craig-Bampton</i>	<i>MSA</i>	<i>Multi-Stripe analysis</i>
<i>CDF</i>	<i>Cumulative distribution function</i>	<i>NEE</i>	<i>Normalized energy error</i>
<i>CLMs</i>	<i>Classical Lagrange multipliers</i>	<i>NPP</i>	<i>Nuclear power plant</i>
<i>COV</i>	<i>Coefficient of variation</i>	<i>NRMSE</i>	<i>Normalized root mean square error</i>
<i>CSB</i>	<i>Concave sliding bearing</i>	<i>NS</i>	<i>Numerical substructure</i>
<i>DAE</i>	<i>Differential algebraic equations</i>	<i>OBE</i>	<i>Operating based earthquake</i>
<i>DM</i>	<i>Damage measure</i>	<i>PBEE</i>	<i>Performance-based earthquake engineering</i>
<i>DoF</i>	<i>Degree of freedom</i>	<i>PDF</i>	<i>Probability distribution function</i>
<i>DSC</i>	<i>Dynamic substructuring coupling</i>	<i>PGA</i>	<i>Peak ground acceleration</i>
<i>DV</i>	<i>Decision variables</i>	<i>PGD</i>	<i>Proper generalized decomposition</i>
<i>EDP</i>	<i>Engineering demand parameter</i>	<i>PRA</i>	<i>Probabilistic risk assessment</i>
<i>EDS</i>	<i>Experimental dynamic substructuring</i>	<i>PS</i>	<i>Physical substructure</i>
<i>ERA</i>	<i>Eigensystem realization algorithm</i>	<i>PSDA</i>	<i>Probabilistic seismic demand analysis</i>
<i>FBS</i>	<i>Frequency based substructuring</i>	<i>PSDM</i>	<i>Probabilistic seismic demand model</i>
<i>FE</i>	<i>Finite element</i>	<i>RBS</i>	<i>Receptance based substructuring</i>
<i>FRF</i>	<i>Frequency response function</i>	<i>RF</i>	<i>Receptance functions</i>
<i>HDS</i>	<i>Heterogeneous dynamic substructuring</i>	<i>RLG</i>	<i>Refrigerated liquefied gas</i>
<i>IBS</i>	<i>Impulsive based substructuring</i>	<i>SNR</i>	<i>Signal to noise ratio</i>
<i>IDA</i>	<i>Incremental dynamic analysis</i>	<i>SSE</i>	<i>Safe shut-down earthquake</i>
<i>IM</i>	<i>Intensity measure</i>	<i>TES</i>	<i>Twice elastic slope</i>
<i>IRF</i>	<i>Impulse response function</i>		
<i>LLMs</i>	<i>Localized Lagrange multipliers</i>		
<i>LNG</i>	<i>Liquefied natural gas</i>		

Introduction

Background and motivation

Natural hazards, such as earthquakes, may cause severe damages to the environment and the community. For instance, in 1999 the Izmit earthquake damaged the largest Turkish petrochemical plant and set it on fire. The fire took five and a half days to extinguish and almost spread to other industrial sites (Barka, 1999). Such events can be described as natural technological events or NaTech events (Cruz and Steinberg, 2006) (Steinberg, et al., 2008). It is of critical importance for the community and the environment to prevent such incidents from happening. On the other hand, “special risk” industrial plants and their components are considered with particular attention for their strategic importance and heavy consequences both to the environment and human lives. In fact, according to the French environmental code (articles R. 563-1 to R. 563-8, 1991), “special risk” structures refer to facilities for which damage is severe also on their personnel and consequences can exceed the immediate vicinity of these structures. As a result, for these kind of plants, there is the need of a probabilistic risk analysis for seismic hazard and justifications by owners about the maintenance of safety functions in the case of specific earthquakes. Then, in order to prevent or limit incidents due to earthquakes in “special risk” industrial plants, in this thesis different strategies are proposed and validated through theoretical, analytical and experimental investigations.

The first part of the thesis is dedicated to specific features of a petrochemical plant, i.e. fuel storage tanks. In particular, the feasibility of a metamaterial-based foundation for the seismic isolation of storage tanks is investigated. Three- and two-component new foundations were conceived by Cheng and Zhifei (2013), Cheng and Shi (2017). A two-dimensional (2D) array of steel cylinders coated with rubber and embedded in a reinforced concrete matrix constituted the three-component foundation. Conversely, the two-component design was based on the same geometry, but replacing the steel cylinders inside the rubber with homogeneous rubber inclusions. By comparing these two designs, they showed that a three-component periodic foundation can generate useful band gaps for seismic vibration isolation. Furthermore, they concluded that the reinforcement of the concrete matrix has a negligible influence on the band gaps. However, it is important to underline the 2D nature of their proposed designs, which would have to be improved for an omnidirectional wave. Another 2D approach was studied by Gaofeng and Zhifei (2010); while a three-dimensional (3D) approach for a phononic crystal-based structure was proposed by Cheng et al. (2013). The latter design showed the possibility for a 3D foundation to generate stop bands in the low frequency region. Furthermore, they carried out a parametric study on the structural components and their influence on the band gaps. The mass of the resonator core, the thickness of the rubber coating as well as the stiffness of the rubber have proven to be of special importance for the frequency range of the stop bands. In order to validate the effects of stop bands in periodic structures Yan et al. (2014) conducted field experiments on scaled 2D periodic foundations. The comparison between experimental outcomes and numerical

results showed that periodic foundations are able to mitigate seismic waves. Furthermore, they found good agreement between experimental tests and dispersion analyses. The work by Achaoui et al. (2016) provides additional insights on filtering waves propagating through a foundation made of inertial resonators. The recent work by Carta et al. (2016) has addressed the suppression of vibrations in fuel tanks *via* specially tuned systems of many multiscale resonators attached to the tanks.

The second part of the thesis focuses on the seismic risk assessment of “special risk” industrial plants. This risk evaluation, which is based on dynamic analysis, is fundamental to ensure an adequate design against earthquake hazards, even though these “special risk” plants present components very tough to be numerically modelled due to their complexity and nonlinearity. In order to reduce the computational effort of dynamic analysis for these facilities, Experimental Dynamic Substructuring (EDS) methods often reveal their efficiency. Among the EDS methods, the Heterogeneous (numerical/physical) Dynamic Substructuring (HDS) represents a form of online simulation, which has been shown to be very efficient in solving non-linear structural dynamic problems (Bursi and Wagg, 2008; Pan et al., 2016). In particular, the HDS isolates the physical sub-system(s) (PS), which is experimentally tested since it contains a key region (or component) exhibiting non-linear behavior, from the remainder of the system, which is numerically simulated, i.e. the numerical sub-system(s) (NS). In summary, HDS appears to be a very versatile method that can be applied to any class of multiphysics and multiscale engineering problems with strong/weak nonlinearities (Bursi et al., 2017; Turso et al., 1995; Stansberg et al., 2002). When HDS is applied to a complex mechanical system, some issues arise. For instance, a piping system response is characterized by weak and localized non-linearities in elbows, flange joints, tee joints; modal damping is low (of the order of 1.5 per cent); proper boundary conditions are difficult to reproduce, etc. (Bursi et al., 2014). Therefore, an adequate identification of modal damping and boundary conditions, especially at the interfaces where substructures are split, becomes crucial for the fidelity of heterogeneous simulations. Due to faster and more accurate testing equipment, the DSC method has been broadly employed in mechanical engineering through the implementation of several experimental substructuring methods (de Klark et al., 2008) like the impulse-based substructuring method (IBS, Rixen and Van der Valk, 2013; Van der Valk and Rixen, 2014) and the so-called Lagrange multiplier frequency-based substructuring (LM-FBS) method (Voormeeren et al., 2010). Both LM-FBS and IBS are offline methods that can quickly characterize the response of linear PSs by means of experimental and operational modal analysis tools. Therefore, they appear to be suitable methods for complementing certain modeling phases of the online HDS method.

The final part of the research study presents the application of the fully probabilistic Performance-Based Earthquake Engineering (PBEE) approach to a Liquefied Natural Gas (LNG) plant. Together with a clear strategic importance, LNG plants also carry a significant risk related to possible consequences of incidents caused by natural events. Moreover, leakage of hazardous or polluting substances can badly affect the local environment. The resulting hazard was evaluated in different situations by means of case studies (Cozzani et

al. 2014, Baesi et al. 2013, and Young et al. 2005). The considerable variability of seismic events and the related domino effects were partly taken into account in the overall hazard estimation by the application of complex methodologies (Campedel et al., 2008 and Antonioni et al., 2007). Nevertheless, historic data shows that earthquakes can lead to severe losses due to the failure of different components of industrial plants; in this respect see Lanzano et al., (2015) and Krausmann et al. (2010). An industrial plant typically has many structural and mechanical components, with different resistance thresholds and different failure behaviours. One of the most dangerous failure effects is loss of containment (LOC) or leakage, which can lead to explosion, fire and environmental damage. An LNG plant includes a number of component types that can experience leakage, under certain conditions of stress and strain caused by a seismic event. Common vulnerable components of LNG pipelines are bolted flange joints (BFJs) and piping bends or elbows. With respect to BFJs, current European technical standards, like EN 1591-1,2 (2009), do not have tools to predict leakage. Moreover, studies whether focusing on leak-before-break, i.e. that concentrate on the steady growth of through-cracks in pipes (Xie, 1998) or tracing the plastic behaviour of elbows (Li and Mackenzie, 2006), do not predict leakage thresholds. To fill this gap, a practical predictive model based on EN 1591 (2009) was developed by La Salandra et al. (2016), also using experimental data found by Reza et al. (2014). As far as a probabilistic approach is concerned, the risk estimation of leakage events is usually based on historic evidence found in databases; for a review, see Barros da Cunha (2016). In order to quantify induced seismic risk in an LNG plant, a seismic Probabilistic Risk Assessment (PRA) approach suggested by IAEA (2009) for nuclear power plants (NPPs) is available. The procedure is as follows: i) Seismic hazard analysis; ii) Fragility analysis; iii) System analysis and consequence evaluation. The outcome of a seismic PRA includes seismic hazard of the site, the structural capacity of structures and equipment, incorporation of uncertainties in seismic hazard, structural fragility and response of components. Hoseyni et al., (2014) applied a variant of this approach to take into account soil-structure interaction effects. However, this approach is not directly applicable to (non-nuclear) LNG plants, because data on aleatory randomness and epistemic uncertainties in the capacity of LNG components is not available. As a viable alternative, to rationally quantify the seismic performance of civil facilities, the PBEE methodology has been proposed (Cornell and Krawinkler, 2000). Some examples of application of the PBEE approach can be found in civil engineering literature (Yang et al., 2009, Tondini and Stojadinovic, 2012). Along this line, application of the PBEE approach to petrochemical piping systems by means of codes can be found in Bursi et al. (2015a). Moreover, some applications based on the determination of fragility curves are available for piping systems of NPPs (Firoozabad et al., 2015) and boil-off gas compressors at LNG terminals (Park and Lee, 2015). In both cases, limit states related to leakage were not considered or quantified. Conversely, the selection of engineering demand parameters (EDPs) and corresponding damage levels for piping systems and tanks was carried out by Vathi et al. (2015). Nonetheless, a fragility analysis also requires the analysis of the effects of different intensity measures, e.g. peak ground acceleration (PGA), on the dispersion characteristics of a probabilistic seismic demand model. To the author's knowledge, this analysis has not yet been carried out for LNG plants.

Scope

The first part of the thesis investigates the feasibility of a metamaterial-based foundation for the seismic isolation of fuel storage tanks. In fact, these features need to be regarded as high-risk structures in petrochemical plants, due to their fragility to earthquakes and their potential for cascading effects (Fabbrocino et al., 2005). Their low impulsive frequencies can fall within the excitation frequencies of earthquakes and significant effort is required to isolate them against seismic vibrations. A very innovative solution for isolating tanks at low frequencies is constructing a foundation based on phononic crystals. These crystals can create stop bands, which stop waves from propagating in certain frequency regions (Sigalas et al., 2005). This feature reveals enormous importance in the cases where the main frequency of the structure to isolate can change, as in the case of storage tanks with varying fluid levels.

The second part of the thesis focuses on the seismic risk assessment of petrochemical industrial plants. The latter is important to ensure an adequate design against earthquake hazards and is based on dynamic analysis. On the other hand, due to complexity and nonlinearity of sub-plants and components located in these “special risk” plants, EDS methods, both in time and frequency domains, have shown their great potential in improving the effectiveness of dynamic analysis. Even though a plethora of studies has dealt with EDS methods both in mechanical and civil engineering (de Klerk et al., 2008; Pan et al., 2016) along with consequent error propagation issues (Rixen and Van der Valk, 2013; Mosqueda et al., 2007; Song and Dyke, 2013; D’Ambrosio and Fregolent, 2009; Culla et al., 2011), very few publications have been devoted to: i) the systematic performance comparison among the various methods from a more general uncertainty propagation setting; ii) the possibility of exploiting these methods in a synergic way to both improve and expedite the overall experiment/simulation. As a matter of example, the online HDS method, which can operate in real time with proper delay compensation, can easily accommodate strongly non-linear PSs with rate-dependent behavior. On the other side, both LM-FBS and IBS are offline methods that can quickly characterize the response of linear PSs by means of operational and experimental modal analysis tools. Therefore, they appear to be suitable methods, capable of complementing certain modelling phases of HDS. All together, they represent the basic components of the state-of-the-art simulation methods based upon the principle of fusing numerical and experimental methods, and the comparison of their performances and fusion is presented hereinafter as well as their combination.

Finally, the application of the fully probabilistic PBEE approach to an LNG plant having a piping system coupled to a support structure and a relevant LNG tank is described. The PBEE methodology has been proposed (Cornell and Krawinkler, 2000) and is used to rationally quantify the seismic performance of civil facilities. This probabilistic framework is based on the prediction of structural behaviour under realistic seismic loadings that the structural system is likely to experience in its reference life. It is based on the combination of different quantities, such as seismic hazard, structural response, level of damage, and repair costs after cyclic loading. Finally, in order to characterize the components of the LNG

tank by means of detailed 3D finite element models, a novel mechanical model to predict the leakage limit state of generic BFJs is developed.

Structure of the thesis

This thesis presents the major research outcomes achieved by the author during his years of doctorate. Moreover, it is organized as a collection of three journal publications. A brief overview of the following chapters follows:

- Chapter 1 includes the publication titled: “Conception of a 3D Metamaterial-Based Foundation for Static and Seismic Protection of Fuel Storage Tanks”. In this manuscript a broad fuel storage tank, which poses a significant threat to the community and the environment, is considered as a case study for the design of a metamaterial-based foundation. The materials employed in the foundation are concrete and construction grade silicon, which are commonly used in construction industry. Given the critical frequency region of seismic vibrations for the structure of interest, a unit cell is designed with the aid of a frequency dispersion analysis to cover critical frequencies by means of a stop band. Then, a finite lattice structure is extracted from the infinite lattice of unit cells and is checked on its static behavior at the ultimate limit state (EN 1990, 2004). Furthermore, the coupled (foundation + structure) system is numerically tested on its wave attenuation properties. Finally, the influence of cracks on the dynamic properties of the proposed foundation is also investigated.
- Chapter 2 includes the publication titled: “A composite experimental dynamic substructuring method based on partitioned algorithms and localized Lagrange multipliers”. First, the paper summarizes the basic algorithms, both in time and frequency domain, of the state-of-the-art experimental simulation methods. Then, a comparison of their performances in terms of uncertainty propagation is presented with the scope to explore their possible fusion in a new combined method. In particular, Section 2.2 illustrates the newly conceived composite experimental dynamic substructuring (C-EDS) method, which relies on partitioned algorithms for connecting multiple substructures of heterogeneous systems with a dual approach. Moreover, since various experimental sources of uncertainty affect the measured PS response, a comparative uncertainty propagation analysis is presented based on Monte-Carlo Simulation (MCS) of all described EDS algorithms considering a 5-DoFs benchmark system and probability distributions of main sources of uncertainty characterized after laboratory measurements. Then, in order to highlight the feasibility of the C-EDS method in combining radically different EDS algorithms, a virtual experiment is numerically conducted on a petrochemical prototype plant case study. As a result, versatility and advantages of fusing both online/offline methods are demonstrated. Finally, the Annex 2.A describes the experimental testing campaign conducted on the previously considered realistic case study where most of the earlier treated concepts find a real application.

- Chapter 3 includes the publication titled “Probabilistic Seismic Analysis of an LNG Subplant”. The manuscript analyses the seismic performance of a liquefied natural gas (ethylene) terminal, consisting in a series of process facilities connected by pipelines of various sizes, within the performance-based earthquake engineering framework. Particular attention is paid to component resistance to leakage and loss of containment even though several different limit states are investigated. The LNG tank, support structures and pipework, including elbows and flanges, are analysed with a detailed 3D finite element model. For this purpose, a novel mechanical model to predict the leakage limit state of generic BFJs is developed. Given the complexity of the FE model of the LNG plant, the Cloud method for probabilistic seismic demand analysis is selected, due to its advantages in terms of consistency in the seismic input and of computational savings. In particular, in order to develop fragility curves of critical components such as elbows and BFJs, a set of 36 ground motions from a database of historic earthquake accelerations is selected and used for a series of nonlinear time history analyses. Finally, the Annex 3.A presents in detail the experimental testing campaign and the relevant theoretical assumptions used for the development of the novel mechanical model able to predict the leakage phenomena resistance of a generic BFJ, taking into account the possible interaction between shear and axial forces.

Chapter 1

1. Conception of a 3D Metamaterial-Based Foundation for Static and Seismic Protection of Fuel Storage Tanks

by Vincenzo La Salandra, Moritz Wenzel, Oreste S. Bursi, Giorgio Carta, Alexander B. Movchan

Abstract

Fluid-filled tanks in tank farms of industrial plants can experience severe damage and trigger cascading effects in neighboring tanks due to large vibrations induced by strong earthquakes. In order to reduce these tank vibrations, we have explored an innovative type of foundation based on metamaterial concepts. Metamaterials are generally regarded as manmade structures that exhibit unusual responses not readily observed in natural materials. If properly designed, they are able to stop or attenuate wave propagation. Recent studies have shown that if locally resonant structures are periodically placed in a matrix material, the resulting metamaterial forms a phononic lattice that creates a stop band able to forbid elastic wave propagation within a selected band gap frequency range. Conventional phononic lattice structures need huge unit cells for low-frequency vibration shielding, while locally-resonant metamaterials can rely on lattice constants much smaller than the longitudinal wavelengths of propagating waves. Along this line, we have investigated 3D structured foundations with effective attenuation zones conceived as vibration isolation systems for storage tanks. In particular, the three-component periodic foundation cell has been developed using two common construction materials, namely concrete and rubber. Relevant frequency band gaps, computed using the Floquet-Bloch theorem, have been found to be wide and in the low-frequency region. Based on the designed unit cell, a finite foundation has been conceived, checked under static loads and numerically tested on its wave attenuation properties. Then, by means of a parametric study we found a favorable correlation between the shear stiffness of foundation walls and wave attenuation. On this basis, to show the potential improvements of this foundation, we investigated an optimized design by means of analytical models and numerical analyses. In addition, we investigated the influence of cracks in the matrix material on the elastic wave propagation, and by comparing the dispersion curves of the cracked and uncracked materials we found that small cracks have a negligible influence on

dispersive properties. Finally, harmonic analysis results displayed that the conceived smart foundations can effectively isolate storage tanks.

1.1 Introduction

In 1999 the Izmit earthquake damaged the largest Turkish petrochemical plant and set it on fire. The fire took five and a half days to extinguish and almost spread to other industrial sites (Barka, 1999). Such events can be described as natural technological events or NaTech events. It is of critical importance for the community and the environment to prevent such incidents from happening. Fuel storage tanks in petrochemical plants need to be regarded as high risk structures, due to their fragility to earthquakes and their potential for cascading effects (Fabbrocino, et al., 2005). Their low impulsive frequencies can fall within the excitation frequencies of earthquakes and significant effort is required to isolate them against seismic vibrations. A very innovative solution for isolating tanks at low frequencies is constructing a foundation based on phononic crystals. These crystals can create stop bands, which stop waves from propagating in certain frequency regions (Sigalas, et al., 2009). Various applications could benefit from these properties, for example, noise protection (Liu, et al., 2000), seismic isolation (Shi & Huang, 2013) or coastal protection (Ha, et al., 2002). The present work is dedicated to the feasibility of such metamaterial-based structures for the seismic isolation of fuel storage tanks.

Three- and two-component new foundations were conceived by (Cheng & Zhifei, 2013). A two- dimensional (2D) array of steel cylinders coated with rubber and embedded in a reinforced concrete matrix constituted the three-component foundation. Conversely, the two-component design was based on the same geometry, but replacing the steel cylinders inside the rubber with homogeneous rubber inclusions. By comparing these two designs, they showed that a three-component periodic foundation can generate useful band gaps for seismic vibration isolation. Furthermore, they concluded that the reinforcement of the concrete matrix has a negligible influence on the band gaps. However, it is important to underline the two-dimensional nature of their proposed designs, which would have to be improved for an omnidirectional wave. Another 2D approach was studied by (Gaofeng & Zhifei, 2010), while a three-dimensional (3D) approach for a phononic crystal-based structure was proposed by Cheng, et al., (2013). The latter design showed the possibility for a 3D foundation to generate stop bands in the low frequency region. Furthermore, they carried out a parametric study on the structural components and their influence on the band gaps. The mass of the resonator core, the thickness of the rubber coating as well as the stiffness of the rubber have proven to be of special importance for the frequency range of the stop bands. In order to validate the effects of stop bands in periodic structures, (Yan, et al., 2014) conducted field experiments on scaled 2D periodic foundations. The comparison between experimental outcomes and numerical results showed that periodic foundations are able to mitigate seismic waves. Furthermore, they found good agreement between experimental tests and dispersion analysis. The work by (Achaoui, et al., 2016) provides additional insight on filtering waves propagating through a foundation made of inertial resonators. The recent work by (Carta, et al., 2016) has addressed the suppression of

vibrations in fuel tanks via specially tuned systems of many multi-scale resonators attached to the tanks.

In the present paper, we introduce a *smart foundation* based on metamaterial concepts that can both attenuate seismic waves and withstand static loads. More precisely, the foundation is capable of attenuating waves in targeted frequency ranges. In our analyses, we are particularly interested in the influence that both geometrical and mechanical properties of a foundation inspired by phononic crystals can have on its dynamic performance as well as its capabilities of bearing gravity loads. In fact, for its practical use, it is of outmost importance to design a foundation that can both attenuate seismic waves and withstand static loads relevant to the coupled structure. Therefore, a broad fuel storage tank, which poses a significant threat to the community and the environment, was considered as a case study for the present design. The materials employed in the foundation are concrete and construction grade silicon, which are commonly used in construction industry. With regard to the design process of the foundation, an iterative procedure was employed. Given the critical frequency region of seismic vibrations for the structure of interest, a unit cell is designed with the aid of a frequency dispersion analysis to cover critical frequencies by means of a stop band. Then, a finite lattice structure is extracted from the infinite lattice of unit cells and is checked on its static behavior at the ultimate limit state (Eurocode 1990). Furthermore, the coupled (foundation+structure) system is numerically tested on its wave attenuation properties. Since the proposed smart foundation was still excessive in size, we also investigated an optimized design endowed with improved performance and reduced dimensions. Therefore, an analytical study was performed to derive the wave propagation properties of the design, while numerical simulations assessed its performance. Although the proposed design is still in an early research stage, it already shows a great potential in optimizing such a foundation.

As pointed out by (Carta, et al., 2014) in the analysis of the dynamic behavior of strongly damaged beams, cracks due to static loading can exert marked effects on band gap formation. For this reason, the influence of cracks on the dynamic properties of the proposed foundation is also investigated. Finally, Section 4 discusses main results, draws conclusions and future perspectives.

1.2 Materials and Methods

1.2.1 Modal analysis of a broad tank

From a dynamic viewpoint, broad tanks like the one under study can be thought of being composed of an impulsive mass that vibrates in phase with the tank walls at a higher frequency (e.g. 3-5 Hz) and a sloshing mass that vibrates not in phase with the tank walls at a lower frequency (i.e. about 0.3 Hz), (Malhotra, et al., 2000). The relevant eigenvalue analysis was carried out with the FE software Comsol Multiphysics (version 5.2). The smart foundation under study is conceived for the higher frequency, since sloshing frequencies can be easily suppressed or mitigated with baffles (Belakroum, et al., 2010). Therefore, the design of the unit cell focused on the first impulsive frequency of the fully filled tank, i.e. 4.05 Hz. In fact, this is the eigenfrequency with the largest participant mass in the radial

direction. A horizontal excitation at this frequency results in both the largest stresses and accelerations in the tank walls, and thus governs the requirements for the seismic resilience. After disregarding sloshing frequencies, it was possible to model the liquid as an acoustic medium (Ding & Chen, 2001); (Carta, et al., 2016). This approach significantly reduced the computational cost of the model. As a result, in all forthcoming analyses the liquid inside the tank is assumed to have the same properties as water. The tank itself has a cylindrical shape with a radius, height, liquid height and wall thickness of 24 m, 16 m, 15 m and 20 mm, respectively. A steel plate with a thickness of 50 mm was used as bottom plate. In order to simulate the traditional foundation system, the whole tank was set on a 1 m thick concrete slab, as depicted in Figure 1.1(a). Moreover, a damping ratio of 5 % was imposed at both 3 Hz and 5 Hz by means of proportional Rayleigh damping on all FE models to hand (Liu & Gorman, 1995). Moreover, an additional modal analysis has been carried out to determine the modal frequencies of the coupled (tank + smart foundation) system. The geometry of the proposed smart foundation is presented in Section 1.3 Results and is shown in Figure 1.1(b). In order to further improve the foundation performance in terms of geometry and dynamic properties, we conceived and analyzed a new unit cell. The optimized design was modeled by means of shell and beam elements and the assembly is depicted in Figure 1.1(c). The relevant cell dimensions are shown in Figure 1.2 (a) in Subsection 1.2.6.1, respectively.

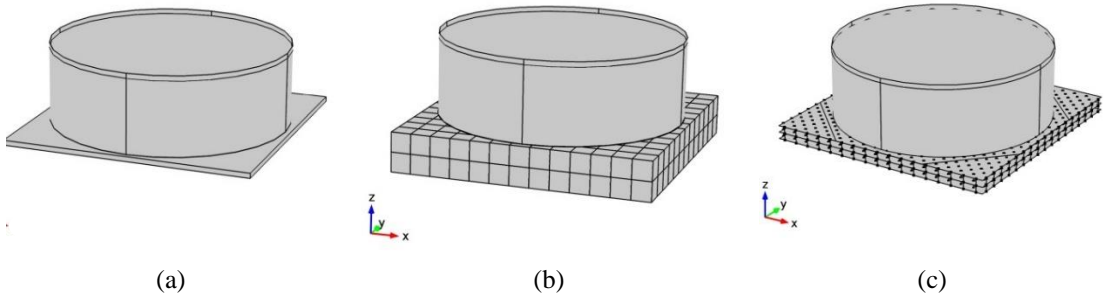


Figure 1.1 (a): broad tank on a standard foundation (b): broad tank on a smart foundation (c): broad tank on a smart foundation with optimized unit cells.

Since the fluid level height is not a constant parameter in a storage tank, the impulsive frequency of the structure changes accordingly. Thus, the variable fluid level results in a frequency region, which is considered governing the foundation design. Clearly, we take into account that the varying fluid level height will change the eigenfrequencies of the coupled foundation-tank system.

1.2.2 Floquet-Bloch theorem and Brillouin zone

Periodic structures can be designed in order to suppress the propagation of seismic waves in a certain frequency region. These regions are called band gaps and can be determined with the Floquet-Bloch theorem (Phani, et al., 2006). This theorem reduces the study to an infinite lattice of unit cells to the analysis of a single unit cell with Floquet-Bloch quasi-periodicity conditions. After imposing these conditions, a frequency dispersion analysis can be carried out and the band gaps of the unit cell can be found as shown in Figure 1.5(b). In order to

obtain the frequency dispersion diagram, we consider the equation of motion for an elastic medium in an Eulerian description,

$$\sum_{j=1}^3 \frac{\partial \sigma_{ij}}{\partial x_j} + F_i = \rho \frac{\partial^2 u_i}{\partial t^2} \quad i = 1,2,3 \quad (1.1)$$

where, the stress-strain relationship reads,

$$\sigma_{ij} = \mu(\mathbf{x}) \left(\frac{\partial u_i}{\partial x_j} + \frac{\partial u_j}{\partial x_i} \right) + \lambda(\mathbf{x}) \delta_{ij} \text{div}(\mathbf{u}(\mathbf{x})) \quad (1.2)$$

In particular, F_i ($i = 1,2,3$) are the components of the body force, ρ the mass density, $\mathbf{u}(\mathbf{x})$ displacement vector, $\mu(\mathbf{x})$ and $\lambda(\mathbf{x})$ Lamè constants, \mathbf{x} position vector and δ_{ij} the Kronecker delta function, respectively. Time t has been omitted for brevity. According to the Floquet-Bloch theorem the solution $\mathbf{u}(\mathbf{x}, t)$ for a periodic system can be expressed as:

$$\mathbf{u}(\mathbf{x}, t) = \mathbf{u}_k e^{i(\mathbf{q}\cdot\mathbf{x} - \omega t)} \quad (1.3)$$

where $\mathbf{q}=[q_x, q_y, q_z]^T$ represents the wave vector in (1.3), while ω denotes the corresponding frequency in rad/s. As a consequence,

$$\mathbf{u}(\mathbf{x} + \mathbf{R}) = \mathbf{u}(\mathbf{x}) e^{i\mathbf{q}\cdot\mathbf{R}} \quad (1.4)$$

with \mathbf{R} being the lattice vector. By imposing these boundary conditions on a system and solving the discrete eigenvalue problem of a typical cell, which takes on the following form:

$$(\mathbf{K} - \omega^2 \mathbf{M})\mathbf{u} = 0 \quad (1.5)$$

it becomes possible to calculate the frequency dispersion curves. In Equation (1.5), \mathbf{K} and \mathbf{M} are the stiffness and mass matrix, respectively. The wave vector \mathbf{q} can be expressed in the reciprocal lattice. Due to the periodicity of the direct as well as the reciprocal lattice, it is possible to reduce the wave space to the first Brillouin zone (Brillouin, 1953). Therefore, in order to find the desired band gaps of the frequency dispersion diagram, it is sufficient to calculate \mathbf{q} along the boundaries of this irreducible Brillouin zone (Kittel, 1962). For clarity, the Brillouin zone for the unit cell considered is depicted in the bottom left of Figure 1.5(A), where q_x , and q_y assume values between 0 and b_z , while remaining on the contour of the Brillouin zone.

1.2.3 Static analysis

For the unit cell to work properly as an element of the foundation, it is necessary to build a static system from the infinite lattice of unit cells. A two-layered grid of unit cells was chosen as a starting point for the foundation. Due to the cubical shape of the cells, it is easy to conceive a framework of walls and slabs suited for the derivation of the static loads. The dispersion analysis of the unit cell resulted in a 4 by 4 meters cube with an outer wall thickness of 10 cm, as shown in Subsection 1.0. When these cells are set adjacent to each other, the outer walls can be combined as a rectangular grid with a wall thickness of 20 cm and a spacing of 4 m. The same holds true for the slab between the two layers of unit cells, which results in a thickness of 20 cm for the intermediate slab, while the static analysis resulted in a slab thickness of 35 cm for the top slab. Figure 1.2 shows the conception of the static system and its dimensions. Details of the foundation are shown in the bottom right of Figure 1.2(a), where the increased top slab and the soil-structure interface are represented.

For the present work, the soil was assumed to be bedrock, which allows the foundation to be sustained by line supports along the walls. Since the compression of the rubber, due to static loading, could influence the dynamic behavior of the system, the inner concrete cubes and the rubber coatings were considered as dead loads.

A sketch of the FE model of the static system is shown in both Figure 1.2(b) and Fig. 1.2(c). The calculation of both stresses and governing forces has been carried out with the FE software RFEM. All walls and slabs were modelled as shell elements with rigid connections to each other. The supports were modelled as simple line supports along the bottom edges of the walls. Once the static system was established, the loads of the tank, rubber and inner cubes were applied. The liquid was assumed to have the same density as water with a maximum liquid level of 15 m. The tank was modelled as a simple face load of 150 kN/m² and imposed on the foundation. A similar approach was chosen for the rubber and the inner concrete cubes. The weight of both the rubber and inner cubes corresponded to a total gravitational force of 1040 kN per cell. This force was then spread evenly across the slab between the layers of unit cells, which resulted in a face load of 65 kN/m². In order to comply with Eurocode 1990 requirements for the ultimate limit state of the foundation, all dead loads (including gravitational forces of walls and slabs) were multiplied by the partial load safety coefficient $\gamma_G=1.35$. Finally, all dimensions and steel reinforcements were checked according to the Eurocode 1992. Shear walls were verified for their compressive strength, while the slabs were reinforced with steel rebars.

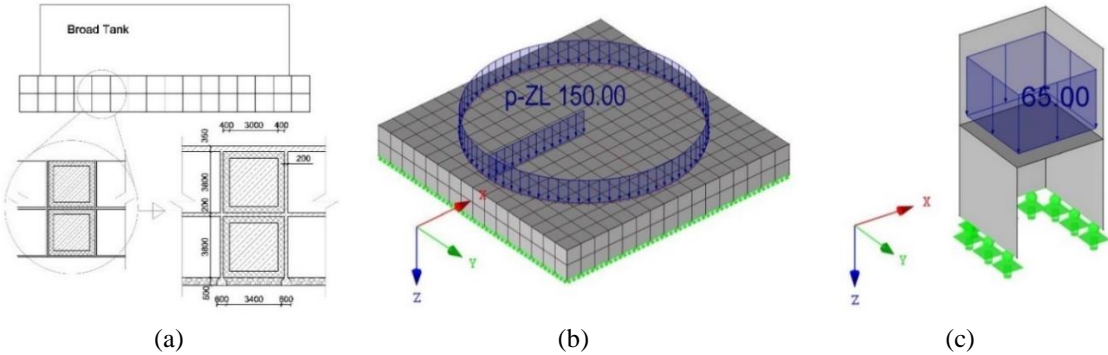


Figure 1.2 (a): Conception of a static system [Dimensions in mm]; (b): FE model of the foundation including the tank weight as a surface load [kN/m²]; (c): two unit cells on line supports including the weights of the rubber and inner concrete cubes as surf

With reference to the optimized unit cell design depicted in Figure 1.3(a), dimensions have been significantly reduced with respect to the original design. In particular, line moments decreased with the reduction of the span width by the power of two and the new slabs 200 mm thick suffice the Eurocode 1992 requirements. The columns of the optimized design need to be checked for their compressive strength. The relevant checks are presented in Subsection 1.3.

1.2.4 Materials

The first proposed model for the foundation consists of three components: the concrete resonator cubes, the rubber coatings and the reinforced concrete framework. For the concrete parts the strength grade was assumed to be C30/37 in agreement with Eurocode 1992, while the rubber was assumed to be construction grade silicon. Fuel storage tanks are commonly made of welded construction steel. For all FE models, the materials were considered homogeneous and linear elastic, and their main mechanical properties are collected in Table 1.1. The design of the optimized solution uses the same concrete as the original one, but replaces the rubber with steel springs as indicated in Figure 1.3(b). The spring stiffness k_2 has been tuned to provide a band gap with a lower bound at 2.4 Hz as discussed in Subsection 1.3.1. It was found that $k_2 = 3.7 \text{ MN/m}$.

Table 1.1 Mechanical properties of materials.

Material	Density [kg/m ³]	Elastic modulus [N/mm ²]	Bulk modulus [N/mm ²]	Poisson ratio [-]	Strength [N/mm ²]
Concrete C30/37	2500	30000		0.35	30 (compressive)
Rubber	1300	1.375		0.463	
Steel	7860	210000		0.3	235
Liquid	1000		2200	-	-
Reinforcement	7860	195000		0.3	550

1.2.5 Functionality evaluation of the original design

Due to the finite dimensions of the original foundation and the necessary redesign for its static behavior, the foundation can no longer be treated as an infinite lattice of perfectly equal unit cells. In order to determine the wave propagation properties, it is crucial to carry out additional computations, since the appearance of a stop-band in a finite structure is unrealistic. However, an attenuation zone is expected to appear in the frequency region of the predicted stop-band. In order to understand the behavior of the finite structure, two models are investigated: i) the first model of the foundation does not include the tank; ii) the second one contains the complete system, including the tank and the fluid inside. The optimized design was carried out similarly and is described in Subsection 1.2.6.

A horizontal harmonic acceleration was imposed at the bottom of the foundation. When comparing the response of the top of the foundation to the imposed wave, it becomes possible to show the effectiveness of the attenuation at a certain frequency. This results in a frequency response function of the type shown in Figure 1.8. The analysis was then carried out for a foundation with one, two and three layers. Furthermore, the foundation has also

been analyzed with a thinner concrete wall thickness, in order to see whether the horizontal stiffness of the structure has an influence on the attenuation behavior.

The FE model of the complete system, including foundation, tank and liquid as an acoustic medium, has 531684 DoFs. In order to minimize the computational effort due to the transient nature of seismic waves, all calculations were carried out in the frequency domain; accordingly, the steady-state response of the coupled system was checked for the frequencies of interest. In order to show the effectiveness of the attenuation, the steady state response of the broad tank on a traditional concrete slab foundation was compared to that of the tank sitting on the smart foundation. In particular, maximum accelerations of the uncoupled/coupled system were considered to be of special interest, since they correlate with the highest stresses appearing in the system.

1.2.6 Optimization of the unit cell

In order to reduce the foundation's size while maintaining its performance, the foundation was redesigned according to the results obtained in the Subsection 1.3.4 "Functionality evaluation". We found that: i) the shear stiffness plays an important role for the effectiveness of the foundation, see Figure 1.8; ii) the rubber, due to its fixed Elastic Modulus, constrains our design in terms of variability of the band gap. The two main advantages of the redesign are the reduction in stiffness, by replacing the walls with columns, and attaching the resonators to the columns with steel springs instead of rubber as indicated in Figure 1.3(B). As evident from Figure 1.8, the reduction of stiffness leads to a more pronounced attenuation zone, while the steel springs provide the option of tuning the boundaries of the unit cell's band gap. As a result, see Figure 1.3(A), the new dimensions of the unit cell are 3x3x1.5 m, 0.3x0.3 m column thickness, 0.2 m slab thickness and 2.5x2.5x1 m resonator size. Note that due to the reduction of the overall stiffness of the coupled system, the first impulsive frequency observed, decreased to 2.4 Hz, see Table 1.2, and, therefore, a band gap has to be tuned to this lower frequency. Furthermore, we assumed that the resonators move on a frictionless surface in the horizontal direction. This is a necessary assumption in order to keep the calculations linear for the frequency domain analysis.

The functionality evaluation of the optimized design followed the same steps presented in Subsection 1.2.5. However, in contrast to the model of the original design, the optimized cell variant was discretized with beam and shell elements, which further reduced the computational effort.

1.2.6.1 Analytical model of the optimized design

In order to investigate the metamaterial-like properties of the new design, we conceived an analytical model of the foundation and calculated both the frequency response and the dispersion analysis of unit cells. The main dimensions of the unit cell, the horizontal shear model and the 1D MDoF system are depicted in Figure 1.3(a), (b), and (c), respectively. This model allows only shear type waves that act in the horizontal and propagate in the vertical direction.

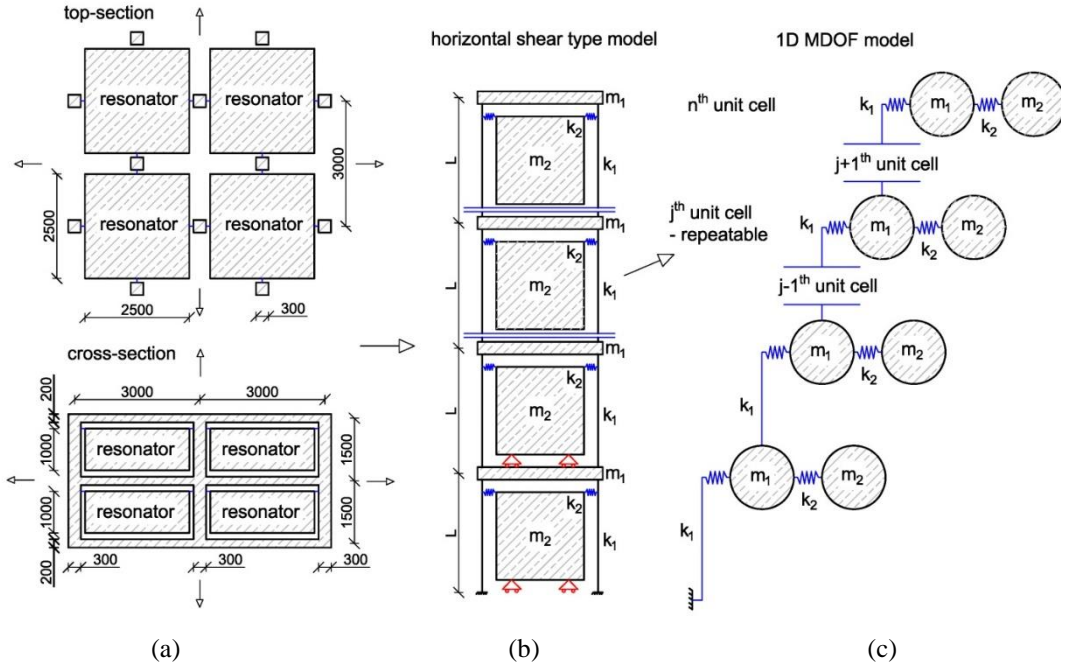


Figure 1.3 (a): Top-section and cross-section of the optimized foundation; (b): Simplified model for shear-wave propagation; (c): 1D mass-resonator chain model.

As can be seen in Figure 1.3 (c), the j^{th} unit cell can be repeated in order to achieve as many layers as desired. The equations of motion read,

$$m_1^j \frac{d^2 u_1^j}{dt^2} - k_1 u_1^{j-1} + k_1 u_1^j + k_2 u_1^j + k_1 u_1^j - k_2 u_2^j - k_1 u_1^{j+1} = 0 \quad (1.6)$$

$$m_2^j \frac{d^2 u_2^j}{dt^2} - k_2 u_1^j + k_2 u_2^j = 0 \quad (1.7)$$

where, m_1 denotes the mass of a slab between two layers of foundation including half the columns of the layer below and half the columns of the layer above; m_2 denotes the mass of the resonator; k_1 denotes the horizontal stiffness of two columns, which represents the equivalent stiffness of the columns pertaining to each resonator; k_2 represents the equivalent stiffness of the steel springs holding the resonator; and u describes the horizontal displacement. In order to relate the state variables across the system, the equations of motion must contain the displacement of the $(j-1)^{\text{th}}$ and $(j+1)^{\text{th}}$ unit cell. Therefore, u is endowed with a subscript (1, 2) that describes the corresponding mass, while the unit cell is determined by the superscript ($j-1, j, j+1$). For a finite system these equations can be written in matrix form. The generalized stiffness and mass matrix for a system with n unit cells reads,

$$K = \left[\begin{array}{c|cccc} 1 & k_1 + k_2 + k_1 & -k_2 & -k_1 & \dots \\ 2 & & -k_2 & k_2 & 0 & \dots \\ \vdots & & \vdots & \vdots & \ddots & \\ j^{th} & & & -k_1 & 0 & k_1 + k_2 + k_1 & -k_2 & -k_1 & \dots \\ j^{th} & & & \vdots & \vdots & -k_2 & k_2 & 0 & \dots \\ \vdots & & & & & \vdots & \vdots & \ddots & \\ n^{th} & & & & & & -k_1 & 0 & k_1 + k_2 & -k_2 \\ n^{th} & & & & & & & & -k_2 & k_2 \end{array} \right] \quad (1.8)$$

$$M = \left[\begin{array}{c|ccc} 1 & m_1 & & \dots \\ 2 & & m_2 & \dots \\ \vdots & \vdots & \vdots & \ddots \\ j^{th} & & & m_1 & \dots \\ j^{th} & & & & m_2 & \dots \\ \vdots & & & \vdots & \vdots & \ddots \\ n^{th} & & & & & m_1 \\ n^{th} & & & & & & m_2 \end{array} \right] \quad (1.9)$$

The relevant dispersion relation of the system can be found by imposing the Floquet-Bloch boundary conditions (1.4) on the equations (1.6) and (1.7), imposing a time-harmonic solution and looking for non-trivial solutions. The dispersion relation is given by:

$$m_1 m_2 \omega^4 - [(m_1 + m_2)k_2 + 2m_2 k_1 (1 - \cos(qL))] \omega^2 + 2k_1 k_2 (1 - \cos(qL)) = 0 \quad (1.10)$$

A similar solution has been found by (H.H. Huang et al. 2009), who analyzed the negative effective mass effect in an acoustic metamaterial. Here, ω denotes the circular frequency; L the length of the column or height of one layer; and q the wave number with dimension 1/m. The values for m_1 , m_2 , k_1 , k_2 , and L are 5850 kg, 15625 kg, 12e7 N/m, 3.6e6 N/m, and 1.5 m, respectively.

In order to compare the results provided by the numerical models, also quantitatively, damping ratios of 1, 3, and 5 % were imposed to 3 and 5 Hz by means of a Rayleigh model. Furthermore, a model with 1, 2, and 3 layers with damping of 5 % between 3 and 5 Hz was analyzed too.

1.3 Results

1.3.1 Modal analysis of a coupled broad-tank-foundation system

The analyzed broad tank with the maximum fluid level of 15 m anchored to a standard foundation has its first impulsive frequency at 4.15 Hz. On the other hand, for the same tank on the proposed smart foundation, the first impulsive frequency appears at 3.95 Hz. The corresponding impulsive mode shapes for the two foundation typologies are shown in Figure 1.4(a) and (b), respectively. The coupled system obtained from the optimized design exhibits its first impulsive frequency at 2.4 Hz and is depicted in Figure 1.4(c). It is apparent that the impulsive frequency for a tank on the smart foundation is lower than for one on a standard foundation and decreases even further for the optimized design.

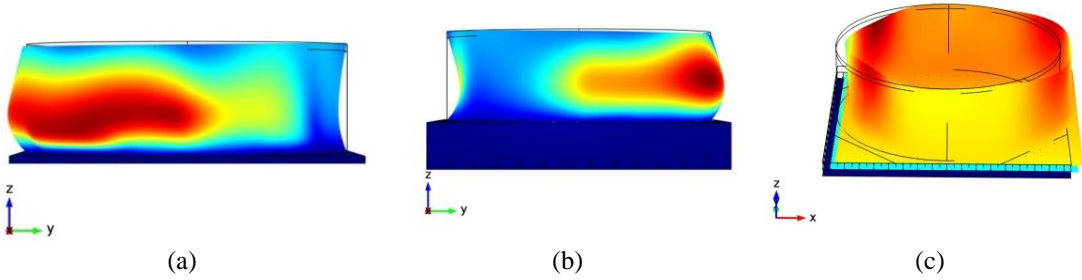


Figure 1.4 (a): first impulsive mode at 4.15 Hz for a broad tank on a traditional foundation; (b): first impulsive mode of a broad tank on the proposed smart foundation at 3.95 Hz; (c): first impulsive mode at 2.4 Hz for a broad tank on the optimized found

The impulsive frequency of the structure increases as the fluid level decreases. For this reason, the tank with a liquid level of 12 m was also studied. Relevant outcomes of the modal analysis for the two tank configurations are reported in Table 1.2. On the basis of these results, a frequency region that covers both frequencies for each tank would be desirable. Due to the fact that the fluid level can drop below 12 m, band gaps that stretch even beyond the increased impulsive frequency of the 12 m fluid level constellation were chosen for all the designs. For the standard tank this resulted in an aspired frequency region between 3.5 Hz and 6 Hz, while the optimized design was aimed at a frequency range between 2.40 Hz and 4.5 Hz.

Table 1.2 First impulsive eigenfrequencies of broad-tank-foundation systems with various liquid heights.

Foundation typology	Liquid level height [m]	Impulsive frequency of the tank [Hz]
Traditional	15	4.15
	12	4.95
Smart	15	3.95
	12	4.80
Optimized	15	2.40
	12	3.70

1.3.2 Unit cell design of the original smart foundation

The unit cell was studied as a 2D problem in Comsol Multiphysics. When applying the Floquet-Bloch boundary conditions introduced in Subsection 1.1.2.2, the dispersion relation can be obtained by calculating the eigenfrequencies of the system for different values of the wave vector \mathbf{q} . Therefore, it is sufficient to calculate the eigenfrequencies along the

boundaries of the Brillouin zone, depicted for clarity, in the bottom left of Figure 1.5(a). Here, T, X, M mark the corners of the Brillouin zone, while b_z denotes the edge length, which amounts to $\pi/a = 0.7854$ 1/m, where a defines the size of the unit cell.

Our parametric study shows that a unit cell with side length, outer wall thickness, rubber coating and inner concrete cube size equal to 4 m, 0.1 m, 0.4 m and 3 m, respectively, see Figure 1.5 (a), creates a band gap with a lower bound of 3.5 Hz and an upper bound of 6.4 Hz as highlighted in Figure 1.5 (b). By looking at the results in Table 1.2, this configuration represents the optimal design to reduce tank vibrations in the frequency range where waves can cause the greatest damage.

Note that the shear wave velocity is very close to the pressure wave velocity for the diagonal path M to T of the Brillouin zone. Therefore, the shear wave branch is almost coincident with the pressure wave branch in both Figure 1.5(b) and 1.15(b).

The effectiveness of the proposed solution in the low frequency range is in line with the results presented by Achaoui et al. (2016), who proposed iron spherical resonators endowed with ligaments embedded in soil. However, the actual feasibility of their interesting design proposal has yet to be investigated.

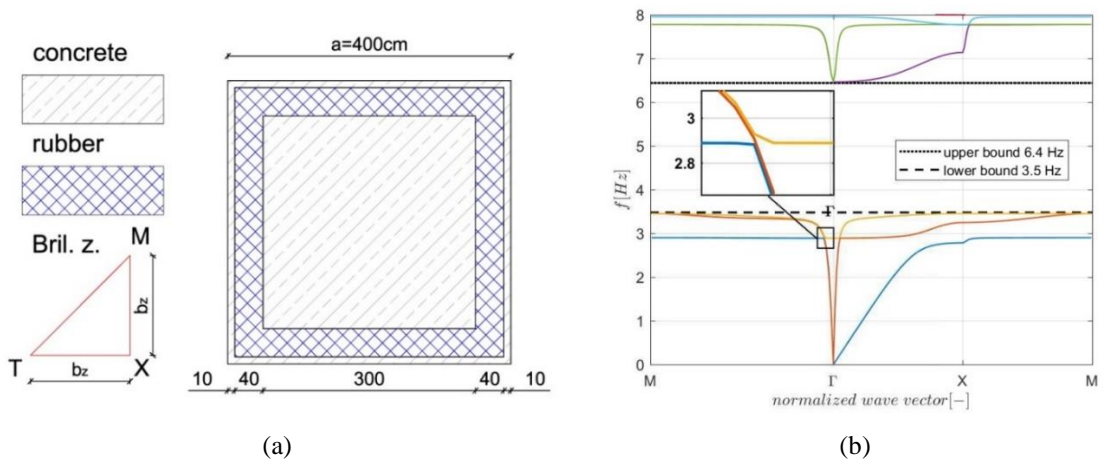


Figure 1.5 (a): The unit cell and its Brillouin zone (dimensions in cm); (b): Dispersion analysis of the unit cell.

1.3.3 Static analysis

Three essential components have to be verified under static loads for the original design: the top slab, the walls and the intermediate slab. When the system is subjected only to static loads, the walls need to resist only compressive stresses. According to Eurocode 1992, it is sufficient to verify that the compressive stress is lower than the design strength of concrete. As stated in Section 1.2.4 Materials, a strength grade of C30/37 was assumed. Since the maximum stress of 3.6 N/mm² shown in Figure 1.6(a) is below the design strength of 20 N/mm², the walls are checked for gravity loads.

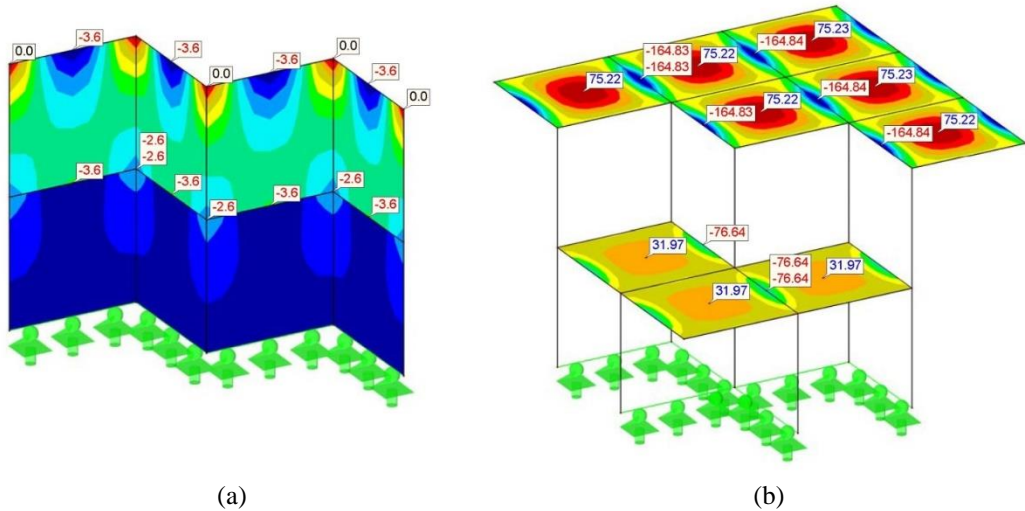


Figure 1.6 (a): compressive stresses in the walls at the ultimate limit state [N/mm²]; (b): line bending moments in slabs at the ultimate limit state [kNm/m].

The slabs need to sustain the flexural moments produced by static loads. This results in tension regions in the concrete matrix, see Figure 1.6(b), which need to be reinforced in order to offer sufficient load-bearing capacity. Additionally, for corrosion protection a minimum concrete cover of the reinforcement bars is needed. Since the present work considers a general case, the concrete cover was chosen to be 5 cm, which satisfies most exposition classes mentioned in Eurocode 1992. Given the negative line moment of -164.84 kNm/m at the ultimate limit state in the top slab above the walls, see Figure 1.6(b), the final chosen dimensions are 35 cm for the plate thickness and 12.12 cm²/m for the reinforcements depicted in Figure 1.7(a) top left. A grid of 8 rebars with a diameter of 14 mm is sufficient for this part of design. Due to the symmetry of the system, the moments are the same in x and y direction. Therefore, the selected grid has to be set in both directions. The lower layer of reinforcements needs to cover a maximum moment of 75.22 kNm/m in the slab, which results in a minimum reinforcement area of 5.39 cm²/m indicated in Figure 1.7(b) top right. A grid of 11 reinforcement bars per meter with a diameter of 8 mm fulfills the requirement.

The intermediate slab shows bending moments of -76.63 kNm/m above the walls and 31.97 kNm/m in the fields. When setting the slab thickness to 20 cm, the necessary reinforcement has to be 11.89 cm²/m for the top layer, see Figure 1.7(c) bottom left, and 4.64 cm²/m for the lower layer of reinforcements, look at Figure 1.7(d) bottom right. Thus, the same reinforcement grid chosen for the top slab was also sufficient for the intermediate slab.

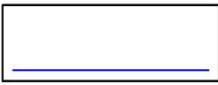
<p>Top Slab Wall</p> <p>As=12.12 cm²</p> 	<p>Strain</p> <p>$\epsilon_s=2\%$</p>  <p>$\epsilon_c=-0.288\%$</p>	<p>Top Slab Field</p> <p>As=5.39 cm²</p> 	<p>Strain</p> <p>$\epsilon_c=-0.159\%$</p>  <p>$\epsilon_s=2\%$</p>
<p>Interm. Slab Wall</p> <p>As=11.89 cm²</p> 	<p>Strain</p> <p>$\epsilon_s=1.145\%$</p>  <p>$\epsilon_c=-0.35\%$</p>	<p>Interm. Slab Field</p> <p>As=4.64 cm²</p> 	<p>Strain</p> <p>$\epsilon_c=-0.232\%$</p>  <p>$\epsilon_s=2\%$</p>

Figure 1.7 Summary of results for: (a): top slab above wall (top left); (b): the top slab in the field (top right); (c): intermediate slab above wall (bottom left); (d): intermediate slab in field (bottom right).

The preliminary static evaluation of the optimized cell has been carried out as before. For the sake of brevity, only the design of columns is presented, while the remaining checks have been omitted. More precisely, the compressive concrete stresses in the columns of dimension 0.3x0.3 m amount to 18 N/mm². This figure must be compared with a design strength of 20 N/mm² and, therefore, the optimized design is statically valid.

1.3.4 Functionality evaluation

The frequency response function at the top of the foundation for a sinusoidal excitation of amplitude 1 m/s², plotted in Figure 1.8, shows a clear attenuation zone in the frequency region from 3.5 Hz to 6.4 Hz. In this frequency region, a reader can observe that the acceleration output at the top of the foundation is smaller than the input at its bottom. An amplification area appears in the frequency region below 3.5 Hz, which is not relevant for the seismic protection of the tank. Furthermore, the influence of the number of unit cell layers has been studied. The diagrams of Figure 1.8 show that the number of layers is clearly connected to the attenuation effectiveness. Moreover, the effectiveness of another model with a decreased concrete wall thickness from 20 cm to 10 cm has been evaluated. The comparison of Figure 1.8(a) with Figure 1.8(b) highlights that a smaller wall thickness enhances the attenuation behavior and increases the intensity of the amplification area.

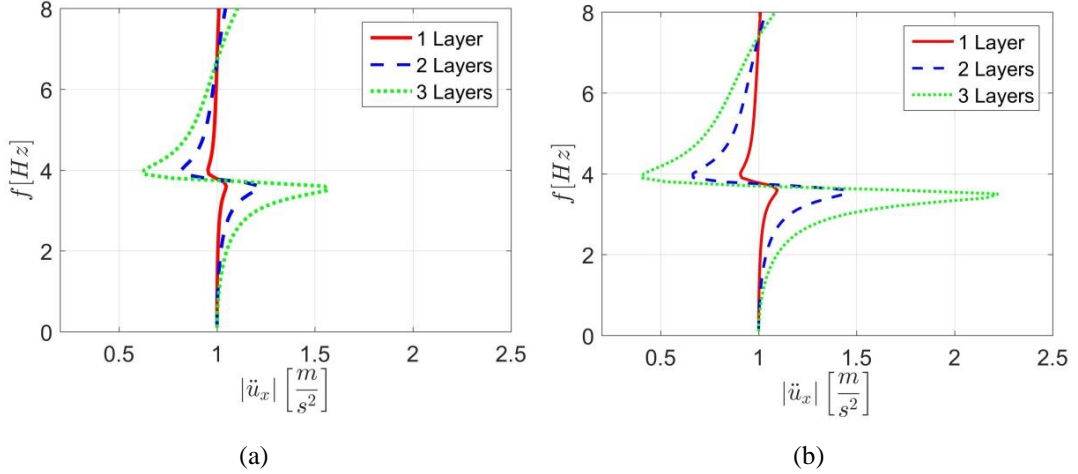


Figure 1.8 (a): acceleration response at the top of the foundation with a wall thickness of 20 cm;
 (b): acceleration response with a wall thickness of 10 cm.

In order to compare foundation typologies, the response of the complete coupled (foundation+tank) system has been studied. The model is depicted in Figure 1.1(b) and was analyzed with a concrete wall thickness both of 20 cm and 10 cm. For the sake of brevity, only the results corresponding to the wall thickness of 10 cm are reported herein, due to its increased effectiveness. Since the maximum acceleration does not appear at the top of the tank, the maximum acceleration along the full height of the tank wall was plotted. The comparison in terms of maximum acceleration in the frequency domain between the smart and a traditional foundation is shown in Figure 1.9(a); the attenuation and advantages of using the smart foundation become clearly visible. Finally, the analysis of the tank with a fluid level of 12 m has been performed. Relevant outcomes in terms of accelerations are reported in Figure 1.9(b). A careful reader can note that the attenuation due to the smart foundation is still clear but less pronounced than in the case of a fully filled tank.

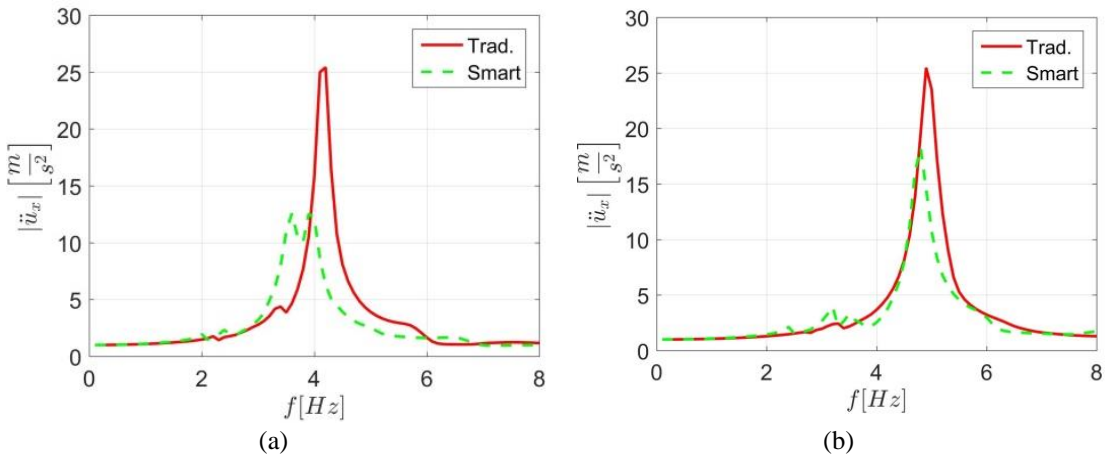


Figure 1.9 (a): maximum acceleration response function of the tank wall for traditional and smart foundation;
 (b): acceleration responses for a tank with a reduced liquid height of 12 m.

In order to complement the FRF analysis, a transient analysis of the structure subjected to a real earthquake signal -Northridge (1994) in Fig. 1.10- is carried out.

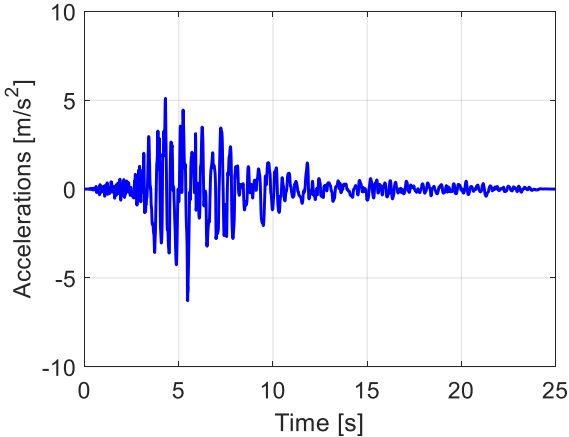


Figure 1.10 The Northridge earthquake signal

The analysis covered the first 10 seconds of the signal, i.e. the strongest part. The maximum acceleration along the tank shell was monitored and a comparison between the two foundation typologies is provided in both Figs. 1.11 and 1.12.

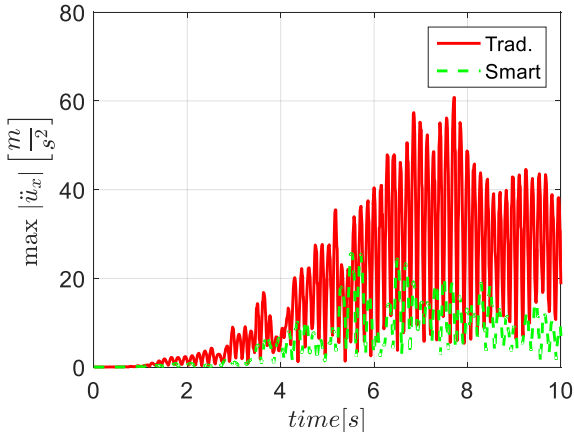


Figure 1.11 Time histories of maximum absolute values of accelerations along the tank shell

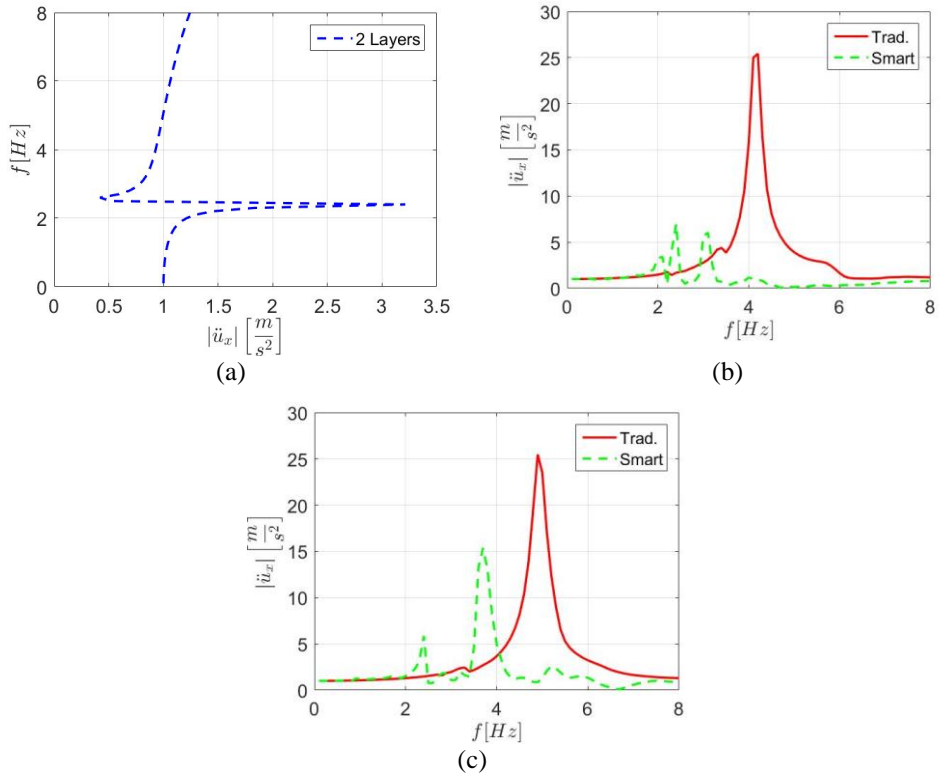
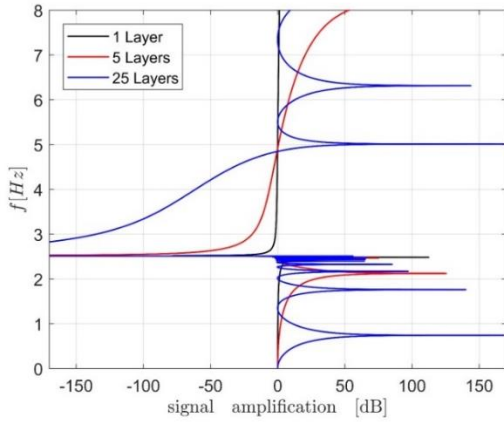


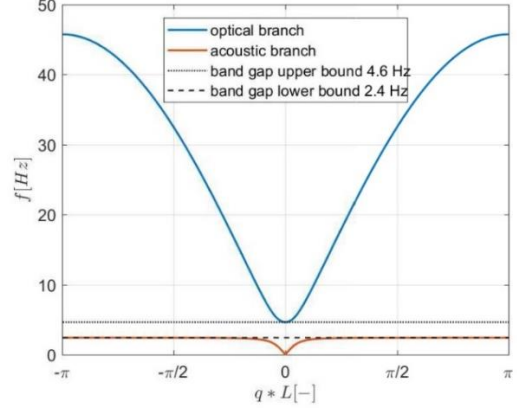
Figure 1.13 (a): Frequency response function of the optimized foundation alone subjected to a base acceleration of 1 m/s^2 ; (b): Tank response for a fully filled tank, on the optimized foundation, for a base acceleration of 1 m/s^2 [m/s^2]; (c): Tank response for a 12 meters filled tank, on the optimized foundation, for a base acceleration of 1 m/s^2 [m/s^2];

1.3.5.2 Analytical model of the optimized cell

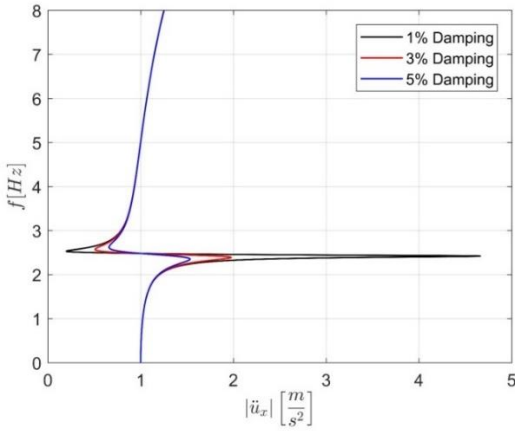
In order to ascertain the results of our numerical study, we carried out various calculations on the analytical model introduced in Subsection 1.2.6.1. Firstly, we performed a frequency response analysis on the model with 1, 5, and 25 layers. Also in this case, a base excitation \ddot{u}_{in} of amplitude 1 m/s^2 was selected and compared to the output \ddot{u}_{out} at the top of the foundation. As shown in Figure 1.14(a), the foundation exhibits a distinctive attenuation zone that increases with the number of layers. This calculation was carried out without damping and is depicted in decibel dB ($20 \cdot \log(\ddot{u}_{out}/\ddot{u}_{in})$). Furthermore, we were interested whether a dispersion analysis of the system would yield a band gap in the predicted attenuation zone. Figure 1.14(b) shows the dispersion relation and the corresponding band gap of an infinite stack of unit cells, calculated with (1.10). In order to check how well the analytical model represents the numerical one and whether the analytical model can be used for further optimization investigations, we also conducted calculations on a damped system. Relevant results are shown in Figure 1.14(c) and 1.14(d) for Rayleigh damping of 1, 3, and 5 % imposed to both 3 Hz and 5 Hz. Moreover, an analytical study on the damped system (5 % of Rayleigh damping for both 3 Hz and 5 Hz) with a variation of the layers is reported in Figure 1.14(d). Relevant results are discussed in Section 1.4.



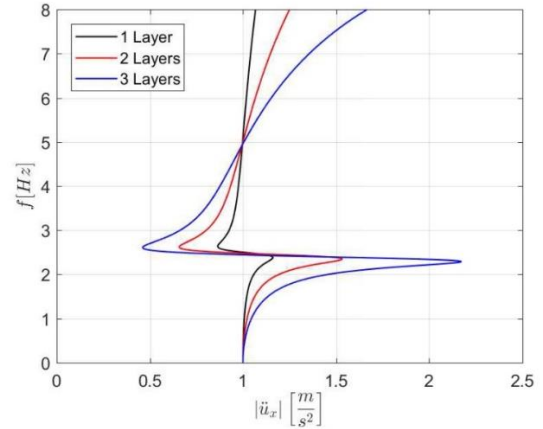
(a)



(b)



(c)



(d)

Figure 1.14 (a) Undamped frequency response function for 1, 5, and 25 layers of foundation for a base excitation of 1 m/s²; (b) dispersion relations for the optimized unit cell; (c) frequency response function of the analytical model for two layers and Rayleigh damping of 1, 3, and 5%; and (d) frequency response function of the analytical model with 5% Rayleigh damping and 1, 2, and 3 layers.

1.3.6 Influence of small cracks

In order to assess the influence of small cracks on elastic wave propagation, a cracked cell of the smart foundation was investigated. In fact, as shown in Figure 1.6(b) of Subsection 1.3.3, the maximum bending moment is located where the slabs join the walls. Due to the resulting tension in concrete, small cracks appear in the area close to the internal boundaries of the walls. Therefore, the cracks were modeled as 5 cm-deep and 1 cm-wide physical gaps with no stiffness as indicated Figure 1.15(a). This was considered a conservative approach, since the presence of reinforcement bars was neglected in the cracks. In particular, two adjacent cubes along the vertical direction were endowed with small cracks and modeled in Comsol imposing Floquet-Bloch conditions.

The relevant dispersion analysis, shown in Figure 1.15(b), must be compared to the results depicted in Figure 1.5(b) that corresponds to the uncracked unit cell. The comparison shows

that the presence of small cracks slightly modifies the group velocity of propagating elastic waves.

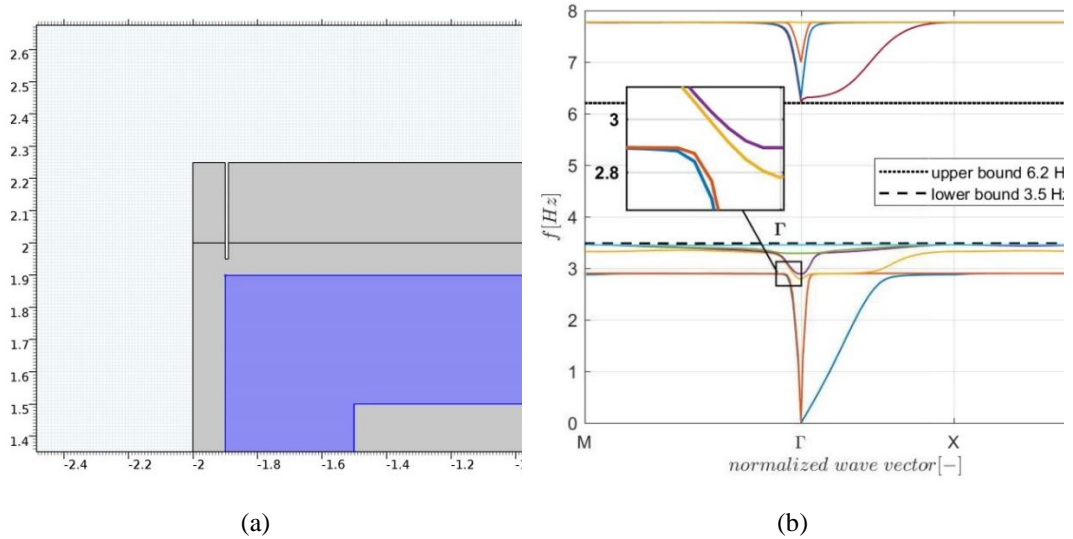


Figure 1.15 (a): Crack modeled as a physical gap in the slabs due to static loads [dimensions in m]; (b): Dispersion analysis of the cracked foundation sector.

1.4 Discussion

In Subsection 1.0, we showed the dispersion relation of a unit cell that suits the needs for the isolation of a broad tank introduced in Subsection 1.3.1, with the first foundation design. Based on this unit cell, we designed a foundation and checked its static and dynamic properties in Subsection 1.3 and 1.3.4, respectively. The static analysis proved that the design is feasible, while the functionality evaluation showed that the metamaterial concept is applicable even for a finite foundation. The construction practice is assumed to be in situ for the present study. Furthermore, the first design of the foundation was rather excessive in size and needed to be reduced. Based on the functionality evaluation, where in Subsection 1.3.4 we found a correlation between the shear stiffness of foundation walls and the attenuation effectiveness, we introduced a new design that improves the isolation performance of the foundation and reduces its size. The optimized design includes columns instead of walls, in order to reduce its shear stiffness, and replaces the rubber with uniaxial steel springs, which make the structure more versatile. The new design discussed in Subsection 1.1.3.5 showed promising results by steady state analyses with a reduction of the foundation from 8m to 3m in height, while improving its performance. Besides this, we verified the results with an analytical model that returned very similar outcomes compared to numerical calculations and showed that the new design still exhibits band gaps. The small discrepancy between the results with the damped analytical model shown in Figure 1.14(c) and 1.14(d) and those of the numerical model presented in Figure 1.13(a) are mainly due to the difference between the two models, continuous and discrete, as well as the consequences of the imposed Raileigh damping. Additionally, in order to determine the potential influence

that static cracks can have on the dispersion analysis, a crack investigation was carried out. The relevant results obtained in Subsection 1.3.6 compared to those of Subsection 1.3 prove that this issue can be neglected for the isolation design of the foundation.

1.4.1 Conclusions and future developments

In order to check the feasibility of a metamaterial-based foundation for seismic application we conceived a smart foundation that was also designed and checked for gravity loads. As a result, we found that such a structure can be realized in accordance with the Eurocode standards while maintaining favorable band-gap like properties against seismic waves. In particular, we designed two versions of the smart foundation bearing a fuel storage tank with a varying fluid level and we showed that the proposed designs can attenuate the resulting frequency range. In addition, we found that the shear stiffness of the foundation due to lateral concrete walls has a significant impact on the attenuation efficiency, and, subsequently, we proposed an optimized design where the walls were replaced with less stiff concrete columns. Though the proposed smart foundation was able to attenuate the impulsive frequencies of the fuel storage tank under different liquid levels, it cannot yet be considered as a fully optimized solution. In particular, the dynamic behavior of the system with other liquid levels needs to be investigated, as well as the performance of the coupled system under several seismic waves. Moreover, soil-structure interaction will be taken into account; especially for the benefit that soil flexibility can entail for vertical seismic excitations or vertical motions of the coupled (foundation+tank) system. Finally, given the main drawback of standard isolators, i.e. the inherent high vertical stiffness, we expect that the use of the investigated foundation for large structures characterized by rocking motion can reveal great innovative potential and undiscovered advantages.

Chapter 2

2. A Composite Experimental Dynamic Substructuring Method Based on Partitioned Algorithms and Localized Lagrange Multipliers

by Giuseppe Abbiati, Vincenzo La Salandra, Oreste S. Bursi, Luca Caracoglia

Abstract

Successful online hybrid (numerical/physical) dynamic substructuring simulations have shown their potential in enabling realistic dynamic analysis of almost any type of non-linear structural system (e.g., an as-built/isolated viaduct, a petrochemical piping system subjected to non-stationary seismic loading, etc.). Moreover, owing to faster and more accurate testing equipment, a number of different offline experimental substructuring methods, operating both in time (e.g. the impulse-based substructuring) and frequency domains (i.e. the Lagrange multiplier frequency-based substructuring), have been employed in mechanical engineering to examine dynamic substructure coupling. Numerous studies have dealt with the above-mentioned methods and with consequent uncertainty propagation issues, either associated with experimental errors or modelling assumptions. Nonetheless, a limited number of publications have systematically cross-examined the performance of the various EDS methods and the possibility of their exploitation in a complementary way to expedite a hybrid experiment/numerical simulation. From this perspective, this paper performs a comparative uncertainty propagation analysis of three EDS algorithms for coupling physical and numerical subdomains with a dual assembly approach based on localized Lagrange multipliers. The main results and comparisons are based on a series of Monte Carlo simulations carried out on a five-DoF linear/non-linear chain-like systems that include typical aleatoric uncertainties emerging from measurement errors and excitation loads. In addition, we propose a new Composite-EDS (C-EDS) method to fuse both online and offline algorithms into a unique simulator. Capitalizing from the results of a more complex case study composed of a coupled isolated tank-piping system, we provide a feasible way to employ the C-EDS method when nonlinearities and multi-point constraints are present in the emulated system.

2.1 Introduction

2.1.1 Background and motivation

In the field of simulation-based science and engineering, there are several challenges posed by the *virtual structural testing* of complex systems, e.g. the curse of dimensionality,

the treatment of uncertainties, adequate parametric modelling, process/shape optimization, etc. (Neron and Ladeveze, 2010). The fundamental issue is that all these problems cannot be easily solved using standard numerical methods. As an example, Chinesta and his co-workers (Chinesta et al., 2013) have actively developed and implemented the proper generalized decomposition (PGD) method to address the simulation of high-dimension physical systems. The PGD can be viewed as an approach to enhance the reduced-order modelling; it is based on the numerical approximation of the unknown fields (or variable spaces) by subsequent separation of variables, successively enriched, involving a set of a-priori unknown functions of clustered coordinates (or degrees of freedom). However, difficulties still persist in relation to the solution of both non-linear models and stochastic problems requiring multiscale and multiphysics methods. In this context, the DSC method is very powerful because it can simulate system non-linearities and enable the identification and updating of damaged components/sub-systems. Thus, when the properties of one or more sub-systems are altered, the modified sub-systems alone need to be re-analyzed whilst other sub-structures are unchanged and no further analysis is needed (de Klerk et al., 2008).

Owing to DSC, the numerical/physical HDS represents a form of online simulation, which has been shown to be very efficient in solving non-linear structural dynamic problems (Bursi and Wagg, 2008; Pan et al., 2016). In particular, the HDS isolates the physical sub-system(s) (PS), which is experimentally tested since it contains a key region (or component) exhibiting non-linear behavior, from the remainder of the system, which is numerically simulated, i.e. the numerical sub-system(s) (NS). In this context, the term online indicates that a time stepping algorithm solves the system of equations of motion of the global emulated system whilst the PS response, which is treated in a FE fashion, is being measured. In detail, at each iteration of the simulation loop, a set of servo-controlled actuators imposes displacement/velocity predictors to the PS boundary and feeds back corresponding restoring forces to the time stepping algorithm, which solves the coupled equations of motion. The ratio between the wall-clock time taken by the HDS simulator to solve a single time step and the time step size itself is named testing time scale. Real-time indicates a testing time scale equal to one whilst both fast-time and pseudodynamic testing consider testing time scales larger than one, which can be afforded when the PS restoring force is rate independent. Since the inertial component of the PS restoring force measured by load cells reduces of a factor proportional to the square of the testing time scale, hardware-in-the-loop testing, which treats the PS as a black-box, always runs in real time. However, when an extended time scale is adopted, physical inertia must be numerically accounted for. This is the so called substructuring approach, which imposes to numerically solve the PS system of equation of motion as analogously done for the NS. In addition, it is important to stress that mass at interface degrees-of-freedom (DoFs) can be virtually moved from NS to PS. Although this could sound as an unnecessary complication, such approach allows for controlling the stability of the coupled simulation (Bursi et al., 2008). As an example of application to a civil engineering structure, both an as-built viaduct and the corresponding isolated and retrofitted structure, equipped with substructured sliding bearings, were part of a comprehensive investigation to evaluate the structural response under several earthquake ground motions (Abbiati et al., 2015). In particular, the HDS method was employed to study two 1:2.5 scale specimens of single-bay RC frames with 2 levels (total height, 7.0 m) and 3 levels (total height, 11.5 m) at the European Laboratory for Seismic Assessment (ELSA) of

the Joint Research Center of the European Community. Model reduction and updating were successfully used for the numerical modelling of pier/sliding bearings. In addition, parallel partitioned time integration algorithms played a crucial role, because the inherent subcycling capabilities enabled the synchronization of two separated integration processes (with a fine and a coarse integration time step), which were implemented to simultaneously solve the PSs and NSs, respectively (Bursi et al., 2017). More recently, the HDS method was applied to the seismic evaluation of critical industrial piping systems, by testing real components of full-scale three-dimensional piping systems in the laboratory without the need to physically model the whole piping/tank system (Bursi et al., 2014). For this purpose, two relatively inexpensive electrohydraulic actuators were employed to avoid the complexity of shaking table tests. Appropriately calibrated a-posteriori reduction of bases enabled the extension of the DSC to the PS, characterized by distributed masses (piping equipment, water mass, etc.) In addition, the real time LSRT2 time-stepping algorithm (Bursi et al., 2008) established a more general framework that simultaneously combines time integration algorithms, model reduction, system identification and control. In summary, HDS appears to be a very versatile method that can be applied to any class of multiphysics and multiscale engineering problems with strong/weak nonlinearities (Bursi et al., 2017; Turso et al., 1995; Stansberg et al., 2002). When HDS is applied to a complex mechanical system, such as the aforementioned piping system subjected to seismic loading (Bursi et al., 2014), some issues arise. For instance, the piping system response is characterized by weak and localized non-linearities in elbows, flange joints, tee joints; modal damping is low (of the order of 1.5 per cent); proper boundary conditions are difficult to reproduce, etc. (Bursi et al., 2014). Therefore, adequate identification of modal damping and boundary conditions, especially at the interfaces where substructures are split, become crucial for the fidelity of heterogeneous simulations.

Due to faster and more accurate testing equipment, the DSC method has been broadly employed in mechanical engineering through the implementation of several experimental substructuring methods (de Klark et al., 2008). We recall here the IBS method (Rixen and Van der Valk, 2013; Van der Valk and Rixen, 2014); it evaluates the response of a full (emulated) system by computing the responses of its substructures through a discretization of the Duhamel integral and the enforcement of the interface compatibility at every time step. Moreover, we recall the so-called Lagrange multiplier FBS (LM-FBS) method (Voormeeren et al., 2010), which transposes the IBS method to the frequency domain. It has been recently employed to quantify the uncertainties of coupled systems' frequency response functions (FRFs), propagated in the measured substructure FRFs. Both LM-FBS and IBS are offline methods that can quickly characterize the response of linear PSs by means of experimental and operational modal analysis tools. Therefore, they appear to be suitable methods for complementing certain modeling phases of the online HDS method. In this regard, the PM method, which is a parallel variant of the staggered GC method, was originally conceived for performing pseudo-dynamic testing at the ELSA facility. Nonetheless, the HDS algorithm (PM and GC) presented in this paper can be used both in the real time and the pseudo-dynamic regime. This depends on: i) the complexity of the NS that can be endowed with complex non-linear parts; b) the efficiency of delay compensation procedures for the transfer systems (actuators) (Wu et al., 2013).

2.1.2 Scope

Even though a plethora of studies has dealt with EDS methods both in mechanical and civil engineering (de Klerk et al., 2008; Pan et al., 2016) along with consequent error propagation issues (Rixen and Van der Valk, 2013; Mosqueda et al., 2007; Song and Dyke, 2013; D'Ambrosio and Fregolent, 2009; Culla et al., 2011), very few publications have been devoted to: i) the systematic performance comparison among the various methods from a more general uncertainty propagation setting; ii) the possibility of exploiting these methods in a synergic way to both improve and expedite the overall experiment/simulation. As a matter of example, the online HDS method, which can operate in real time with proper delay compensation, can easily accommodate strongly non-linear PSs with rate-dependent behavior. On the other side, both LM-FBS and IBS are offline methods that can quickly characterize the response of linear PSs by means of operational and experimental modal analysis tools. Therefore, they appear to be suitable methods, capable of complementing certain modelling phases of HDS. All together, they represent the basic components of the state-of-the-art simulation methods based upon the principle of fusing numerical and experimental methods, and the comparison of their performances and fusion is explored hereinafter as well as their combination.

The remainder of the paper is organized as follows. Section 2.2 illustrates the newly conceived C-EDS method, which relies on partitioned algorithms (Farhat and Roux, 1991; Gravouil and Combescure, 2001) for connecting multiple substructures of heterogeneous systems with a dual approach. In this context, an online and two offline EDS algorithms are presented and recast in accordance with the method of localized Lagrange multipliers (LLMs) (Park et al., 2000), which facilitates the derivation of compatibility equations in case of multi-point constraints due to the interaction of several interacting substructures. Various experimental sources of uncertainty affect the measured PS response. From this perspective, Section 2.3 performs a comparative uncertainty propagation analysis based on Monte-Carlo Simulation (MCS) of all presented EDS algorithms. In detail, both a linear and a non-linear variant of a 5-DoFs benchmark system, which is split into a PS and a NS, are considered and probability distributions of main sources of uncertainty are characterized after laboratory measurements. In order to highlight the feasibility of the C-EDS method in combining radically different EDS algorithms, Section 2.4 describes a virtual experiment conducted on a petrochemical prototype plant case study. This heterogeneous system combines a piping network -PS #1-, an array of four Concave Sliding Bearings (CSB) -PS #2- and a simplified model of a liquid storage tank with sloshing fluid -NS #1-. Both NSs and PSs are consistently simulated with the relevant EDS technique. As a result, versatility and advantages of fusing both online/offline methods are demonstrated. Finally, main conclusions are drawn with future perspectives.

2.2 A framework for composite online/offline experimental dynamic substructuring methods

When part of the emulated system lacks a predictive computational model, measuring (instead of modelling) its response represents a convenient approach for deriving low-discrepancy simulators with reduced cost and effort. In this regard, the EDS paradigm provides the response history of a so-called emulated system that includes PSs and NSs (Bursi et al., 2017).

The class of EDS methods is divided into online and offline algorithms, depending on the strategy adopted for the calculation of the emulated system response. In the online case, primal/dual boundary conditions imposed to the PS, e.g. displacements/forces, are updated at each step of the simulation and corresponding dual/primal boundary conditions, e.g. force/displacement, enter into a time integration algorithm, which solves the system of equilibrium equations and advances to the next step. Real-time computing synchronized with precise servo-controlled actuators is crucial for the implementation of the simulation loop. Conversely, offline EDS algorithms require all experimental data to be measured prior to the calculation of the emulated system response. In this case, less expensive and dangerous operational and experimental modal analysis tools such as accelerometers, impulse hammers and shakers are used to characterize the PS response.

2.2.1 The combined experimental dynamic substructuring framework

Non-linear PSs justify the use of online EDS algorithms whilst offline EDS methods are more convenient when PSs exhibit a linear behavior. On this basis, the need for simulating the seismic response history of an industrial prototype plant, substructured into linear and non-linear PSs, motivated the authors to develop a substructuring framework where online and offline EDS algorithms interoperate, i.e. the C-EDS method. In addition, to couple several PSs and NSs using possible multi-point constraints, we adopt the LLMs for dual assembly of subdomains.

The following subsections summarize both the LLM method and an online and two offline state of the art algorithms, which can be profitably combined.

2.2.2 The localized version of the method of Lagrange multipliers

In a primal formulation, a unique set of interface DoFs is retained. Classically, FE models are assembled in this primal manner (de Klerk et al., 2008). Conversely, in a dual assembly formulation, all subdomains' DoFs are retained, all interface DoFs are present as many times as there are subdomains connected to the same DoF; an additional set of Lagrange multipliers enforces compatibility (Gravouil and Combescure, 2001). Although it may sound inconvenient to treat subdomains as separated in a pure numerical context at the price of adding further system unknowns (Lagrange multipliers), this is not the case in EDS. In fact, only the dual approach allows for tailoring algorithms and implementations to specific requirements on single (physical or numerical) subdomains, which guarantee both stability and accuracy.

From this perspective, the localized version of the method of LLM, can provide a dual assembly framework for connecting multiple NSs and PSs within the C-EDS method. It is well known that the classical method of Lagrange multipliers (CLM) allows for multiple sets of interface compatibility equations for the modeling of interfaces connecting more than two subdomains by the same DoF. Nonetheless, to avoid singularity in modeling an arbitrary number of multi-point constraints, Park et al. (2000) proposed a localized version of the CLM method.

In order to elucidate the use of the LLMs as method for dual assembly within the C-EDS framework, let us consider the following system of differential algebraic equations (DAE), in which m mechanical subdomain are coupled by LLMs,

$$\begin{cases} \mathbf{M}^{(l)}\ddot{\mathbf{u}}^{(l)} + \mathbf{R}^{(l)}(\mathbf{u}^{(l)}, \dot{\mathbf{u}}^{(l)}) = \mathbf{L}^{(l)T} \boldsymbol{\Lambda}^{(l)} + \mathbf{F}^{(l)}(t) \\ \mathbf{L}^{(l)}\mathbf{u}^{(l)} + \bar{\mathbf{L}}^{(l)}\mathbf{u}_g = \mathbf{0} \text{ or } \mathbf{L}^{(l)}\dot{\mathbf{u}}^{(l)} + \bar{\mathbf{L}}^{(l)}\dot{\mathbf{u}}_g = \mathbf{0} \end{cases} \quad \forall l \in \{1, \dots, m\} \quad (2.2.1a)$$

$$\sum_{l=1}^m \bar{\mathbf{L}}^{(l)T} \boldsymbol{\Lambda}^{(l)} = \mathbf{0} \quad (2.2.1b)$$

where, $\mathbf{M}^{(l)}$ and $\mathbf{R}^{(l)}$ are the mass matrix and the restoring force vector of the l -th subdomain, respectively, whilst $\ddot{\mathbf{u}}^{(l)}$, $\dot{\mathbf{u}}^{(l)}$ and $\mathbf{u}^{(l)}$ denote acceleration, velocity and displacement vectors. For a linear system, $\mathbf{R}^{(l)}$ reads,

$$\mathbf{R}^{(l)}(\mathbf{u}^{(l)}, \dot{\mathbf{u}}^{(l)}) = \mathbf{K}^{(l)}\mathbf{u}^{(l)} + \mathbf{C}^{(l)}\dot{\mathbf{u}}^{(l)} \quad (2.2.2)$$

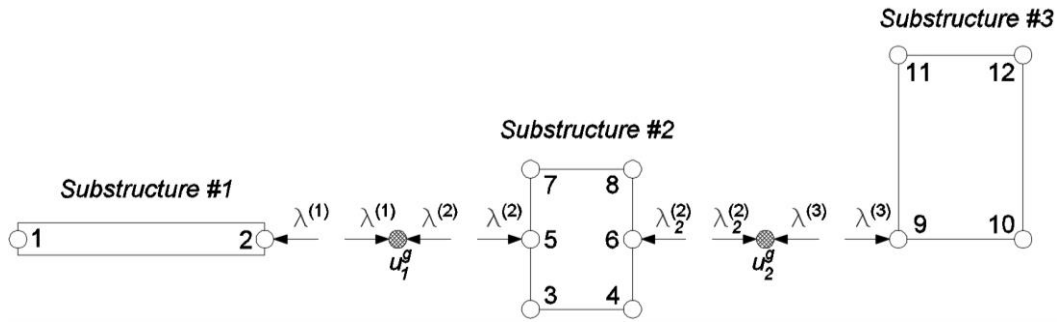
with $\mathbf{C}^{(l)}$ and $\mathbf{K}^{(l)}$ damping and stiffness matrices of domain l . Vector $\mathbf{F}^{(l)}(t)$ represents the external time-varying load that, for seismic response history analyses, is typically defined as

$$\mathbf{F}^{(l)}(t) = -\mathbf{M}^{(l)}\mathbf{T}^{(l)}a_g(t) \quad (2.2.3)$$

where $\mathbf{T}^{(l)}$ is a Boolean vector depending on the direction of the seismic acceleration $a_g(t)$. For the sake of brevity, time dependence is omitted and therefore the independent variable t is dropped in the following. $\mathbf{L}^{(l)}$ and $\bar{\mathbf{L}}^{(l)}$ are Boolean signed matrices that collocate interface DoFs on the single subdomain DoF vector $\mathbf{u}^{(l)}$ and the generalized interface DoF vector \mathbf{u}_g , respectively. The latter gathers all coupled systems' interface DoFs taken once. According to Eq. (2.2.1a), each Lagrange multiplier vector $\boldsymbol{\Lambda}^{(l)}$ enforces compatibility between the corresponding subdomain l -th and the generalized interface DoF vector \mathbf{u}_g . Finally, Eq. (2.2.1b) imposes self-balance among all m interface force fields represented by Lagrange multiplier vectors.

As a dual-assembly approach, the LLM introduces additional sets of Lagrange multipliers, which satisfy interface equilibrium a priori through Eq. (2.2.1b) and enforce kinematic compatibility a posteriori by means of Eq. (2.2.1a). More precisely, at each simulation step displacement and velocity solutions of (2.2.1) split into free and link components. The former are calculated discarding coupling conditions and used to compute the latter by means of a linearized Steklov-Poincaré operator.

To crystallize the idea, Fig. 2.1 illustrates an example of three-substructure coupling achieved by using the LLMs.



$$\begin{aligned}
\mathbf{u}^{(1)T} &= [u_1^{(1)}, u_2^{(1)}] \\
\mathbf{u}^{(2)T} &= [u_3^{(2)}, u_4^{(2)}, u_5^{(2)}, u_6^{(2)}, u_7^{(2)}, u_8^{(2)}] \\
\mathbf{u}^{(3)T} &= [u_9^{(3)}, u_{10}^{(3)}, u_{11}^{(3)}, u_{12}^{(3)}] \\
\mathbf{u}_g^T &= [u_1^g, u_2^g] \\
\mathbf{L}^{(1)} &= [0, 1], \bar{\mathbf{L}}^{(1)} = [-1, 0] \\
\mathbf{L}^{(2)} &= [0, 0, 1, 0, 0, 0], \bar{\mathbf{L}}^{(2)} = \begin{bmatrix} -1, & 0 \\ 0, & -1 \end{bmatrix} \\
\mathbf{L}^{(3)} &= [1, 0, 0, 0], \bar{\mathbf{L}}^{(3)} = [0, -1]
\end{aligned}$$

Figure 2.1 Three substructure coupling based on the LLM

We underline that Eq. (2.2.1a) permits both coupling on displacement and velocity. The latter approach is pursued when the coupled system response is calculated by using a time stepping algorithm. As proved by Gravouil and Combescure (2001), this preserves stability of the coupled simulation as long as local stability conditions are satisfied for each subdomain taken independently.

As clearly explained by Park et al. (2000), in the most general multi-point constraint case, that is, when $m > 2$ subdomains share all same interface DoFs, the CLM method leads to $m(m - 1)/2$ linearly dependent systems of constraint equations, which cast kinematic compatibility among all possible pairs of subdomains. The task of retaining a subset of linearly independent constraint equations, which is not unique, has been a major issue in the CLM method. On the other side, the LLM method casts all constraint equations with respect to a single set of generalized interface DoFs \mathbf{u}_g , see Eq. (2.2.1), which leads to a unique set of m linearly independent systems of constraint equations for the same multi-point constraint case. As a result, for the same multi-point constraint case, Boolean coupling matrices $\mathbf{L}^{(l)}$ and $\bar{\mathbf{L}}^{(l)}$ are uniquely derived to form a set of m linearly independent systems of constraint equations, which guarantee non-singular Steklov-Poincaré coupling operators, as explained in the following sections. This feature extremely simplifies the implementations of EDS simulations with more than two subdomains and multi-point constraints with respect to state-of-the-art algorithms based on CLM (Bursi et al., 2017).

The setting defined by Eq. (2.2.1) is valid for all EDS methods presented in the following subsections for the simplest case of two subdomains. Accordingly, to indicate PS and NS, respectively, superscript P and N replace (l) .

2.2.3 The online hybrid dynamic substructuring method

As anticipated, online EDS methods compute the emulated system response while the PS is being tested. In the specific case of the HDS method, at each time step of a time integration loop, a set of servo-controlled actuators impose displacement to the PS and measure corresponding restoring forces. A computational driver solves the equation of motion of the coupled system and the simulation moves to the next time step. In the conventional HDS method, the actuator motion stops when the tested specimen reaches the target displacement and holds the position while the restoring force is measured. Conversely, actuators do not stop in the continuous HDS method so that the specimen follows very accurately the target displacement. In this case, the PS restoring force is measured at every controller sampling period Δt^C and the time integration loop shares the same rate of the controller. As a result, any stress-relaxation effect on the specimens is removed, even though the strain-rate effect may still be present if the real-time speed is not reached. However, Δt^C could be too small to accommodate the solution of the NS. In this context, partitioned time integration can play a crucial role: in fact, it allows for the synchronization of time integration of PS and NS, which can be performed with different time integration stepping methods and time steps.

With reference to the continuous HDS method, which is referred to as HDS method hereinafter, two partitioned time integration algorithms, namely the PM algorithm (Bursi et al., 2017) and the GC algorithm (Gravouil and Combescure, 2001) are presented in the following subsection.

Several HDS applications were successfully executed by using the partitioned PM integration method (Bursi et al., 2017), which originates from the GC method (Gravouil and Combescure, 2001). The GC method was originally conceived to combine a pair of arbitrary Newmark schemes (Newmark, 1959) with their own parameters and time steps, as schematically illustrated in Fig. 2.2a. Since the GC is a staggered algorithm where task executions on both subdomains are consecutive or sequential, it does not allow for the continuous simulation of coupled numerical/physical sub-systems or, in other words, for a parallel solution of subdomains' responses. The PM method overcame the above limitation by modifying the task sequence of the GC method as shown in Fig. 2.2b. In detail, a forward prediction of two coarse time steps on the numerical side enabled parallel implementations. However, this variant makes the PM method a non-self-starting procedure; therefore, the GC method initializes the simulation by solving the first coarse time step while the PM method is performing the first two-step forward prediction.

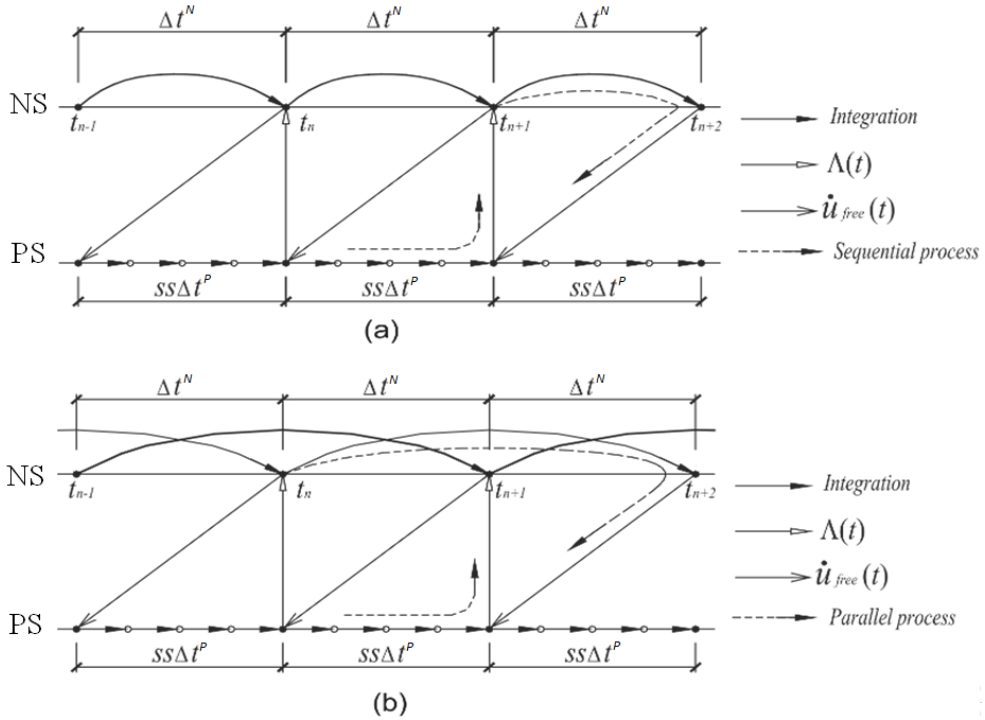


Figure 2.2 Task sequence of: (a) the staggered GC method; (b) the parallel PM method.

According to Figure 2.2, two parameters define the setting of the task sequence of both the GC and the PM algorithm,

- the testing time scale λ , defined as $\lambda = \Delta t^C / \Delta t^P$;
- the subcyclng ss , obtained as $ss = \Delta t^N / \Delta t^P$.

where Δt^N defines the coarse time step, adopted for the NS, whilst Δt^P is the fine time step used to calculate the PS response. The optimal selection of these parameters is the result of a trade-off between numerical accuracy and experimental constraints. In particular, when $\lambda = 1$, one integration time step is performed on the PS in the same wall-clock time, which corresponds to the controller time step Δt^C and the test is conducted in real-time. Conversely, when $\lambda > 1$, the simulation time is extended in comparison with the wall-clock time and the test is conducted in a pseudo-dynamic regime. When the response of the PS does not depend on the rate of loading, λ usually ranges between 50 and 200. Thus, a very small time step Δt^P can be achieved on the PS. This is beneficial for the stability of the explicit scheme. This approach improves the test quality by increasing the signal-to-noise ratio of response signals and reduces the control tracking error. Moreover, an extended simulation time scale λ reduces the destabilizing effect of electro-hydraulic actuator delays, which is typically of the order of $10 \div 20 \text{ ms}$ (Wallace, 2005). If λ is supposed to cope with the limitations of the actuation system performance, the subcyclng parameter ss lets us

adjust the allowable solving time $t^S = ss \Delta t^C$, which constrains the size and complexity of the NS.

For the sake of clarity, the PM method (Bursi et al., 2017), enriched with the LLMs (Park et al. 2000), is summarized in algorithmic form hereinafter for the case of two subdomains, i.e. a PS and a NS. The central difference explicit scheme ($\gamma^P = 1/2$ and $\beta^P = 0$), which does not require an estimate of the tangent stiffness matrix, is typically employed for the PS. The key advantage of velocity coupling is that global dynamic stability is ensured as long as local stability requirements are satisfied for all subdomains taken as stand-alone systems. Accordingly, a PS integration time step $\Delta t^P < T^P/\pi$ is selected, where T^P is the period corresponding to the highest eigen-frequency of the PS. It is important to stress that very few DoFs characterizes the PS, whose eigenfrequencies as a stand-alone system are typically restricted to a low frequency range, e.g. 0-10Hz. In order to guarantee A-stability even for a large number of DoFs, the trapezoidal rule implicit scheme ($\gamma^N = 1/2$ and $\beta^N = 1/4$) is used on the NS. However, other time-stepping schemes can be used (Newmark, 1959; Lamarche et al., 2009). Hence,

Step 1. Solve the free problem in the NS, thus advancing from t_n to t_{n+2} ,

$$\ddot{\mathbf{u}}_{n+2}^{N,free} = \mathbf{D}^{N-1} \left(\mathbf{F}_{n+2}^N - \mathbf{R}^N(\tilde{\mathbf{u}}_{n+2}^N, \tilde{\mathbf{u}}_{n+2}^N) \right) \quad (2.2.4)$$

$$\dot{\mathbf{u}}_{n+2}^{N,free} = \tilde{\mathbf{u}}_{n+2}^{N,free} + \gamma^N (2\Delta t^N) \ddot{\mathbf{u}}_{n+2}^{N,free} \quad (2.2.5)$$

$$\mathbf{u}_{n+2}^{N,free} = \tilde{\mathbf{u}}_{n+2}^{N,free} + \beta^N (2\Delta t^N)^2 \ddot{\mathbf{u}}_{n+2}^{N,free} \quad (2.2.6)$$

with,

$$\mathbf{D}^N = \mathbf{M}^N + \gamma^N (2\Delta t^N) \mathbf{C}^N + \beta^N (2\Delta t^N)^2 \mathbf{K}^N \quad (2.2.7)$$

$$\tilde{\mathbf{u}}_{n+2}^{N,free} = \mathbf{u}_n^N + (2\Delta t^N) \dot{\mathbf{u}}_n^N + (1/2 - \beta^N) (2\Delta t^N)^2 \ddot{\mathbf{u}}_n^N \quad (2.2.8)$$

$$\tilde{\mathbf{u}}_{n+2}^{N,free} = \dot{\mathbf{u}}_n^N + (1 - \gamma^N) (2\Delta t^N) \ddot{\mathbf{u}}_{n+2}^{N,free} \quad (2.2.9)$$

In line with the Operator Splitting (OS) method (Bursi and Wagg, 2008), which underlays the one-step corrector solution approach of the PM algorithm, tangent stiffness and damping matrices of Eq. (2.2.7) are obtained by linearizing the restoring force vector as $\mathbf{K}^N = \frac{\partial \mathbf{R}^N}{\partial \mathbf{u}^N} \Big|_{\mathbf{u}^N=\mathbf{0}}$ and $\mathbf{C}^N = \frac{\partial \mathbf{R}^N}{\partial \dot{\mathbf{u}}^N} \Big|_{\dot{\mathbf{u}}^N=\mathbf{0}}$, respectively. In order to reduce the computational burden, this operation is done once at the beginning of the simulation and matrices are never updated. Particular care must be devoted to linearization error which remain negligible for sufficiently small time steps, as confirmed by numerical studies of Sections 2.4 and 2.5. When the NS

restoring force is rate independent, a proportional formulation (Bernal, 1994), e.g. Rayleigh or Caughey, is typically used to build up the damping matrix \mathbf{C}^N .

Step 2. Start the subcycling loop over $j = \{1, \dots, ss\}$ in the PS.

Step 3. Solve the *free problem* in the PS at $t_{n+\frac{j}{ss}}$ as,

$$\ddot{\mathbf{u}}_{n+\frac{j}{ss}}^{P,free} = \mathbf{D}^{P-1} \left(\mathbf{F}_{n+\frac{j}{ss}}^P - \mathbf{R}^P \left(\tilde{\mathbf{u}}_{n+\frac{j}{ss}}^P, \tilde{\mathbf{u}}_{n+\frac{j}{ss}}^P \right) \right) \quad (2.2.10)$$

$$\dot{\mathbf{u}}_{n+\frac{j}{ss}}^{P,free} = \tilde{\mathbf{u}}_{n+\frac{j}{ss}}^{P,free} + \gamma^P (\Delta t^P) \ddot{\mathbf{u}}_{n+\frac{j}{ss}}^{P,free} \quad (2.2.11)$$

$$\mathbf{u}_{n+\frac{j}{ss}}^{P,free} = \tilde{\mathbf{u}}_{n+\frac{j}{ss}}^{P,free} + \beta^P (\Delta t^P)^2 \ddot{\mathbf{u}}_{n+\frac{j}{ss}}^{P,free} \quad (2.2.12)$$

with,

$$\mathbf{D}^P = \mathbf{M}^P + \gamma^P \Delta t^P \mathbf{C}^P + \beta^P \Delta t^{P2} \mathbf{K}^P \quad (2.2.13)$$

$$\tilde{\mathbf{u}}_{n+\frac{j}{ss}}^{P,free} = \mathbf{u}_{n+\frac{j-1}{ss}}^P + \Delta t^P \dot{\mathbf{u}}_{n+\frac{j-1}{ss}}^P + (1/2 - \beta^P) \Delta t^{P2} \ddot{\mathbf{u}}_{n+\frac{j-1}{ss}}^P \quad (2.2.14)$$

$$\tilde{\mathbf{u}}_{n+\frac{j}{ss}}^{P,free} = \dot{\mathbf{u}}_{n+\frac{j-1}{ss}}^P + (1 - \gamma^P) \Delta t^P \ddot{\mathbf{u}}_{n+\frac{j-1}{ss}}^P \quad (2.2.15)$$

In a real-time setting, both displacement and the velocity vectors, $\tilde{\mathbf{u}}_{n+\frac{j}{ss}}^P$ and $\dot{\tilde{\mathbf{u}}}_{n+\frac{j}{ss}}^P$, predicted by the Newmark scheme (1959) are imposed onto the PS, so as to measure the rate dependent restoring force $\mathbf{R}^P \left(\tilde{\mathbf{u}}_{n+\frac{j}{ss}}^P, \dot{\tilde{\mathbf{u}}}_{n+\frac{j}{ss}}^P \right)$ to be used in (2.2.10). Conversely, a reduced velocity $\tilde{\mathbf{u}}_{n+\frac{j}{ss}}^P / \lambda$ is physically imposed to the PS in the pseudo-dynamic regime. However, a rate-independent restoring term is expected in this case. With regard to Eq. (2.2.13), it is worthwhile to recall that an explicit Newmark integrator ($\beta^P = 0$) is used and, therefore, it is not necessary to estimate/measure the physical tangent stiffness matrix \mathbf{K}^P . Moreover, a perfectly hysteretic damping is assumed on the PS (Molina et al., 2011), which is taken into account through the measured restoring force $\mathbf{R}^P \left(\tilde{\mathbf{u}}_{n+\frac{j}{ss}}^P, \dot{\tilde{\mathbf{u}}}_{n+\frac{j}{ss}}^P \right)$. As a result, the physical tangent damping matrix \mathbf{C}^P is set to zero and matrix \mathbf{D}^P of Eq. (2.2.13) is simply defined as $\mathbf{D}^P = \mathbf{M}^P$. This is one of the most valuable features of the PM method, which avoids assumptions on PS tangent stiffness and damping matrices. It is important to stress that mass at

interface DoFs can be arbitrarily moved from NS to PS, which imposes to numerically integrate the PS response as done on the NS. Accordingly, our implementation of HDS considers a numerical mass for the PS also in the real-time case. Although this could sounds as an unnecessary complication, such approach allows for controlling the stability domain of the coupled simulation (Bursi et al., 2008).

Step 4. Interpolate the *free velocity* in subdomain,

$$\tilde{\mathbf{u}}_{n+\frac{j}{SS}}^{N,free} = \left(1 - \frac{j}{SS}\right) \dot{\mathbf{u}}_n^{N,free} + \left(\frac{j}{SS}\right) \dot{\mathbf{u}}_{n+1}^{N,free} \quad (2.2.16)$$

Step 5. Compute the Lagrange multiplier sets $\mathbf{\Lambda}_{n+\frac{j}{SS}}^N$ and $\mathbf{\Lambda}_{n+\frac{j}{SS}}^P$ and the reference velocity vector $\dot{\mathbf{u}}_{g,n+\frac{j}{SS}}$ by solving the condensed interface problem,

$$\mathbf{G} \begin{bmatrix} \mathbf{\Lambda}_{n+\frac{j}{SS}}^N \\ \mathbf{\Lambda}_{n+\frac{j}{SS}}^P \\ \dot{\mathbf{u}}_{g,n+\frac{j}{SS}} \end{bmatrix} = - \begin{bmatrix} \mathbf{L}^N \dot{\mathbf{u}}_{n+\frac{j}{SS}}^{N,free} \\ \mathbf{L}^P \dot{\mathbf{u}}_{n+\frac{j}{SS}}^{P,free} \\ \mathbf{0} \end{bmatrix} \quad (2.2.17)$$

where the linearized Steklov-Poincaré operator \mathbf{G} reads,

$$\mathbf{G} = \begin{bmatrix} \gamma^N (2\Delta t^N) \mathbf{L}^N \mathbf{D}^{N-1} \mathbf{L}^{NT} & \mathbf{0} & \bar{\mathbf{L}}^N \\ \mathbf{0} & \gamma^P \Delta t^P \mathbf{L}^P \mathbf{D}^{P-1} \mathbf{L}^{PT} & \bar{\mathbf{L}}^P \\ \bar{\mathbf{L}}^{NT} & \bar{\mathbf{L}}^{PT} & \mathbf{0} \end{bmatrix} \quad (2.2.18)$$

Step 6. Solve the *link problem* in the PS at $t_{n+\frac{j}{SS}}$

$$\ddot{\mathbf{u}}_{n+\frac{j}{SS}}^{P,link} = \mathbf{D}^{P-1} \mathbf{L}^P \mathbf{\Lambda}_{n+\frac{j}{SS}}^P \quad (2.2.19)$$

$$\dot{\mathbf{u}}_{n+\frac{j}{SS}}^{P,link} = \gamma^P \Delta t^P \ddot{\mathbf{u}}_{n+\frac{j}{SS}}^{P,link} \quad (2.2.20)$$

$$\mathbf{u}_{n+\frac{j}{SS}}^{P,link} = \beta^P \Delta t^{P^2} \ddot{\mathbf{u}}_{n+\frac{j}{SS}}^{P,link} \quad (2.2.21)$$

Step 7. Compute the kinematic quantities of the PS at $t_{n+\frac{j}{SS}}$, which is equal to the sum of *free quantities* (Step 3) and *link quantities* (Step 6)

$$(\cdot) = (\cdot)^{free} + (\cdot)^{link} \quad (2.2.22)$$

Step 8. If $j = ss$, then end the loop in the PS, otherwise $j = j + 1$ and go back to *Step 3*.

Step 9. Solve the *link problem* in the NS using the time step Δt_N from t_n to t_{n+1}

$$\ddot{\mathbf{u}}_{n+1}^{N,link} = \mathbf{D}^{N-1} \mathbf{L}^N \mathbf{\Lambda}_{n+1}^N \quad (2.2.23)$$

$$\dot{\mathbf{u}}_{n+1}^{N,link} = \gamma^N (2\Delta t^N) \ddot{\mathbf{u}}_{n+1}^{N,link} \quad (2.2.24)$$

$$\mathbf{u}_{n+1}^{N,link} = \beta^N (2\Delta t^N)^2 \ddot{\mathbf{u}}_{n+1}^{N,link} \quad (2.2.25)$$

Step 10. Compute the kinematic quantities of the NS at t_{n+1} by employing the *free problem* (Step 1) and the *link problem* (Step 9)

$$(\cdot) = (\cdot)^{free} + (\cdot)^{link} \quad (2.2.26)$$

According to (2.2.12) and (2.2.21) when the central difference scheme is used on the PS, *link* displacements are null and corrections are exclusively needed for velocities and accelerations. As a result, the specimen smoothly follows the prototype response. In any case, the mass matrix \mathbf{M}^P contributes to \mathbf{D}^P , which dominates the right-hand side of Eq. (2.2.13); thus, the physical link acceleration $\ddot{\mathbf{u}}_{n+\frac{j}{ss}}^{P,link}$ computed in Eq. (2.2.19) could generate discontinuities on actuator trajectories. Hence sometimes, it is convenient to modulate the magnitude of each *link* solution by moving interface mass from the NS to the PS. To this end, we can modulate the mass fraction parameter m_f for a generic *i-th* interface DoF. More precisely, m_f is defined as the ratio between physical and total interface mass,

$$m_{f,i} = \frac{M_i^P}{M_i^N + M_i^P} \quad (2.2.27)$$

where M_i^P and M_i^N are physical and numerical contributions to the mass of the *i-th* interface DoF. As a result, we can reduce the magnitude of physical link quantities by tuning m_f without affecting the structure prototype response. For the sake of brevity, the GC method procedure is omitted but can be easily derived by replacing the NS time step ($2\Delta t^N$) with Δt^N in Eqs. (2.2.4) to (2.2.26).

2.2.4 Two offline experimental dynamic substructuring methods

As explained in Section 2.2, when offline EDS methods are used the experimental response of the PS needs to be acquired before the calculation of the emulated system response. In this context, both the IBS (Rixen and Van der Valk, 2013; Van der Valk, Rixen, 2014) and the Receptance-Based Substructuring (RBS) method, which is formally derived from the LM-FBS method of Voormeeren et al. (2010) are presented in the following subsections. The former operates in time domain and the PS is represented in terms of measured Impulse Response Functions (IRFs); the latter operates in the Laplace domain and measured Receptance Functions (RFs) account for the PS response. Both methods rely on operational and experimental modal analysis tools such as accelerometers, shakers and impact hammers. The IBS methods allows for combining linear PSs to non-linear NSs whilst the RBS can be used for both coupling and decoupling linear NSs and PSs.

2.2.4.1 The impulse-based substructuring method

The easiest way to introduce the IBS framework is to briefly revisit the equation of motion of a generic M-DoF linear dynamic system subjected to an arbitrary force vector $\mathbf{F}(t)$,

$$\mathbf{M}\ddot{\mathbf{u}} + \mathbf{C}\dot{\mathbf{u}} + \mathbf{K}\mathbf{u} = \mathbf{F}(t) \quad (2.2.28)$$

Let us designate $\mathbf{H}_d(t)$ the matrix of the displacement response for a linear system that is at rest at $t = 0$ and is subjected to a unit impulse excitation applied to a specific DoF, described by a Dirac δ function. The elements $[\mathbf{H}_d(t)]_{ij}$ of the impulse response matrix represent the displacement response of DoF i to a unit impulse at DoF j . Since any arbitrary force function of time can be expressed as a sequence of force impulses over time, the impulse response functions can be used to evaluate the response of a generic system in the time domain. As a result, the displacement response of the linear system can be evaluated through the Duhamel's convolution integral between $\mathbf{H}_d(t)$ and $\mathbf{F}(t)$,

$$\mathbf{u}(t) = \int_0^t \mathbf{H}_d(t - \tau)\mathbf{F}(\tau)d\tau \quad (2.2.29)$$

Likewise, velocity and acceleration responses can be evaluated as follows,

$$\dot{\mathbf{u}}(t) = \int_0^t \mathbf{H}_v(t - \tau)\mathbf{F}(\tau)d\tau \quad (2.2.30)$$

$$\ddot{\mathbf{u}}(t) = \int_0^t \mathbf{H}_a(t - \tau) \mathbf{F}(\tau) d\tau \quad (2.2.31)$$

where $\mathbf{H}_v(t)$ and $\mathbf{H}_a(t)$ are the first and second time derivatives of $\mathbf{H}_d(t)$, respectively. Clearly, $\mathbf{H}_d(t)$, $\mathbf{H}_v(t)$ and $\mathbf{H}_a(t)$ contain information on the input-output relationship of the system dynamics. Typically, the following convolution sums are used in a discrete-time setting,

$$\begin{aligned} \mathbf{u}_n &= \sum_{i=0}^n \mathbf{H}_{d,n-i} \mathbf{F}_i \Delta t \\ \dot{\mathbf{u}}_n &= \sum_{i=0}^n \mathbf{H}_{v,n-i} \mathbf{F}_i \Delta t \\ \ddot{\mathbf{u}}_n &= \sum_{i=0}^n \mathbf{H}_{a,n-i} \mathbf{F}_i \Delta t \end{aligned}$$

The previous equations approximate the exact convolution integrals (2.2.29-2.2.31) and, therefore, the IRF matrices are discretized according to the sampling rate of $\mathbf{F}(t)$. In a greater detail, $\mathbf{H}_{*,n-i}$ corresponds to the IRF matrix $\mathbf{H}_*(t)$ evaluated at $t = \Delta t \cdot (n - i)$. In principle, $\mathbf{H}_d(t)$ can be obtained: i) analytically, relying on matrix exponentials -this method ensures the exact sampling of the impulse response function-; ii) numerically, by simulating the dynamic response of the system subjected to an impulse load by means of a time history response analysis; iii) experimentally, by using impact hammers and accelerometers. The resulting discretized coupled equations of motion for a two-subdomain system read,

$$\begin{cases} \mathbf{M}^N \ddot{\mathbf{u}}_n^N + \mathbf{R}^N(\mathbf{u}_n^N, \dot{\mathbf{u}}_n^N) = \mathbf{L}^{N^T} \boldsymbol{\Lambda}_n^N + \mathbf{F}_n^N \\ \dot{\mathbf{u}}_n^P = \sum_{i=0}^n \mathbf{H}_{v,n-i}^P (\mathbf{L}^{P^T} \boldsymbol{\Lambda}_i^P + \mathbf{F}_i^P) \Delta t \end{cases} \quad (2.2.35)$$

$$\begin{cases} \mathbf{L}^N \dot{\mathbf{u}}_n^N + \bar{\mathbf{L}}^N \dot{\mathbf{u}}_{g,n} = \mathbf{0} \\ \mathbf{L}^P \dot{\mathbf{u}}_n^P + \bar{\mathbf{L}}^P \dot{\mathbf{u}}_{g,n} = \mathbf{0} \end{cases} \quad (2.2.36)$$

$$\bar{\mathbf{L}}^{N^T} \boldsymbol{\Lambda}_n^N + \bar{\mathbf{L}}^{P^T} \boldsymbol{\Lambda}_n^P = \mathbf{0} \quad (2.2.37)$$

The solution of (2.2.35) is obtained by discretizing the time integral needed to evaluate the convolution product and to solve for the additional interface force fields $\boldsymbol{\Lambda}_n^N$ and $\boldsymbol{\Lambda}_n^P$ at each

step n , which ensures the interface kinematic continuity. It is noteworthy that the original IBS algorithm (Rixen and Van der Valk, 2013) was conceived to combine exclusively subdomains represented in terms of impulse response matrices. In our hybrid experimental/numerical setting, only the PS is represented in terms of its impulse response matrices, whilst the NS is integrated using a Newmark-based time stepping scheme (2000), which can also account for nonlinearities (Van der Valk and Rixen, 2014). According to Gravouil and Combescure (2001), in order to obtain an unconditionally stable algorithm, as long as stability requirements are satisfied in all individual subdomains, a velocity continuity condition at the interface DoFs suffices; this is achieved in Eq. (2.2.36). The implementation of the IBS algorithm based on the coupled scheme of the GC method is summarized herein for the case without subcycling, that is, $\Delta t^P = \Delta t^N = \Delta t$.

Step 1. Solve the free problem in the NS, thus advancing from t_n to t_{n+1} ,

$$\ddot{\mathbf{u}}_{n+1}^{N,free} = \mathbf{D}^{N-1} \left(\mathbf{F}_{n+1}^N - \mathbf{R}^N(\tilde{\mathbf{u}}_{n+1}^N, \tilde{\mathbf{u}}_{n+1}^N) \right) \quad (2.2.38)$$

$$\dot{\mathbf{u}}_{n+1}^{N,free} = \tilde{\mathbf{u}}_{n+1}^{N,free} + \gamma^N \Delta t \ddot{\mathbf{u}}_{n+1}^{N,free} \quad (2.2.39)$$

$$\mathbf{u}_{n+1}^{N,free} = \tilde{\mathbf{u}}_{n+1}^{N,free} + \beta^N \Delta t^2 \ddot{\mathbf{u}}_{n+1}^{N,free} \quad (2.2.40)$$

with,

$$\mathbf{D}^N = \mathbf{M}^N + \gamma^N \Delta t \mathbf{C}^N + \beta^N \Delta t^2 \mathbf{K}^N \quad (2.2.41)$$

$$\tilde{\mathbf{u}}_{n+1}^{N,free} = \mathbf{u}_n^N + \Delta t \dot{\mathbf{u}}_n^N + (1/2 - \beta^N) \Delta t^2 \ddot{\mathbf{u}}_n^N \quad (2.2.42)$$

$$\tilde{\mathbf{u}}_{n+1}^{N,free} = \mathbf{u}_n^N + (1 - \gamma^N) \Delta t \dot{\mathbf{u}}_{n+1}^{N,free} \quad (2.2.43)$$

As analogously done in Eq. (2.2.7) for the HDS method, tangent stiffness and damping matrices of Eq. (2.2.41) are obtained by linearizing the restoring force vector as $\mathbf{K}^N = \frac{\partial \mathbf{R}^N}{\partial \mathbf{u}^N} \Big|_{\mathbf{u}^N = \mathbf{0}}$ and $\mathbf{C}^N = \frac{\partial \mathbf{R}^N}{\partial \dot{\mathbf{u}}^N} \Big|_{\dot{\mathbf{u}}^N = \mathbf{0}}$, respectively. In order to reduce the computational burden, this operation is done once at the beginning of the simulation and matrices are never updated. Particular care must be devoted to linearization errors which remain negligible for sufficiently small time steps, as confirmed by numerical studies of Sections 2.4 and 2.5. When the NS restoring force is rate independent, a proportional formulation (Bernal, 1994), e.g. Rayleigh or Caughey, is typically used to build up the damping matrix \mathbf{C}^N .

Step 2. Solve the *free problem* in the PS at from t_n to t_{n+1} ,

$$\ddot{\mathbf{u}}_{n+1}^{P,free} = \sum_{i=0}^n \mathbf{H}_{a,n+1-i}^P (\mathbf{L}^{PT} \boldsymbol{\Lambda}_i^P + \mathbf{F}_i^P) \Delta t + \mathbf{H}_{a,0}^P \mathbf{F}_{n+1}^P \Delta t \quad (2.2.44)$$

$$\dot{\mathbf{u}}_{n+1}^{P,free} = \sum_{i=0}^n \mathbf{H}_{v,n+1-i}^P (\mathbf{L}^{PT} \boldsymbol{\Lambda}_i^P + \mathbf{F}_i^P) \Delta t + \mathbf{H}_{v,0}^P \mathbf{F}_{n+1}^P \Delta t \quad (2.2.45)$$

$$\mathbf{u}_{n+1}^{P,free} = \sum_{i=0}^n \mathbf{H}_{d,n+1-i}^P (\mathbf{L}^{PT} \boldsymbol{\Lambda}_i^P + \mathbf{F}_i^P) \Delta t + \mathbf{H}_{d,0}^P \mathbf{F}_{n+1}^P \Delta t \quad (2.2.46)$$

According to (2.2.44-2.2.46) convolution series are truncated at n because the interface force field $\boldsymbol{\Lambda}_{n+1}^P$ is unknown at this point of the procedure. As a result, the external load \mathbf{F}_{n+1}^P only determines the last step of the free solution.

Step 3. Compute the Lagrange multiplier sets $\boldsymbol{\Lambda}_{n+1}^N$ and $\boldsymbol{\Lambda}_{n+1}^P$ and the reference velocities $\dot{\mathbf{u}}_{g,n+1}$ by solving the condensed interface problem

$$\mathbf{G} \begin{bmatrix} \boldsymbol{\Lambda}_{n+1}^N \\ \boldsymbol{\Lambda}_{n+1}^P \\ \dot{\mathbf{u}}_{g,n+1} \end{bmatrix} = - \begin{bmatrix} \mathbf{L}^N \dot{\mathbf{u}}_{n+1}^{N,free} \\ \mathbf{L}^P \dot{\mathbf{u}}_{n+1}^{P,free} \\ \mathbf{0} \end{bmatrix} \quad (2.2.47)$$

where,

$$\mathbf{G} = \begin{bmatrix} \gamma^N \Delta t \mathbf{L}^N \mathbf{D}^{N-1} \mathbf{L}^{NT} & \mathbf{0} & \bar{\mathbf{L}}^N \\ \mathbf{0} & \mathbf{L}^P \mathbf{H}_{v,0}^P \mathbf{L}^{PT} & \bar{\mathbf{L}}^P \\ \bar{\mathbf{L}}^{NT} & \bar{\mathbf{L}}^{PT} & \mathbf{0} \end{bmatrix} \quad (2.2.48)$$

Step 4. Solve the *link problem* in the PS at t_{n+1}

$$\ddot{\mathbf{u}}_{n+1}^{P,link} = \mathbf{H}_{a,0}^P \boldsymbol{\Lambda}_{n+1}^P \quad (2.2.49)$$

$$\dot{\mathbf{u}}_{n+1}^{P,link} = \mathbf{H}_{v,0}^P \boldsymbol{\Lambda}_{n+1}^P \quad (2.2.50)$$

$$\mathbf{u}_{n+1}^{P,link} = \mathbf{H}_{d,0}^P \boldsymbol{\Lambda}_{n+1}^P \quad (2.2.51)$$

Step 5. Compute the kinematic quantities of the PS at t_{n+1} , which is equal to the sum of *free quantities* (Step 2) and *link quantities* (Step 4)

$$(\cdot) = (\cdot)^{free} + (\cdot)^{link} \quad (2.2.52)$$

Step 6. Solve the *link problem* in the NS using the time step Δt_N from t_n to t_{n+1}

$$\ddot{\mathbf{u}}_{n+1}^{N,link} = \mathbf{D}^{N^{-1}} \mathbf{L}^N \boldsymbol{\Lambda}_{n+1}^N \quad (2.2.53)$$

$$\dot{\mathbf{u}}_{n+1}^{N,link} = \gamma^N \Delta t \ddot{\mathbf{u}}_{n+1}^{N,link} \quad (2.2.54)$$

$$\mathbf{u}_{n+1}^{N,link} = \beta^N \Delta t^2 \ddot{\mathbf{u}}_{n+1}^{N,link} \quad (2.2.55)$$

Step 7. Compute the kinematic quantities of the NS at t_{n+1} by employing the *free problem* (Step 1) and the *link problem* (Step 6)

$$(\cdot) = (\cdot)^{free} + (\cdot)^{link} \quad (2.2.56)$$

In order to account for various sources of uncertainty, which contaminate the “exact” impulse response functions, the process of measuring $\mathbf{H}_d^P(t)$, $\mathbf{H}_v^P(t)$ and $\mathbf{H}_a^P(t)$ matrices from hammer tests on the PS was simulated numerically.

2.2.4.2 The receptance-based substructuring method

Under the assumption that both NS and PS are linear -or linearized-, time invariant and operating at steady state, the LM-FBS method can be derived by Fourier transform of Eq. (2.2.1-2.2.2) (Voormeeren et al., 2010). However, the use of the Fourier transform is limited to periodic signals and, therefore, to stationary response analyses. Accordingly, the inverse Fourier transform cannot revert the dynamic response of the coupled system subjected to a transient excitation calculated in the frequency domain to the time domain. Therefore, the FBS method is reformulated in the Laplace domain as RBS method. The joint use of numerical Laplace transform and its inverse allowed for including the RBS method in the comparative uncertainty propagation analysis that quantifies the effect of various experimental sources of uncertainty on the time domain response of two benchmark systems subjected to a non-stationary excitation, as explained in Section 2.3. A detailed description of the algorithm follows,

$$\begin{cases} \pm \mathbf{Z}^N(s) \mathbf{u}^N(s) = \mathbf{L}^{N^T} \boldsymbol{\Lambda}^N(s) + \mathbf{F}^N(s) \\ \mathbf{Z}^P(s) \mathbf{u}^P(s) = \mathbf{L}^{P^T} \boldsymbol{\Lambda}^P(s) + \mathbf{F}^P(s) \end{cases} \quad (2.2.57)$$

$$\begin{cases} \mathbf{L}^N \mathbf{u}^N(s) + \bar{\mathbf{L}}^N \mathbf{u}_g(s) = \mathbf{0} \\ \mathbf{L}^P \mathbf{u}^P(s) + \bar{\mathbf{L}}^P \mathbf{u}_g(s) = \mathbf{0} \end{cases} \quad (2.2.58)$$

$$\bar{\mathbf{L}}^{N^T} \boldsymbol{\Lambda}^N(s) + \bar{\mathbf{L}}^{P^T} \boldsymbol{\Lambda}^P(s) = \mathbf{0} \quad (2.2.59)$$

where s denotes the complex Laplace variable such that $Real(s) = \alpha$ and $Imag(s) = \omega$ whilst $\mathbf{Z}^N(s)$ and $\mathbf{Z}^P(s)$ are the impedance matrices of the NS and PS, respectively, calculated as,

$$\mathbf{Z}^{(l)} = \mathbf{M}^{(l)}s^2 + \mathbf{C}^{(l)}s + \mathbf{K}^{(l)} \quad (2.2.60)$$

In order to avoid the singularity of coupling operators for all values of s , compatibility conditions must be expressed in terms of displacements as in Eq. (2.2.58). The set of Eqs. (2.2.57-2.2.59) encompasses both substructure coupling and decoupling cases. In fact, the \pm sign before \mathbf{Z}^N indicates that the NS can be either added to or subtracted from the PS. The former is the case where two substructures form the global emulated system but only one is measured in the laboratory; the latter case occurs, for example, when the substructure of interest cannot be separately measured from a system with well-known dynamic properties, which is subtracted numerically afterwards (Voormeeren and Rixen, 2011).

Analogously to the IBS method, the RBS method relies on operational modal analysis tools such as impact hammers, shakers and accelerometers. In detail, each component $[\mathbf{Y}^P(s)]_{ij}$ of the PS receptance matrix $\mathbf{Y}^P(s) = \mathbf{Z}^{P^{-1}}(s)$ is typically calculated as the ratio between Laplace transforms of displacement response and loading excitation and measured at DoFs i and j , respectively. The trapezoidal rule is used to evaluate all Laplace integrals over a range of ω that includes all system and excitation frequencies assuming a constant and negative value of α , which is optimized according to the time span of the signals. The RBS algorithm expressed in terms of directly measurable receptance matrices reads,

$$\mathbf{u}(\mathbf{s}) = \mathbf{Y}(\mathbf{s})(\mathbf{F}(\mathbf{s}) + \mathbf{L}^T \boldsymbol{\Lambda}(\mathbf{s})) \quad (2.2.61)$$

$$\boldsymbol{\Lambda}(\mathbf{s}) = -(\mathbf{L}\mathbf{Y}(\mathbf{s})\mathbf{L}^T)^{-1} (\mathbf{L}\mathbf{Y}(\mathbf{s})\mathbf{F}(\mathbf{s}) + \bar{\mathbf{L}}\mathbf{u}_g(\mathbf{s})) \quad (2.2.62)$$

$$\mathbf{u}_g(\mathbf{s}) = -(\bar{\mathbf{L}}^T(\mathbf{L}\mathbf{Y}(\mathbf{s})\mathbf{L}^T)^{-1}\bar{\mathbf{L}})^{-1}(\bar{\mathbf{L}}^T(\mathbf{L}\mathbf{Y}(\mathbf{s})\mathbf{L}^T)^{-1}\mathbf{L}\mathbf{Y}(\mathbf{s})\mathbf{F}(\mathbf{s})) \quad (2.2.63)$$

where block matrices and vectors \mathbf{u} , \mathbf{Y} , \mathbf{L} , $\bar{\mathbf{L}}$ and \mathbf{F} are defined as,

$$\mathbf{u}(s) = \begin{bmatrix} \mathbf{u}^N(s) \\ \mathbf{u}^P(s) \end{bmatrix}, \mathbf{Y}(s) = \begin{bmatrix} \pm \mathbf{Y}^N(s) & \mathbf{0} \\ \mathbf{0} & \mathbf{Y}^P(s) \end{bmatrix}, \mathbf{F}(s) = \begin{bmatrix} \mathbf{F}^N(s) \\ \mathbf{F}^P(s) \end{bmatrix}, \mathbf{\Lambda}(s) = \begin{bmatrix} \mathbf{\Lambda}^N(s) \\ \mathbf{\Lambda}^P(s) \end{bmatrix}, \quad (2.2.64)$$

$$\mathbf{L} = \begin{bmatrix} \mathbf{L}^N & \mathbf{0} \\ \mathbf{0} & \mathbf{L}^P \end{bmatrix}, \bar{\mathbf{L}} = \begin{bmatrix} \bar{\mathbf{L}}^N \\ \bar{\mathbf{L}}^P \end{bmatrix}$$

Although (2.2.57-2.2.59) refers to the collocated case, the dual formulation allows for non-collocated setting, i.e. interface force fields and compatibility conditions defined on different DoF subsets. The superior versatility and performance with respect to noise propagation of the non-collocated approach is well documented for the case of interface rotational DoFs (D'Ambrogio and Fregolent, 2012).

In order to examine the practical implementation of the RBS method, the characterization of the PS receptance matrix $\mathbf{Y}^P(s)$ by means of hammer tests was simulated numerically considering as experimental sources of uncertainty both the variability of hammer impacts and noise on acceleration measurements.

In order to convert the emulated system response $\mathbf{u}(s)$ from the Laplace domain to the time domain, where it can be easily compared to both HDS and IBS simulations, the truncated series proposed by Durbin (Durbin, 1974) is used to approximate inverse Laplace transform integrals,

$$f(t) = \mathcal{L}^{-1}\{F(s)\} \approx \frac{2e^{\alpha t}}{T} \left(-\frac{\text{Re}(F(\alpha))}{2} + \sum_{k=1}^q \text{Re} \left(F \left(\alpha + i \frac{2\pi k}{T} \right) \right) \cos \left(\frac{2\pi k}{T} t \right) - \text{Im} \left(F \left(\alpha + i \frac{2\pi k}{T} \right) \right) \sin \left(\frac{2\pi k}{T} t \right) \right) \quad (2.2.65)$$

where $\mathcal{L}^{-1}\{\cdot\}$ represents the inverse Laplace transform operator, $F(s)$ is the Laplace transform of a generic time domain signal $f(t)$ of length T in s , α is a convergence parameter that constitutes the real part of the Laplace variable and q defines the number of terms, equal to 10^4 in our simulations, retained by the truncated series.

It is noteworthy that impulse response matrices defined by (2.2.29-2.2.31) can be derived from corresponding receptance matrices via inverse Laplace transform as,

$$\left[\mathbf{H}_d^{(l)}(t) \right]_{ij} = \mathcal{L}^{-1} \left\{ \left[\mathbf{Y}^{(l)}(s) \right]_{ij} \right\} (t) \quad (2.2.66)$$

$$\left[\mathbf{H}_v^{(l)}(t) \right]_{ij} = \mathcal{L}^{-1} \left\{ \left[s \mathbf{Y}^{(l)}(s) \right]_{ij} \right\} (t) \quad (2.2.67)$$

$$\left[\mathbf{H}_a^{(l)}(t) \right]_{ij} = \mathcal{L}^{-1} \left\{ \left[s^2 \mathbf{Y}^{(l)}(s) \right]_{ij} \right\} (t) \quad (2.2.68)$$

Accordingly, in the context of C-EDS, the truncated series of Eq. (2.2.65) is also proposed to convert coupled/decoupled receptance matrices to impulse response matrices, which can be used in combination with IBS and HDS methods.

2.3 Comparative uncertainty propagation analysis of the selected EDS methods

In order to examine a realistic scenario involving uncertainty propagation, the PS response was simulated numerically by including sources of errors/uncertainties due to operators/sensors. Various experimental sources of uncertainty affect the PS response and propagate through the emulated system depending on the specific EDS method and the relevant testing equipment. For example, the noise associated with both displacement and force readings is the primary source of uncertainty in HDS. The inherent randomness of hammer impulse, which is influenced by the Signal-to-Noise Ratio (SNR) of the output response measurements, is a notable source of uncertainty for both IBS and RBS methods. In order to compare the performance of the EDS methods presented in Section 2.2, a 5-DoFs benchmark system is employed to realistically investigate uncertainty propagation. The main experimental sources of uncertainty entering in EDS methods are examined; relevant probability distributions of the input random variables are characterized from laboratory measurements. Then, statistical moments of two error scores, which quantify the accuracy of each single EDS method in reproducing the reference -exact- emulated system response, are estimated via MCSs.

2.3.1 The 5-DoF benchmark system

In order to support the numerical uncertainty propagation analysis of the EDS methods presented in Section 2.2, a 5-DoF benchmark mechanical system with two interface DoFs between the PS and the NS and depicted in Fig. 2.3 is used. The study considers both a linear system configuration and a second one, see Fig 2.3a and 2.3b, respectively, characterized by localized non-linear behavior in the NS. In fact, and in contrast with the HDS method, both the proposed IBS and RBS methods require the PS to be linear. Moreover, a non-stationary input excitation, which represents a realistic dynamic loading condition, is selected.

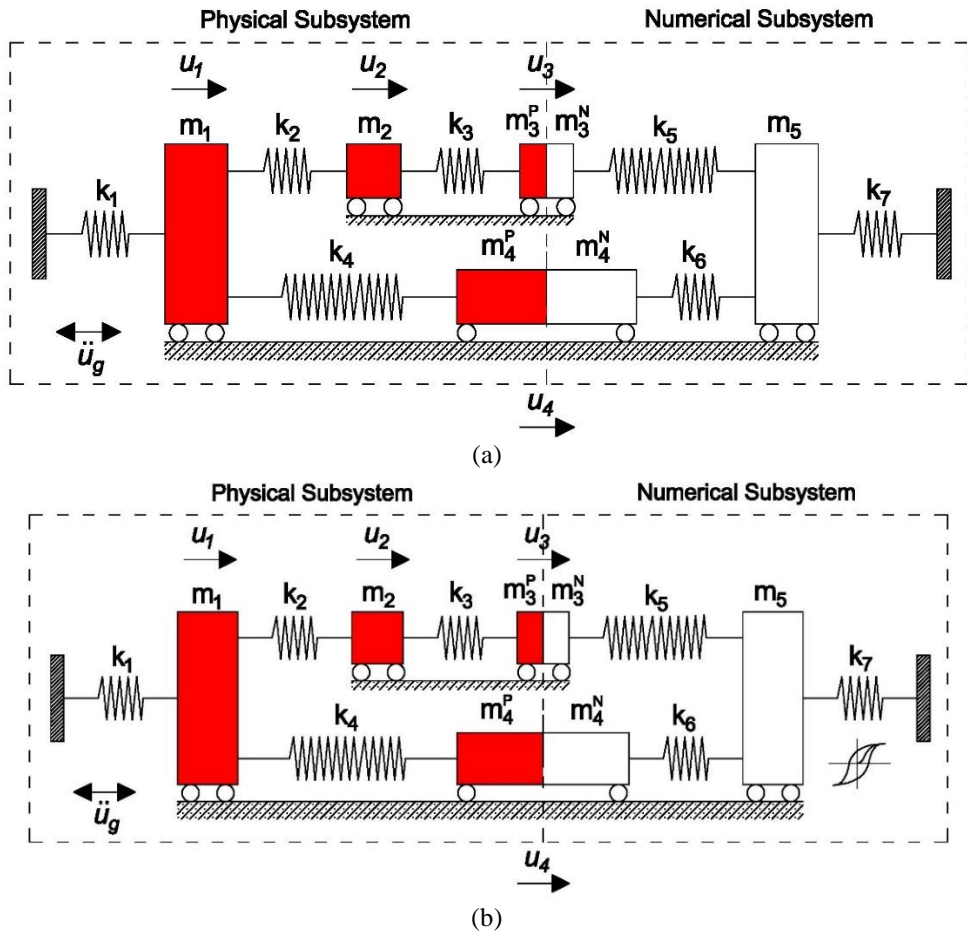


Figure 2.3 The 5-DoF benchmark system: a) linear; and b) nonlinear variants

In order to examine the influence of damping and mass fraction, which is defined in Eq. (2.2.27) for the i -th interface DoF, the uncertainty propagation analysis was repeated considering all four combinations of two different values for both parameters. In detail, the damping matrix of the actual system was derived from undamped natural frequencies and mode shapes after pre-assigning a constant modal damping ratio of 1% and 3%. Similarly, values of 0.5 and 0.9 were assigned to mass fraction parameters assumed as uniform along with the entire interface between NS and PS. Table 2.1 summarizes the physical properties and modal parameters of the linear variant of the 5-DoFs benchmark system.

Table 2.1 Main parameters and modal properties of the linear 5-DoF system.

Mass (kg)		Stiffness (N/m)		Eigen-freq. (Hz)	
m_1	500	k_1	14800	1 st mode	0.55
m_2	250	k_2	14800	2 nd mode	1.16
$m_3^P + m_3^N$	350	k_3	14800	3 rd mode	1.29
$m_4^P + m_4^N$	500	k_4	14800	4 th mode	1.75
m_5	600	k_5	14800	5 th mode	2.09
		k_6	14800		
		k_7	14800		

As can be appreciated from Table 2.1, the dynamic properties of the 5-DoFs benchmark system are representative of typical civil and mechanical engineering structures (Bursi and Wagg, 2008; Pan et al., 2016; Maghareh et al., 2014; Wen, 1976; Voormeeren, 2010).

In order to simulate non-linear local behavior in the NS, a hysteretic-type restoring-force element simulated by a Bouc-Wen model replaced spring k_7 in Fig. 2.3b. Thus, the following ordinary differential equation,

$$\dot{z}(t) = K_0 \dot{u}(t) - |z(t)|^{n'} [\beta \text{sign}(z(t)\dot{u}(t)) + \gamma] \dot{u}(t) \quad (2.3.1)$$

describes the Bouc-Wen restoring force $z(t)$, which offers a compact and continuous representation of hysteresis. Suitable values for the parameters K_0 , β , γ and n' can replicate either hardening or softening type nonlinearities. It can be shown that z attains an inelastic force plateau, $z_y = (K_0/(\beta + \gamma))^{n'}$, provided that $(\beta + \gamma) > 0$. Parameters n' , β and γ control the hysteresis shape: a hardening behaviour is simulated when $|\beta| > |\gamma|$ and $\gamma < 0$; otherwise, a softening behavior is obtained. The quantity n' modulates the sharpness of material yielding and as $n' \rightarrow \infty$ the formulation tends to the elasto-plastic hysteresis case. Table 2.2 summarizes the main parameters of the non-linear 5-DoFs benchmark system.

Table 2.2 Main parameters of the non-linear 5-DoF system.

Mass (kg)		Stiffness (N/m)		Parameters of Bouc-Wen model	
m_1	500	k_1	14800	K_0	14800
m_2	250	k_2	14800	β	40
$m_3^P + m_3^N$	350	k_3	14800	γ	-7
$m_4^P + m_4^N$	500	k_4	14800	n'	1
m_5	600	k_5	14800		
		k_6	14800		

A single accelerogram of the 1989 Loma Prieta earthquake of 4.25 m/s² PGA and recorded from the UCSC station (PEER, 2016), was selected as the reference seismic excitation signal. Additional acceleration records are not included, since the objective of this study is the comparison between propagation of uncertainties associated with measurement errors and experimental methods, rather than the quantification of the emulated system response variability owing to the seismic excitation uncertainty. Usually, the latter represents a predominant source of uncertainty in the context of seismic reliability analysis (Lomiento et al., 2013).

2.3.2 Characterization of experimental sources of uncertainty

SNR, defined as the ratio between the power of the measured signal (meaningful information) and the power of background noise (unwanted signal), is proportional to the intensity of the excitation, which modulates the effect of measurement errors on the measured PS response. Therefore, in order to examine uncertainty propagation for both IBS and RBS methods, a probabilistic model of the hammer impact loading history was defined as a constant piecewise function characterized by two random variables, namely impact duration (D) and maximum force intensity (J). The selection of suitable random distribution models and the calibration of the model parameters were based on the repeated acquisition of about 200 hammer “hits” on a rigid support in the laboratory.

Both D and J data exhibited negligible asymmetry about their mean values. Therefore, it was concluded that a truncated Gaussian model was reasonable to describe the marginal distributions of both random variables. Fig. 2.4 and Fig. 2.5 illustrate the comparison between empirical and analytical cumulative density functions (CDFs) and probability density functions (PDFs), respectively of both random variables D and J .

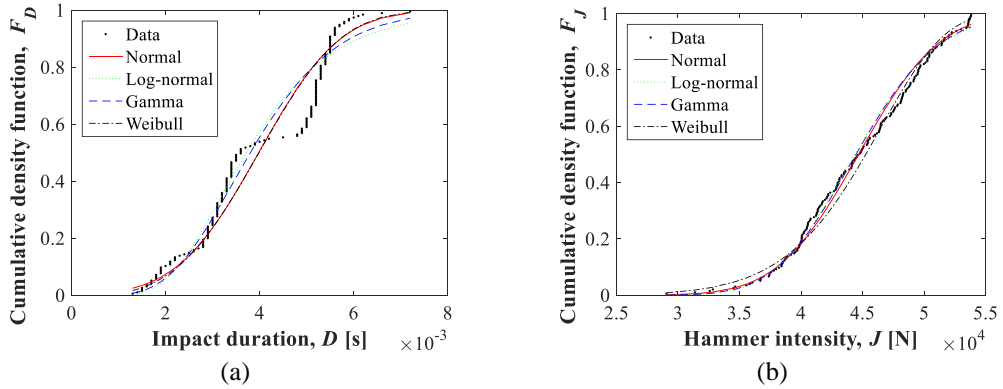


Figure 2.4 Empirical CDF of experimental data (“Data”) vs. theoretical CDF curves of several distribution models, used to examine an experimental hammer test (“hit”): a) duration (D), b) intensity (J).

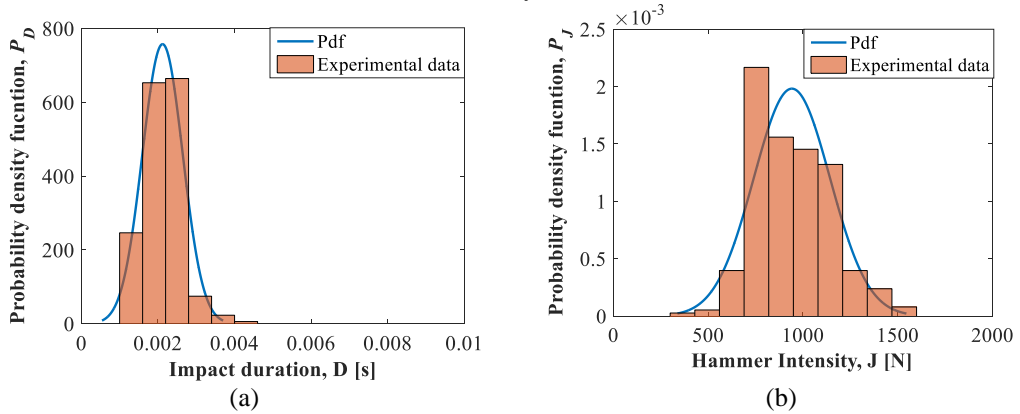


Figure 2.5 Truncated Gaussian PDF vs. experimental data (empirical histogram), normalized to unit area of experimental hammer tests: (a) Duration (D), (b) Intensity (J).

For the sake of simplicity, random variables D and J were assumed independent even though some correlation was observed in the experimental data. This assumption is adequate since the main goal of this work is to compare the relative uncertainty propagation performance exhibited by the various EDS methods described in Section 2.2, rather than the exact quantification of experimental uncertainties on the emulated system response. In addition, force measurement noise was discarded because it was negligible in comparison with the inherent variability of the hammer impulse. Moreover, verification of the above-described assumptions is provided in Fig. 2.6, which compares an experimental and a numerical hammer test both in time and frequency domains. The reader can appreciate the degree of accuracy of the numerical approximation.

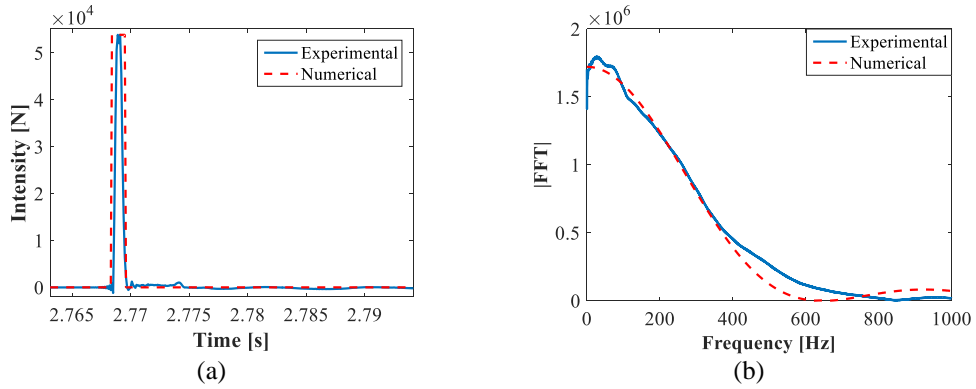


Figure 2.6 Comparison between an experimental and a numerical hammer test (“hit”): (a) time domain, (b) frequency domain.

Accelerometers, which convert physical acceleration into voltage signal, typically measure the PS response in operational and experimental modal analysis; acceleration measurements are needed by both IBS and RBS methods. An ICP accelerometer from PCB Piezotronics™ -Model Number 393 C- was used to characterize noise-contaminated measurements in our study. Table 2.3 summarizes the main characteristics of the sensor.

Table 2.3 Parameters of the reference ICP accelerometer – Model Number 393 C.

Parameters	Values	Units
Sensitivity ($\pm 15\%$)	1000	mV/g
Measurement Range	± 2.5	g
Frequency Range ($\pm 10\%$)	0.01÷1200	Hz
Broadband Resolution (from 1 to 10000 Hz)	0.00008	m/s ² RMS

Uncorrelated zero mean Gaussian white noise samples were used to contaminate simulated acceleration measurements at different PS DoFs. In this regard, a uniform variance $\sigma_{noise}^2 = (8e^{-5})^2 = 6e^{-9}$ was derived from the SNR parameter reported on the sensor datasheet for a reference signal power of $P_{signal} = 10 \times \log(\sigma_{noise}^2) = -82$ dBW. An ETB 80 electromagnetic actuator from Parker™, with load capacity equal to 8.3 kN and ± 250 mm stroke, was used as reference device for the HDS method. Actuator displacements were acquired by an additional set of laser sensors with displacement range of 200 mm. In this case, we assumed that the delay of the actuation system was perfectly compensated. Both actuator displacement disturbance (C) and force measurement noise (F) random variables were empirically characterized in the laboratory. Table 2.4 reports the parameters of all random variables used to model the experimental sources of uncertainty included in the comparative uncertainty propagation analysis.

Table 2.4 Probabilistic characterization of experimental sources of uncertainty.

Substructuring method	Sources of uncertainty	Probability density function	Mean	Standard deviation	Units
IBS and RBS	Impact force intensity (J)	Gaussian	$46 \cdot 10^3$	$8.3 \cdot 10^3$	N
	Impact force duration (D)	Gaussian	$3.5 \cdot 10^{-3}$	$1.5 \cdot 10^{-3}$	s
	Acceleration meas. noise (A)	Gaussian	0	$8 \cdot 10^{-5}$	m/s ²
HDS	Force meas. noise (F)	Gaussian	0	12	N
	Actuator disp. disturbance (C)	Gaussian	0	$1 \cdot 10^{-4}$	m

The main results of the comparative uncertainty propagation analysis based on MCS are reported in the following subsection.

2.3.3 Results of Monte Carlo samplings

In order to quantify the effect of the various experimental sources of uncertainty, described in Section 2.3.2, on the response of the 5-DoFs benchmark system defined in Section 2.3.1, a comprehensive set of MCSs was performed. The experimental testing of the PS was simulated consistently with each specific EDS method, as described in Table 2.5 for a single MC sample.

Table 2.5 Numerical simulation of the EDS methods for a single MC simulation.

<i>HDS method</i>	<p>The PM algorithm was used to solve the time history response of the 5-DoFs benchmark system. A pseudo-dynamic regime was assumed and, therefore, the pure elastic restoring force was measured at the PS interface. In order to account for both actuator displacement disturbances and noise on force measurements, the restoring force was calculated as,</p> $\mathbf{R}_{n+j/ss}^P = \mathbf{K}^P (\tilde{\mathbf{u}}_{n+j/ss}^P + \mathbf{c}) + \mathbf{f}$ <p>where, \mathbf{f} and \mathbf{c} are vectors of samples of F and C random variables, respectively. The simulation was conducted without subcycling ($ss = 1$).</p>
-------------------	--

<i>IBS method</i>	Each column of the impulse response matrix of the PS was calculated with the Newmark algorithm ($\gamma = 1/2$ and $\beta = 1/4$) considering a stochastic hammer impact, sampled from relevant D and J random variables as external loading applied to a single interface DoF. Gaussian noise generated from A was summed to acceleration responses before normalizing (re-scaling) by a factor equal to the hammer impact impulse. Then, scaled acceleration responses were numerically integrated to obtain velocity and displacement impulse responses. The same procedure was repeated for each PS interface DoF so as to form impulse response matrices $\mathbf{H}_a^p(t)$, $\mathbf{H}_v^p(t)$ and $\mathbf{H}_d^p(t)$. Finally, the IBS method was used to calculate the time history response of the 5-DoFs benchmark system.
<i>RBS method</i>	A time history analysis of the PS alone was performed with the Newmark method ($\gamma = 1/2$ and $\beta = 1/4$) considering a stochastic hammer impact sampled from relevant D and J random variables as external loading applied to a single interface DoF. Gaussian noise generated from A contaminated acceleration responses. The same procedure was repeated for each PS interface DoF and the receptance matrix $\mathbf{Y}^p(s)$ multiplied by s^2 was estimated as the ratio between Laplace transforms of PS acceleration response and corresponding hammer impact excitation histories. Then, the RBS method was used to solve the response of the 5-DoF system in the Laplace domain, which was converted to time domain via numerical inversion of the Laplace transform as shown in Eq. (2.2.65).

Normalized Root-Mean-Square Error (NRMSE) and Normalized Energy Error (NEE) scores,

$$NRMSE(\mathbf{u}, \mathbf{u}_{ref}) = \frac{1}{\sqrt{N}} \frac{\|\mathbf{u} - \mathbf{u}_{ref}\|_2}{\max(\mathbf{u}_{ref}) - \min(\mathbf{u}_{ref})} \quad (2.3.2)$$

$$NEE(\mathbf{u}, \mathbf{u}_{ref}) = \left| \frac{\|\mathbf{u}\|_2^2 - \|\mathbf{u}_{ref}\|_2^2}{\|\mathbf{u}_{ref}\|_2^2} \right| \quad (2.3.3)$$

were used to quantify the deviation of a single EDS simulation with respect to the reference (REF) solution, which was derived by using the Newmark time integrator combined to a Newton-Raphson iteration scheme with a time step $\Delta t = 0.001$ s. In Eqs. (2.3.2-2.3.3) \mathbf{u} and \mathbf{u}_{Ref} , both functions of time, represent the displacement responses calculated by a generic EDS method and the reference displacement response of the 5-DoF benchmark system, respectively; N defines the total number of simulation time steps.

A previous study (Bursi et al., 2014) showed that NMRSE is more sensitive to phase-related errors whilst NEE is more sensitive to amplitude-related errors. Other performance indicators, capable of taking into account both actuator dynamics and partitioning effects have been suggested for the HDS method in (Maghareh et al., 2014). Both NRMSE and NEE were evaluated using 1000 MC samples and relevant mean and standard deviation estimates were used to compare the EDS methods presented in Section 2.2. Figure 2.7 illustrates the

convergence of the statistical moments of both NEE and NRMSE, evaluated for the IBS method at interface Node #3 of the 5-DoF benchmark system.

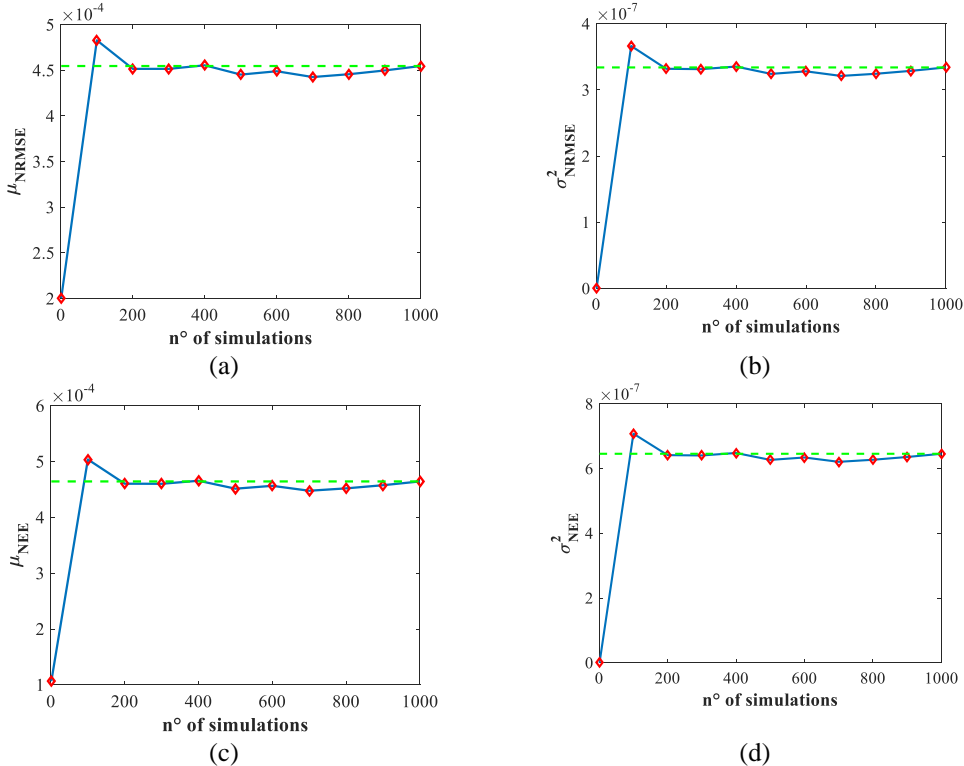
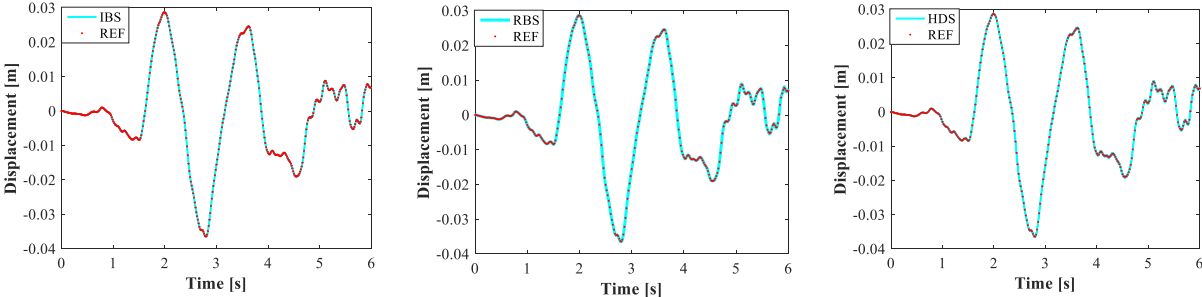


Figure 2.7 Convergence of error score statistical moments evaluated at interface Node #3 of the linear 5-DoF benchmark system considering the IBS method: (a) mean and (b) variance of NRMSE; (c) mean and (d) variance of NEE.

The same convergence trend was observed for all EDS methods included in the present uncertainty propagation comparative study. Fig. 2.8 compares the average dynamic response of the linear 5-DoF benchmark system of Fig. 2.3a calculated at Node #3 and relevant 99% confidence intervals for the specific case of damping ratio $\zeta = 0.01$ and split mass ratio $m_f = 0.5$.



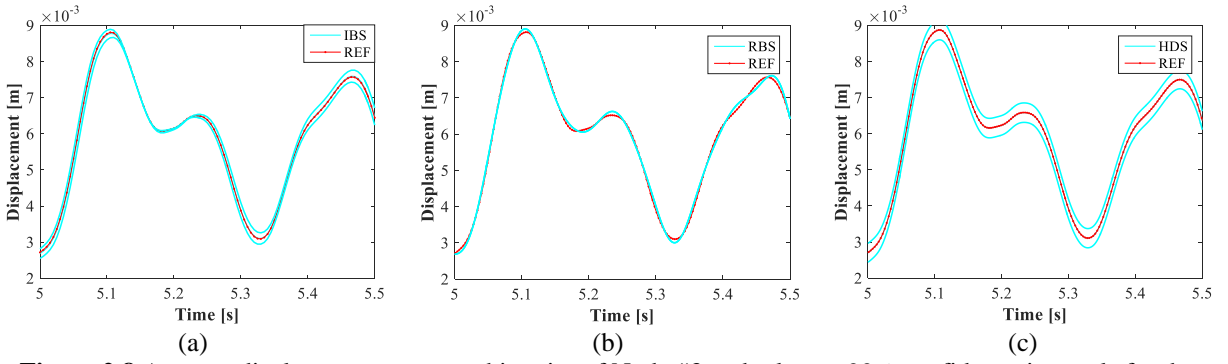
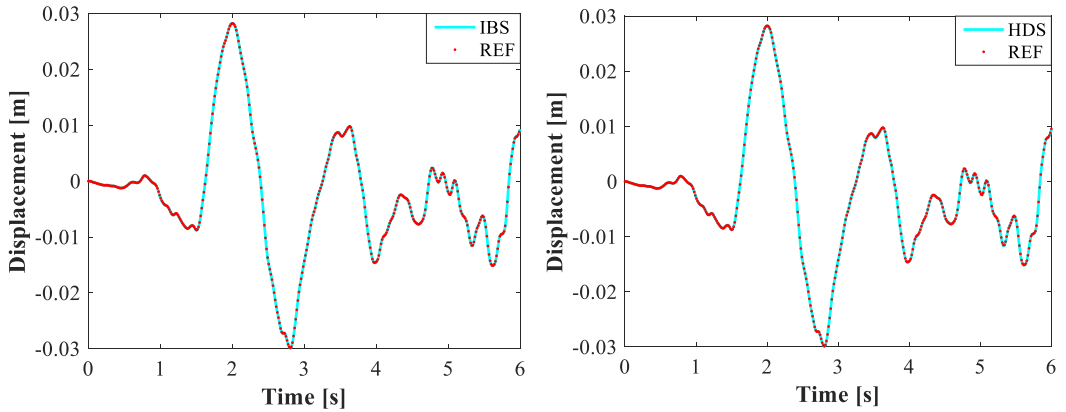


Figure 2.8 Average displacement response histories of Node #3 and relevant 99% confidence intervals for the linear 5-DoF system with $\zeta = 0.01$ and $m_f = 0.5$: (a) IBS and REF; (b) RBS and REF; (c) HDS and REF.

As can be appreciated from Fig. 2.8, plots reveal narrow confidence intervals and average displacements that are almost indistinguishable from the reference solutions for all three EDS methods.

Analogously and assuming $\zeta = 0.01$ and $m_f = 0.5$, Fig. 9 compares displacement histories calculated at Node #3 and relevant 99% confidence intervals for the non-linear 5-DoF benchmark system of Fig. 2.3b.



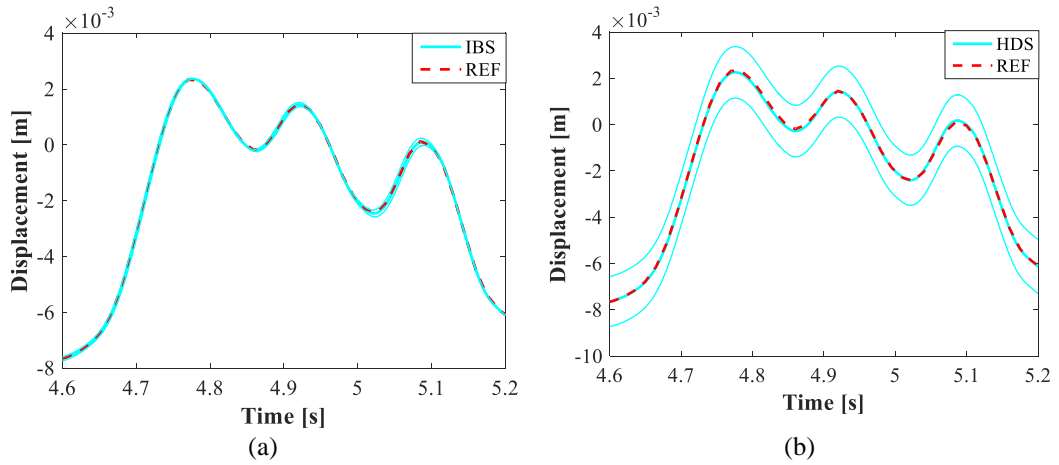


Figure 2.9 Average displacement response histories of Node #3 and relevant 99% confidence intervals for the non-linear 5-DoF system with $\zeta = 0.01$ and $mf = 0.5$: (a) IBS and REF; (b) HDS and REF.

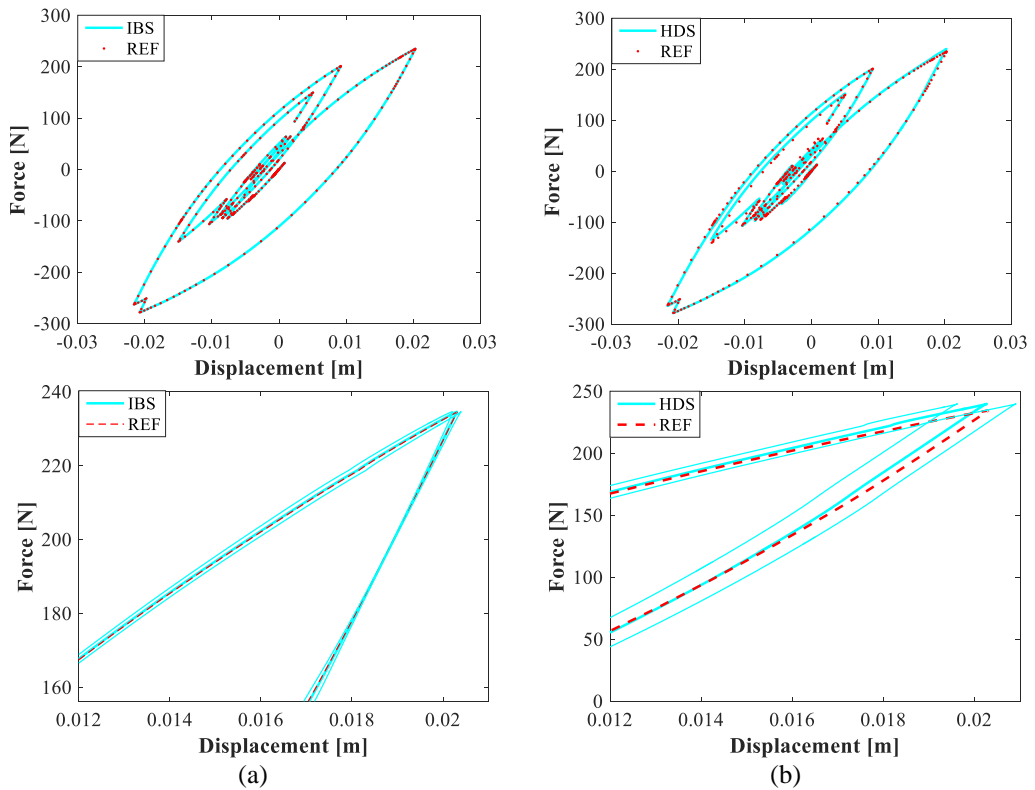


Figure 2.10 Average force-displacement hysteretic loops of the non-linear spring element and relevant 99% confidence intervals for the non-linear 5-DoF system with $\zeta = 0.01$ and $mf = 0.5$: (a) IBS and REF; (b) HDS and REF.

Since the RBS cannot be used in combination with non-linear substructures, the comparison is limited to IBS and HDS methods. In this respect, Fig. 2.10 compares force-displacement hysteretic loops of the non-linear spring element as well as relevant 99%

confidence intervals. As can be appreciated from both Fig. 2.9 and 2.10, the disagreement between EDS simulations and reference solutions is always minimal also in presence of non-linearities. Table 2.6 and 2.7 summarize mean and standard deviation estimates of both NRMSE and NEE scores, for the linear as well as the non-linear variants of the 5-DoFs benchmark system, respectively, after MCSs.

Table 2.6 Comparison of error score statistics for the linear variant of the 5-DoFs benchmark system after MCS.

	μ_{NRMSE}			σ_{NRMSE}			μ_{NEE}			σ_{NEE}		
	<i>IBS</i>	<i>RBS</i>	<i>HDS</i>	<i>IBS</i>	<i>RBS</i>	<i>HDS</i>	<i>IBS</i>	<i>RBS</i>	<i>HDS</i>	<i>IBS</i>	<i>RBS</i>	<i>HDS</i>
$m_f = 0.5$ $\zeta = 0.01$	4.5e-4	9.3e-4	4.1e-4	5.8e-4	1.2e-3	1.6e-3	4.6e-4	8.8e-4	1.4e-3	8.0e-4	2.8e-3	1.0e-3
	4	4	3	4	6	3	4	4	2	4	5	2
$m_f = 0.9$ $\zeta = 0.03$	5.6e-4	1.1e-3	3.9e-4	1.1e-3	3.1e-3	1.4e-3	1.3e-3	1.4e-3	1.3e-3	3.1e-3	4.3e-3	9.3e-3
	4	3	3	3	6	3	3	3	2	3	5	3

Table 2.7 Comparison of error score statistics for the non-linear variant of the 5-DoFs benchmark system after MCS.

	μ_{NRMSE}		σ_{NRMSE}		μ_{NEE}		σ_{NEE}	
	<i>IBS</i>	<i>HDS</i>	<i>IBS</i>	<i>HDS</i>	<i>IBS</i>	<i>HDS</i>	<i>IBS</i>	<i>HDS</i>
$m_f = 0.5$ $\zeta = 0.01$	3.8e-4	3.5e-3	5.4e-4	9.9e-4	9.4e-4	8.1e-3	1.6e-3	6.2e-3
$m_f = 0.9$ $\zeta = 0.03$	6.0e-4	3.5e-3	9.8e-4	9.6e-4	1.3e-3	7.8e-3	2.6e-3	5.9e-3

A careful reader can observe that in the linear case, see Table 2.6, the RBS method outperforms IBS in terms of σ_{NRMSE} . This must be ascribed to the fact that simulated hammer impact forces used to derive impulse response matrices have random durations exceeding the single time step, which is in contrast with the definition of discrete impulse response function of Eqs. (2.2.32)-(2.2.34). Input deconvolution, which is implicitly performed in the calculation of receptance matrices, would certainly improve the performance of the IBS method and justify the better performance of the RBS method. Conversely, all methods exhibit similar performance in the non-linear case, for any combination of ζ and m_f parameters. Therefore, they can be conveniently employed in conjunction with the C-EDS framework, as shown hereinafter, to examine the response of a virtual petrochemical prototype plant case study.

2.4 Application of the C-EDS method to a petrochemical prototype plant

In order to highlight the versatility of the presented C-EDS framework in combining radically different EDS methods for simulating the response of heterogeneous systems, a virtual experiment was conducted on the petrochemical prototype plant case study depicted in Fig. 2.11. In this prototype example, all the PSs are simulated numerically in a noise-free condition.

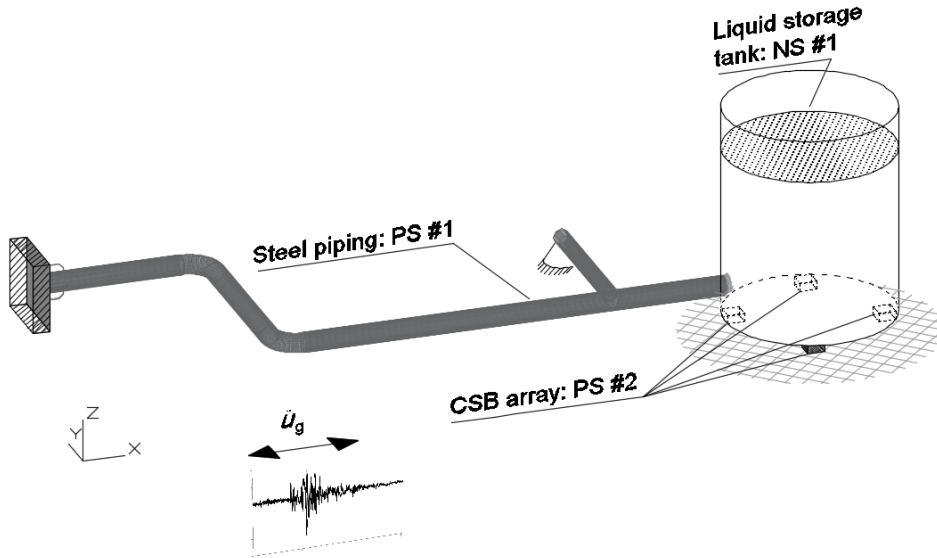


Figure 2.11 Petrochemical prototype plant case study with highlighted substructures.

As shown in Fig. 2.11, four CSBs support a liquid storage tank that is connected to a steel piping. Water at ambient temperature fills both the tank and the piping. The same accelerogram of the 1989 Loma Prieta earthquake with 4.25 m/s^2 PGA, used for the uncertainty propagation analysis in Section 3, was selected as the reference seismic excitation signal. The goal of this virtual experiment is to estimate residual displacements of CSBs, which must remain small to guarantee safe operating conditions for the piping system. To this end, a simulator of the petrochemical plant case study was developed by combining different PSs and NSs by means of the presented C-EDS framework.

It was assumed that the piping response remains linear but boundary conditions are highly uncertain. However, such substructure is available onsite for dynamic characterization; offline EDS can be conveniently used to emulate its response. On the other hand, the difficulty in the modelling of friction effects between sliding parts, which depends on speed, vertical load, temperature and wear (Guyan, 1965), justifies the use of online EDS to account for the non-linear hysteretic response of the CSB array that can be tested in the laboratory. Under these premises, Fig. 2.12 depicts a schematic of the substructuring configuration assumed for the virtual experiment.

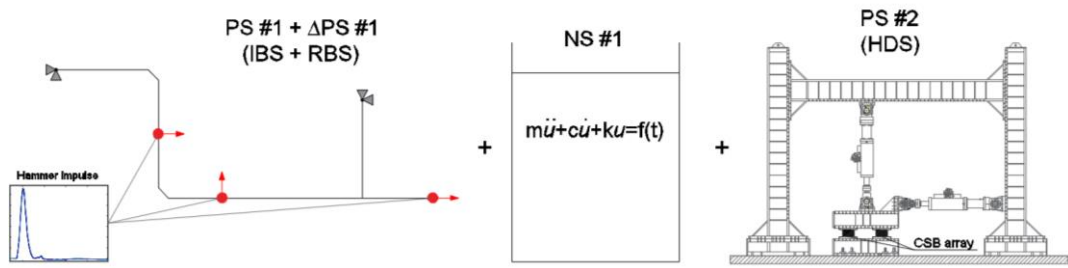


Figure 2.12 Substructuring schematics of the petrochemical prototype plant case study.

As can be appreciated from Fig. 2.12, an impulse response matrix is needed to represent the piping system -PS #1-, which is characterized offline by using the RBS, whilst the sliding liquid storage tank with sloshing fluid -NS #1- is numerically simulated. Consequently, in order to account for the hysteretic response of the CSB array -PS #2-, which was tested in the laboratory, IBS and HDS methods were combined. Detailed descriptions of all substructures as well as the main results of the virtual C-EDS experiment are reported in the next subsections.

2.4.1 Physical piping system

The piping system combines 40 straight elements of 8” (outer diameter: 219.08 mm; thickness: 8.18 mm) and 6” diameter (outer diameter: 168.28 mm; thickness: 7.11 mm) and several critical components such as elbows and one tee joint. API 5L Gr. X52 steel material (nominal yield strength f_y and tensile strength f_u equal to 418 MPa and 554 MPa, respectively) characterizes all elements. A temporary support frame, which will be replaced by the liquid storage tank, provides additional mass and stiffness to the displacement DoF of the end flange of the piping system in the X direction. Three accelerometers are installed on the system, which was assumed to be available onsite for experimental modal analysis based on hammer tests. Fig. 2.13 depicts the piping system including the temporary support frame and the locations of three accelerometers.

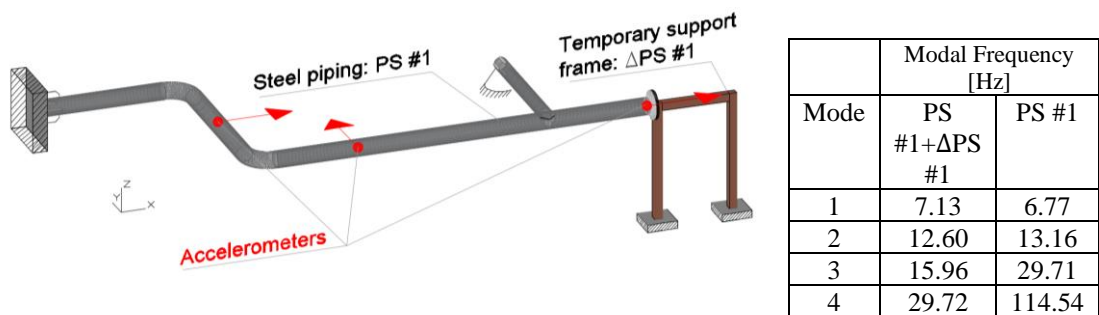


Figure 2.13 Piping system with main dimensions and locations of accelerometers for experimental modal analysis.

In order to simulate the substructuring process, the 30-DoF FE model of the piping system including the temporary support frame, which is depicted in Fig. 2.14, was implemented. All pipes including elbows were modelled using straight beam elements with

an equivalent linear stiffness. An equivalent material density accounts for filling water at 3.2 MPa pressure (Bursi et al., 2014). Two additional lumped masses $M_v = 1e3 \text{ kg}$ account for valves and other components connected to the piping system whilst the lumped mass $M_f = 1e3 \text{ kg}$ and the stiffness $K_f = 1e5 \text{ N/m}$ simulate the effect of the temporary support frame.

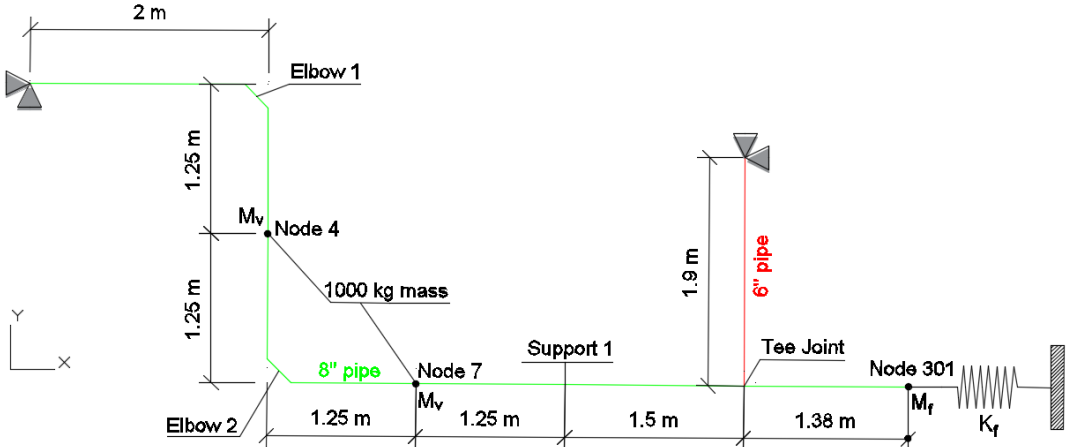


Figure 2.14 FE model and main characteristics of both piping system and temporary support frame

The receptance matrices of the piping system with temporary support frame -PS #1 + ΔPS #1- and the temporary support frame alone -ΔPS #1- were calculated according to Eq. (2.2.60) based on FE matrices. Subsequently, the DoFs measured by accelerometers were retained via static condensation. In order to obtain the receptance matrix of the piping system alone -PS #1-, RBS was used to subtract the contribution of the temporary support frame -ΔPS #1- from the measured receptance matrix of the entire system, i.e. the piping system connected to the temporary support frame -PS #1 + ΔPS #1-. Finally, the corresponding impulse response matrix was calculated via numerical inverse Laplace transform according to Eqs. (2.2.66-2.2.68), considering $\alpha = 0.2, T = 15 \text{ s}$ and $q = 1e4$. Fig. 2.15 compares coupled/decoupled receptance and impulse response functions and relevant reference solutions analytically obtained from the FE matrices of the piping system according to Eq. (2.2.60).

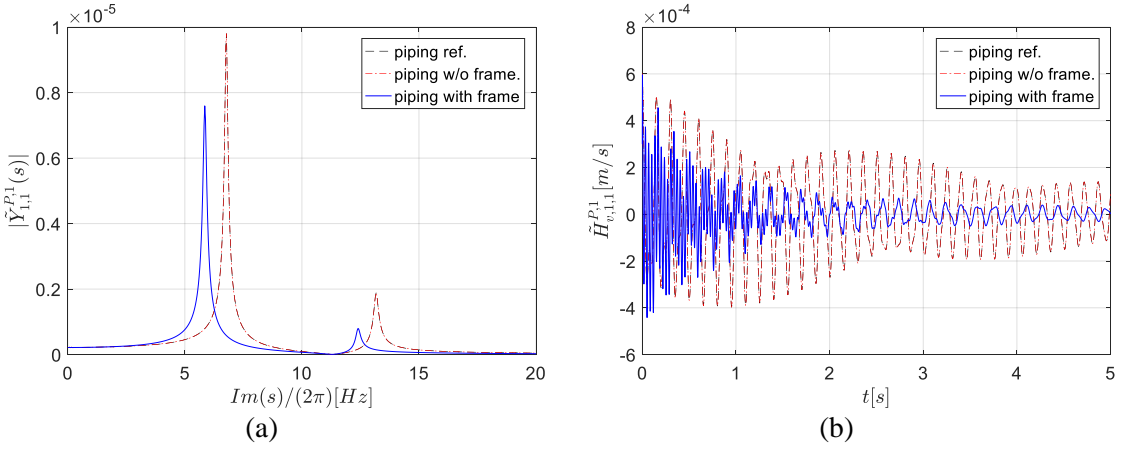


Figure 2.15 EDS of the piping system: a) receptance function -Laplace domain- and b) corresponding impulse response function -time domain- relevant to Node #301, dir. X.

In Fig. 2.15, the label “piping ref.” designates the reference analytical response, derived from FE matrices of the piping system alone; “piping with frame” represents the piping coupled with the anchorage frame whilst “piping w/o frame” indicates the decoupled piping network after RBS. As can be appreciated from Fig. 2.15 where curves of “piping ref.” and “piping w/o frame” overlap, the procedure yields an accurate estimation of impulse response functions that can be used for time history response analysis with the IBS. In order to solve Eq. (2.2.35), the last step of the EDS of the piping network consists in condensing the external load vector to the set of retained DoFs measured by the accelerometers. Accordingly, the approach suggested by Bursi and co-workers (2014) was followed, which relies on the Guyan method (1965). First, the stiffness matrix of the piping system extracted from the relevant FE model was partitioned according to the retained (r) and discarded (d) DoFs.

$$\mathbf{K}^{P,1} = \begin{bmatrix} \mathbf{K}_{rr}^{P,1} & \mathbf{K}_{rd}^{P,1} \\ \mathbf{K}_{dr}^{P,1} & \mathbf{K}_{dd}^{P,1} \end{bmatrix} \quad (2.4.1)$$

Then, the matrix of restraint modes $\Phi^{P,1}$ was derived as,

$$\Phi^{P,1} = \begin{bmatrix} \mathbf{I}_{rr} \\ -\mathbf{K}_{dd}^{P,1-1} \mathbf{K}_{dr}^{P,1} \end{bmatrix} \quad (2.4.2)$$

where \mathbf{I}_{rr} is an identity square matrix of size equal to the number of retained DoFs. Thus, restraint modes were used to condense the external seismic load to the master DoFs.

$$\tilde{\mathbf{F}}^{P,1}(t) = -\boldsymbol{\Phi}^{P,1T} \mathbf{M}^{P,1} \mathbf{T}^{P,1} a_g(t) \quad (2.4.3)$$

Impulse response matrices $\tilde{\mathbf{H}}_d^{P,1}(t)$, $\tilde{\mathbf{H}}_v^{P,1}(t)$ and $\tilde{\mathbf{H}}_a^{P,1}(t)$ and external vector $\tilde{\mathbf{F}}^{P,1}(t)$ emulate the response of the piping network -PS #1- within the coupled simulation. The tilde “hats” emphasize the Guyan condensation to the retained DoFs.

2.4.2 Physical concave sliding bearing array

An array of 2x2 CSBs with a single sliding surface -PS #2- supports the liquid storage tank; therefore, based on the considerations of Section 2.4, we use HDS to emulate the non-linear hysteretic response of the seismic isolation devices through virtual testing in the laboratory. Fig. 2.16 depicts the adopted CSB as well as the test setup for HDS.

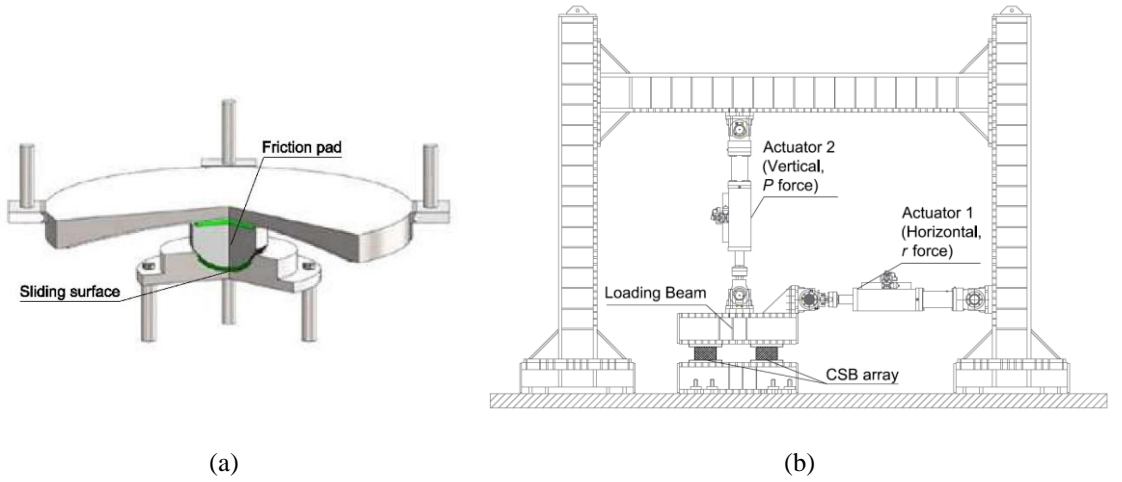


Figure 2.16 Details of the CSB and test setup of the CSB array

Since the variability in the force response among different devices is small, it is reasonable to test a reduced CSB array in the laboratory and multiply the measured restoring force so as to simulate the full CSB array. Thus, as can be appreciated in Fig. 2.16b, only two CSBs out of four were virtually tested in the laboratory. An example of a more complex testing setup for CSBs, which controls tilting angles and out-of-plane moments can be found in (Abbiati et al., 2015; Bursi et al., 2017). From a mechanical viewpoint, a single CSB device can be characterized by a simplified linear piece-wise force-displacement relationship,

$$\left\{ \begin{array}{l} r = \frac{\mu_f P}{\Delta} u, u \leq \Delta \\ r = \mu_f \text{sign}(\dot{u})P + \frac{P}{R}u, u > \Delta \end{array} \right. \quad (2.4.4)$$

where μ_f is the friction coefficient, R is the device curvature radius, \dot{u} and u are the instantaneous velocity and sliding displacement of the isolator, respectively; P is a constant vertical load whilst r is the transversal restoring force of the CSB, which are measured by both vertical and horizontal actuators of Fig. 2.16, respectively. More precisely, all CSB devices are characterized by surface radius R equal to 5000 mm, friction coefficient μ_f equal to 8 % and initial yield displacement Δ of 0.5 mm. Moreover, each single CSB device carries a vertical load P equal to 1360 kN, which corresponds to one fourth of the weight of the liquid storage tank filled with water up to its maximum capacity.

The interaction of multiple displacement-controlled actuators, connected to the same very stiff specimen, can easily trigger dynamic instability. In order to overcome this problem, common testing practice of seismic isolation devices consists in applying the nominal value of vertical loading via force control and imposing transverse displacement via position control.

In order to replicate the slip-based behaviour of the CSB array -PS #2- the differential model proposed by Mostaghel (1999) was adopted. Fig. 2.17 shows both a schematic of the aforementioned model and its bilinear hysteretic loop.

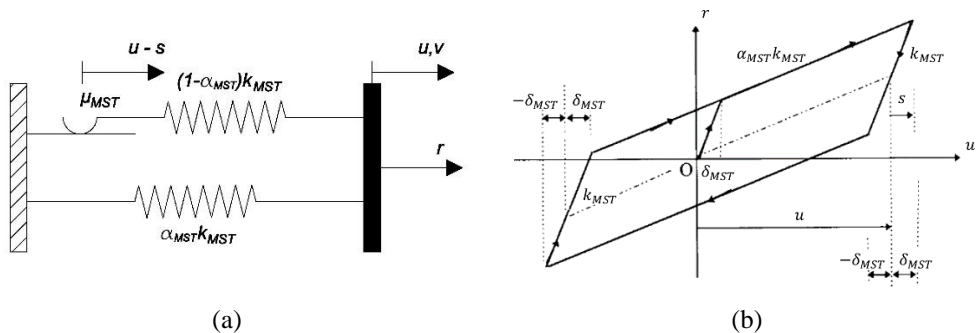


Figure 2.17 Bilinear Mostaghel model: a) S-DoF idealization; b) Hysteretic loop.

The corresponding ODE set, which defines the hysteretic Mostaghel model subjected to a given velocity history $v(t)$, reads,

$$\begin{cases} \dot{r} = \left(\alpha_{MST} k_{MST} + (1 - \alpha_{MST}) k_{MST} (\bar{N}(v) \bar{M}(s - \delta_{MST}) + M(v) N(s + \delta_{MST})) \right) v \\ \dot{u} = v \end{cases} \quad (2.4.5)$$

with,

$$s = \frac{r - \alpha_{MST} k_{MST} u}{(1 - \alpha_{MST}) k_{MST}} \quad (2.4.6)$$

where, u and r represents displacement and restoring force state variables of the element and s defines slip displacement. The remaining functions N, M, \bar{N} and \bar{M} read,

$$\begin{aligned} N(w) &= 0.5(1 + \text{sgn}(w)) \left(1 + (1 - \text{sgn}(w))\right) \\ M(w) &= 1 - N(w) \\ \bar{N}(w) &= M(-w) \\ \bar{M}(w) &= N(-w) \end{aligned} \quad (2.4.7)$$

where $\text{sgn}(\cdot)$ is the sign function. The parameters k_{MST}, α_{MST} and δ_{MST} represent initial stiffness, post-yielding stiffness reduction factor and yielding displacement of a single CSB device, respectively. They are related to the physical parameters of the CSB model of Eq. (2.4.4) as,

$$\begin{aligned} \delta_{MST} &= \Delta = 5e - 4 \text{ m} \\ \alpha_{MST} &= \frac{\Delta}{\mu_f R} = 1.30e - 3 \\ k_{MST} &= \frac{\mu_f P}{\Delta} = 2.18e + 8 \frac{N}{m} \end{aligned} \quad (2.4.8)$$

In order to assemble Mostaghel's hysteretic springs in a FE fashion, a finite element driver was implemented, which numerically integrates Eq. (2.4.5) for a given displacement increment by using a 4-th order Runge-Kutta scheme. Four Mostaghel's elements in parallel simulated the response of the CSB array -PS #2-.

2.4.3 Numerical model of a sliding liquid storage tank

In order to simulate the response of the liquid storage tank -NS #1-, the 3-DoFs linear model proposed by Malhotra and co-workers (2000) was adopted. The model accounts for fluid-structure interaction in a simplified yet accurate manner. A schematic of the liquid storage tank model is illustrated in Fig. 2.18. In detail, H and r define height and radius of the tank whilst h is the equivalent uniform thickness of the tank wall.

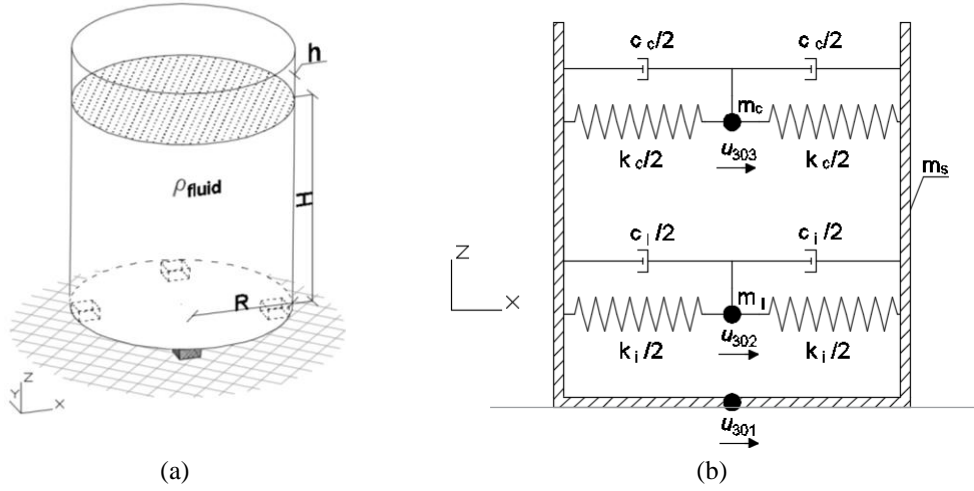


Figure 2.18 Sliding liquid storage tank according to Malhotra et al. (2000); a) schematic; b) numerical model with mass DoF numbering

As depicted in Fig. 2.18, two S-DoF damped oscillators emulate impulsive and convective vibration modes of the sloshing fluid. In this regard, natural vibration periods T_i and T_c and masses m_i and m_c associated with impulsive and convective fluid oscillation modes are respectively calculated as,

$$T_i = C_i H \sqrt{\frac{\rho r}{E h}}, T_c = C_c \sqrt{r} \quad (2.4.9)$$

$$m_i = \gamma_i m_l, m_c = \gamma_c m_l \quad (2.4.10)$$

where, ρ the mass density of liquid, E the modulus of elasticity of the tank material; C_i , C_c , γ and γ_c are four coefficients depending on the tank wall slenderness H/r ; m_l is the total mass of the liquid. Values of stiffness parameters k_c and k_i were calibrated to match pre-selected target periods; convective and impulsive damping ratios, $\zeta_c = 0.5\%$ and $\zeta_i = 5\%$ respectively, determine the parameters of equivalent linear dashpots in the model.

$$k_i = m_i \left(\frac{2\pi}{T_i} \right)^2, k_c = m_c \left(\frac{2\pi}{T_c} \right)^2 \quad (2.4.11)$$

$$c_i = \frac{4\pi m_i \zeta_i}{T_i}, c_c = \frac{4\pi m_c \zeta_c}{T_c} \quad (2.4.12)$$

For the sake of completeness, mass, damping and stiffness matrices, needed to study the dynamic response of the liquid storage tank -NS #1-, are reported below,

$$\mathbf{M}^N = \begin{bmatrix} m_s & 0 & 0 \\ 0 & m_i & 0 \\ 0 & 0 & m_c \end{bmatrix}, \mathbf{C}^N = \begin{bmatrix} (c_i + c_c) & -c_i & -c_c \\ -c_i & c_i & 0 \\ -c_c & 0 & c_c \end{bmatrix}, \quad (2.4.13)$$

$$\mathbf{K}^N = \begin{bmatrix} (k_i + k_c) & -k_i & -k_c \\ -k_i & k_i & 0 \\ -k_c & 0 & k_c \end{bmatrix}$$

where $m_s = m_t + m_l - m_i - m_c$ is the residual sliding mass and m_t is the storage tank mass without liquid. Table 2.8 reports all parameter values whilst Table 2.9 summarizes the global parameters of the sloshing fluid model.

Table 2.8 Parameters of the liquid storage tank model.

Parameter	Value	Unit
E	210	GPa
ρ_{fluid}	900	kg/m ³
ρ_{tank}	7850	kg/m ³
γ_c	0.1580	
γ_i	0.8320	
C_c	1.48	
C_i	7.03	
H	12	m
R	4	m
h	6e-3	m
m_t	28000	kg
m_l	5.43e5	kg
m_s	33200	kg

Table 2.9 Global parameters of the sloshing fluid model.

Sloshing mode	Mass [kg]	Damping [Ns/m]	Stiffness [N/m]	Vibration period [s]	Damping ratio ζ
Convective	8.58e4 (m_c)	1.82e3 (c_c)	3.86e7 (k_c)	2.96 (T_c)	0.50 % (ζ_c)
Impulsive	4.52e5 (m_i)	1.99e6 (c_i)	8.77e10 (k_i)	0.14 (T_i)	5.00 % (ζ_i)

2.4.4 Simulation of the emulated system with the C-EDS method

In order to simulate the seismic response of the petrochemical prototype plant of Fig. 2.11 a partitioned model of the emulated system was implemented in Matlab (2012). In detail, all NS and PS models described in Subsections 2.4.1-2.4.3 were coupled together by using the LLMs presented in Subsection 2.2.2 within the C-EDS method. Fig. 2.19 illustrates a sketch of the partitioned model with node numbering.

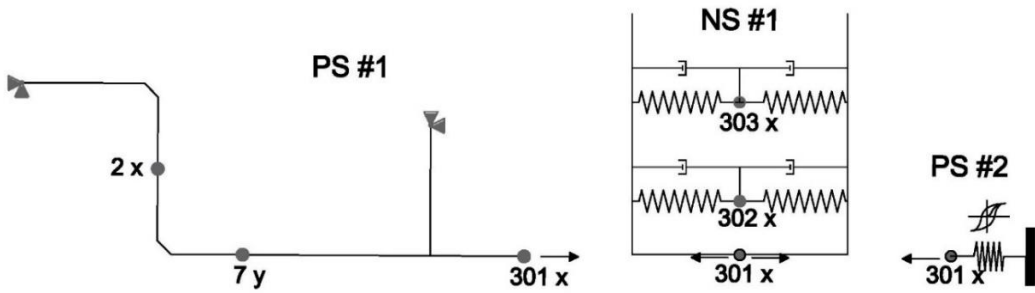
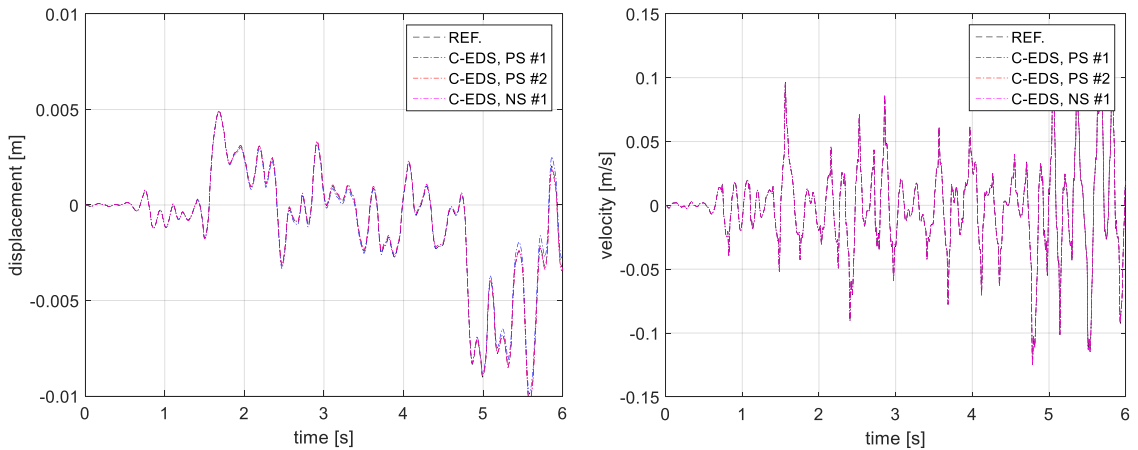


Figure 2.19 Partitioned model of the petrochemical prototype plant case study.

The time history response of the system was numerically obtained by considering a time integration step $\Delta t = 0.1$ ms without subcycling ($ss = 1$). In line with the goal of this virtual experiment, which aims at estimating the residual shift of the liquid storage tank, Fig. 2.20 compares both displacement and velocity response histories relevant to Node 301, which is shared by all substructures, to a reference solution. The reference “exact” solution was calculated by Newmark method ($\Delta t = 0.1$ ms, $\gamma = 1/2$, $\beta = 1/4$), considering a monolithic model of the prototype plant case study that merges the FE models of all substructures condensed to the same DoFs retained by the partitioned model of Fig. 2.19.



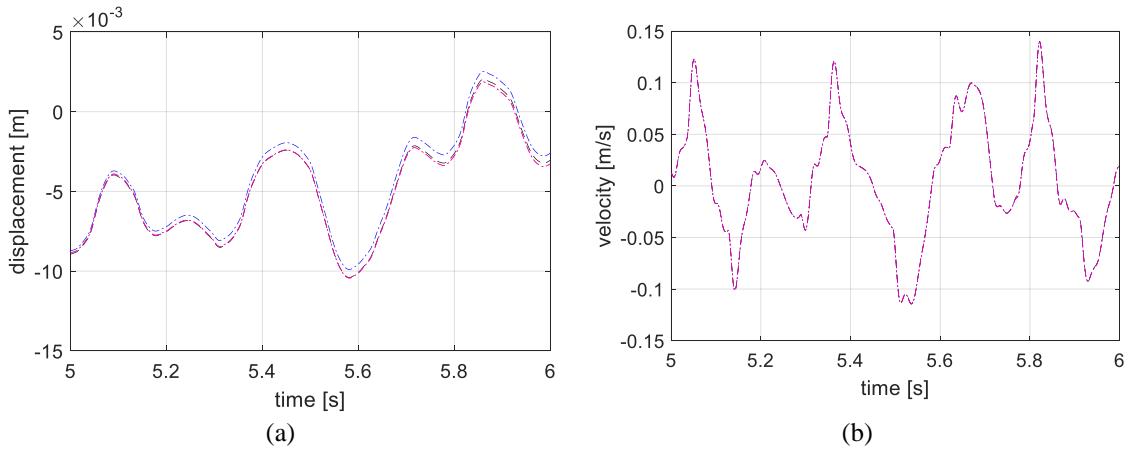
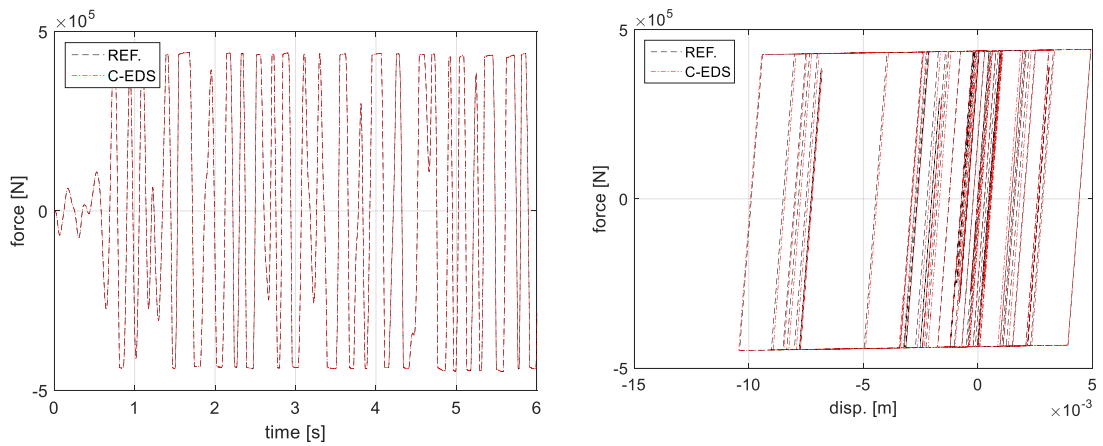


Figure 2.20 Time history responses of Node 301: a) displacement; b) velocity and relevant zoomed views.

As can be appreciated from Fig. 2.20a, a small drift is observed among displacement histories corresponding to the same coupling DoF that belong to different subdomains. On the other hand, as illustrated in Fig. 2.20b, interface velocity coupling ensures exact matching of velocity histories. Similarly, Fig. 2.21 compares both force time history response and displacement-force hysteretic loop of the CSB array -PS #2-.



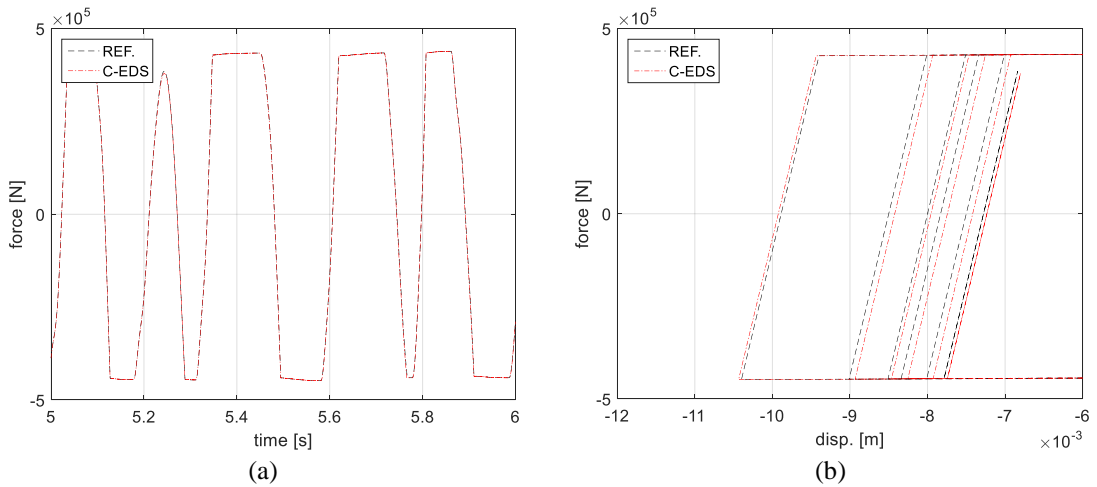


Figure 2.21 Dynamic response of the CSB array: a) force time history; b) displacement-force hysteretic loop and relevant zoomed views.

As can be appreciated from Fig. 2.21a, force response histories calculated with the C-EDS agree with the reference solution. However, a small discrepancy is observed in the displacement-force hysteretic loops, which is ascribed to the small drift that characterizes displacement response histories.

2.5 Conclusions

This paper is centered upon the comparison and the generalized use of online and offline methods for EDS. With this perspective, a comprehensive uncertainty propagation analysis of experimentally-based online/offline dynamic substructuring methods was investigated. In particular, the performance comparison included the following methods: the online (numerical/physical) HDS method and two offline methods, i.e. the IBS and the RBS method. This investigation also explored the possibility of a combined exploitation of the three techniques, the novel C-EDS method, both to improve and accelerate the execution of the experiment/simulation. In this respect, we described the main characteristics of three EDS methods, which include the coupling algorithms based on dual assembly of PS and NS performed with a localized version of the Lagrange multiplier method. Furthermore, we introduced the methods, through which uncertainties related to the various simulation methods can be accounted for and quantified; thus, a five-DoF linear/non-linear chain-like system was examined by including typical uncertainties emerging from measurements errors and laboratory operators. The simulation results, presented in terms of statistics of both NRMSE and NEE scores, suggested that the RBS method exhibits a better performance in the linear case whilst all methods are equivalent in the nonlinear regime. Finally, capitalizing from the results of a more complex case study composed of a virtual petrochemical prototype plant, we provided a feasible approach to employ the C-EDS method along with a comprehensive verification. In particular, a linear PS -a piping- and a non-linear PS -four isolating devices- were coupled to a linear NS – a slender tank-. The comparison between substructuring and reference results, obtained from a monolithic model of the system, were

satisfactory. Encouraged by these results presented in Section 2.4, the C-EDS method is currently being applied to an actual prototype plant in the laboratory.

2.A Additional research on real time/pseudo dynamic testing of piping systems with dynamic substructuring

In order to characterize the dynamic interaction between tanks and critical components of piping systems, e.g., flange joints, Tee joint etc., a series of real-time/pseudodynamic tests were performed at the University of Trento. In this respect, Fig. 2.A.1 depicts the physical substructure tested in the lab and the numerical substructure numerically modelled.

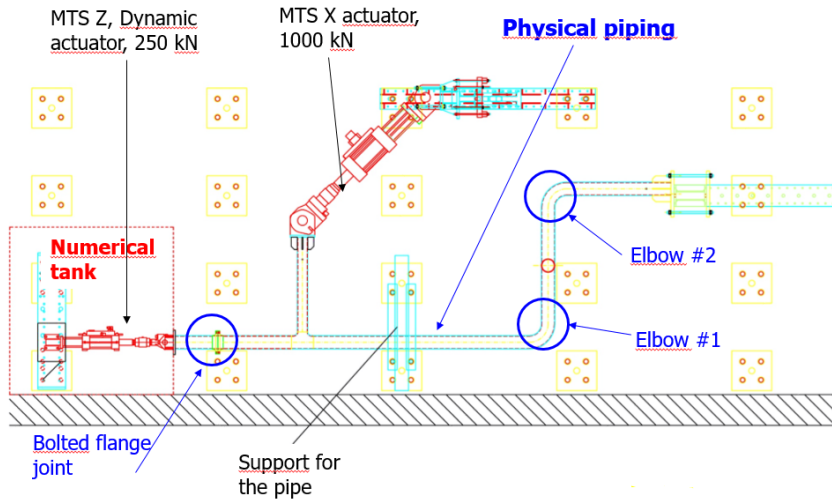


Figure 2.A.1 Physical and numerical substructures for real-time/pseudodynamic tests

2.A.1 Introduction

The interaction between coupled components is a critical point to consider during seismic events. In this experimental test campaign, the interaction between two types of liquid storage tanks, i.e. a slender tank and a broad tank, and a steel piping system is investigated by means of both real time and pseudo-dynamic tests. In particular, the online continuous HDS method is adopted with the PM (Bursi et al., 2017) partitioned time integration algorithm. Moreover, to guarantee A-stability, the trapezoidal rule implicit scheme ($\gamma^N = 1/2$ and $\beta^N = 1/4$) is used on the NS. In addition, to couple the PS and the NS, we adopt the LLMs (Park et al., 2000) for dual assembly of subdomains.

Allowable stress tests are conducted in real time with dynamic substructuring and actual inertia effects of PS; in fact hydraulic actuators, reproducing coupling forces, see Fig. 2.A.1, are capable of reproducing small displacements. Conversely, elasto-plastic and ultimate strength tests are carried out by means of the pseudo-dynamic test method, where inertia forces of the PS are also modelled into the computer; as a result, hydraulic actuators are able to reproduce large displacements applied to the PS. The internal pressure (pressurized medium: water) is held constant during load application. The sequence of real time/pseudo-dynamic tests at increasing peak ground acceleration values takes into account degradation effects of components; as a result, a consistent degradation of the PS is simulated. In order

to identify modal damping ratios of the piping component, preliminary system identification tests are conducted on the specimen.

2.A.2 Case Study selection

Two kinds of liquid storage tanks were chosen from the Case Study #1 of the project, i.e. the storage tank family plant. In particular, as reported in Fig. 2.A.2, the slender tank #23 and the broad tank #60 were selected.



Figure 2.A.2 Selected storage tanks from the Case Study #1

The storage tanks were supposed to be seismically isolated by means of CSB. Both geometrical and mechanical details for storage tanks and base-isolator devices are reported hereinafter.

2.A.2.1 Evaluation of the input earthquake acceleration history

Several standards deal with seismic analysis of onshore petrochemical and process plants, e.g. *EN 13480-3 (2002)*, *ASME B31.1 (2001)*, *ASME B31.3 (2006)* and *NFPA 59A (2013)*, among others, use the same seismic hazard definitions adopted by nuclear standards *NEA/CSNI/R(2007)17 (2008)*. These standards prescribe an allowable stress-based verification of pipes under two types of earthquakes, namely the operating basis (OBE) and the safe shut-down (SSE) earthquake, see Table 2.A.1.

Table 2.A.1 Comparison between Nuclear and Italian standards.

<i>Limit states of piping+tank</i>	<i>Nuclear standards</i>	<i>Italian standards</i>	<i>Return Period (Tr)</i>
<i>Ultimate Limit States</i>	<i>OBE</i>	<i>Safe Life Limit State (SLLS)</i>	<i>475 years (Pr = 10% in 50 years)</i>
	<i>SSE</i>	<i>Near Collapse Limit State (NCLS)</i>	<i>2475 years (Pr = 2% in 50 years)</i>

With reference to the uniform hazard spectrum of Priolo Gargallo, different spectra-compatible natural earthquakes were provided by UNIRM3, as depicted in Fig 2.A.3. For this experimental test campaign, natural signals with both 475 and 2475 years as return period were selected.

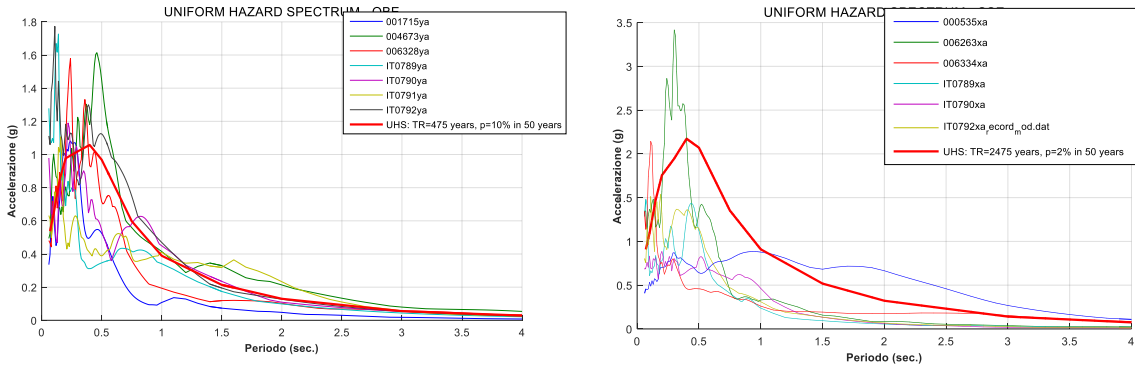


Figure 2.A.3 Natural earthquake spectra that fit the Uniform Hazard Spectrum of Priolo Gargallo: RP = 475 years (left) and RP = 2475 years (right).

2.A.3 Numerical Substructure (NS)

2.A.3.1 Liquid storage tank

In order to simulate the response of the liquid storage tank -NS #1-, the 3-DoFs linear model proposed by Malhotra and co-workers (2000) was adopted. The model accounts for fluid-structure interaction in a simplified yet accurate manner. A schematic of the liquid storage tank model is illustrated in Fig. 2.A.4. In detail, H and r define height and radius of the tank whilst h is the equivalent uniform thickness of the tank wall.

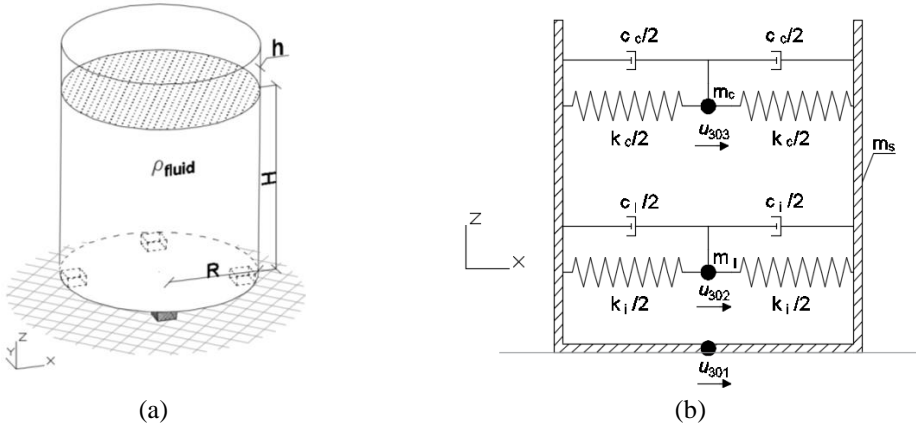


Figure 2.A.4 Sliding liquid storage tank according to Malhotra et al. (2000); a) schematic; b) numerical model with mass DoF numbering

As depicted in Fig. 2.A.4, two S-DoF damped oscillators emulate impulsive and convective vibration modes of the sloshing fluid. In this regard, natural vibration periods T_i and T_c and

masses m_i and m_c associated with impulsive and convective fluid oscillation modes are respectively calculated as,

$$T_i = C_i H \sqrt{\frac{\rho r}{E h}}, T_c = C_c \sqrt{r} \quad (2.A.1)$$

$$m_i = \gamma_i m_l, m_c = \gamma_c m_l \quad (2.A.2)$$

where, ρ the mass density of liquid, E the modulus of elasticity of the tank material; C_i , C_c , γ and γ_c are four coefficients depending on the tank wall slenderness H/r ; m_l is the total mass of the liquid. Values of stiffness parameters k_c and k_i were calibrated to match pre-selected target periods; convective and impulsive damping ratios, $\zeta_c = 0.5\%$ and $\zeta_i = 5\%$ respectively, determine the parameters of equivalent linear dashpots in the model.

$$k_i = m_i \left(\frac{2\pi}{T_i} \right)^2, k_c = m_c \left(\frac{2\pi}{T_c} \right)^2 \quad (2.A.3)$$

$$c_i = \frac{4\pi m_i \zeta_i}{T_i}, c_c = \frac{4\pi m_c \zeta_c}{T_c} \quad (2.A.4)$$

For the sake of completeness, mass, damping and stiffness matrices, needed to study the dynamic response of the liquid storage tank -NS #1-, are reported below,

$$\begin{aligned} \mathbf{M}^N &= \begin{bmatrix} m_s & 0 & 0 \\ 0 & m_i & 0 \\ 0 & 0 & m_c \end{bmatrix}, \mathbf{C}^N = \begin{bmatrix} (c_i + c_c) & -c_i & -c_c \\ -c_i & c_i & 0 \\ -c_c & 0 & c_c \end{bmatrix}, \mathbf{K}^N \\ &= \begin{bmatrix} (k_i + k_c) & -k_i & -k_c \\ -k_i & k_i & 0 \\ -k_c & 0 & k_c \end{bmatrix} \end{aligned} \quad (2.A.5)$$

where $m_s = m_t + m_l - m_i - m_c$ is the residual sliding mass and m_t is the storage tank mass without liquid. Table 2.A.2 reports all parameter values whilst Table 2.A.3 summarizes the global parameters of the sloshing fluid model.

Table 2.A.2 Parameters of the liquid storage tank model.

Parameter	Value	Unit
E	210	GPa
ρ_{fluid}	900	kg/m ³
ρ_{tank}	7850	kg/m ³
γ_c	0.1580	
γ_i	0.8320	
C_c	1.48	
C_i	7.03	
H	12	m
R	4	m
h	6e-3	m
m_t	28000	kg
m_l	5.43e5	kg
m_s	33200	kg

Table 2.A.3 Global parameters of the sloshing fluid model.

Sloshing mode	Mass [kg]	Damping [Ns/m]	Stiffness [N/m]	Vibration period [s]	Damping ratio ζ
Convective	8.58e4 (m_c)	1.82e3 (c_c)	3.86e7 (k_c)	2.96 (T_c)	0.50 % (ζ_c)
Impulsive	4.52e5 (m_i)	1.99e6 (c_i)	8.77e10 (k_i)	0.14 (T_i)	5.0 (ζ_i)

2.A.3.2 Physical concave sliding bearing array (CSB)

An array of CSBs with a single sliding surface supports the liquid storage tank; Fig. 2.A.5 depicts the adopted CSB numerically tested.

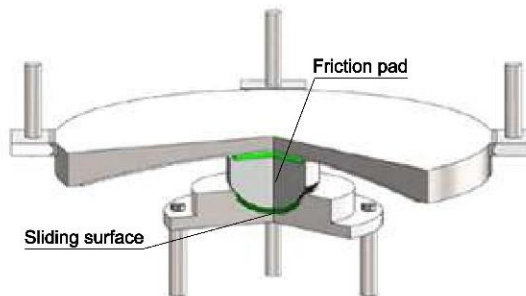


Figure 2.A.5 Details of the CSB and test setup of the CSB array.

From a mechanical viewpoint, a single CSB device can be characterized by a simplified linear piece-wise force-displacement relationship,

$$\left\{ \begin{array}{l} r = \frac{\mu_f P}{\Delta} u, u \leq \Delta \\ r = \mu_f \text{sign}(\dot{u})P + \frac{P}{R} u, u > \Delta \end{array} \right. \quad (2.A.6)$$

where μ_f is the friction coefficient, R is the device curvature radius, \dot{u} and u are the instantaneous velocity and sliding displacement of the isolator, respectively; P is a constant vertical load whilst r is the transversal restoring force of the CSB. More precisely, all CSB devices are characterized by surface radius R equal to 5000 mm , friction coefficient μ_f equal to 8% and initial yield displacement Δ of 0.5 mm .

In order to replicate the slip-based behaviour of the CSB array the differential model proposed by Mostaghel (1999) was adopted. Fig. 2.A.6 shows both a schematic of the aforementioned model and its bilinear hysteretic loop.

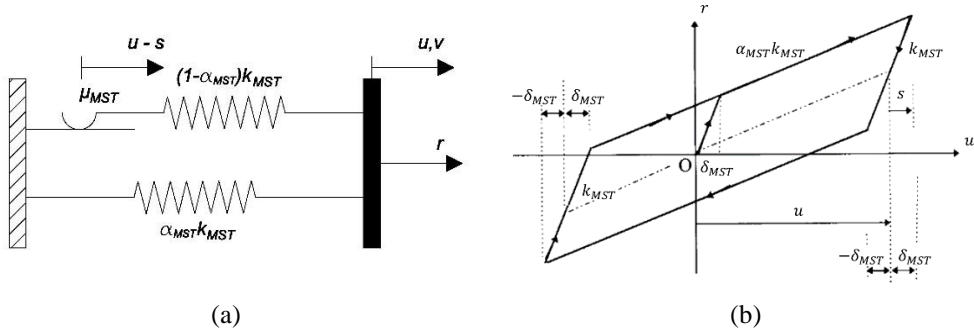


Figure 2.A.6 Bilinear Mostaghel model: a) S-DoF idealization; b) Hysteretic loop.

The corresponding ODE set, which defines the hysteretic Mostaghel model subjected to a given velocity history $v(t)$, reads,

$$\left\{ \begin{array}{l} \dot{r} = \left(\alpha_{MST} k_{MST} + (1 - \alpha_{MST}) k_{MST} (\bar{N}(v) \bar{M}(s - \delta_{MST}) + M(v) N(s + \delta_{MST})) \right) v \\ \dot{u} = v \end{array} \right. \quad (2.A.7)$$

with,

$$s = \frac{r - \alpha_{MST} k_{MST} u}{(1 - \alpha_{MST}) k_{MST}} \quad (2.A.8)$$

where, u and r represents displacement and restoring force state variables of the element and s defines slip displacement. The remaining functions N, M, \bar{N} and \bar{M} read,

$$\begin{aligned}
 N(w) &= 0.5(1 + \text{sgn}(w)) \left(1 + (1 - \text{sgn}(w)) \right) \\
 M(w) &= 1 - N(w) \\
 \bar{N}(w) &= M(-w) \\
 \bar{M}(w) &= N(-w)
 \end{aligned}
 \tag{2.A.9}$$

where $\text{sgn}(\cdot)$ is the sign function. The parameters k_{MST}, α_{MST} and δ_{MST} represent initial stiffness, post-yielding stiffness reduction factor and yielding displacement of a single CSB device, respectively. They are related to the physical parameters of the CSB model of Eq. (2.A.6) as,

$$\begin{aligned}
 \delta_{MST} &= \Delta = 5e - 4 \text{ m} \\
 \alpha_{MST} &= \frac{\Delta}{\mu_f R} = 1.30e - 3 \\
 k_{MST} &= \frac{\mu_f P}{\Delta} = 2.18e + 8 \frac{N}{m}
 \end{aligned}
 \tag{2.A.10}$$

In order to assemble Mostaghel's hysteretic springs in a FE fashion, a finite element driver was implemented, which numerically integrates Eq. (2.A.7) for a given displacement increment by using a 4-th order Runge-Kutta scheme.

2.A.4 Physical Substructure (PS)

The physical substructure consists of a standard 8" (NPS 8) pipe and a PN40 EN1092 standard bolted flange joint with water inside at a pressure of about 3.2 MPa; see in this respect, Fig 2.A.7. Its general dimensions and other geometrical properties are depicted in Fig. 2.A.8.

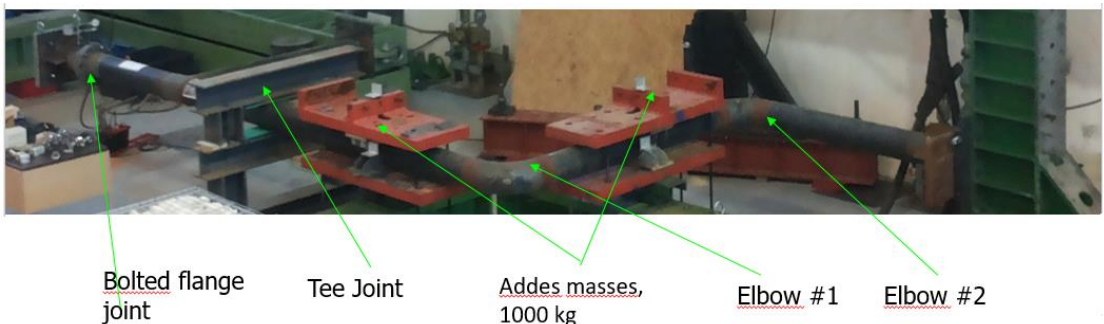


Figure 2.A.7 Physical substructure in the laboratory

The piping network contained 8" (outer diameter: 219.08mm; thickness: 8.18mm) and 6" (outer diameter: 168.28mm; thickness: 7.11mm) schedule 40 straight pipes and several critical components, i.e. elbows and a Tee joint. Even though physically tested, the FE model

of the piping was required. In detail, the pipes were modelled with API 5L Gr. X52 material (nominal f_y and f_u equal to 418 MPa and 554 MPa, respectively) and the water inside at an internal pressure of 3.2 MPa was taken into account by means of an equivalent pipe material density. Since at this stage the PS is supposed to exhibit a linear behaviour, all pipes including elbows were modelled using straight beam elements with pipe sections and provided with an equivalent stiffness. Moreover, in order to take into account valves and other components, two 1000 kg masses were connected to two relevant joints on the piping. Outcomes from the modal analysis of the entire piping system are reported in Table 2.A.4.

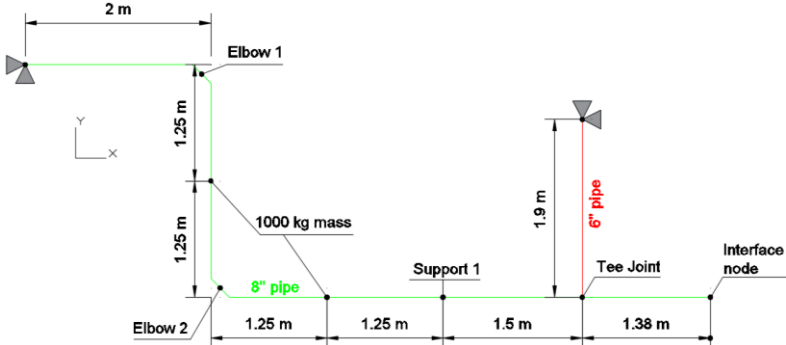


Figure 2.A.8 Schematic of the FE model and relevant dimension of the piping system conceived as PS.

Table 2.A.4 Outcomes from the modal analysis of the entire PS.

Mode #	Freq. [Hz]	Modal mass ratio in x dir. [-]	Modal mass ratio in y dir. [-]	Modal mass ratio in z dir. [-]
1	5.27	0.000	0.000	0.292
2	6.74	0.729	0.204	0.000
3	10.77	0.000	0.000	0.619
4	12.42	0.104	0.518	0.000
5	19.02	0.000	0.000	0.013
6	24.37	0.016	0.073	0.000
7	30.14	0.092	0.147	0.000
8	54.95	0.000	0.000	0.018
9	67.24	0.000	0.000	0.051
10	71.30	0.019	0.000	0.000
		0.959	0.942	0.993

In this test we dealt with a continuous PS in which excitation locations, both for hammer impacts and earthquakes forces, needed to be applied to all DoF of the PS shown in Fig.

2.A.8. This was not a feasible task since it would have required an actuator to be applied at each DoF of the PS. To overcome the above-mentioned problem, we adopted model reduction techniques, which condense DoF of a dynamic system retaining main properties of the original model.

Concerning the characterization tests, a reduced representation of the entire PS, whose DoF matched the accelerometer location, was required. In order to optimize the reduced model, the Guyan method (1965) was employed. Relevant outcomes after the reduction procedure are reported in Fig. 2.A.9.

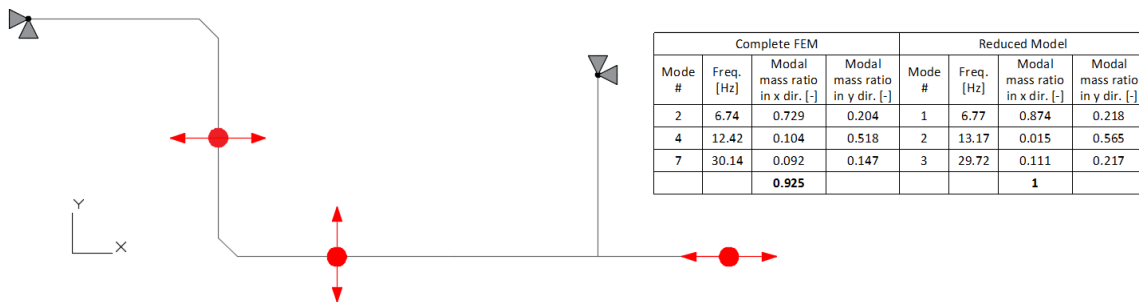


Figure 2.A.9 Reduced model and location of accelerometers devoted to numerically evaluate $H_d(t)$.

On the other hand, in order to provide reduced matrices and compatible loading vectors for HDS, the Craig Bampton (CB) reduction technique was applied herein. It is based on a reformulation of the equations of motion for a structure from the set of physical coordinates to a set of coordinates consisting of physical coordinates at some subset of boundary points, i.e. interfaces nodes, and modal or generalized coordinates at the non-boundary points. Resulting reduced matrices and vectors read:

$$\tilde{\mathbf{K}} = \mathbf{T}^T \mathbf{K} \mathbf{T}; \quad \tilde{\mathbf{M}} = \mathbf{T}^T \mathbf{M} \mathbf{T}; \quad \tilde{\mathbf{f}} = \mathbf{T}^T \mathbf{f} \quad (2.A.11)$$

where $\tilde{\mathbf{K}}$, $\tilde{\mathbf{M}}$, $\tilde{\mathbf{f}}$ represent reduced stiffness matrix, mass matrix and force vector, respectively. In order to perform an optimal selection of reduction basis vectors, a sweep analysis was conducted on the number of retained fixed interface vibration modes. As a result, only two fixed interface vibration modes were enough to entail asymptotic values of the complete FEM of the piping and allowed for a quite accurate reduction. The dynamic responses of the reduced PS with the CB method - keeping two fixed interface vibration modes - and of the complete FEM of the piping system subjected to the seismic excitation of Table 2.A.3 are compared in Fig. 2.A.10.

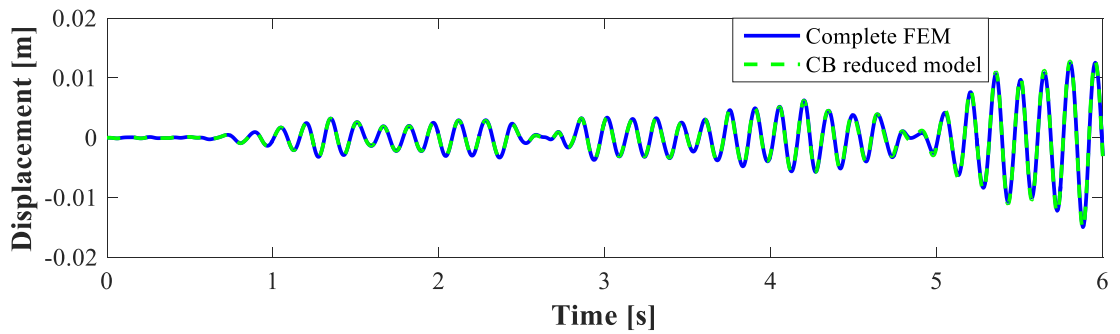


Figure 2.A.10 Comparison of displacement responses of the RM and CB reduced models at coupling interface DoF.

We can conclude that the CB method allowed for an effective simulation of the piping system by means of HDS.

2.A.4.1 Strain gauges' placement

Strain gauges were placed on the critical components of the piping to monitor and record the strains. In particular, both elbows were equipped of strain gauges as depicted in Figs 2.A.11 -12.

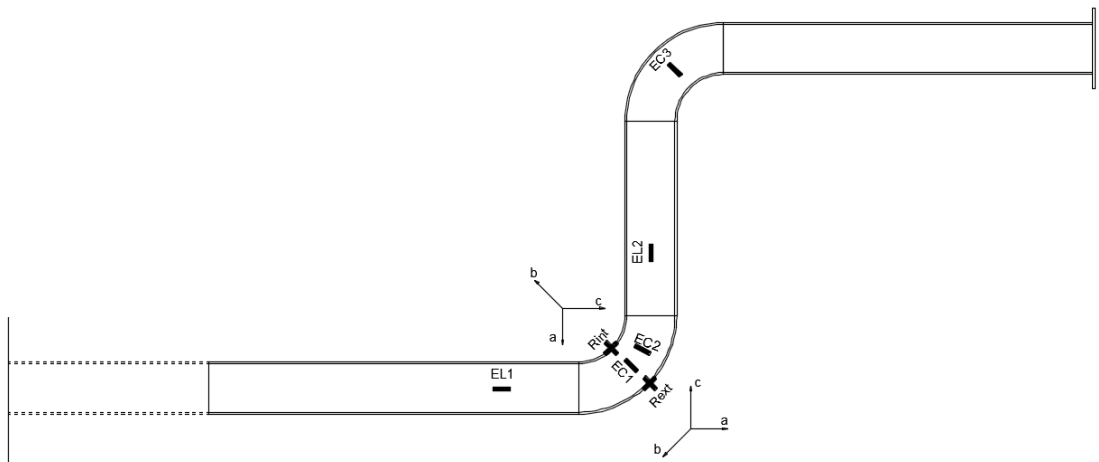


Figure 2.A.11 Comparison of displacement responses of the RM and CB reduced models at coupling interface DoF.



Figure 2.A.12 Particular of the strain gauges placement

2.A.4.2 Identification tests (IDTs)

The IDTs were conducted by means of an impact hammer and ICP accelerometers 393C. Moreover, the Eigensystem Realization Algorithm (ERA) was used for damping evaluation of PS and relevant results are shown below.

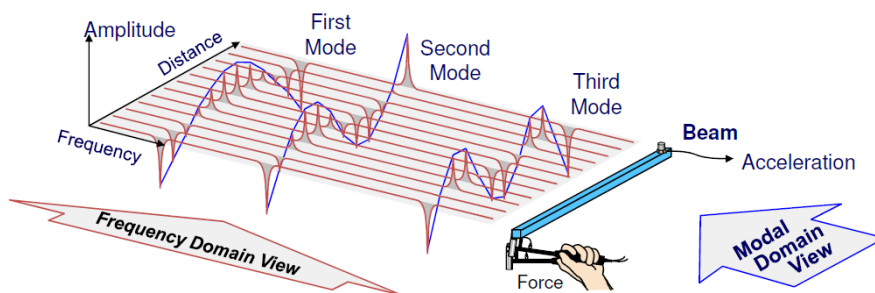


Figure 2.A.13 ERA algorithm procedure

The main steps of the ERA algorithm are reported hereinafter:

- Response measured at one point
- Excitation of the structure at a number of points by hammer with force transducer
- FRF's between excitation points and measurement point calculated

- Vibration modes of the structure are identified

According to ERA analysis, the damping at the first frequency of the piping was set equal to 0.5 %.

2.A.5 Application of PDT and RT testing techniques to the piping-tank system

In order to carry out both PDT and RTs, the LSRT2 method developed by Bursi et al. (2008-2011) for time integration of linear and non-linear systems was employed. In detail, both mass and stiffness matrices were extracted from a linear elastic FE model of the NS developed in ANSYS FE software. In order to carry out hybrid simulations, those matrices were then used to model the NS by means of the Matlab/Simulink code in the Host PC. The Host PC compiled the system of equations discretized in time by the LSRT2 algorithm, which was then sent to an xPC target -a real time operating system installed in a target PC- via a LAN connection. During experimental tests, integration algorithms solved motion equations in the xPC target and estimated displacement commands for the PS. These displacement commands were written to the xPC target, which instantaneously copied these signals to an MTS controller through a SCRAMNET -a reflective memory between the Host PC and the controller-. The controller then commanded two actuators to move the coupling DoFs to desired positions. Again, the SCRAMNET memory instantaneously supplied corresponding restoring forces measured by load cells to the xPC target. The hardware-software scheme used for hybrid tests is sketched in Fig. 2.A.14.

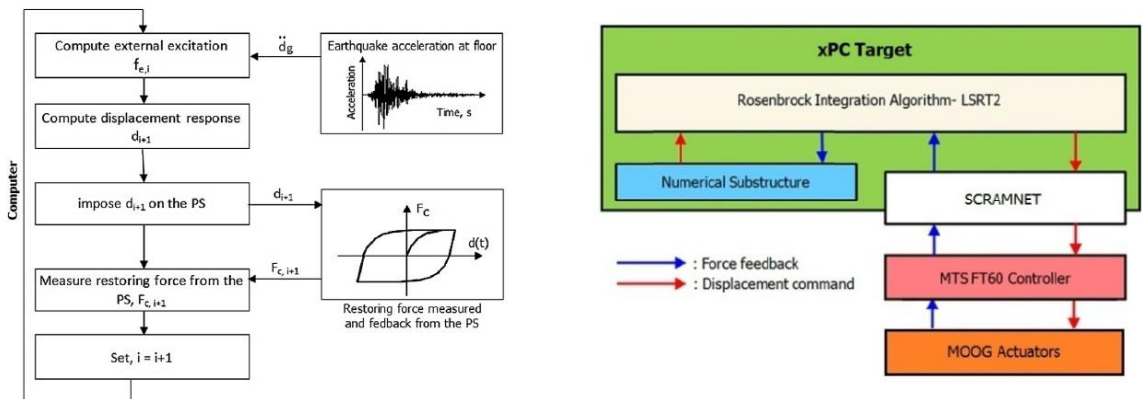


Figure 2.A.14 Hardware-Software architecture.

2.A.6 Main results

The main results of the experimental testing campaign are reported.

2.A.6.1 004673ya signal ($Tr = 475$ years)

Slender Tank #23

The isolated slender tank #23, see Fig. 2.A.2, was tested with the 004673 signal. The main results are shown below.

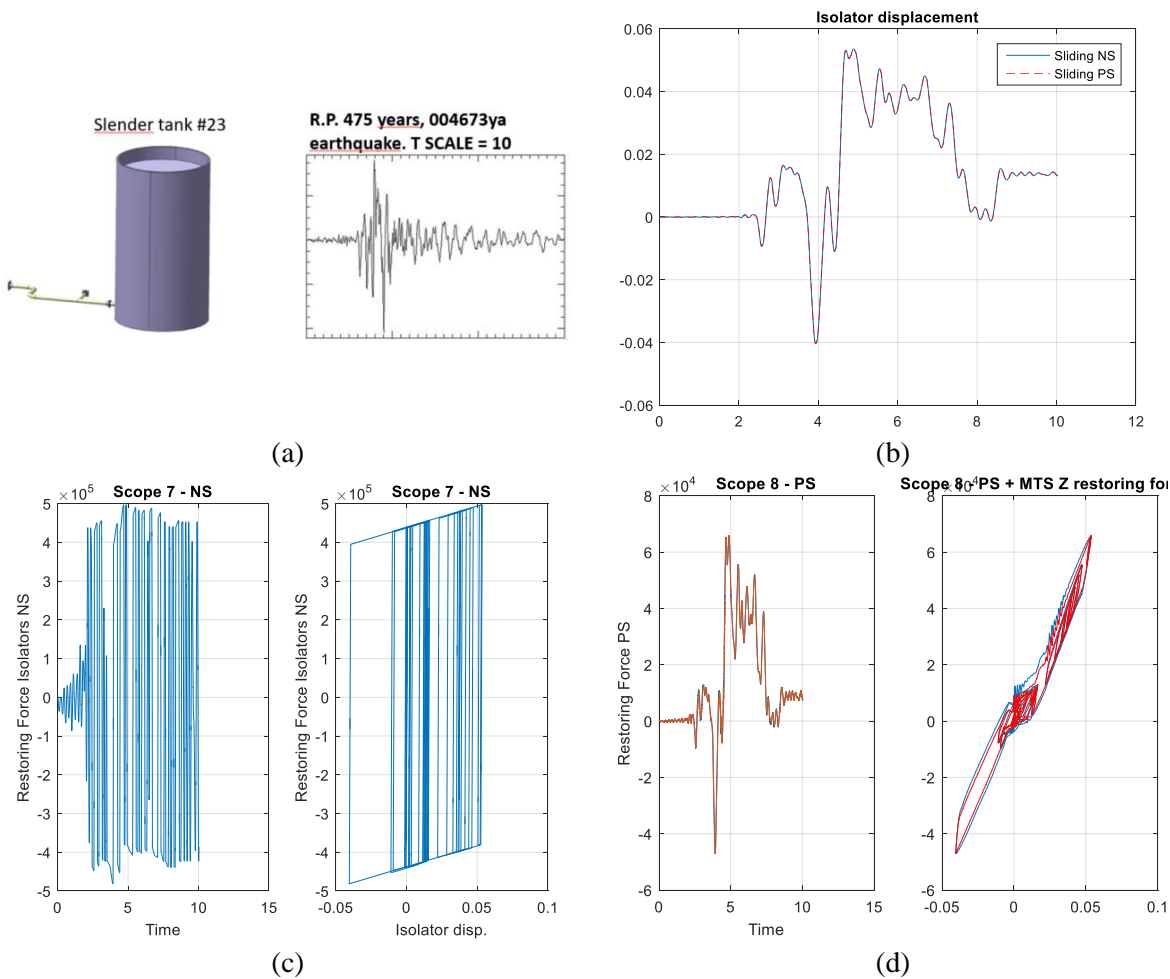


Figure 2.A.15 (a) Selected slender tank and accelerogram, (b) experienced isolator displacement, (c) NS restoring force, (d) PS restoring force.

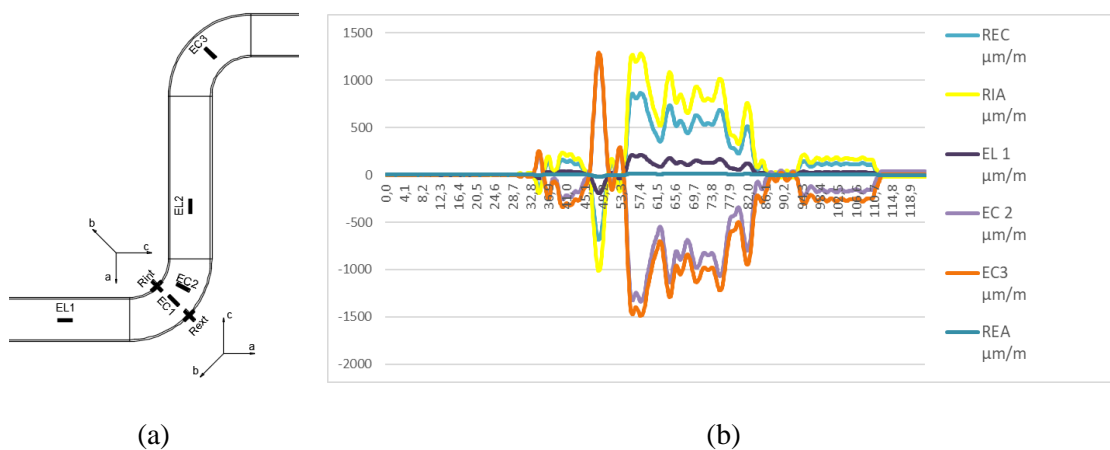


Figure 2.A.16 (a) strain gauges placement, (b) strain on the elbows.

Broad tank #60

The isolated broad tank #60, see Fig. 2.A.2, was tested with the 004673 signal. The main results are shown below.

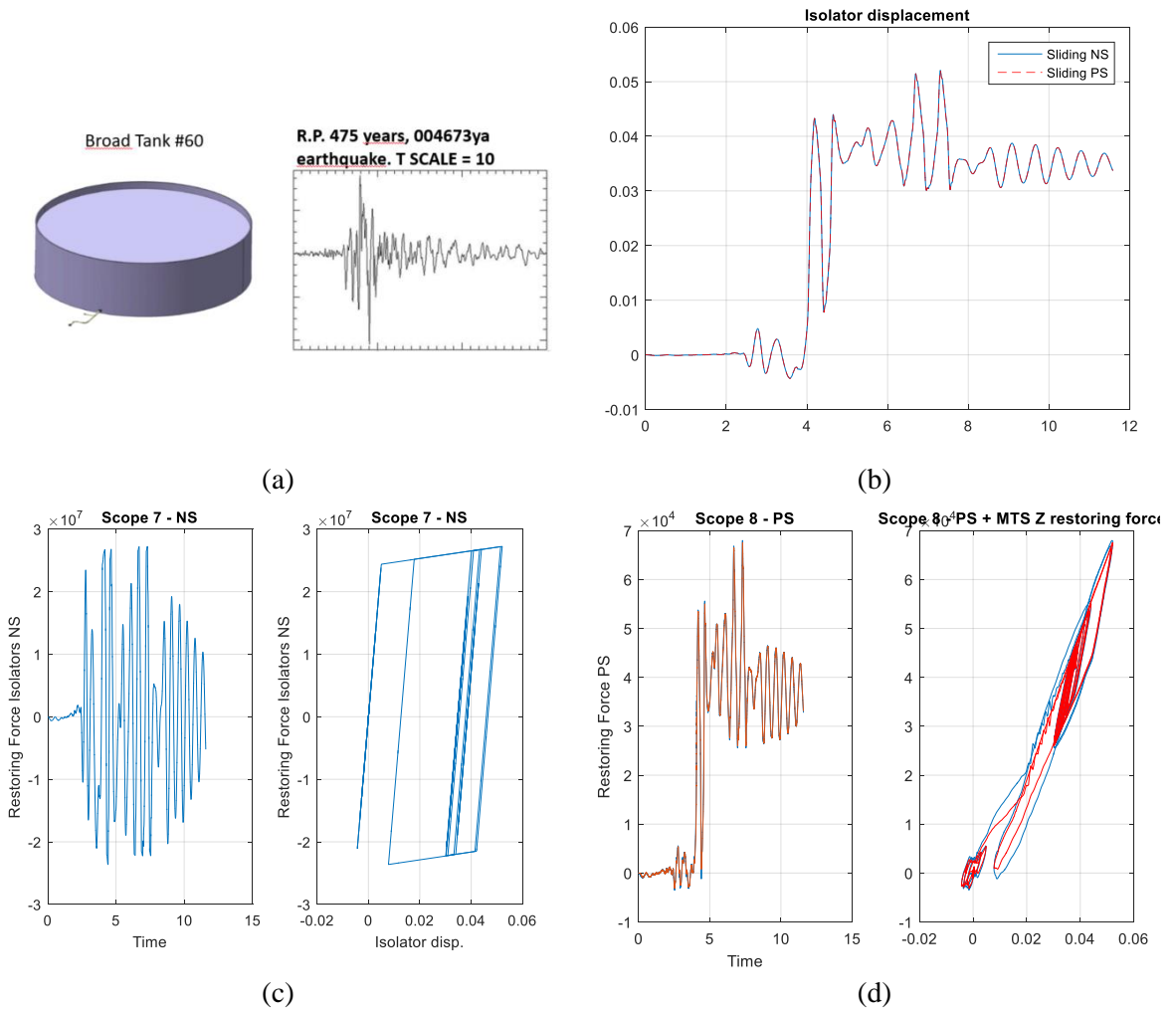


Figure 2.A.17 (a) Selected slender tank and accelerogram, (b) experienced isolator displacement, (c) NS restoring force, (d) PS restoring force.

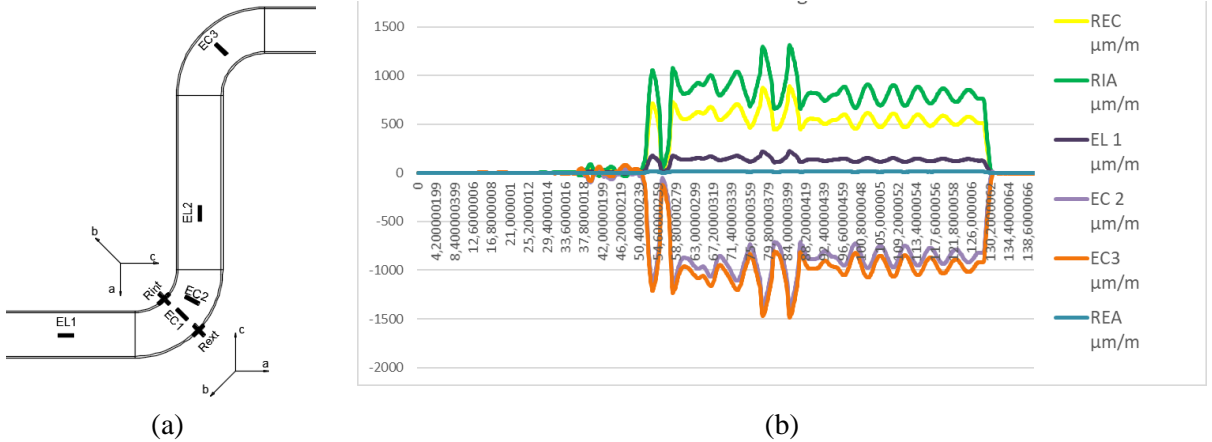
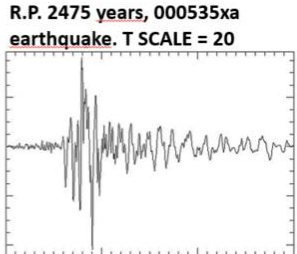


Figure 2.A.18 (a) strain gauges placement, (b) strain on the elbows.

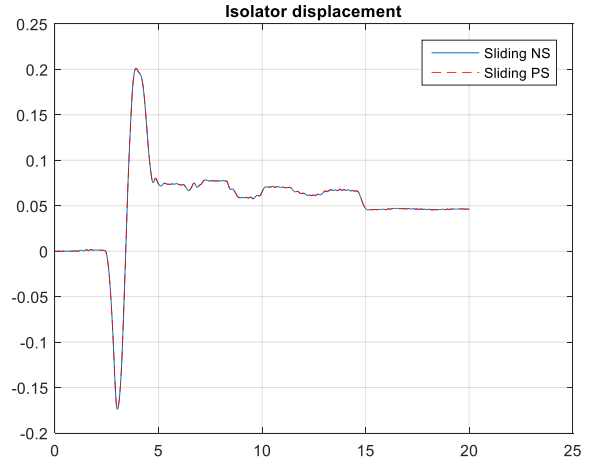
2.A.6.2 000535xa signal ($T_r = 2475$ years)

Slender Tank #23

The isolated slender tank #23, see Fig. 2.A.2, was tested with the 000535 signal. The main results are shown below.



(a)



(b)

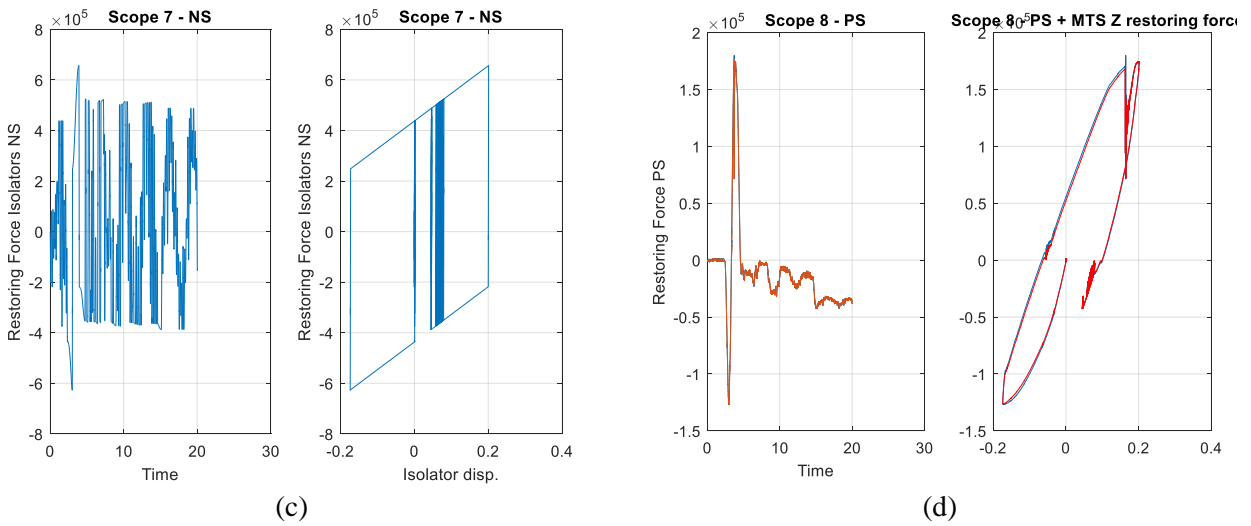


Figure 2.A.19 (a) Selected slender tank and accelerogram, (b) experienced isolator displacement, (c) NS restoring force, (d) PS restoring force.

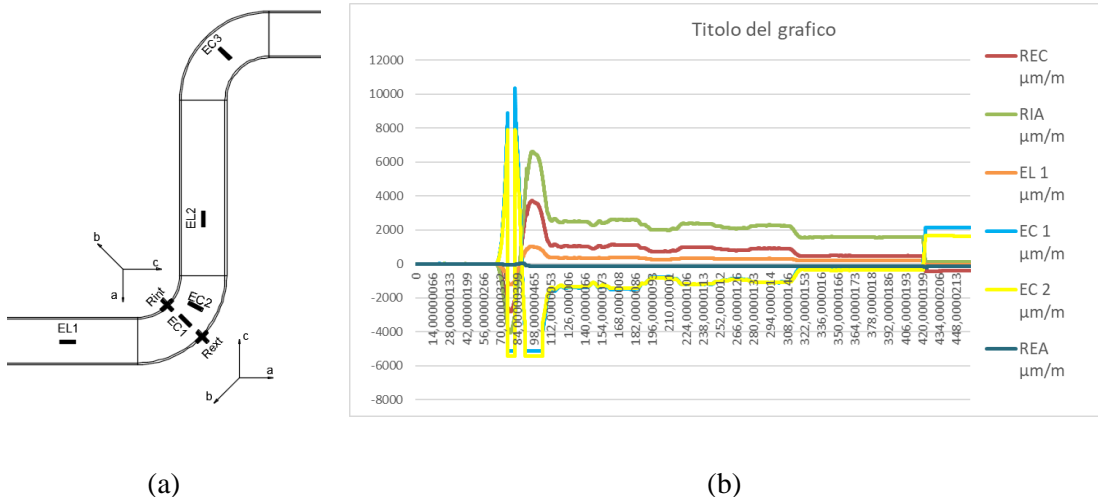


Figure 2.A.20 (a) strain gauges placement, (b) strain on the elbows.

2.A.7 Conclusions

Tests corresponding to the OBE (Nuclear standards) or the Safe Life Limit State (SLLS) (475 years return period) have been conducted in real time with dynamic substructuring and actual inertia effects of the Physical Substructure on coupled tank-piping systems. Conversely, tests corresponding to the SSE (Nuclear standards) or Near Collapse Limit State (NCLS) (2475 years return period) have been carried out by means of the pseudo-dynamic test method, where inertia forces of the PS are also modelled into the computer; as a result, hydraulic actuators are able to reproduce large displacements applied to the PS. The internal pressure (pressurized medium: water of 32 bars) was held constant during load application.

In order to identify modal damping ratios of the piping component, preliminary system identification tests have been conducted on the specimen. Results showed that slender tanks entail a significant effect on elbows due to the impulsive component of the contained liquid; whereas broad tanks induced smaller effects on elbows owing to the smaller influence of the impulsive component. In addition, some elbow experienced inelastic tensile hoop strains of the order of 1 %. In any case, the limit state of leakage, corresponding to an approximate value of 2 % for the tensile hoop strain, was not exceeded.

Chapter 3

3. Probabilistic Seismic Analysis of an LNG Subplant

by Oreste S. Bursi, Rocco di Filippo, Vincenzo La Salandra, Massimiliano Pedot, Md S. Reza

Abstract

Refrigerated liquefied gas (RLG) terminals that are part of lifeline facilities must be able to withstand extreme earthquakes. A liquefied natural gas (LNG, ethylene) terminal consists of a series of process facilities connected by pipelines of various sizes. Although tanks, pipes, elbows and bolted flanges have been a major concern in terms of seismic design, generally, they have not been analysed with modern performance-based procedures. In this study, the seismic performance of pipes, elbows and bolted flanges is analysed and seismic fragility functions are presented within the performance-based earthquake engineering framework. Particular attention was paid to component resistance to leakage and loss of containment even though several different limit states were investigated. The LNG tank, support structures and pipework, including elbows and flanges, were analysed with a detailed 3D finite element model. For this purpose, we developed a mechanical model of bolted flange joints, able to predict the leakage limit state, based on experimental data. A significant effort was also devoted to identification of a leakage limit state for piping elbows, and we found the level of hoop plastic strain to be an indicator. Given the complexity of the FE model of the LNG plant, we selected the Cloud method for probabilistic seismic demand analysis, due to its advantages in terms of consistency in the seismic input and of computational savings. Then, using a series of nonlinear time history analyses, we studied the behaviour of critical components such as elbows and bolted flange joints. In order to develop fragility curves, we selected a set of 36 ground motions from a database of historic earthquake accelerations. The results of seismic analysis show that bolted flange joints remain significantly below their leakage threshold whilst elbows at the top of the LNG tank are likely to show leakage. Moreover, fragility functions were computed, based on a linear regression approach, and we deduce that elbows located on the tank platform are relatively unsafe against earthquakes. Finally, the estimated probability of loss of containment was above the probability associated with ultimate limit states involved in structural Eurocodes.

3.1 Introduction

3.1.1 Background and Motivation

RLG terminals represent strategic infrastructure for energy supplies all over the world. They play an important role in the overall energy cycle, as their main purpose is to store and distribute RLG. For storage and transport by trains, ships and pipelines, natural gas like ethylene is liquefied. This is achieved by compression and cooling to low temperature. For these reasons, liquefied natural gas LNG terminals usually consist of a port and transport infrastructure, with all the systems related to both liquefaction and regasification, as shown in Fig. 1. In this respect, LNG handles 10% of the global energy supply with 28 LNG terminals in Europe (GIE LNG Map, 2015).

Together with a clear strategic importance, LNG plants also carry a significant risk related to possible consequences of incidents caused by natural events. The Na-tech risk is a central aspect in different types of petrochemical plants due to possible damage to other nearby plant and communities, or to those who rely on them for energy or other needs. Moreover, leakage of hazardous or polluting substances can badly affect the local environment. The resulting hazard has been evaluated in different situations by means of case studies (Cozzani et al. 2014, Baesi et al. 2013, and Young et al. 2005). The considerable variability of seismic events and the related domino effects have been partly taken into account in the overall hazard estimation by the application of complex methodologies (Campedel et al., 2008 and Antonioni et. al., 2007). Nevertheless, historic data shows that earthquakes can lead to severe losses due to the failure of different components of industrial plants; in this respect see Lanzano et al., (2015) and Krausmann et. al (2010).

An industrial plant typically has many structural and mechanical components, with different resistance thresholds and different failure behaviours. One of the most dangerous failure effects is loss of containment (LOC) or leakage, which can lead to explosion, fire and environmental damage. An LNG plant includes a number of component types that can experience leakage, under certain conditions of stress and strain caused by a seismic event. Common vulnerable components of LNG pipelines are bolted flange joints (BFJs) and piping bends or elbows. With respect to BFJs, current European regulations, like EN 1591-1,2 (2009), do not have tools to predict leakage. Moreover, studies whether focusing on leak-before-break, i.e. that concentrate on the steady growth of through-cracks in pipes (Xie, 1998) or tracing the plastic behaviour of elbows (Li and Mackenzie, 2006), do not predict leakage thresholds. To fill this gap, a practical predictive model based on EN 1591 (2009) was developed by La Salandra et al. (2016), also using experimental data found by Reza et al. (2014). As far as a probabilistic approach is concerned, the risk estimation of leakage events is usually based on historic evidence found in databases; for a review, see Barros da Cunha (2016).

In order to quantify induced seismic risk in an LNG plant, a seismic Probabilistic Risk Assessment (PRA) approach suggested by IAEA (2009) for nuclear power plants (NPPs) is available. The procedure is as follows: i) Seismic hazard analysis; ii) Fragility analysis; iii) System analysis and consequence evaluation. The outcome of a seismic PRA includes

seismic hazard of the site, the structural capacity of structures and equipment, incorporation of uncertainties in seismic hazard, structural fragility and response of components. Hoseyni et al., (2014) applied a variant of this approach to take into account soil-structure interaction effects. However, this approach is not directly applicable to (non-nuclear) LNG plants, because data on aleatory randomness and epistemic uncertainties in the capacity of LNG components is not available.

As a viable alternative, to rationally quantify the seismic performance of civil facilities, the Performance-Based Earthquake Engineering (PBEE) methodology has been proposed (Cornell and Krawinkler, 2000). This probabilistic framework is based on the prediction of structural behaviour under realistic seismic loadings that the structural system is likely to experience in its reference life. It is based on the combination of different quantities, such as seismic hazard, structural response, level of damage, and repair costs after cyclic loading.

Some examples of application of the PBEE approach can be found in civil engineering literature (Yang et al., 2009, Tondini and Stojadinovic, 2012). Along this line, application of the PBEE approach to petrochemical piping systems by means of codes can be found in Bursi et al. (2015a). Moreover, some applications based on the determination of fragility curves are available for piping systems of NPPs (Firoozabad et al., 2015) and boil-off gas compressors at LNG terminals (Park and Lee, 2015). In both cases, limit states related to leakage were not considered or quantified. Conversely, the selection of engineering demand parameters (EDPs) and corresponding damage levels for piping systems and tanks was carried out by Vathi et al. (2015). Nonetheless, a fragility analysis requires also the analysis of the effects of different intensity measures, e.g. peak ground acceleration (PGA), on the dispersion characteristics of a probabilistic seismic demand model. To the authors' knowledge, this analysis has not yet been carried out for LNG plants.

3.1.2 Scope

On these premises, this paper presents the application of the fully probabilistic PBEE approach to an LNG plant having a piping system coupled to a support structure and a relevant LNG tank. More precisely, we define limit states and engineering demand parameters related to damage of piping components, i.e. BFJs and elbows. Moreover, among different damage levels, we calculate the correlation between the probability of leakage and the IM of the seismic event represented by the PGA and the spectral acceleration ($S_a(T)$). We represent these by the mean of fragility curves adopting the Cloud Analysis method (Baker, 2015).

For clarity, the paper is organized as follows: Section 3.2 presents the methodology for the application of the PBEE method. A description of the LNG plant and the main components modelled by means of finite elements (FEs) is contained in Section 3.3. Section 3.4 presents a simple component-based mechanical model able to predict leakage of BFJs and a methodology to evaluate seismic performances of piping elbows. Successively, Section 3.5 presents a 3D non-linear stick model of the LNG terminal, fully developed in the ANSYS environment (ANSYS, 2015). This FE global model allows for evaluation of

the seismic response of structural components of the plant by means of a non-linear analysis presented in Section 3.6. Thus, the demand model of the main components of the piping system is investigated in the spirit of the PBEE method. Finally, Section 3.7 draws the main conclusions and future perspectives.



Figure 3.1 Refrigerated liquefied gas plant overview

3.2 Performance-based earthquake engineering procedure

The PBEE procedure was mainly developed by the Pacific Earthquake Engineering Research (PEER) Center and estimates the probabilistic future seismic performance of buildings and bridges in terms of system-level decision variables (DVs), i.e., performance measures that are meaningful to the owner, such as repair cost, casualties, and loss of use - dollars, casualties and downtime-. It is based on four quantities:

- Intensity Measure (*IM*), which represents a measure of the ground motion intensity. Several *IM* variables are available, such as PGA, Spectral Acceleration at the fundamental period ($Sa(T)$), etc.;
- Engineering Demand Parameter (EDP), which describes the structural response in terms of global and local parameters such as deformation, forces, etc;
- Damage Measure (DM), which identifies the most significant structural damage conditions;
- Decision Variable (DV), which transforms the damage conditions into useful quantities for the risk management decision process.

Let's denote $G(x/y)=Pr(x<X/Y=y)$ the complimentary cumulative distribution function of the considered variables and $dG(x/y)$ the derivative of the conditional complimentary cumulative distribution function, which is identical to the negative of the conditional probability density function. The evaluation of the mean annual rate λ of *DV* exceeding the threshold dv reads,

$$\lambda(dv < DV) = \int_{im} G(dv|im) |d\lambda(im)| \quad (3.1)$$

where the conditional probability $G(dv|im)$ can be obtained by use of total probability (Yang et al., 2009) as follows,

$$G(dv|im) = \int_{dm} \int_{edp} G(dv|im) dG(dm|edp) dG(edp|im) \quad (3.2)$$

Substituting (3.2) in (3.1), we obtain the mean annual rate of a decision variable DV exceeding a threshold value dv ,

$$\lambda(dv < DV) = \int_{im} \int_{dm} \int_{edp} G(dv|im) dG(dm|edp) dG(edp|im) |d\lambda(im)| \quad (3.3)$$

It is evident that Equation (3.3) encompasses four components of performance assessment. Specifically, the quantification of $\lambda(im)$ requires a site hazard analysis, usually performed by a probabilistic seismic demand analysis (PSDA); $G(edp|im)$ needs a response analysis, usually performed by using numerical techniques, e.g. Cloud analysis, $G(dm|edp)$ requires a damage analysis often based on experiments whilst $G(dv|dm)$ requires cost-effective or loss analysis (Cornell and Krawinkler, 2000). Moreover, the quantification of Equation (3.3) requires a fully probabilistic approach. Given the scarcity of data, at this stage of the research, only the probability of exceeding of a certain edp will be quantified in Section 3.6. For this purpose, the following relationship is adopted:

$$\begin{aligned} P(edp) &= \int_{im} P(EDP > edp|im) |d\lambda(im)| \\ &= \int_{im} P(D > C_{LS}|IM = im) |\lambda(im) dim| \end{aligned} \quad (3.4)$$

where we introduce the structural demand D and C_{LS} , i.e. the capacity of the component/system associated with a prescribed limit state.

3.3 LNG Plant

3.3.1 Introduction

The case study investigated in this paper reproduces a realistic RLG plant, depicted in Fig. 3.1 and 3.2, i.e. the Case Study #2 analysed in the European research project INDUSE-2-SAFETY (Bursi et al., 2016b). Originally, this plant was designed for low seismic lateral loads; in stark contrast, in order to acquire additional information on the plant performance for extreme lateral loadings, we considered the LNG plant located in a high seismic-prone area of Priolo Gargallo in Sicily, in the south of Italy. The hazard curve for

this site is depicted in Fig. 3.3 and was calculated within the activities of INDUSE-2-SAFETY (Bursi et al., 2015b). The main component of the plant is a 50 000 m³ ethylene tank that supplies the LNG to the different process areas via a stainless-steel piping system.

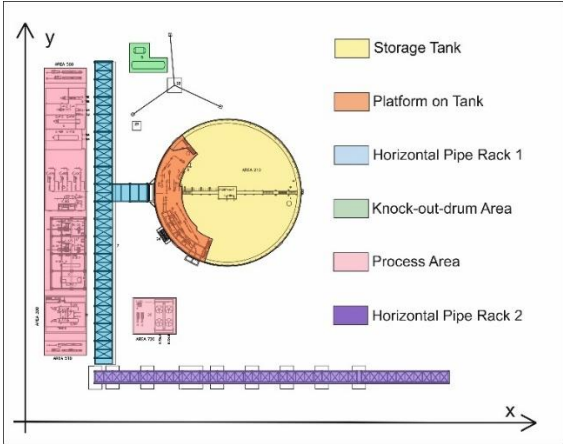


Figure 3.2 LNG plant layout

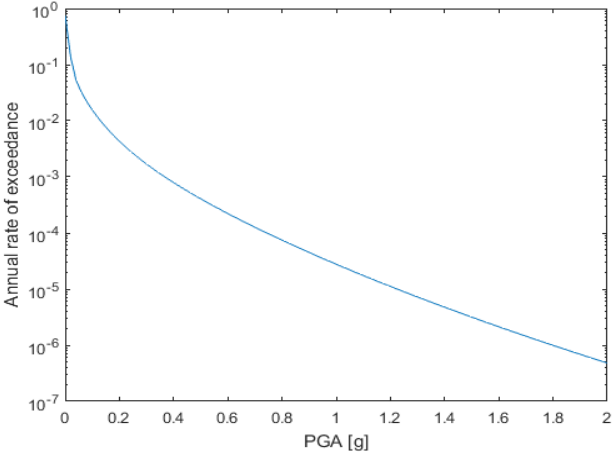


Figure 3.3 Hazard Curve of the high-seismic site of Priolo Gargallo (Sicily, Italy).

3.3.2 LNG Tank

Typically, LNG tanks are used to store LNG at very low temperatures, i.e. -100 °C. A relatively common kind of LNG tank is the full containment tank, where the inner steel tank encloses the LNG and the outer structure is generally thicker and of concrete and includes both an outer steel tank and the insulation material.

The tank of the LNG plant under study, depicted in Fig. 3.4, has two main different layers: i) the inner one has high resilience steel shells (X8Ni9) of thickness varying from 18

mm for the lower rings to 8 mm for the upper rings and of radius 23 meters; ii) the outer layer is concrete C30/37 with a total thickness of 650 mm. This concrete wall has an inner radius of 24.5 m and a height of 38 m. The roof is a concrete dome, with thickness ranging from 850 to 350 mm, reaching an overall height of 47.4 m.

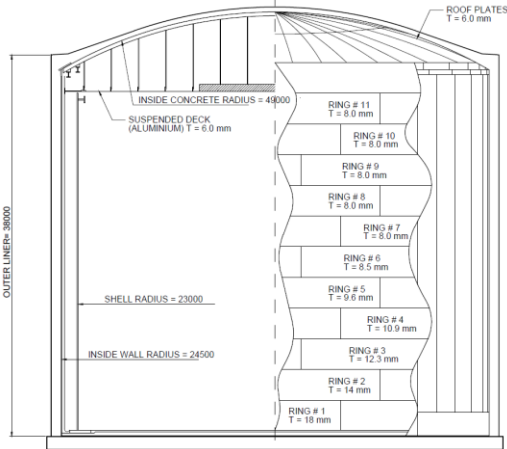


Figure 3.4 Main tank layout.

3.3.3 Substructures

Two different structures support the pipework: i) a steel platform located over the dome as shown in Fig. 3.5, and ii) a concrete structure placed at the base of the tank as in Fig. 3.6.

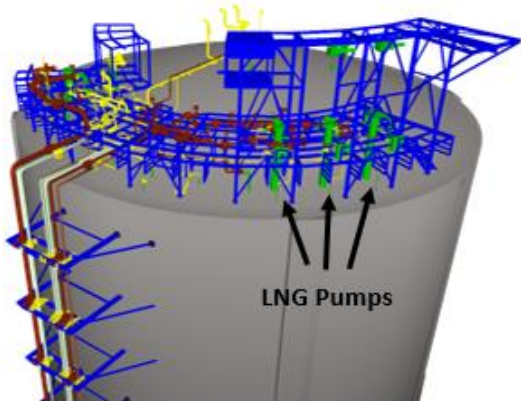


Figure 3.5 Steel platform and position of the three pump columns

The platform at the top of the tank is built with 17 different kinds of commercial steel profiles grade S235, arranged on three different levels, located respectively at 41, 45 and 48 m above ground. These steel profiles were selected in the range 100-280 for the HEB

profiles and in the range 120-240 for the IPE profiles. Three pumps, located above the dome, transport the ethylene from the tank to the pipework.

At the base of the tank, the piping system distributes ethylene to the different process areas. The pipelines are supported by a concrete structure 102 m long, 6.5 m wide and 7.3 m high with an intermediate level placed 5.3 m above the ground. The span between the columns along the longest dimension is 6 m, whilst the span between the beams along the same direction is 3 m. The concrete compressive strength class is C50/40.

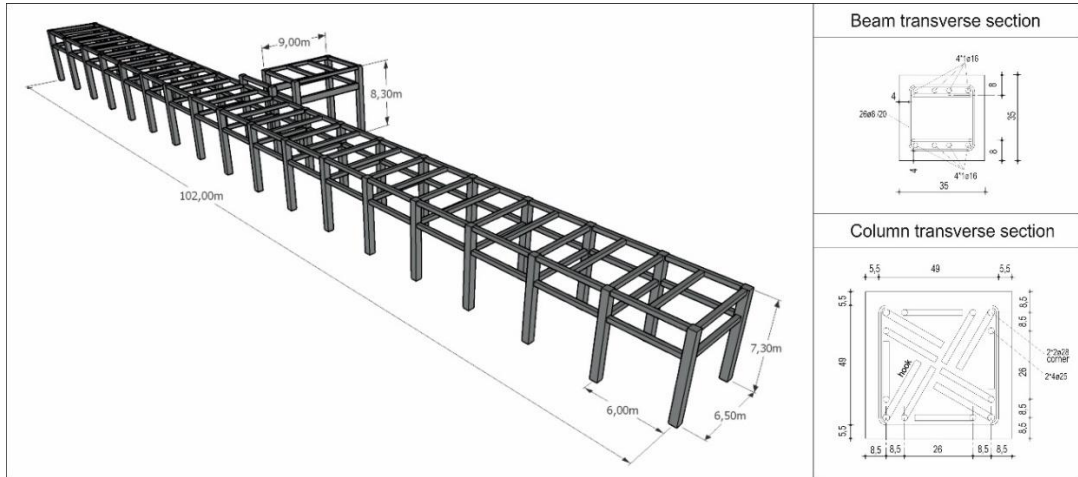


Figure 3.6 Concrete support structure

The columns have a 600 mm square section with 8 steel reinforcement bars $\phi 25$ and 4 steel re-bars $\phi 28$. The beams are 350 mm square section with 4 steel re-bars $\phi 20$.

3.3.4 Knock-Out Drum Area

The knock-out drum process area, the function being to separate liquid from gas in the ethylene mixture, is located at the far end of the concrete support structure as shown in Fig. 3.2. Separation occurs in two stainless steel tanks, shown in Fig. 3.7, connected to the concrete support structure by a piping system for the ethylene supply. The tank considered in the analysis is named C608 and it is highlighted in red in Fig. 3.7. The vessel dimensions are in Table 3.1.

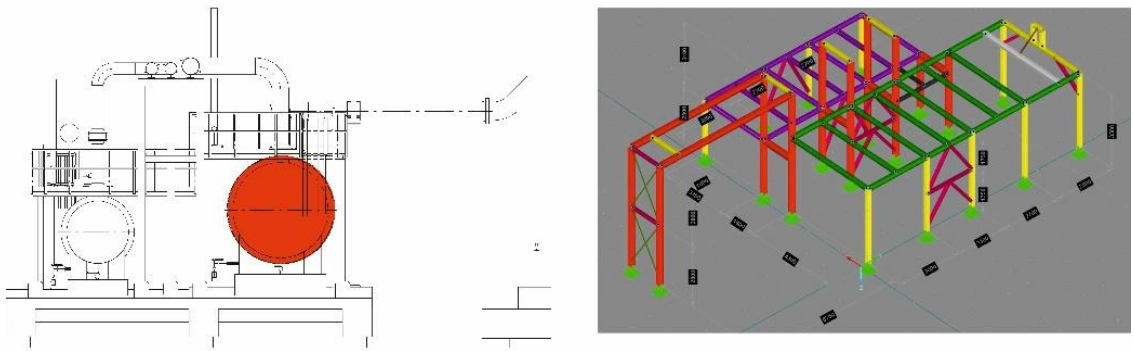


Figure 3.7 Knock-out drum process area

Table 3.1 Properties of Knock-out drum C608 tank

Knock-out drum C608 tank	
Capacity [m ³]	52
Diameter [m]	2.6
Length [m]	10.15
Wall thickness [mm]	8

The two tanks of the knock-out drum area are surrounded by a grade S235 steel support structure that is 17.5 m long, 9.2 m wide and 3.5 m high. The structural steel profiles are in the ranges 120-200 HEB and 160-220 IPE.

3.3.5 Piping System

The piping system, depicted in Fig. 3.5 and 3.8, is arranged into 8 different welded pipelines of stainless steel grade ASTM A312/TP304L.

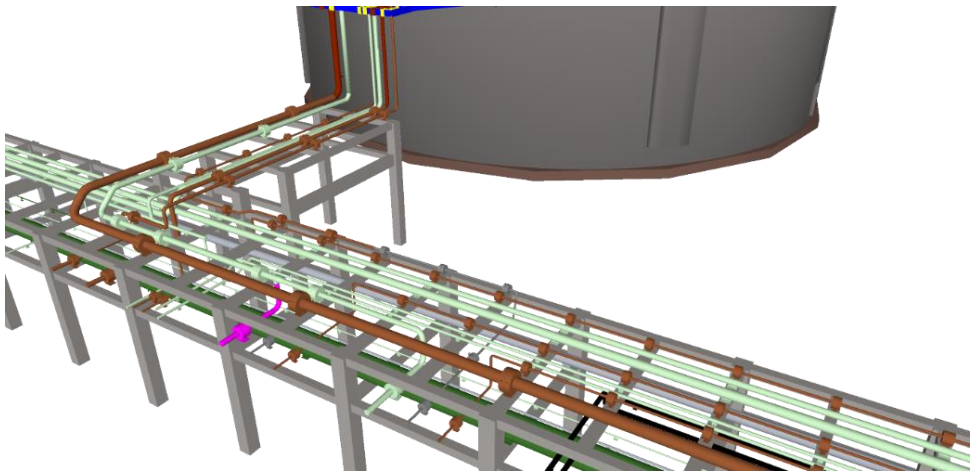


Figure 3.8 Pipelines layout on concrete support structure

The cross section properties of each pipeline are summarised in Table 3.2.

Table 3.2 Properties of Knock-out drum C608 tank

Cross section properties of the pipelines					
Pipeline number	Pipe specification	External radius [mm]	Wall thickness [mm]	Curvature radius [mm]	Max Operating Pressure [barg]
1	16'' - SCH20	406.4	7.92	610	2.8
2	10'' - SCH10S	273.05	4.19	381	0.2
3	4'' - SCH10S	114.3	3.05	152	0.2
4	6'' - SCH10S	168.28	3.40	229	0
5	12'' - SCH10S	323.85	4.57	457	0.3
6	6'' - SCH10S	168.28	3.40	229	16.3
7	8'' - SCH10S	219.08	3.76	305	16.3
7	6'' - SCH10S	168.28	3.40	229	1
8	18'' - SCH10S	457.2	4.78	686	0

The mechanical properties of the pipeline steel were defined during the INDUSE-2-SAFETY project, with experimental tests on metallographic samples of seamless pipes (Bursi et al., 2016a). In order to characterize the steel constitutive law for the operating conditions of the plant, tensile testing was done at room temperature and at -80°C. The relevant results are shown in Fig. 3.9 and Fig. 3.10.

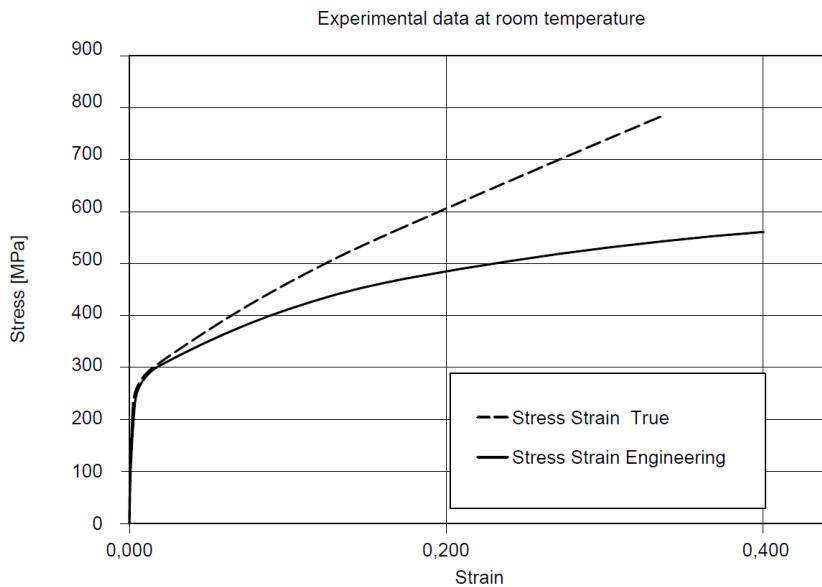


Figure 3.9 Stress-strain curve for A312/TP304L at room temperature

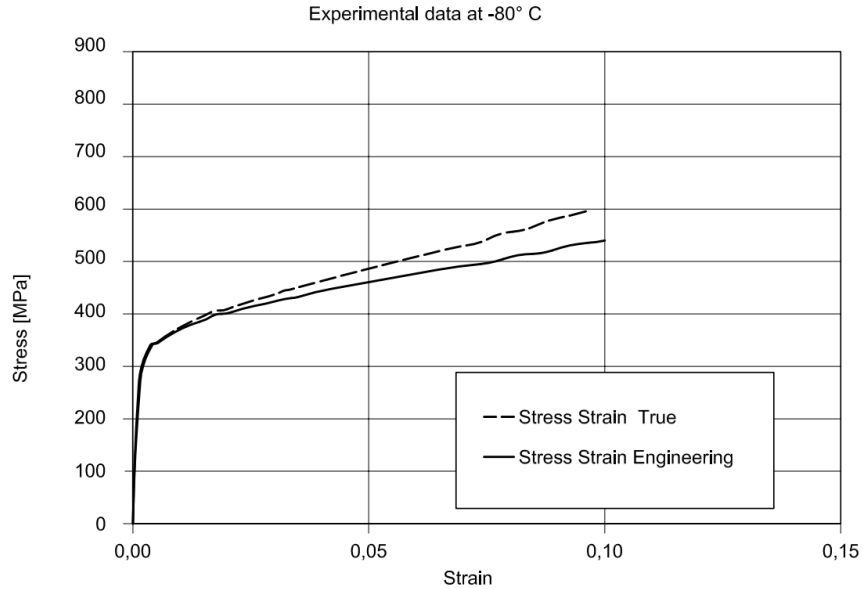


Figure 3.10 Stress-strain curve for A312/TP304L at -80°C

As expected for steel materials, the A312/TP304L showed a higher elastic modulus and a decrease in ductility at the lower temperature.

The connections between the piping system and other elements such as the pumps over the main tank or the nozzles in the knock-out drum area, are by BFJs. In particular, the connection between pipeline #6 and the three pump columns over the dome of the tank was made with a 6'' SCH10S CL300 welded neck flanges, as shown in Fig. 3.11. In addition,

pipeline #8 and the knock-out drum tank were connected with an 18'' SCH10S CL150 welded neck flange as depicted in Fig. 3.12.

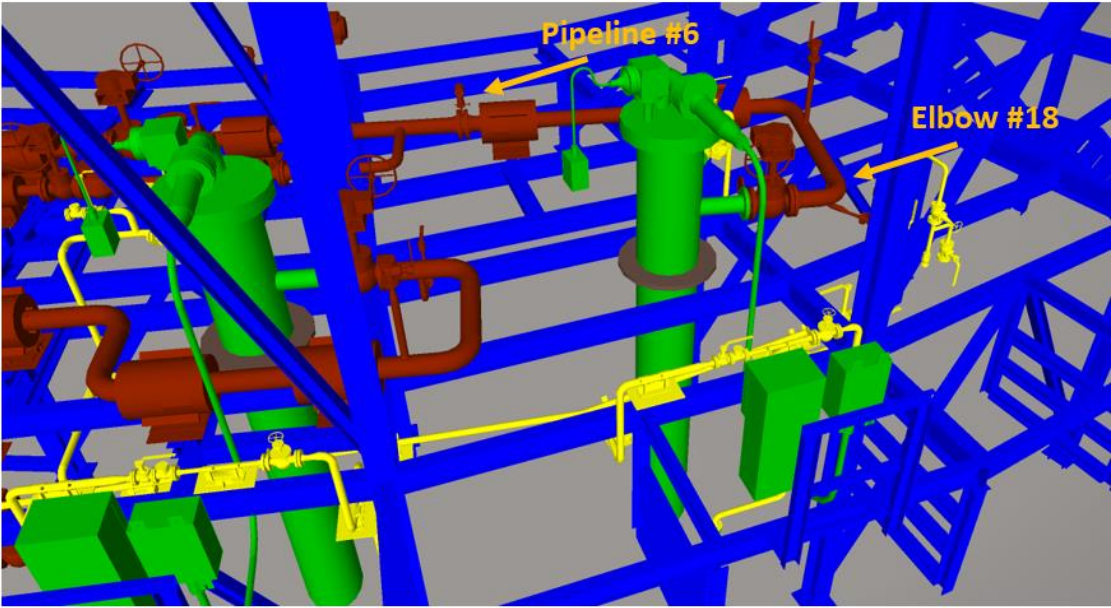


Figure 3.11 BFJs connecting the pumps to the piping system

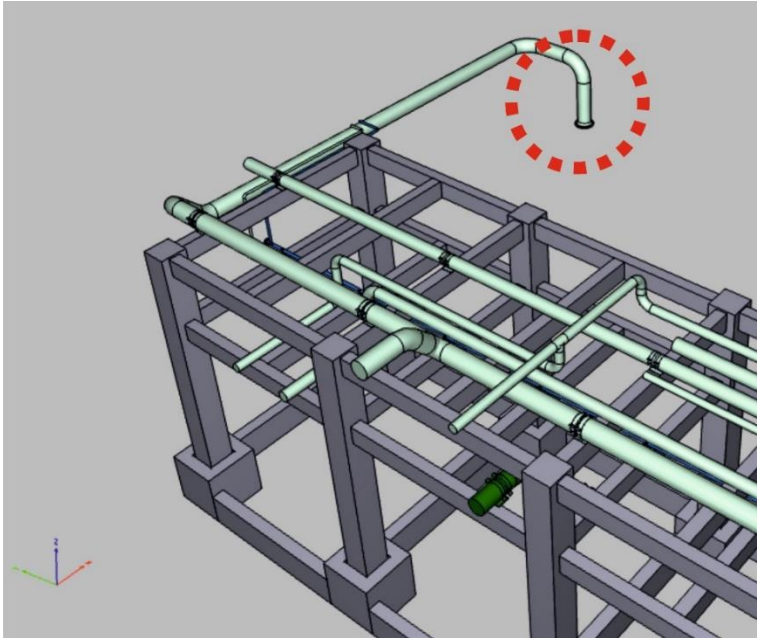


Figure 3.12 BFJ between the tank of the knock-out drum and the piping system

3.4 Critical components for leakage in the LNG plant

Pipelines and their components like BFJs, pipe bends and Tee joints are widely used in LNG plants including the one described in Section 3.3. With regard to BFJs, these joints are quite complex because they are highly confined statically indeterminate systems and also because they involve a high degree of non-linearity. As a result, it is difficult to correctly estimate their resistance and stiffness, as also the threshold of leakage. They have been investigated in Zerres and Guerot, (2004) and Reza et al., (2014), among others. Here we summarize the research work accomplished by La Salandra et al., (2016), see Subsection 3.4.1, whose results represent the basis for the mechanical model presented in Subsection 3.4.2. With reference to pipe bends, they are a vulnerable component of pipelines and we discuss their seismic performance evaluation in Subsection 3.4.3. Lastly, we do not explicitly mention Tee joints, since only one of them is encompassed into the pipelines. Nonetheless, the experimental campaign carried out allowed for its detailed modelling (Bursi, Reza et al., 2016b). More precisely, the Tee joint did not exhibit a significant stress level being located on the concrete rack, see Fig. 3.8, at a relatively low height.

3.4.1 Test campaign and main results

The mechanical model of BFJs was obtained by means of four experimental tests on two different BFJs, both for 8'' pipes, subjected to cyclic and monotonic loading. The two different types of BFJs had flanges of non-standard thickness; in greater detail, thicknesses of 18 and 27 mm (respectively Design 01 and Design 02) were employed, values less than those employed in industry, of the order of 35 mm. Therefore these flanges can be classified as non-standard flanges (Reza et al, 2014). During the test campaign, the BFJs specimens were loaded in the testing equipment depicted in Fig. 3.13. In greater detail, the joints were located at 45° with respect to the vertical loading axis. The main reason for this choice was the fact that we had no data to predict whether the axial or the shear force would have most influenced the leakage threshold in BFJs. Therefore, we decided to adopt a testing configuration with equal intensity axial and shear forces.

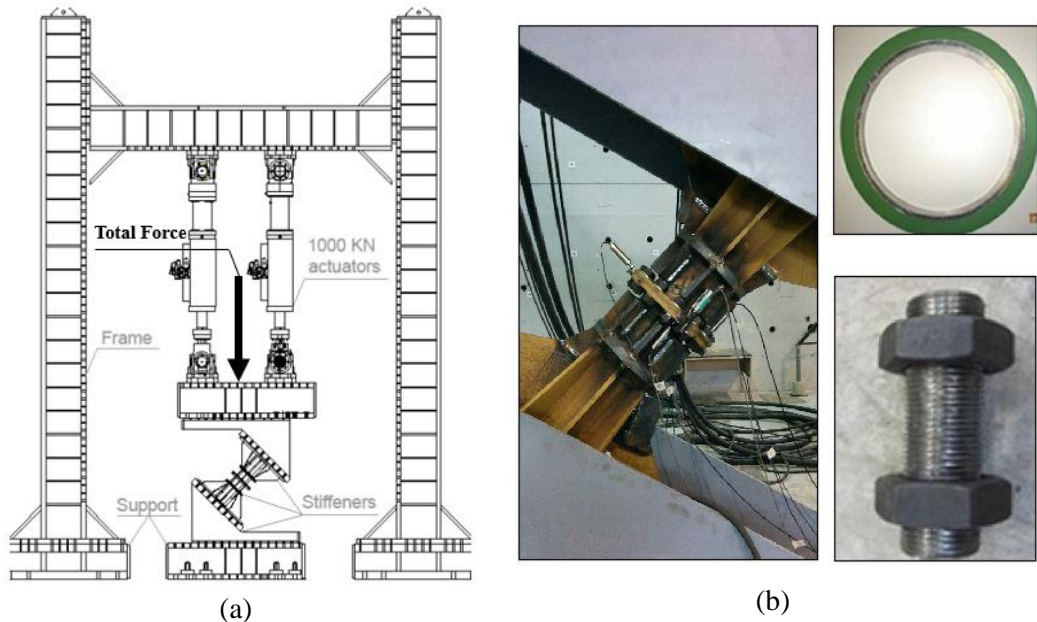


Figure 3.13 (a) BFJ setup. (b) Design 02 specimen, gasket, and a relevant bolt.

Both axial and shear force values corresponding to the onset of leakage are collected in Table 3.3.

Table 3.3 Leakage forces for the experimental tests

Specimen Flange Thickness and Loading Type	Leakage Axial Force [kN]	Leakage Shear Force [kN]
18 mm (Design 01) – Monotonic	1175	1175
18 mm (Design 01) – Cyclic	1100	1100
27 mm (Design 02) – Monotonic	1000	1000
27 mm (Design 02) – Cyclic	1470	1470

Although cyclic loading is more severe than monotonic loading for BFJ components, this is not reflected in the leakage forces of Design 02 joints. Moreover, it is worthwhile noting that the onset of leakage corresponds to an inside pressure of 32 bar which is far greater than the internal service pressure in the LNG pipelines, summarized in Table 3.2.

The corresponding force-displacement relationships are depicted in Figs 3.14 (a) and 3.14 (b) for monotonic and cyclic loading, respectively, where the Total Force shown in Fig. 3.13 (a), is equal to the sum of the forces exerted by the two actuators. These results show that the onset of leakage occurred after first yielding and before plastic collapse.

It is possible to notice that cyclic loading triggered leakage in Design 01 joints, with lower external forces compared to monotonic loading whilst the opposite happened for Design 02. This can be explained considering the differences between the deformation modes of Design 01 and 02. As a matter of fact, Design 01 experiences leakage through the bolts holes with a minimum involvement of flange plates; therefore, the bolts were the components that controlled leakage and similar leakage force levels were exhibited in both monotonic and cyclic loading. Conversely, in Design 02, leakage started from flange plates with a little involvement of bolts. As a result, cyclic loading pre-compressed flange plates increasing their leakage resistance and making the BFJ less vulnerable than that subjected to monotonic loading.

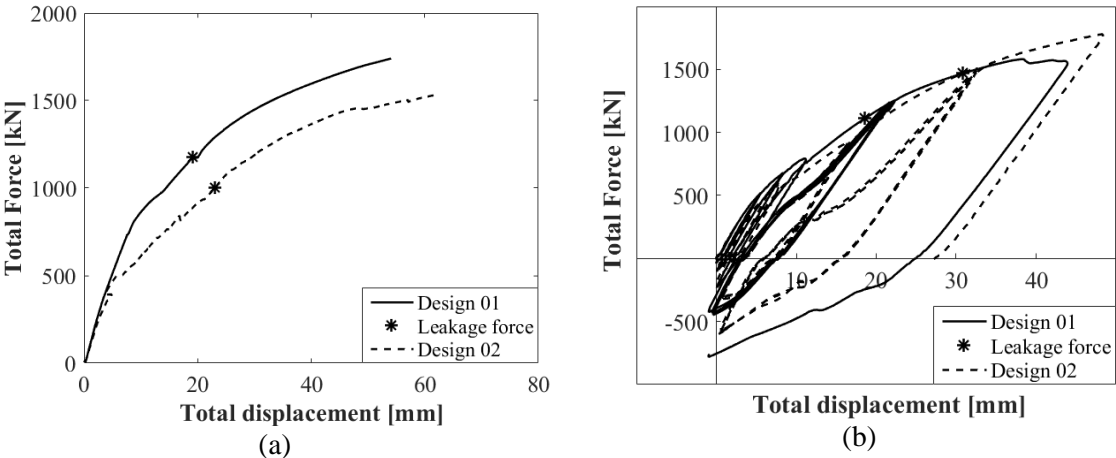


Figure 3.14 Load-Displacement diagrams for 18 mm (Design 01) and 27 mm (Design 02) BFJs: (a) Monotonic loading and (b) Cyclic Loading.

3.4.2 Predictive model for leakage and mechanical model of BFJs

Because pipelines and relevant BFJs of the LNG plant under study are characterized by a variety of diameters, from 4” to 18”, as listed in Table 3.2, a mechanical model is needed to predict the onset of leakage for the remaining diameters. To this end, the experimental work of La Salandra et al. (2016) provides the basis for the predictive mechanical model summarized here.

The proposed mechanical model is based on the framework of EN 1591 standard (2009). More precisely, the model considers the BFJ as composed of three main components: bolts, flange and gasket, as reported in Fig. 3.15, where F_{BI} and F_{GI} define the tensile bolt and the gasket compressive axial forces, respectively; F_{QI} equals the force due to internal pressure whilst F_{RI} represents the resulting external force acting on the joint. Additionally, all these forces are referred to a generic design load condition I .

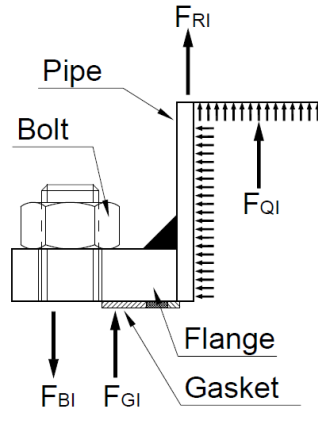


Figure 3.15 Bolt, flange and gasket components and force balance in the mechanical model of a BFJ proposed in EN 1591-1 (2009).

This model is based on the assumption that the flange is infinitely stiff in bending, see in this respect Fig. 3.17, differing from bolts and gasket which can exhibit axial deformation. Moreover, we assume that leakage occurs when the compressive stress on the gasket σ_{GI} is lower than a certain threshold $Q_{s,min,I}^{(L)}$ (EN 1591-1 standard, 2009). Starting from these hypotheses, the proposed model employs the following equation of the joint compliance at the load condition I :

$$F_{GI}Y_{GI} + F_{QI}Y_{QI} + F_{RI}Y_{RI} + \Delta U_I = F_{G0}Y_{G0}P_{QRI} \quad (3.5)$$

where, F_{G0} defines the gasket compressive force at the initial state 0 - the assembly condition - due to the bolt force tightening, i.e.

$$\begin{aligned} F_{G0} &= \sigma_{G0}A_{Ge} = \sum_{n^{\circ} bolts} F_{tor} \\ &= \sum_{n^{\circ} bolts} \frac{M_{torq}}{0.18 * d} \end{aligned} \quad (3.6)$$

After some algebraic manipulations, the pressure on the gasket at the load condition I can be calculated and compared to the limit provided by the standard, i.e.

$$\sigma_{GI} = \frac{\sum F_{tor}Y_{G0}P_{QRI} - \frac{\pi}{4}d_{Ge}^2F_{QI}Y_{QI} - F_{RI}Y_{RI}}{Y_{GI}A_{Ge}} \leq Q_{s,min,I}^{(L)} \quad (3.7)$$

If Eq. (7) is satisfied, then the leakage limit state does not occur. As a result, by working out Eqs. (5-7), we can derive the external force F_{RI} ,

$$F_{RI} \geq \frac{\sum F_{tor} Y_{G0} P_{QRI} - \frac{\pi}{4} d_{Ge}^2 F_{QI} Y_{QI} - Q_{s,min,I}^{(L)} Y_{GI} A_{Ge}}{Y_{RI}} \quad (3.8)$$

that corresponds to the leakage onset. Further details of this derivation and relevant symbols can be found in La Salandra et al. (2016).

This model seems to predict satisfactorily the experimental results of the testing campaign by Reza et al. (2014), where BFJs were loaded only axially. Nonetheless, BFJs present in the piping system under study are subjected to multiple actions, in agreement with the experimental testing presented in Subsection 3.4.1. As a result, the mechanical model takes into account the possible interaction between axial and shear loading. More precisely, the leakage force for a BFJ subjected only to the shear loading is supposed equal to the bolt shear strength T_u provided by EN 1993-1-8 (2005), i.e.,

$$T_u = n * \frac{0.6 * f_u * A_{res}}{\gamma_{M2}} \quad (3.9)$$

Additionally, based on the aforementioned test campaign, the relation between the combined axial and shear leakage loading is approximated as linear,

$$T = (N_u - N)\rho, \text{ where } \rho = T_u/N_u. \quad (3.10)$$

Eq. (3.10) is presented graphically in Fig. 3.16 and the reader can appreciate the favourable agreement between model and test data.

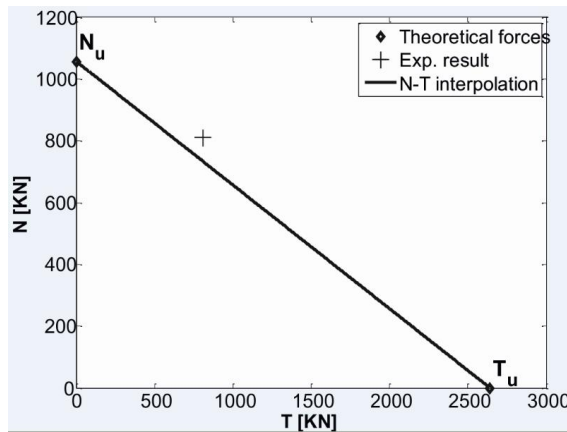


Figure 3.16 Comparison between axial and shear leakage forces from the predictive model and experimental results.

Therefore, it is possible to calculate both axial and shear leakage forces of relevant BFJs under study, i.e. both 6'' and 18'' weld neck flanges, and relevant values are summarized in Table 3.4.

In order to accomplish the FE analysis presented in Subsection 3.6.3, we also needed to characterize BFJs in terms of axial and shear stiffness. With reference to the axial stiffness, we start from the mechanical model proposed in EN 1591 (2009). In particular, the mechanical model – sketched in Fig. 3.17 - considers the joint axial deformation δ_s due to an external force F_R as:

$$\delta_s = u_{an} + v_{an}. \quad (3.11)$$

where, u_{an} defines the bolt axial elongation and v_{an} identifies the axial deformation due to rigid flange rotation.

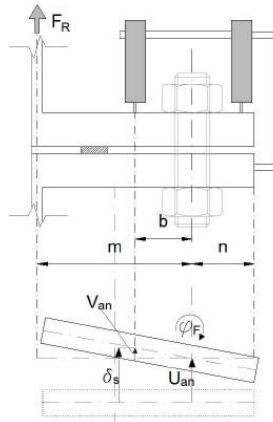


Figure 3.17 Axial deformation model for BFJs.

Moreover, the equivalent shear stiffness K_s is estimated considering two plates of equal thickness t and joined by means of one bolt, i.e.

$$\frac{1}{K_s} = \frac{10t^3}{24E_b I_b} + \frac{4t}{3A_b G_b} + \frac{2tE_f}{t^2 E_f^2} \quad (3.12)$$

where the first and the second term on the right hand side refer to bending and shear compliance of the bolt, respectively; whilst the third term is related to the bearing compliance of plates. Finally, linear stiffness values for BFJs under study are collected in Table 3.4. As a result, BFJs add stiffness to the whole piping system under study.

Table 3.4 Axial and shear stiffness and leakage forces of BFJs.

	6'' Weld Neck Flange CL300	18'' Weld Neck Flange CL150
Axial stiffness [kN/mm]	14400	26000
Shear stiffness [kN/mm]	1270	4700
Axial leakage force [kN]	939	1034
Shear leakage force [kN]	2228	6097

With regard to leakage forces, one can notice that their values are significant; moreover, leakage due to shear needs greater force values.

3.4.3 Elbows performances

Piping elbows are critical component in a piping system and are characterized by a high flexibility, relevant level of stresses and strains and a significant cross-sectional deformation. Since the goal of this study was the investigation of the onset of leakage triggered by seismic action, particular attention was paid to pipe bends due to their vulnerability. Therefore, we focused on the identification of reliable EDPs related to leakage. Present regulations such as ASME BPVC (2004) do not explicitly treat leakage but consider “gross plastic deformation” instead. In particular, they are defined by means of the twice elastic slope (TES) method. In addition, very few papers are available on the topic; see Karamanos (2016) and Brinnel et al., (2016). A useful tool to classify the performance of piping elbows was developed by Vathi et al. (2015), which defines a set of damage levels, see in this respect Table 3.5, and the related limit states associated with several failure modes and relevant EDPs: they are collected in Table 3.6.

Table 3.5 Performance levels (after Vathi et al., 2015)

Level	Description
0	No damage
I	Minor (non-severe) damage
II	Major damage, but no loss of containment
III	Major damage with loss of containment

As stated before, our main interest was the LOC that corresponds to the Level III of damage.

Table 3.6 Failure modes with relevant EDPs and limit states (after Vathi et al., 2015)

Failure mode	EDP	Performance level and corresponding range	
Tensile fracture	Tensile strain ε_T	$\varepsilon_T < \varepsilon_\gamma$	0
		$\varepsilon_\gamma < \varepsilon_T < 0.5\%$	I
		$0.5\% < \varepsilon_T < \varepsilon_{Tu}$	II
		$\varepsilon_T \geq \varepsilon_{Tu}$	III
Local buckling	Compressive strain ε_C	$\varepsilon_C < \varepsilon_\gamma$	0
		$\varepsilon_\gamma < \varepsilon_C < \varepsilon_{Cu}$	I
		$\varepsilon_{Cu} < \varepsilon_C < 5\varepsilon_{Cu}$	II
		$\varepsilon_C \geq 5\varepsilon_{Cu}$	III
Low-cycle fatigue cracking failure	Damage factor $D = \sum_i \frac{n_i}{N_i}$	$D < 0.5$	0
		$0.5 < D < 0.8$	I
		$0.8 < D < 1$	II
		$D > 1$	III

In particular, the threshold for tensile strain ε_{Tu} suggested by Vathi et al. is equal to 2%; conversely, to compute the same limit state for compressive strains, i.e. $5\varepsilon_{Cu}$, we adopted the following relationship,

$$\varepsilon_{Cu} = 0.5 \left(\frac{t}{D} \right) - 0.0025 + 3000 \left(\frac{\sigma_h}{E} \right)^2 \quad (3.13)$$

where t is the thickness of the pipe walls, D is the diameter, σ_h the internal pressure and E the Young's modulus.

The leakage compressive strains for pipeline #1 and #6 are calculated by means of Table 3.2, where no internal pressure is considered to simulate the worst conditions. The resulting strain values are 3.6% for pipeline #1 and 4.7% for pipeline #6, significantly higher than the leakage tensile strain assumed to be 2%.

With regard to low-cycle fatigue defined in Table 3.6, we relied on the design low-cycle fatigue curves proposed by Otani et al., (2017), based on data derived from several experimental campaigns. Therefore, on the basis of the records 007162 and 006277, see Table 3.8, characterized by PGA of 1.04 g and 0.86 g, respectively, the seismic analysis on the plant was carried out. The corresponding time histories of elbow hoop strains were treated by means of a rainflow analysis. The subsequent application of the Palmgren-Miner rule entails damage values corresponding to $D=8.52 \cdot 10^{-5}$ and $8.89 \cdot 10^{-5}$, respectively. On this basis and also in the case of some strong aftershock event, one can exclude LOC of elbows due to low-cycle fatigue failure.

In sum, the tensile strain can be considered the most important indicator of leakage in seismic assessment. This is also confirmed by the extensive test campaign conducted by the Japan Nuclear Energy Safety Organization and the Nuclear Power Engineering Corporation of Japan (JNES/NUPEC, 2008); and we recall the experimental work of Karamanos and co-workers that produced an overview of the mechanical behaviour of elbows, reporting analytical solutions, numerical results and experimental data. (Karamanos, 2016). As a result, we assume that piping elbows experience the onset of leakage when tensile hoop strains reach values of about 2% at the outer surface, in agreement with experiments. Indeed, studies by Singh and co-workers confirm that fatigue crack growth appears on the inside as well as the outside surface of the flank region (Singh et al., 2014).

3.5 FE modelling of LNG plant components and preliminary analyses

After the design of the BFJ mechanical model, FE modelling of other components in the LNG plant is reported in this section. For this purpose, the FE software ANSYS was employed.

3.5.1 LNG Storage Tank

The outer concrete layer of the storage tank was modelled by means of 4-node SHELL181 elements. In this respect, the design of the mesh was conceived with 34 elements along the circumference section, 19 elements along the wall height and 11 elements along the radius of the dome, as depicted in Fig. 3.18 (a). Moreover, the outer tank was fixed to the ground by means of rigid constraints. On the other hand, the inner steel tank was modelled by assigning the total mass of the LNG content when filled at the maximum capacity, i.e. 290,000 tons, to a single MASS21 element placed in the middle of the tank and connected to the concrete tank by means of 4 MPC184 Rigid Link elements; see Fig. 3.18 (b) in this respect.

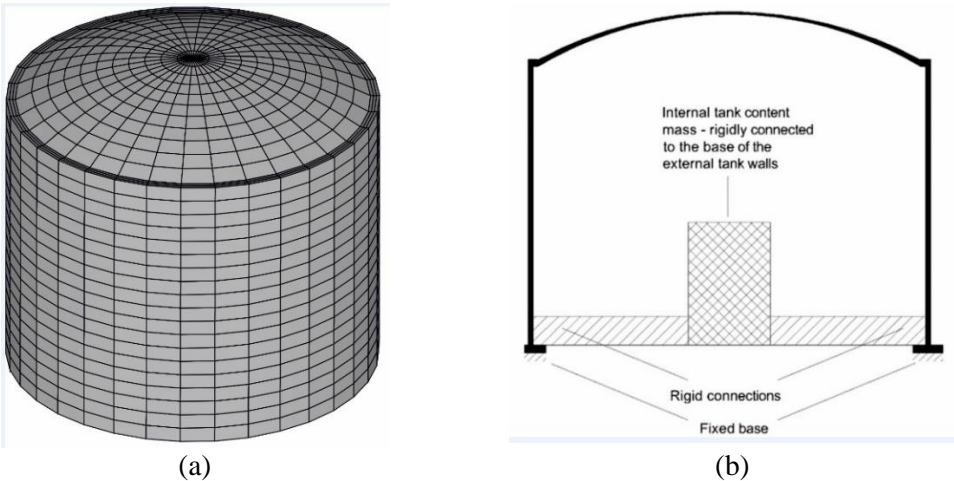


Figure 3.18 (a) Mesh design for the outer tank; (b) FE model of the inner tank.

The assumption of rigid walls is mainly due to the large outer tank thickness. Then, since forces generated by liquid modes (Malhotra et al., 2000) on the structure did not produce significant effects, we decided not to monitor local stresses on tank walls. Thus, from a dynamic point of view, we only take into account inertial effects of the LNG content in the calculation of reaction forces at the tank base.

3.5.2 Support Structures

The steel platform supporting piping systems and pumps, is on the top of the tank, as depicted in Fig. 3.19 (a). It is modelled by means of the BEAM4 and LINK180 elements for beams and axial members, respectively. All these elements are modelled with a linear constitutive law. On the other hand, the concrete support structure at the base of the tank is modelled with the same BEAM4 elements used for the steel platform. Moreover, it is rigidly constrained to the ground. In agreement with the Seismic Italian Standards (Norme Tecniche, 2008), the elastic modulus of concrete was reduced by 50 percent to account for cracking at the ultimate limit state. Nonetheless, during seismic analyses stress levels never exceeded plastic limits in reinforced concrete elements. Therefore, a linear elastic constitutive law was considered also for this substructure.

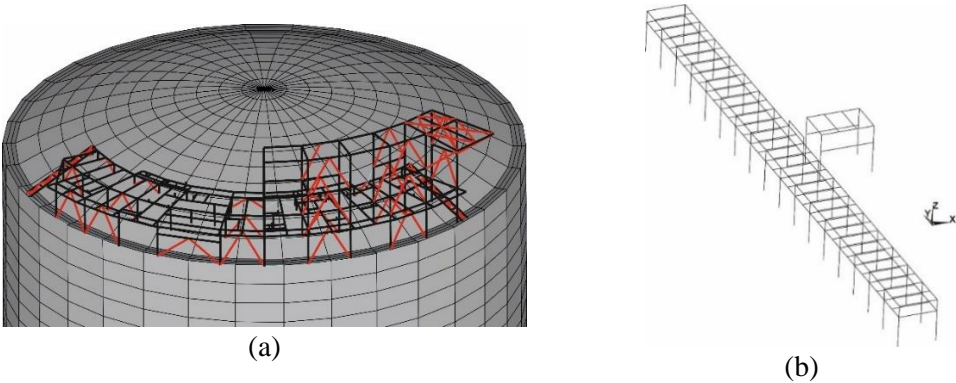


Figure 3.19 ANSYS FE model: (a) steel platform; (b) concrete support structure.

3.5.3 Piping System and Knock-Out Drum Area

The piping system was modelled by means of PIPE289 and ELBOW290 elements; these are both 3-node 3D elements with 6 DoFs per node. Lateral walls were modelled with SHELL181 elements with the shell thickness equal to the real pipe thickness. The design of the mesh was conceived with 20 shell elements along the circumference section. Furthermore, in order to correctly model the elbow constitutive law, the A312/TP304L stress-strain curve depicted in Fig. 3.20 (a) was reproduced with a bilinear relationship accounting for kinematic hardening.

Due to their complexity, only two of the seven pipelines on the steel platform on the tank dome were entirely modelled in ANSYS, i.e. pipeline #1 – the largest - and #6 – the

smallest - as reported in Fig. 3.20 (b). Given the relevant involved weights, the unmodeled pipelines did not influence the dynamic response of the system. According to design requirements, two types of constraints were applied in modelling the contact between the piping system and the two support structures: i) a fixed constraint and ii) a roller allowing the piping to slide in its longitudinal direction.

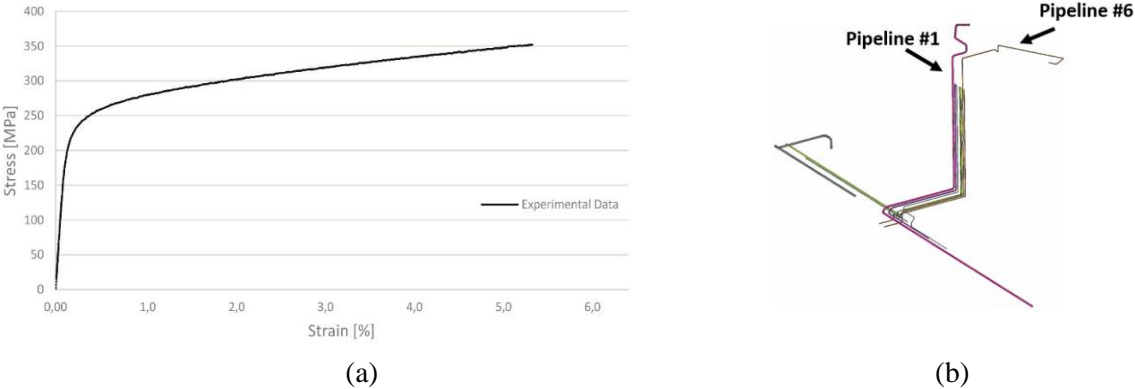


Figure 3.20 (a) Experimental results for A312/TP304L steel (b) FE model of the piping layout.

On the other hand, BFJs were modelled by means of a longitudinal and two transversal springs as presented in Subsection 3.4.2. To this end, and to take into account the different responses for tensile and compression forces, the COMBIN39 element was used for the axial spring. The values of both longitudinal and shear stiffness for BFJs modelling are in Table 3.4. Finally, the knock-out drum area is placed on the ground, close to the LNG storage tank, see Fig. 3.2 in this respect. The FE model developed by Kondorfer et al. (2016) was used for modelling both the pressure vessel C608 and the relative steel support structure. In particular, the support structure was modelled by means of BEAM4 elements, whilst the pressure vessel C608 was simplified with a mass-spring model, as depicted in Fig. 3.21.

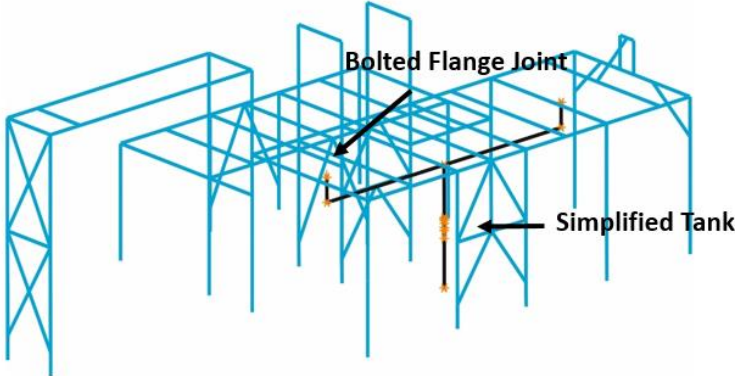


Figure 3.21 FE model of Knock-out drum process area.

3.5.4 The whole ANSYS model

Once each single component was modelled, they were assembled to build up the complete FE model of the plant, as depicted in Fig. 3.22.

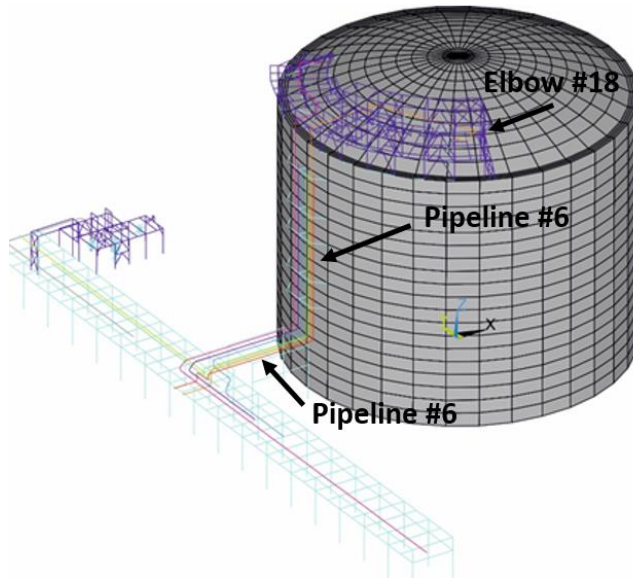


Figure 3.22 ANSYS complete FE model of the LNG plant.

The complete model is highly complex, with totals of 19568 DoFs, 1338 BEAM4 elements, 159 PIPE289, 95 ELBOW290 and 1122 SHELL181.

3.5.5 Preliminary seismic analyses for boundary conditions and mesh sizes.

In order to assemble a FE model of the plant, a sensitivity analysis was conducted on important elements like tanks and elbows. As a result, the proper number of FE for the tank was set to 1122 shell elements; also, the number of integration points along the wall thickness of elbows was selected equal to 2. The FE model was assembled considering the relative boundary conditions between the different components. In a greater detail we had to model the connections between: i) the knock-out drum area and the concrete support structure; ii) the steel platform and the dome of the LNG tank; iii) the two different sections of the concrete rack and the LNG tank; iv) the pipelines and the support structures. The first connection was made only by means of the pipelines that, coming from the support rack, were connected to the 18'' BFJs of the knock-out drum vessel; see, in this respect, both Fig. 3.7 and Table 3.4. The second connection was accomplished with rigid links coupling base nodes of the steel platform with nodes of the LNG tank dome. This was done to simulate a fixed constraint between the tank and the platform. The third coupling, like the first one above, was realised by the set of pipelines running through the different components. With regard to the last set of links, it is well known that pipeline supports are not frictionless (Peng, 1989). For this reason, we employed two different types of constraint: fixed supports

with all displacement blocked in the *FIXED* case; roller supports with free axial displacements in the *FREE* case.

Once assembled the entire FE model of the plant, we needed to define important parameters, such as the amounts of fluids in pipelines and the types of constraint on support structures. For the first parameter, two cases were defined: i) the “LNG” case, in which the mass of the fluid was included in the pipelines, ii) the “EMPTY” case where the liquid mass was neglected. Finally, some preliminary seismic analyses were carried out with different scenarios; the results are reported in Table 3.7.

Table 3.7 Comparison between preliminary simulations.

Earthquake	Record ID	PGA	Pipelines content	Constraints	Max Axial Strain Detected
South Iceland (aftershock)	006334	3.84	EMPTY	FREE	0.32% - Pipeline #6 Elbow 15
South Iceland (aftershock)	006334	3.84	LNG	FIXED	0.32% - Pipeline #6 Elbow 15
L’Aquila Mainshock	IT0792	5.35	EMPTY	FREE	0.45% - Pipeline #6 Elbow 11
L’Aquila Mainshock	IT0792	5.35	LNG	FREE	0.45% - Pipeline #6 Elbow 11
L’Aquila Mainshock	IT0792	5.35	LNG	FIXED	0.45% - Pipeline #6 Elbow 11
South Iceland	006277	5.08	EMPTY	FREE	3.25% - Pipeline #6 Elbow 18
South Iceland	006277	5.08	LNG	FIXED	3.25% - Pipeline #6 Elbow 18

It can be seen that there are no large differences between simulations with the same earthquake input and different pipeline conditions; hence, in order to obtain fragility curves for elbows, all required simulations were carried out considering the same conditions, i.e. the “LNG” case for the pipeline content and the “FREE” condition for pipeline constraints.

3.6 Probabilistic Seismic Analysis

In order to evaluate the probability of exceeding a certain *EDP* i.e. $P(EDP)$ from Eq. (3.4), the conditional probability of exceeding a prescribed *EDP* given the intensity measure, *IM*, i.e. $P(EDP > C_{LS} | IM = im)$ must be estimated. There are several alternative non-linear dynamic analysis procedures available in the literature for characterizing the relationship between *EDP* and *IM* based on recorded ground motion waveforms, such as: i) Incremental Dynamic Analysis (IDA, see Vamvatsikos & Cornell, (2004)); ii) Multiple-Stripe Analysis (MSA, see Jalayer & Cornell, (2009)); and iii) the Cloud Method (Cornell et al. 2002). Both

IDA and MSA are suitable for evaluating the relationship between EDP and IM for a wide range of IM values; however, their application is time-consuming in our context of the LNG plant, about three days per run, as nonlinear dynamic analyses are repeated -usually for scaled ground motions- for increasing levels of IM . Moreover, the Cloud method does not require any amplitude scale factor. In fact, scaling can entail incoherencies in the probabilistic model, especially when all three -X, Y and Z- different components of each waveform are used for seismic demand analysis (Mackie and Stojadinović, 2005). Therefore, a *Cloud Analysis* will be applied in the sequel.

3.6.1 Cloud analyses and seismic input

As a first step, we consider only one scalar IM in the *Cloud Analysis*, i.e. the PGA. In particular, we decided to avoid, in the initial phase of the study, the adoption of any spectral quantity because of the heterogeneity in the modal frequencies of the LNG plant substructures. However, the Cloud Analysis was later performed by considering as additional IM the spectral acceleration $Sa(T)$. Accordingly, the LNG plant described in Section 3.5 is subjected to a suite of 36 ground-motion waveforms shown in Table 3.8, and the associated structural response parameters, as anticipated in Subsection 3.2., are denoted as $D = \{D_i, i = 1:n\}$. In particular, the *Cloud Analysis* is based on two main hypotheses: i) D is characterized by a lognormal distribution; ii) the expected D is modelled as a linear relationship in the logarithmic space of D versus the candidate IM , i.e.

$$E[\ln D|IM] = a + b \ln(IM) \quad (3.14)$$

In particular, a and b are regression coefficients estimated with the least square method. Then, a and b let us set the main parameters of the probabilistic seismic demand model (PSDM), i.e.

$$\sigma_{\ln D|IM} = \beta_{D|IM} = \sqrt{\frac{\sum_{i=1}^n [\ln(D_i) - \ln(a(IM_i)^b)]^2}{n - 2}} \quad (3.15)$$

$$m_D = \left(\frac{C_{LS}}{a}\right)^{1/b} \quad (3.16)$$

$$\beta_D = \frac{1}{b} \beta_{D|IM} \quad (3.17)$$

where:

β_D and m_D are the dispersion and the median of D values that exceed the limit state level, indicated as C_{LS} .

Thus, the conditional probability that the demand D exceeds the limit state capacity C_{LS} , which is known as fragility function, reads,

$$P[D \geq C_{LS} | IM = im] = \Phi \left[\frac{\ln(im/m_D)}{\beta_D} \right] \quad (3.18)$$

In order to cover different values of magnitude M_w and PGA, we chose the suite of ground motions from different European databases (ESM and ITACA). All three components, two horizontal and one vertical, were applied during the seismic analysis. In particular, we applied the strongest of the components along the X axis, as depicted in Fig. 3.2, since we required a more demanding load in the preliminary analyses. The record names and relevant characteristics are collected in Table 3.8.

Table 3.8 Natural records used for Cloud analysis.

Record Name	Record ID	Date	M_w	PGA [m/s ²]
L'Aquila Mainshock	IT0792	06/04/2009	6.3	5.352
L'Aquila Mainshock	IT0789	06/04/2009	6.3	3.947
South Iceland (aftershock)	006334	21/06/2000	6.4	4.123
L'Aquila Mainshock	IT0790	06/04/2009	6.3	4.793
Northern Italy Friuli	IT0049	17/06/1976	4.5	0.811
Friuli	IT0077	11/09/1976	5.8	2.29
Southern Italy	IT0231	16/01/1981	5.2	1.069
Umbria-Marche 3rd shock	IT0491	14/10/1997	5.6	0.435
Garfagnana	IT0157	07/06/1980	4.6	0.595
App. Lucano	IT0607	09/09/1998	5.6	0.427
Ancona	IT0009	21/06/1972	4.0	4.025
South Iceland (aftershock)	006349	21/06/2000	6.4	8.218
Ancona	IT0002	14/06/1972	4.8	5.309
Firuzabad	007162	20/06/1994	5.9	10.444
Gazli	000074	17/05/1976	6.7	7.065
Erzincan	000535	13/03/1992	6.6	5.028
South Iceland	006277	17/06/2000	6.5	5.083
Racha (aftershock)	000501	03/05/1991	5.6	4.989
Pyrgos	000558	26/03/1993	5.4	4.256
Kalamata (aftershock)	000419	15/09/1986	4.9	3.275
NE of Banja Luka	005651	13/08/1981	5.7	3.551
Ionian	006131	24/04/1988	4.8	2.705

Bovec (aftershock)	006247	06/05/1998	4.3	2.801
Kozani (aftershock)	006093	19/05/1995	5.2	2.601
Patras	001932	14/07/1993	5.6	3.337
Faial	007329	09/07/1998	6.1	4.12
Oelfus	005030	13/11/1998	5.1	1.439
Mt. Hengill Area	005149	24/08/1997	4.9	1.691
Mouzakaiika	000566	13/06/1993	5.3	1.428
Holt	005237	23/04/1991	4.7	1.212
Kremidia (aftershock)	002025	25/10/1984	5.0	
Friuli (aftershock)	000707	11/09/1976	5.3	1.931
Valnerina	000246	19/09/1979	5.8	0.870
Izmit (aftershock)	006440	07/11/1999	4.9	3.449
Ancona	000030	14/06/1972	4.3	3.972
Strait of Gibraltar	000878	04/01/1994	4.9	0.596

The response spectrum of the strongest components of the natural records is depicted in Fig. 3.23.

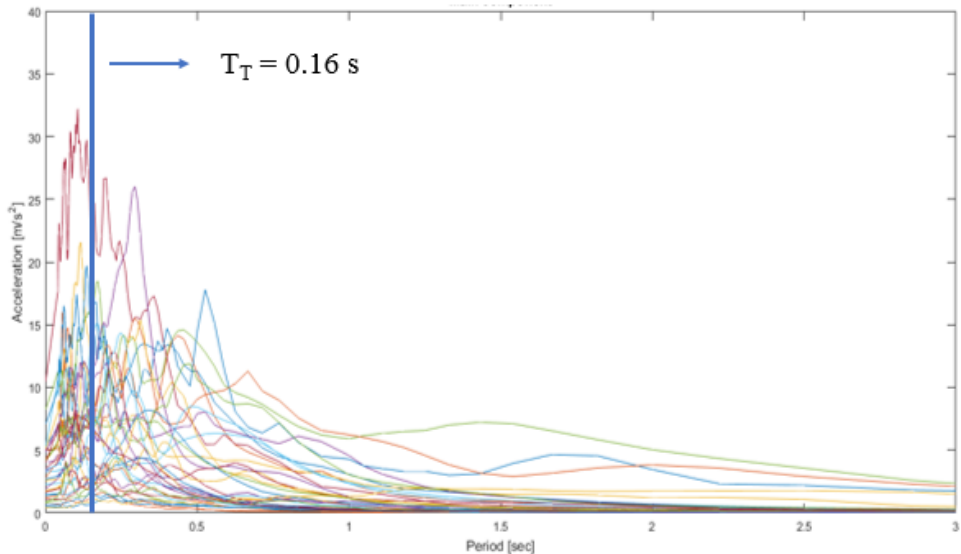


Figure 3.23 Response spectra of the strongest components of natural records employed.

We can see the high variability of spectral acceleration; for instance, the values cover a wide range, from near zero to 3g. This wide range lets us evaluate and improve the efficiency of the PSDM accomplished in Subsection 3.6.4.

3.6.2 EDPs and Limit States

As anticipated in Subsection 3.1.1., because LNG is a hazardous material due to its flammability after vaporization, we must prevent component leakage under environmental hazards: i.e. earthquakes, in our particular case. Therefore, we focused our attention on leak-prone elements like BFJs and piping elbows. In this respect and in agreement with the PBEE framework described in Section 3.2, three EDPs, i.e. demands D in Eq. (3.4), were selected as listed in Table 3.9.

Table 3.9 EDPs description

EDPs Number	Parameter Description
1	BFJs Max Axial Force
2	BFJs Max Shear Force
3	Elbow Max. Tensile Hoop Strain

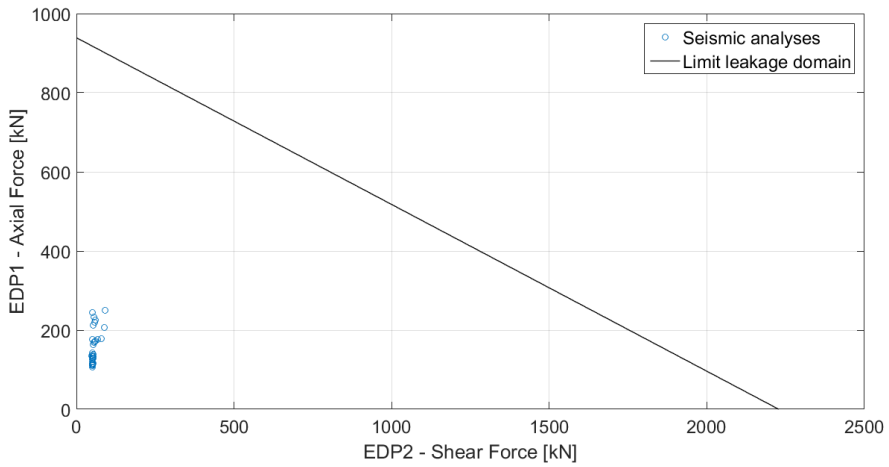
With regard to EDP1 and EDP2, leakage thresholds were discussed and defined in Subsection 3.4.2 and Table 3.3. Conversely, the onset of leakage in elbows was directly defined relating EDP3 to a value of tensile hoop strain according to the literature review and the analyses presented in Subsection 3.4.3. Relevant C_{LS} values – see Eq. (3.4)- associated with leakage thresholds are reported in Table 3.10 and EDP3 reads 2 percent for elbows. As a result to reach the LOC, piping elbows experienced several limit states corresponding to the different damage levels thresholds reported in Table 3.6. Nonetheless and in agreement with EN 1473 (2016), LOC is the most critical limit state for risk assessment and hazard tolerability classification of LNG plants, and therefore, we decided to perform a fragility analysis only for the LOC limit state.

Table 3.9 EDPs leakage limit states

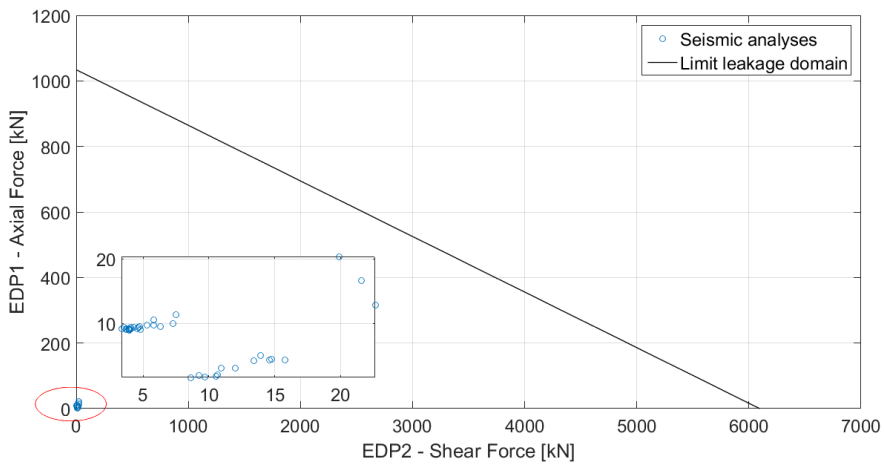
	6" Flange [kN]	18" Flange [kN]
EDP1	939	1034
EDP2	2228	6097
	6" Elbows (%)	
EDP3	2	

3.6.3 Main results of FE analyses

With reference to BFJs and EDP1 and EDP2 values set in Table 3.10, the results of seismic analysis reveal that axial and shear forces do not approach leakage thresholds. Relevant values are shown in Fig. 3.24 for 6" and 18" flanges, respectively. A careful reader can notice that force values experienced by BFJs are substantially lower than limit leakage domains. Other limit states like yielding have not experienced both by flanges and bolts of FBJs.



(a)



(b)

Figure 3.24 Seismic analysis results for: a) 6” BFJs; b) 18” BFJs.

With regard to EDP3, both maximum and minimum absolute values of tensile hoop strains collected in Table 3.11 were detected for the Elbow #18 shown in both Fig. 3.11 and in Fig. 3.22.

Table 3.11 Maximum and minimum absolute values of EDP3

Record Name	Record ID	EDP3 - Elbow Tensile Hoop Strain [%]
Firuzabad	007162	4.77
Mt. Hengill Area	005149	0.106

These values are justified by the fact that Elbow #18 is located at about 40 m above ground on the steel platform that is built above the dome of the LNG tank; and relevant seismic forces are clearly significant. Therefore, we decided to introduce as additional IM, the spectral acceleration $Sa(T)$ at the main vibration period of the LNG tank, i.e. $T_T = 0.16$ s, since we expect a stronger influence upon the EDP3 compared to the PGA. The values of $Sa(T_T)$ can be observed in Fig. 3.23. Moreover, only one of three pipelines associated with pumps was modelled; other non-modelled elbows will likely be subject to similar seismic forces. However, we will consider these effects in the forthcoming subsection.

3.6.4 Efficiency analysis and fragility curves

According to Baker (2015), a PSDM is defined as efficient when the variance of the estimators is low; and in our particular case, the estimator is represented by $\ln D$ of Eq. (3.14). Given the results of the previous Subsection 3.6.3, only EDP3 was worthy of attention and, therefore, it was associated with the demand parameter D . Hence, we rearranged the seismic results as shown in both Fig. 3.25 and 3.26, and computed the coefficient of variation (COV) and the R^2 associated with (3.12). The PSDM based on the PGA achieved values of COV and R^2 equal to 0.6 and 0.6, respectively. These figures show that the correlation between PGA and EDP3 is relatively weak and associated with high dispersion (Mackie and Stojadinović, 2005, and Ebrahimian et al., 2015). On the other hand, the adoption of $Sa(T)$ as IM, with COV and R^2 equal to 0.33 and 0.88, respectively, led to a very efficient PSDM involving a strong correlation on EDP3-

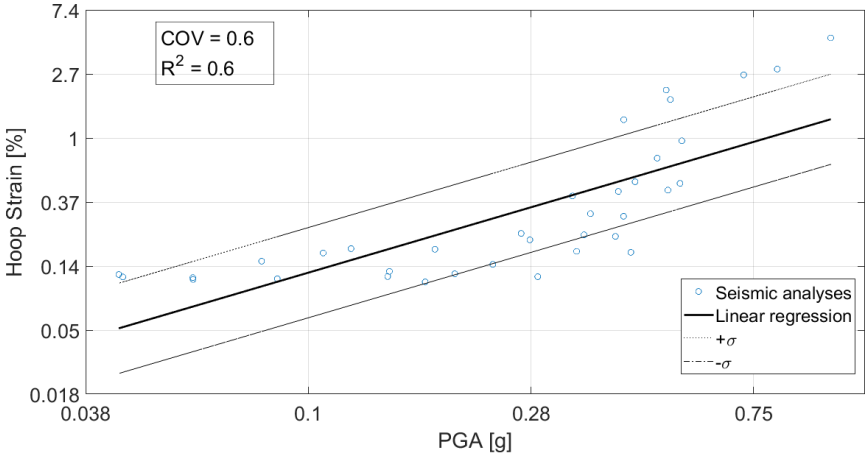


Figure 3.25 Seismic analysis results and linear regression for EDP3 and PGA as IM.

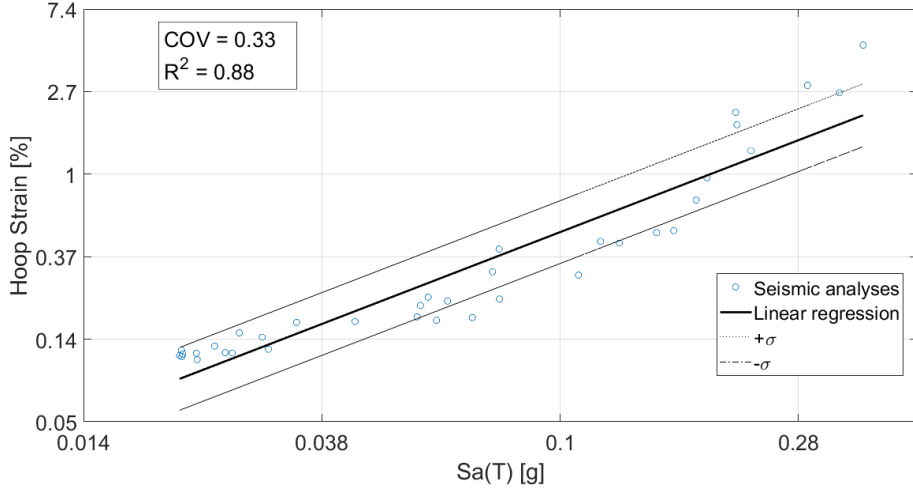


Figure 3.26 Seismic analysis results and linear regression for EDP3 and Sa(T) as IM.

In order to proceed with a fragility analysis, we computed the fragility functions $F_D(IM)$, i.e. the probability of the demand D exceeding C_{LS} as,

$$F_D(IM) = P[D \geq C_{LS} | IM = im] = \Phi \left[\frac{\ln(im/m_D)}{\beta_D} \right] \quad (3.19)$$

We note that $F_D(IM)$ was expressed using a lognormal cumulative distribution function (Baker, 2015). Both $F_D(PGA)$ and $F_D(Sa(T))$ of EDP 3 are reported in Fig. 3.27 and 3.28, respectively, whilst their parameters are listed in Table 3.12.

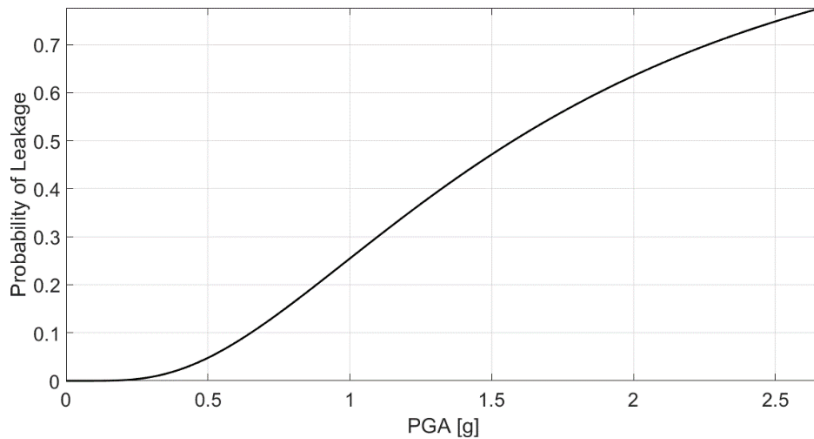


Figure 3.27 Fragility curves for EDP 3 and PGA as IM.

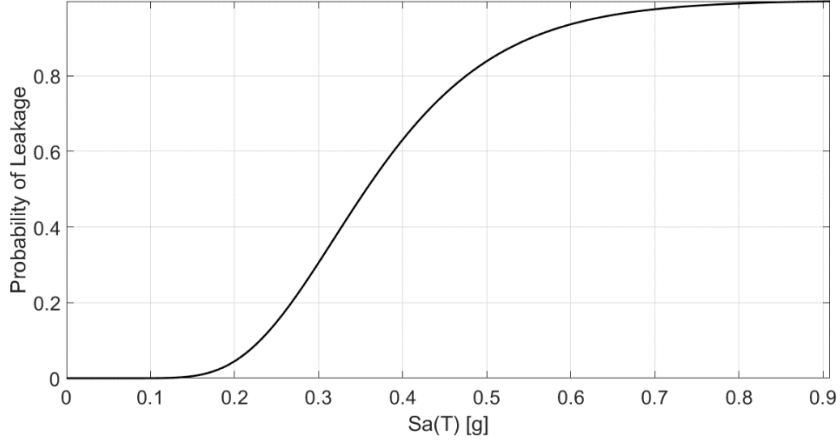


Figure 3.28 Fragility curves for EDP 3 and Sa(T) as IM.

Table 3.12 Fragility function parameters

EDP	IM	Parameters	
		m_D	β_D
3	PGA	1.62	0.71
3	Sa(T)	0.345	0.342

As a result, both $F_D(PGA)$ and $F_D(Sa(T))$ exhibit a substantial vulnerability at low PGA levels even though $F_D(Sa(T))$ is significantly more severe. Moreover, the different values of the dispersion β_D expressed by (3.17), reflect the greater value of COV associated to PGA. Given the fragility function $F_d(PGA)$ and the probability of failures involved in structural regulations EN 1990 (2002), i.e. $P_d = 7.2 \times 10^{-5}$ for ultimate limit states and $P_d = 6.7 \times 10^{-2}$ for serviceability limit states, it is important to estimate the relative annual probability $P(edp)$ by means of Eq. (3.4): this read 1.38×10^{-5} . Nonetheless, we also calculated the leakage probability $P_n(edp)$ over the reference life of the LNG plant, i.e. 100 years by means of

$$P_n(edp) = 1 - (1 - P(edp))^n \quad (3.20)$$

where n defines the number of years. $P_n(edp)$ reads 1.4×10^{-3} and, compared to the aforementioned probability of failure values involved in EN 1990 (2002), we deduce that $P_n(edp)$ appears to be relatively high for LOC. It is worth noting that $P_n(edp)$ refers to the elbow of the pipeline connected to the pump column and located on the tank platform shown in Fig. 3.5. However, as stated in Subsection 3.3.5, the tank platform is characterized by 3 identical pump columns, each connected to one pipeline fitted with elbows. As a result, it is

reasonable to assume that the leakage probability $\widetilde{P}_n(edp)$ referred to all three pipelines must be higher than $P_n(edp)$. In particular, if one assumes that LOC is considered as an independent event in each pipeline, then it follows that $\widetilde{P}_n(edp) = 3 P_n(edp)$.

3.7 Conclusions

In this paper, we present a probabilistic seismic demand analysis of an LNG plant following the Performance-Based Earthquake Engineering procedure. In particular, first we evaluate the non-linear response of the whole LNG plant. Then we express the leakage risk of the most critical components of its pipeline network, i.e. elbows, by means of fragility functions. For this, we developed a mechanical model of bolted flange joints for leakage prediction, then calibrated by monotonic and cyclic joint testing. With regard to the seismic response of LNG plant components, we found that bolted flange joints are relatively safe under seismic action, whilst elbows exhibit a significant degree of vulnerability. Due to the complexity of LNG plant and the high computation demand by the FE model, we used the Cloud method for probabilistic seismic demand analysis. With regard to elbow response, we found that the maximum tensile hoop strain represents a suitable function for fragility analysis. Moreover, we show that fragility can be expressed as a function of peak ground acceleration of natural records. Nonetheless, the spectral acceleration evaluated at the period of the tank is more efficient due to the lower dispersion involved. The results of fragility functions of elbows, i.e. the probability of leakage over the reference life of the plant of about 1.4×10^{-3} , demonstrates that the examined plant characterized by a reference life of 100 years would be at risk. Therefore, an adequate pipework design for LNG plants subjected to strong earthquakes is needed, especially for piping components on top of tall tanks.

Finally, given the limited number of leakage data of elbows and the two unmodeled pipelines connected to the LNG pump columns, both the effects of uncertainty in leakage thresholds and the correlation among damage levels of critical elbows on fragility functions deserve further investigation.

3.A Additional research on the cyclic Response of Enhanced Bolted Flange Joints for Piping Systems

3.A.1 Introduction

Being one of the most common and essential components, BFJs are used nearly in all industrial piping systems, including in Oil & Gas plants which are considered as high-risk facilities (Raj and Lemoff, 2009). Although the proper functioning of BFJs is required to ensure the overall performance of such facilities and to avoid possible accidents, recent seismic events have showed a high vulnerability of piping systems and their components including these joints, which led to severe consequences both to the environment and human lives. Moreover, owing to the involvement of several components and their complex geometry, the behaviour of BFJs is complex and critical under seismic actions. Therefore, they need special attention and are deeply investigated as in (Zerres and Guerout, 2004). The work presented here is part of the large European research project INDUSE-2-SAFETY and is the natural continuation of a previous experimental test campaign (Reza et al., 2014), in which these joints were monotonically/cyclically tested under pure bending and axial loading.

In this respect, a recent experimental test campaign was carried out on a number of seismically enhanced BFJs. In particular, two non-standard BFJs, comparatively thinner than standard ones, i.e. with 18 mm and 27 mm flanges, were designed and their performance was evaluated through several monotonic and cyclic tests. These joints, in fact, were tested under combined loading, i.e. axial and shear, and with 3.2 MPa internal pressure. The choice of thinner and ductile BFJs was made to accommodate some ductility during a seismic event, thus helping to delay a brittle failure of piping systems (Reza et al., 2014). Experimental results exhibited a favourable performance of the examined joints under combined axial and shear loading and medium internal pressure; they showed a good capacity in terms of strength, ductility, energy dissipation and leakage. Successively, the leakage behaviour of BFJs was characterized both in terms of axial/shear stiffness and strength. As a result, a versatile and reliable model capable of predicting the leakage force on a generic BFJ, including the interaction between axial and shear loading, was conceived. The relevant results compared well with those provided by both actual and previous full scale experiments (Reza et al., 2014). Moreover, the model was adapted to predict leakage stiffness values for thick flanges. In sum, the proposed model can represent a promising tool for leakage prediction of BFJs adopted in piping systems of complex plants.



Figure 3.A.1 A typical BFJ and two thick standard flanges.

3.A.2 Experimental tests on Bolted Joints

Due to their complex geometry and the critical role in industrial piping systems, an experimental test campaign was performed on a number of non-standard BFJs in order to investigate their complex behaviour under seismic actions. In fact, in order to design a BFJ using standard flanges, proper required dimensions of flanges should be selected from tabulated values provided by standards, based on operating conditions and connecting pipe dimensions. In this case, the non-standard BFJs were designed in two steps: first, a flange was chosen from European standard 1092-1 (2007); then, the thickness of that flange was optimized and reduced according to EN 1998-1 (Eurocode 3 - Part 1-8, 2005), while retaining its other original dimensions. In particular, the non-standard BFJs were designed for a typical operating condition in petrochemical industries; temperature $-4/290^{\circ}$ and internal pressure 4 MPa. An 8'' pipe (outer diameter equal to 219.08 mm) with Schedule 40 (thickness equal to 8.18 mm) was selected as the connecting pipe. For this conditions, EN 1092-1 (2007) suggests to use a Type 1 flange with 36 mm of thickness and a total of 12 M27 bolts. In greater detail, the relevant design of non-standard BFJs is reported in Section 3.A.2.1.

3.A.2.1 Design of non standard Bolted Flange Joints

According to Eurocode 3-Part 1-8 (2005), a BFJ can exhibit three failure modes under tensile loading. In particular, Mode#1 and Mode#2 failures are associated with comparatively thinner flanges and strong bolts; these modes are capable of providing some ductility and dissipating energy through the formation of plastic hinges for large displacements. On the other hand, Mode#3 is a purely rigid failure mode owing to the presence of a thick plate and weak bolts. The first two failure modes were of our interest, as these exhibit ductility and energy dissipation during a strong earthquake. Hence, based on Eurocode 3, two optimized and reduced flange thicknesses were chosen, i.e. an 18 mm thick flange (Design 01) and a 27 mm (Design 02). The designed BFJs and relevant dimensions are presented both in Fig. 3.A.2 and Table 3.A.1. Required bolt lengths, l_b , for both the BFJs specimens were 115 mm and 134 mm, respectively. Groove welds were chosen to connect flanges to pipes.

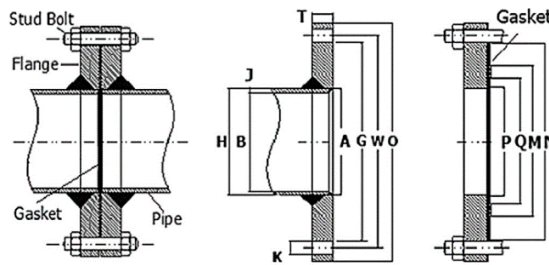


Figure 3.A.2 Non-standard BFJ

Table 3.A.1 Geometrical properties of non-standard BFJs (dimensions in mm).

<i>T</i>	<i>W</i>	<i>G</i>	<i>K</i>	<i>O</i>	<i>J</i>	<i>A</i>
36 (Standard)					8.1	221.
18 (Design 01)	320	290	30	375	8	5
27 (Design 02)						
<i>Bolts</i>	<i>B</i>	<i>H</i>	<i>P</i>	<i>Q</i>	<i>M</i>	<i>N</i>
M27 x 300	202.74	219. 1	216	228	248	290

3.A.2.2 Mechanical properties and testing equipment

Two different types of specimens were used for experimental tests. Test specimens were constructed by joining the two flange plates through bolted connection as shown in Fig. 3.A.3. The flange was welded to two pipe segments made of steel with grade P355N and with the same length; the overall length of specimens was 940 mm, much shorter than the tested specimens in (Reza et al., 2014) to avoid failures in specimen ends due to high bending moments. Moreover, in order to characterize mechanical properties of both flange and pipe materials, four tensile tests on pipe material coupons and two tensile tests on flange material coupons were conducted; average mechanical properties obtained from these tests are reported in Table 3.A.2. One may note that actual mechanical properties, i.e., yield f_y and ultimate f_u strengths, of the pipe material were found to be above their nominal values, i.e. $f_y = 355 \text{ MPa}$ and $f_u = 490 \text{ MPa}$; whereas, the actual yield strength of flange material was found below its nominal value, i.e. $f_y = 325 \text{ MPa}$. In addition, both the pipe and flange materials reached a favourable maximum level of elongation ϵ , which confirmed its good ductile behaviour at the material level. In order to avoid failure in the end welded connections, stiffeners were used in the two ends of specimens, which were welded to 300 mm thick plates, as illustrated in Fig. 3.A.3. The assembly bolt tightening torques of BFJs were calculated according to EN 1591-1 (2009) considering the minimum and maximum assembly gasket stresses. The load was applied on the specimens by means of two 1000 kN MOOG actuators in parallel as illustrated in Fig. 3.A.4. Finally, in order to stress the flange both with an axial and shear load, specimens were tested with an angle of 45° with respect to the load axis, as depicted in Fig. 3.A.3a and Fig. 3.A.4, respectively.

Table 3.A.2 Average mechanical properties of pipes/flanges.

<i>Material</i>	f_y [MPa]	f_u [MPa]	ϵ [%]
Pipe	415	533	18
Flange	325	508	20

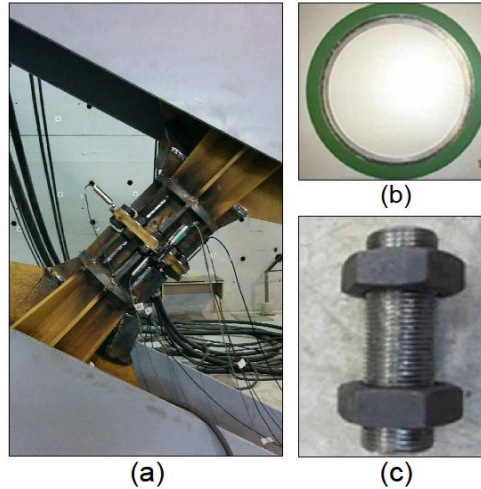


Figure 3.A.3 (a) Design 01 BFJ; (b) spiral wound gasket; (c) stud bolt.

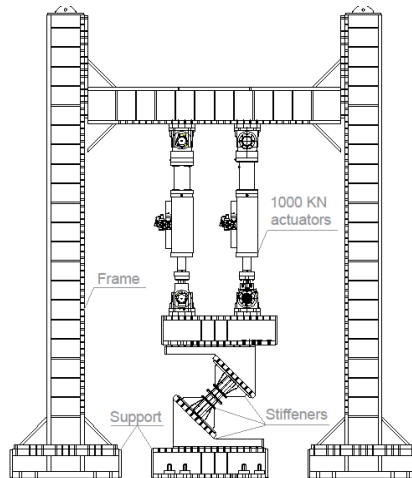


Figure 3.A.4 Test set-up for combined loading tests.

3.A.2.3 Test program

A total of four specimens tested under combined loading, i.e. axial and shear, as listed in Table 3.A.3, were tested at room temperature and under moderate internal pressure of 3.2 MPa. This pressure is equal to the regular operating pressure of a petrochemical industry. Both monotonic and cyclic tests were performed. First, monotonic tests were useful to characterize the elastic behaviour of the BFJ in order to estimate both an equivalent axial and shear stiffness for component-based modelling purposes and to find yield displacements for setting loading protocols for cyclic tests. Then, they were able to provide a leakage force value for a joint subjected to combined loading. On the other hand, cyclic tests were carried out to investigate strength, cyclic ductility, degradation and energy dissipation behaviour of joints.

Table 3.A.3 Test program of non-standard BFJs.

<i>No.</i>	<i>Test type</i>	<i>Test name</i>	<i>Loading protocol</i>	<i>BFJ</i>
1	Combined axial and shear	BF_18_Mo	Monotonic	Design 01
2	Combined axial and shear	BF_18_Cy	Cyclic	Design 01
3	Combined axial and shear	BF_27_Mo	Monotonic	Design 02
4	Combined axial and shear	BF_27_Cy	Cyclic	Design 02

3.A.2.4 Sensors and measurement devices

In order to estimate both axial and shear stiffness of the BFJ, each test specimen was provided with 8 displacement transducers to measure the gap in different points of the flange, as shown in Fig 3.A.5. In particular, 6 transducers were placed to measure the axial gap of the joint, while the transducers #16 and #17 were used to assess the relative shear displacements between the plates. To define an equivalent axial stiffness of the BFJ, see Fig. 3.A.6 in this respect, the equivalent axial displacement δ_s referred to a measuring section of the flange was defined as:

$$\delta_s = \left(\frac{\delta_1 + \delta_2}{2} \right) \quad (3.A.1)$$

Note that, to take into account the possible axial-shear interaction on the axial deformation of the joint, 4 values of δ_s were calculated, each for a specific measuring section. Thus, the equivalent axial displacement δ_{ax} was set equal to the average value among the different δ_s .

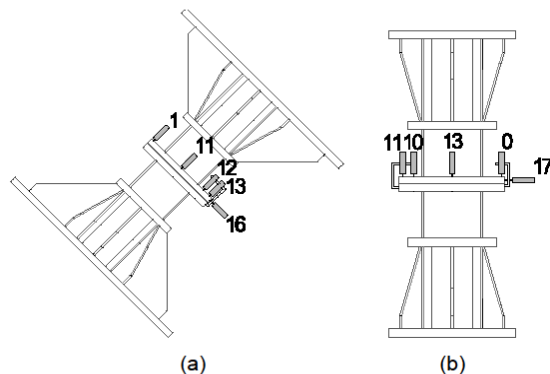


Figure 3.A.5 Placement of the both axial and shear displacement transducers in the Design_02-BFJ: (a) frontal view; (b) bottom view.

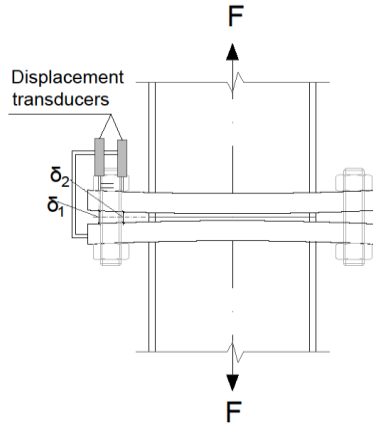


Figure 3.A.6 Definition of the equivalent axial flange displacement.

3.A.2.5 Test protocol

The cyclic loading procedures for the experiments were constructed according to the ECCS45 loading protocols (ECCS TC1 TWG 1.3, 1986). These loading procedures are based on the evaluation of a yielding displacement e_y , caused by a force, P_y corresponding to the conventional yield stress of the tested component. In the case of complete procedure, e_y is determined for the tension and compression parts, separately. In our case, being the specimens made of steel, we supposed e_y to be the same both in tension and in compression. See in this respect Fig. 3.A.7 that summarizes the suggestion by Bursi, Ferrario and Fontanari (2002). The cyclic test is designed as a displacement controlled one with the increase of amplitude of subsequent cycles at $e_y/4$, $e_y/2$, $3e_y/4$, e_y , $2e_y$, $(2 + 2n)e_y$ for $n = 1, 2, 3 \dots$. Nevertheless, to avoid the specimen buckling under compression loading, only the positive half of the load cycles was applied. Moreover, we were mainly interested to observe the opening behaviour of the BFJs, i.e. to estimate both an equivalent elastic axial and shear stiffness for component-based modelling purposes and to find the leakage force, for which the use of only tensile loading was appropriate.

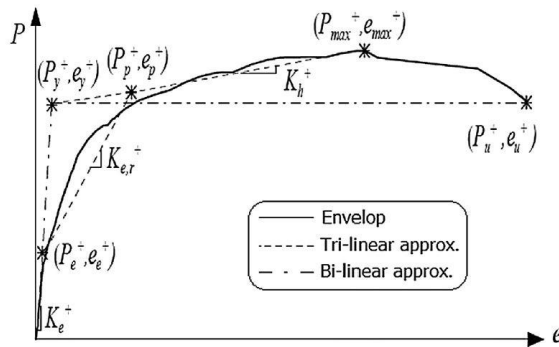


Figure 3.A.7 Bi-linear and tri-linear approximations of a non-linear response after Bursi et al. (2002).

3.A.2.6 Main observations and results

Performances in terms of leakage detection of designed BFJs were evaluated through four axial tests, under both monotonic and cyclic loading as reported in Table 3.A.3. Relevant results of the four tests in terms of yielding force and leakage force are reported in Table 3.A.4. Furthermore, load-displacement curves referred to resulting forces of both Design 01 and Design 02 BFJs for monotonic/cyclic tests are depicted in Fig. 3.A.8 and Fig. 3.A.9, respectively. Despite the fact that only tension loads were applied to avoid some buckling, a careful reader can note from Fig. 3.A.9 that about 600 kN of compressive load was required during both tests to bring actuators back to their neutral position, i.e., zero displacement. Note that specimens did not reach the failure because of the limited load capacity of the actuators to 2000 kN. Nevertheless, our main purpose was to provide values for leakage forces and equivalent elastic stiffness.

Table 3.A.4 Main experimental forces after testing.

<i>Test name</i>	F_y [kN]	F_{leak} [kN]	$N_{leak} = T_{leak}$ [kN]
BF_18_Mo	610	1175	830
BF_18_Cy	315	1100	785
BF_27_Mo	-	1000	710
BF_27_Cy	-	1470	1040

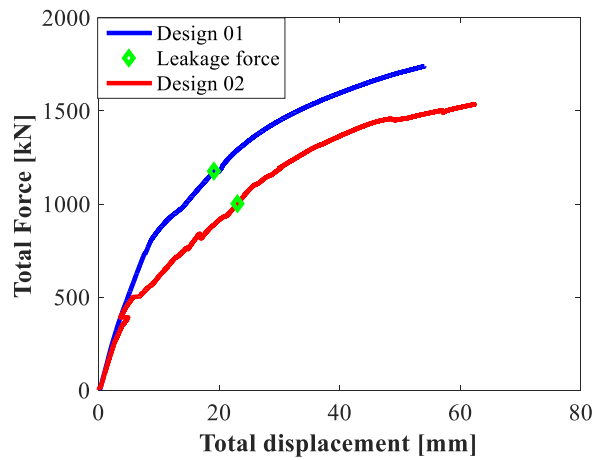


Figure 3.A.8 Load-displacement curves for monotonic tests and leakage force detection.

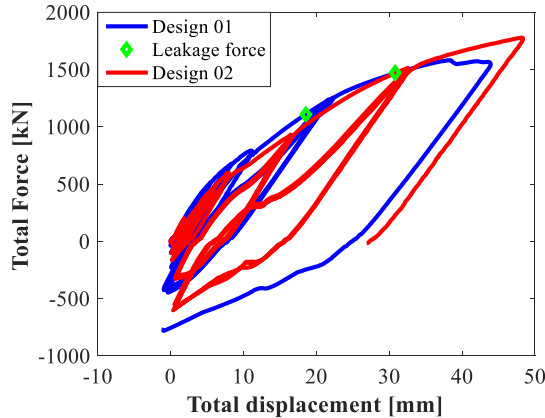


Figure 3.A.9 Load-displacement curves for cyclic tests and leakage force detection.

However, some considerations can be made about the leakage occurrence between this experimental test campaign, i.e. combined loading and high internal pressure, and tests in Reza et al. (2014), i.e. only axial loaded joints and moderate pressure. In particular, the leakage force in the Design 01 BFJ, $F_{leak} = 1170 \text{ kN}$, is almost equal to the force obtained in Reza et al. (2014), $F_{leak} = 1175 \text{ kN}$. In addition, considering the same specimen tested cyclically, in this test the leakage appears for smaller force, $F_{leak} = 1000 \text{ kN}$, than $F_{leak} = 1243 \text{ kN}$. On the other hand, both the different loading condition and the internal pressure seem to have a more severe influence on the Design 02 BFJ. In fact, the force to achieve the leakage in this test campaign, for the 27 mm thick flange tested cyclically, $F_{leak} = 1470 \text{ kN}$, is much smaller than the force found in Reza et al. (2014), $F_{leak} = 1812 \text{ kN}$. Moreover, it is important to note the different leakage occurrence between the tested joints, as shown in the two details in Fig. 3.A.10. Indeed, as a reader can note, in the case of Design 01 BFJ, the loss of containment seems to be less severe than the other case. This can be explained considering the different opening behaviour of the joints, see Fig. 3.A.6 in this respect, due to the different flange stiffness. In particular, in the Design 01 BFJ, the water comes out of the joint through the holes of bolts, drop by drop, due to the prying forces acting at the end of the flange. Conversely, because of a higher gap between the flange plates in the Design 02 BFJ, the pressured containment does not encounter obstacles and copiously comes out of the specimen.

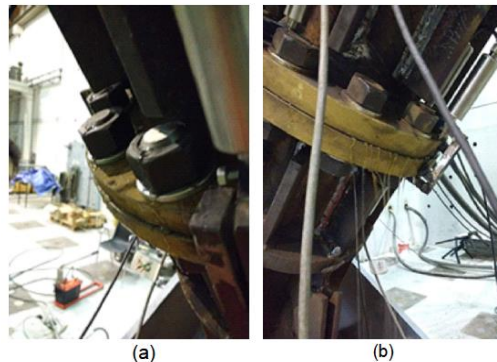


Figure 3.A.10 Details of the loss of containment through the joints: (a) Design 01 and (b) Design 02 BFJs.

3.A.3 Leakage characterization from experimental data

In order to avoid a complete analysis by means of an accurate modeling of a complex component like a BFJ, a simple procedure is proposed to model a BFJ by means of both an axial and a shear equivalent linear spring. In this respect, to characterize relevant spring stiffness of the joint, load-displacement curves referred to the flange are reported in Fig. 3.A.11 and Fig. 3.A.12. Note that an equivalent secant stiffness was evaluated and the experimental results are reported in Table 3.A.5. Once the values of the two stiffness and the leakage force limits are known for a generic BFJ, see Section 3.A.4 in this respect, one may model it by means of two linear springs and check if the leakage occurs. A detail of the deformed configuration of the BF_18_Mo specimen is reported in Fig. 3.A.13.

Table 3.A.5 Main experimental forces after testing.

<i>Test name</i>	k_{axial} [kN/mm]	$k_{trans.}$ [kN/mm]
BF_18_Mo	16600	1050
BF_27_Mo	5750	221

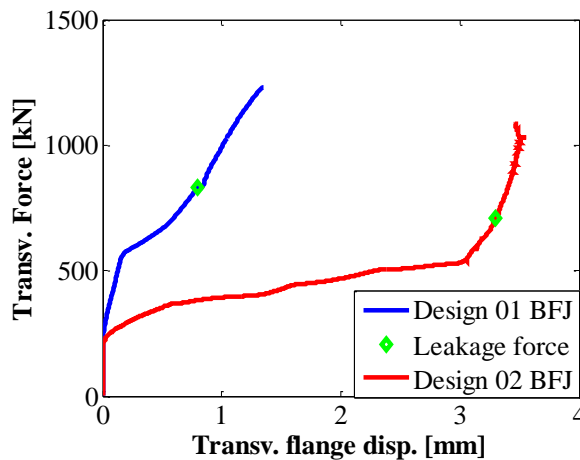


Figure 3.A.11 Flange load-displacement curves in the transverse direction for monotonic tests.

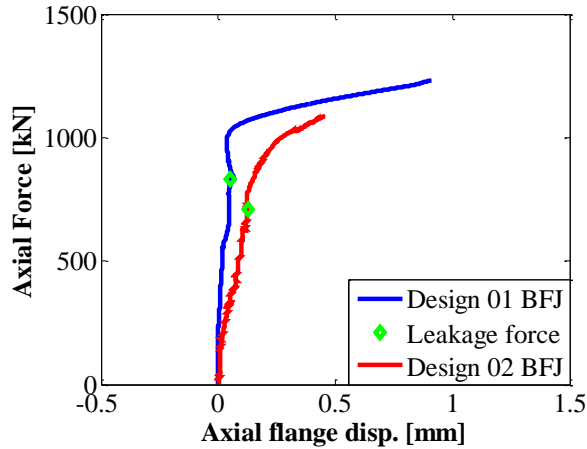


Figure 3.A.12 Flange load-displacement curves in the axial direction for monotonic tests.



Figure 3.A.13 Detail of the displaced configuration of the tested BF_18_Mo BFJ specimen

3.A.4 A parametric model for leakage prediction

3.A.4.1 The EN 1591-2009 standard for BFJ modelling

The EN 1591-2009 1-2 (2009) characterizes the behavior of a bolted joint equipped with a gasket between the metallic contact components. In addition, the method suggested in this standard is valid beyond a minimum flange thickness, so to ensure a uniform pressure distribution on the gasket (EN 1591-1, 2009). Note that in our case due to their thinner flange thickness, non-standard BFJs do not satisfy this condition. Nonetheless, a parametric model capable of predicting the leakage force of BFJs based on the assumptions of EN 1591 is proposed and validated herein.

In particular, the joint is modeled as depicted in Fig. 3.A.14.

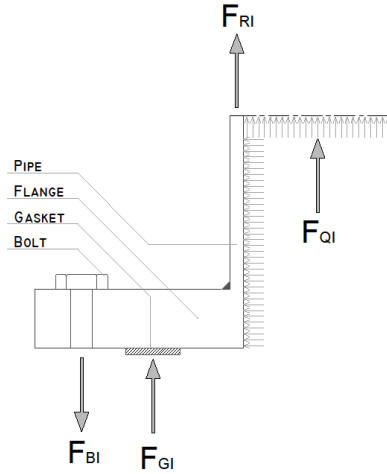


Figure 3.A.14 The BFJ model proposed by EN 1591-2009.

The aim of the calculation method described in the standard is to analyze the BFJ behavior for given load conditions and to check the admissibility of the BFJ at all the load conditions for a given initial bolt tightening. The calculation method is based on an axially symmetrical mechanical model, taking into account the whole flanges–bolts–gasket system behavior. It is not only based on an axial force balance, it also considers laws of rheology and deformation compatibility of the BFJ components. Three different flange configurations are treated in the EN 1591: integral flanges, loose flanges and collars and blank flanges. The flanges are considered as rectangular ring cross sections which remain undeformed. Flanges are treated in rotation. Shells connected to the flange rings may be cylindrical, conical or spherical. Connected shells are treated like equivalent cylindrical shells: the loads acting on the mechanical model are not only the bolt load, the end thrust effect due to the internal pressure and the reaction on the gasket, but also the radial effect of the internal pressure, the external forces and bending moments that may be applied to the flanges and the differential axial thermal expansion between bolts and flanges. The relations between loads and deformations for all the components, i.e. the flange rotation, the bolt elongation and the gasket compression, are reported in Eqs. (3.A.2)-(3.A.4), respectively.

$$\varphi_F = \frac{Z_F}{E_F} M_F \quad (3.A.2)$$

$$l_B = \frac{X_B}{E_B} F_B \quad (3.A.3)$$

$$e_G = \frac{-X_G}{E_G} F_G \quad (3.A.4)$$

In particular, Eq. (3.A.2) states that the flange rotation φ_F is related to the applied bending moment M_F by means of the flexibility rotational modulus Z_F and the Young's modulus of the flange E_F . In Eq. (3.A.3), the relation between the bolt elongation l_B and the applied axial load F_B by means of the flexibility axial modulus X_B and the Young's modulus of the bolts E_B is reported. Finally, Eq (3.A.4) states that the gasket shortening e_B is related to the compressive applied load on F_G by means of the flexibility modulus X_B and the Young's modulus of the gasket E_G .

From all these deformation terms, a deformation compatibility equation is established between the axial deformations of the bolts and the axial deformations at the gasket place, taking into account the flange rotation. In EN1591-1 the deformation compatibility equation is used between the initial state O which is the assembly condition and a subsequent load condition I . This relation combined with the axial forces balance leads to the following compliance equation:

$$\Delta_{0 \rightarrow I}(F_G Y_G) + \Delta_{0 \rightarrow I}(F_Q Y_Q) + \Delta_{0 \rightarrow I}(F_R Y_R) = 0 \quad (3.A.5)$$

In Eq. (3.A.5) Y_G , Y_Q and Y_R are the flexibility coefficients of the joint, in [mm/N], and are used to calculate the axial displacement due to the gasket force, the internal pressure and the resulting external loads, respectively (EN 1591-1, 2009). Moreover, the contribution of the differential thermal expansion among the elements was neglected. From this equation, F_G is determined at every load condition for a given initial tightening force. Finally, F_B is deduced from the axial force balance:

$$F_B = F_G + F_Q + F_R \quad (3.A.6)$$

As a result, the recommended initial bolt tightening force F_{B0} provided by EN 1591 is between a lower and an upper limit. The lower limit corresponds to the minimum force able to avoid leakage occurrences on the joint during both service and ultimate limit state conditions. This is obtained ensuring that the gasket pressure Q_G , due to F_G , is higher than the selected $Q_{G,lim}$ at every design load conditions I . Nonetheless, F_{B0} should not be higher than the overloading limit, which could cause damages on the joint due to excessive deformations.

3.A.4.2 A model to predict the leakage force on a bolted flange joint

The framework of the EN 1591 standard was used to develop a simple model able to predict, given a known initial bolt tightening, the leakage force of a generic BFJ. First we consider the equation of the joint compliance in the load condition I :

$$F_{GI}Y_{GI} + F_{QI}Y_{QI} + F_{RI}Y_{RI} + \Delta U_I = F_{G0}Y_{G0}P_{QRI} \quad (3.A.7)$$

In particular, we considered the load on the gasket, due to the initial tightening force, as the only load acting in the condition 0. As a result, the relation to obtain F_{G0} states:

$$F_{G0} = \sigma_{G0}A_{Ge} = \sum_{n^\circ \text{ bolts}} F_{tor} = \sum_{n^\circ \text{ bolts}} \frac{M_{torq}}{0.18 * d} \quad (3.A.8)$$

In Eq. (3.A.8), F_{tor} is the axial force on one bolt of diameter d due to the initial tightening moment, M_{torq} . After some calculations, one can obtain the pressure on the gasket in a generic condition and compare it to the limit provided by the standard in order to prevent the leakage occurrence. In particular, assuming the thermal expansion coefficients $\alpha_B = \alpha_F = \alpha_G$ as equal, i.e. neglecting the term ΔU_I , the leakage will arise in the joint when the inequality in Eq. (3.A.9) is satisfied:

$$\sigma_{GI} = \frac{\sum F_{tor}Y_{G0}P_{QRI} - \frac{\pi}{4}d_{Ge}^2F_{QI}Y_{QI} - F_{RI}Y_{RI}}{Y_{GI}A_{Ge}} \leq Q_{s,min,I}^{(L)} \quad (3.A.9)$$

In Eq. (3.A.9), $Q_{s,min,I}^{(L)}$ is the minimum compressive pressure on the gasket need to avoid the loss of containment from the BFJ related to the chosen level L . In fact, this value is provided by (EN 1591-2, 2009) and depends on the amount of the allowed rate of leakage. Hence, the minimum resulting external force for the leakage occurrence states:

$$F_{RI} \geq \frac{\sum F_{tor}Y_{G0}P_{QRI} - \frac{\pi}{4}d_{Ge}^2F_{QI}Y_{QI} - Q_{s,min,I}^{(L)}Y_{GI}A_{Ge}}{Y_{RI}} \quad (3.A.10)$$

A dimensionless equation can be easily derived from Eq. (3.A.10) in order to estimate a value for the equivalent axial force acting on a generic BFJ, i.e. changing its geometric/mechanical parameters and initial/service load conditions, able to produce some leakage phenomena. Introducing three dimensionless factors, see Eqs. (3.A.11-12-13), the condition to reach the leakage is written in Eq. (3.A.14).

$$\alpha = \frac{4 \sum F_{tor}P_{QRI} Y_{G0}}{\pi d_{Ge}^2 F_{QI} Y_{QI}} \quad (3.A.11)$$

$$\beta = \frac{4 Q_{s,min,I}^{(L)} b_{Ge} Y_{GI}}{d_{Ge} F_{QI} Y_{QI}} \quad (3.A.12)$$

$$f = \frac{4 F_{RI} Y_{RI}}{\pi d_{Ge}^2 F_{QI} Y_{QI}} \quad (3.A.13)$$

$$f \geq \alpha - \beta - 1 \quad (3.A.14)$$

As a careful reader can see from the definition of Eqs. (3.A.11-12), both the factors α and β include both geometrical and mechanical parameters of the BFJ and gasket information by means of the compliance coefficients Y_{G0} , Y_{GI} and Y_{QI} . Moreover, the pressure inside the joint P , and the initial load state induced by the tightening moment on bolts $\sum F_{tor}$, are taken into account. On the other hand, f is proportional to the flexibility modulus Y_{RI} . Once the dimensionless parameters α and β are calculated for a generic BFJ, then f and the minimum axial force need to observe leakage F_{RI} are easily obtained. Both a numerical and a graphical comparison between the prediction of the axial leakage force of ASML18 in Reza et al., 2014, i.e. on a BFJ with the plate thickness of 18 mm and subjected to pure axial load, and the actual experimental tests are reported in Table 3.A.6 and in Fig. 3.A.15, respectively.

Table 3.A.6 Prediction of the axial leakage force for ASML18 in Reza et al., 2014 and comparison with experimental result.

Test	α [-]	β [-]	f [-]	F_{leak} [KN]
Model	16.63	0.30	15.33	1057
ASML18			16.97	1170

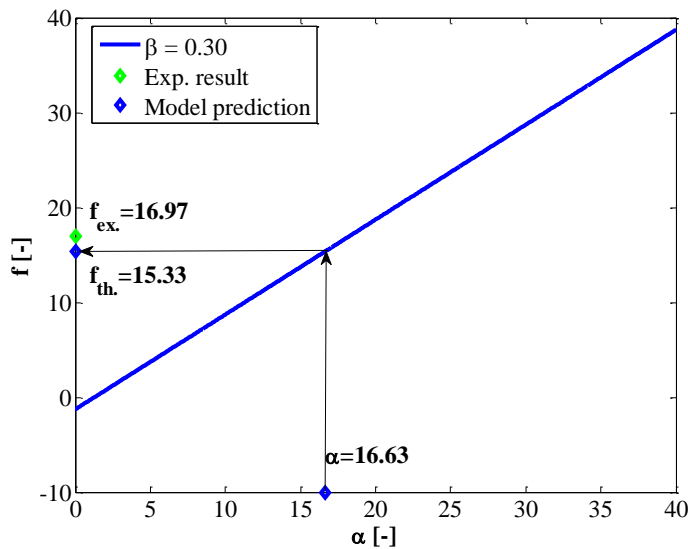


Figure 3.A.15 Comparison between the predicted axial force of ASML18 in Reza et al., 2014 and the experimental result.

The model seems to predict in a satisfactory manner the actual results. Moreover, in order to provide a useful tool for an easy and quick reference, two different BFJs are studied and their results are shown in Fig. 3.A.16.

Beyond the scope of providing a simple model to estimate the resulting axial leakage force for a generic BFJ, the experimental test campaign presented in this paper had the aim of studying and possibly characterizing the interaction between the axial and shear loads.

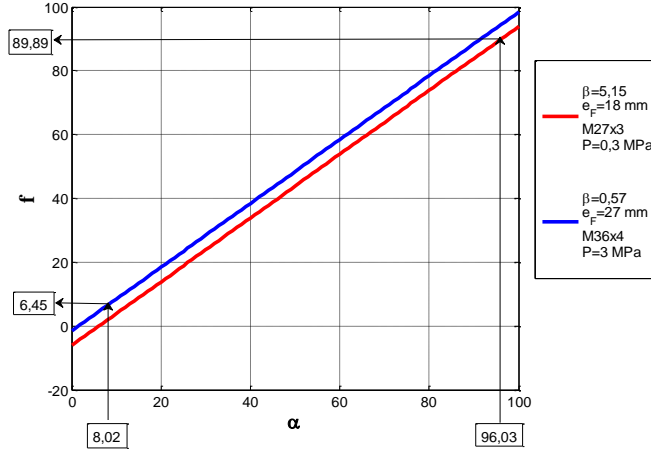


Figure 3.A.16 Examples of the axial leakage force prediction for different BFJs.

In this respect, the specimens were tested under combined loading, as depicted in Fig 3.A.4. First, we made a hypothesis about the leakage force for a BFJ subjected only to a shear load. According to Tate and Rosenfeld, an estimate of the equivalent shear stiffness K_S for a BFJ with an equal thickness of plates t is provided in Eq. (3.A.15):

$$\frac{1}{K_S} = \frac{10t^3}{24E_b I_b} + \frac{4t}{3A_b G_b} + \frac{2tE_f}{t^2 E_f^2} \quad (3.A.15)$$

In Eq. (3.A.15), the first and the second term of the right hand side refer to the bending and to the shear compliance of the bolt, respectively, while the third term is related to the bearing compliance of plates. Since the equivalent shear stiffness K_S reaches very high values, e.g., considering a BFJ section with the plate thickness of 18 mm and one bolt M27, $K_S = 635 \frac{KN}{mm}$, the shear force causing the leakage occurrence on a BFJ is supposed to be equal to the bolt shear strength T_u . In particular, according to EN 1998-1 (2005), the equation to calculate T_u states:

$$T_u = n * \frac{0.6 * f_u * A_{res}}{\gamma_{M2}} \quad (3.A.16)$$

where n is the number of bolts, f_u and A_{res} are the axial strength and the resistance area referred to one bolt, respectively, while γ_{M2} is a safety coefficient set equal to one. In Fig 3.A.17, both the axial and shear values causing the leakage during the BF_Mo_18 test are reported. Moreover, the values T_u and $N_u = F_{RI}$ are calculated from the relevant theoretical models, see Eqs. (3.A.16) and (3.A.13-14) in this respect, considering the same BFJ. Based on the results shown in Fig. 3.A.17, we choose to approximate the relation between the combined axial and shear leakage load as linear. Hence, introducing the parameter $\rho = T_u/N_u$, the N-T relation reads:

$$T = (N_u - N)\rho \quad (3.A.17)$$

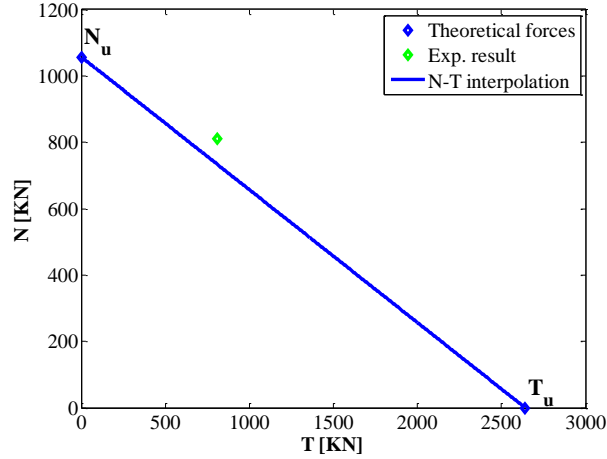


Figure 3.A.17 Axial and shear leakage forces after Design 01 for the BFJ monotonic test.

It is worth to note that the experimental result of Fig. 3.A.17 refers to a BFJ with an inclination $\vartheta = 45^\circ$ respect to the force direction, as depicted in Fig. 3.A.18. On the other hand, N_u and T_u refer to the same BFJ with an inclination $\vartheta = 0^\circ$ and $\vartheta = 90^\circ$, respectively.

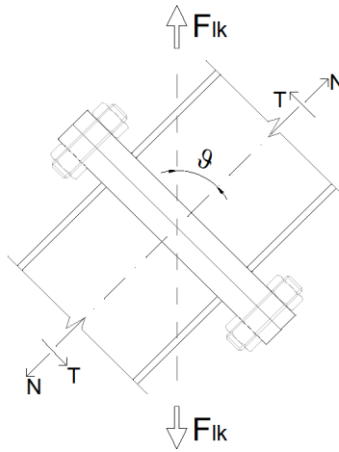


Figure 3.A.18 Sketch of an inclined BFJ.

Moreover, in order to provide a simple dimensionless model, we can easily obtain both the axial and the shear load for a generic inclined BFJ, see Fig. 3.A.18, subjected to the leakage force $F_{lk}(\vartheta)$:

$$\begin{cases} N(\vartheta) = F_{lk}(\vartheta)\cos\vartheta \\ T(\vartheta) = F_{lk}(\vartheta)\sin\vartheta \end{cases} \quad (3.A.18)$$

From Eq. (3.A.18), and recalling Eq. (3.A.17), we obtain:

$$\tan\vartheta = \frac{\rho T(\vartheta)}{\rho N_u - T(\vartheta)} \quad (3.A.19)$$

Thus, introducing the dimensionless variable $v = N/N_u$ and $\tau = T/T_u$, Eq. (3.A.19) reads:

$$\tan\vartheta = \frac{\rho\tau(\vartheta)}{1 - \tau(\vartheta)} \quad (3.A.20)$$

From Eq. (3.A.20), we are able to link a generic BFJ inclination ϑ and the relative dimensionless shear load τ coming from the leakage force $F_{lk}(\vartheta)$. Finally, a simple graph can be derived as shown in Fig. 3.A.19.

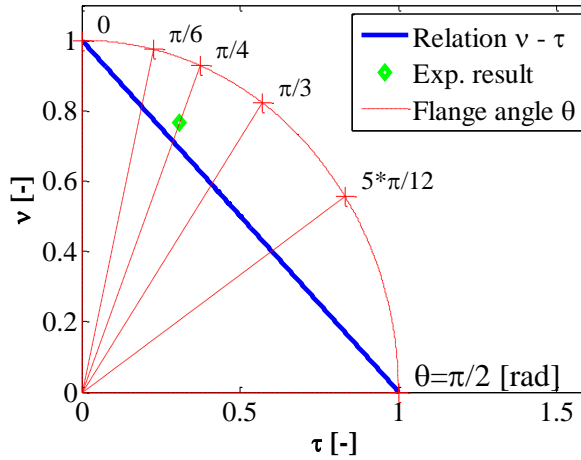


Figure 3.A.19 Sketch of an inclined BFJ.

3.A.4.3 The BFJ stiffness provided by the EN 1591-2009 standard

By means of the compliance factor Y_{RI} provided by the EN 1591 standard, the analytical axial stiffness for a BFJ is obtained. In fact, the total axial displacement of the joint is calculated as the sum of two terms, i.e. u due to the bolt elongation and v due to flange rotation, as depicted in Fig. 3.A.20. In particular, for a half of the BFJ, one gets:

$$u = \frac{X_B}{E_{BI}} F_{RI} \quad (3.A.21)$$

$$v = \frac{Z_F}{E_{FI}} F_{RI} * m \left(m - \frac{m+n}{2} \right) \quad (3.A.22)$$

where Z_F and X_B represent the rotational flexibility modulus of the flange and the axial flexibility modulus of bolts, respectively. A comparison between the experimental results and analytical prediction in the leakage condition of Design 02 BFJ are reported in Table 3.A.7. The axial stiffness $k_{an.}$ of BFJ provided by UNI 1591 standard differs from the relevant experimental value due to the flange rotation as depicted in Fig. 3.A.20.

Table 3.A.7 Comparison between experimental and theoretical results at leakage after Design 02 test.

<i>Test name</i>	δ_s [mm]	$k_{exp.}$ [kN/mm]	$u_{an.}$ [mm]	$v_{an.}$ [mm]	$k_{an.}$ [kN/mm]
BF_27_Mo	0.13	5750	0.04	0.32	1050

However, it is worth to note that the model offered by EN 1591 does not take into account the axial/shear interaction and is valid only for standard (thick) BFJs. As a result, the capability of this model of predicting the leakage stiffness, especially for thin BFJs, requires further investigations.

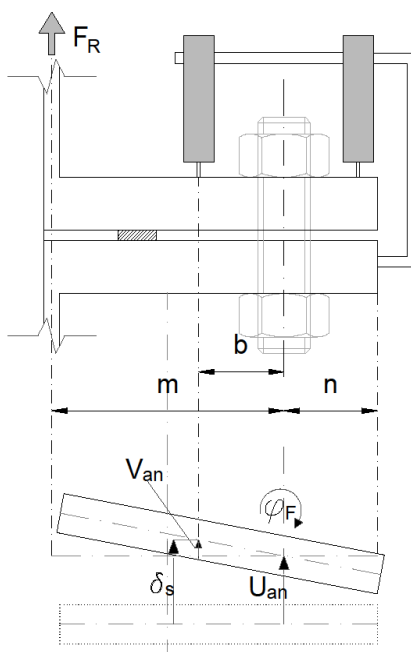


Figure 3.A.20 Model for the joint axial stiffness evaluation.

3.A.5 Conclusions

Two seismically enhanced –thin and thick- bolted flange joints (BFJs) were designed on the base of the structural Eurocode 3, Part 1-8 (2005), and their performance was examined through a number of monotonic and cyclic tests. In particular, as the natural continuation of a previous experimental test campaign, the BFJs were tested under combined loading, i.e. axial and shear, with 3.2 MPa of internal pressure. Experimental results displayed a favourable performance of both joints in terms of leakage, ductility and energy dissipation. Moreover, the BFJs exhibited a favourable energy dissipation capacity and almost no degradation was observed under cyclic loading. Successively, specific values of both stiffness and strength, with reference to leakage, were estimated. Then, a reliable model capable of predicting the leakage force for a generic BFJ, including the interaction between

the axial and shear load was proposed and validated; both actual and previous full scale experimental data were involved in the validation. As a result, the values predicted by the model agreed well with those obtained by the full scale experiments. As a result, the proposed analytical model can represent a wide and promising tool for the prediction of the leakage force of complex piping systems. The extension of this model to the prediction of leakage stiffness, especially for thin BFJs, deserve further studies.

Summary, conclusions and future perspectives

Summary

Natural hazards such as earthquakes can cause severe damages to the environment and the community. On the other hand, “special risk” industrial plants and components are considered with particular attention for their strategic importance and heavy consequences both to the environment and human lives. In fact, according to the French environmental code (articles R. 563-1 to R. 563-8, 1991), “special risk” structures refer to facilities for which damage is severe also on their personnel and consequences can exceed the immediate vicinity of these structures. As a result, for these kind of plants, there is the need of a probabilistic risk analysis for seismic hazard and justifications by owners about the maintenance of safety functions in the case of specific earthquakes. Then, in order to prevent or limit incidents due to earthquakes in “special risk” plants and facilities, in this thesis different strategies were proposed and validated through theoretical, analytical and experimental investigations.

In the first part of the thesis a broad fuel storage tank, which poses a significant threat to the community and the environment, was considered as a case study for the design of a metamaterial-based foundation. The materials employed in the foundation are concrete and construction grade silicon, which are commonly used in construction industry. Given the critical frequency region of seismic vibrations for the structure of interest, a unit cell was designed with the aid of a frequency dispersion analysis to cover critical frequencies by means of a stop band. Then, a finite lattice structure was extracted from the infinite lattice of unit cells and was checked on its static behaviour at the ultimate limit state (EN 1990, 2004). Finally, the coupled (foundation + structure) system was numerically tested and the influence of cracks on the dynamic properties of the proposed foundation was also investigated.

The second part of the research activity aimed to improve the seismic risk assessment of “special risk” industrial plants through experimental dynamic analysis methods. First, the basic algorithms of the state-of-the-art experimental simulation methods were summarized. Then, a comparison of their performances in terms of uncertainty propagation was presented with the scope to explore their possible fusion in a new combined method. In particular, Section 2.2 illustrated the newly conceived composite experimental dynamic substructuring (C-EDS) method, which relies on partitioned algorithms for connecting multiple substructures of heterogeneous systems with a dual approach. Moreover, since various experimental sources of uncertainty affect the measured PS response, a comparative uncertainty propagation analysis was presented based on Monte-Carlo Simulation (MCS) of all described EDS algorithms considering a 5-DoFs benchmark system and probability distributions of main sources of uncertainty characterized after laboratory measurements. Then, in order to highlight the feasibility of the C-EDS method in combining radically different EDS algorithms, a virtual experiment was numerically conducted on a

petrochemical prototype plant case study. As a result, versatility and advantages of fusing both online/offline methods were demonstrated. Finally, the Annex 2.A described the experimental testing campaign conducted on the previously considered realistic case study where most of the earlier treated concepts have found a real application.

The last part of the thesis analysed the seismic performance of a liquefied natural gas (LNG, ethylene) terminal, consisting in a series of process facilities connected by pipelines of various sizes, within the Performance-Based Earthquake Engineering (PBEE) framework. Particular attention was paid to component resistance to leakage and loss of containment, even though several different limit states were investigated. The LNG tank, support structures and pipework, including elbows and flanges, were analysed with a detailed 3D finite element model. For this purpose, a novel mechanical model to predict the leakage limit state of generic bolted flange joints (BFJs) was developed. Given the complexity of the FE model of the LNG plant, the Cloud method for probabilistic seismic demand analysis was selected, due to its advantages in terms of consistency in the seismic input and of computational savings. In particular, in order to develop fragility curves of critical components, such as elbows and BFJs, a set of 36 ground motions from a database of historic earthquake accelerations was selected and used for a series of nonlinear time history analyses. Finally, the Annex 3.A presented in detail the experimental testing campaign and the relevant theoretical assumptions used for the development of the novel mechanical model able to predict the leakage phenomena resistance of a generic BFJ, taking into account the possible interaction between shear and axial forces.

Conclusions

In order to check the feasibility of a metamaterial-based foundation for seismic application, a smart foundation was conceived in the first part of the thesis, designed and also checked for gravity loads. As a result, it was found that such a structure can be realized in accordance with the Eurocode standards while maintaining favourable band-gap like properties against seismic waves. In particular, two versions of the smart foundation bearing a fuel storage tank with a varying fluid level were designed and it was shown that the proposed designs can attenuate the resulting frequency range. In addition, the shear stiffness of the foundation due to lateral concrete walls displayed to have a significant impact on the attenuation efficiency, and, subsequently, an optimized design, where the walls were replaced with less stiff concrete columns was proposed.

The second part of the research activity was centered upon the comparison and the generalized use of online and offline methods for Experimental Dynamic Substructuring (EDS). With this perspective, a comprehensive uncertainty propagation analysis of experimentally-based online/offline dynamic substructuring methods was investigated. In particular, the performance comparison included the following methods: the online Hybrid (numerical/physical) Dynamic Substructuring (HDS) method and two offline methods, i.e. the Impulse-Based Substructuring method (IBS) and the Receptance-Based Substructuring

(RBS) method. This investigation also explored the possibility of a combined exploitation of the three techniques, the novel composite (C-EDS) method, both to improve and accelerate the execution of the experiment/simulation. In this respect, we described the main characteristics of three EDS methods, which include the coupling algorithms based on dual assembly of Physical and Numerical Subdomains (PS and NS, respectively) performed with a localized version of the Lagrange multiplier method. Furthermore, we introduced the methods, through which uncertainties related to the various simulation methods can be accounted for and quantified; thus, a five-DoF linear/non-linear chain-like system was examined by including typical uncertainties emerging from measurements errors and laboratory operators. The simulation results, presented in terms of statistics of both NRMSE and NEE scores, suggested that the RBS method exhibits a better performance in the linear case, whilst, all methods are equivalent in the nonlinear regime. Finally, capitalizing from the results of a more complex case study composed of a virtual petrochemical prototype plant, a feasible approach to employ the C-EDS method along with a comprehensive verification was provided. In particular, a linear PS -a piping- and a non-linear PS -four isolating devices- were coupled to a linear NS – a slender tank-. The comparison between substructuring and reference results, obtained from a monolithic model of the system, were satisfactory.

In the last part of the thesis, a probabilistic seismic demand analysis of an LNG plant following the Performance-Based Earthquake Engineering procedure was presented. First, the non-linear response of the whole LNG plant was evaluated. Then, the leakage risk of the most critical components of its pipeline network, i.e. elbows and bolted flange joints, was expressed by means of fragility functions. For this, a mechanical model of bolted flange joints for leakage prediction, was developed and calibrated by monotonic and cyclic joint testing. Regarding the seismic response of LNG plant components, the bolted flange joints were found relatively safe under seismic action, whilst elbows exhibited a significant degree of vulnerability. Due to the complexity of LNG plant and the high computation demand by the FE model, the Cloud method for probabilistic seismic demand analysis was used. With regard to elbow response, it was found that the maximum tensile hoop strain represents a suitable function for fragility analysis. Moreover, it was showed that fragility can be expressed as a function of peak ground acceleration of natural records. Nonetheless, the spectral acceleration evaluated at the period of the tank is more efficient due to the lower dispersion involved. The results of fragility functions of elbows, i.e. the probability of leakage over the reference life of the plant of about 1.4×10^{-3} , demonstrates that the examined plant characterized by a reference life of 100 years would be at risk. Therefore, an adequate pipework design for LNG plants subjected to strong earthquakes is needed, especially for piping components on top of tall tanks.

Future perspectives

Though the proposed smart foundation was able to attenuate the impulsive frequencies of the fuel storage tank under different liquid levels, it cannot yet be considered as a fully optimized solution. In particular, the dynamic behavior of the system with other liquid levels

needs to be investigated, as well as the performance of the coupled system under several seismic waves. Moreover, soil–structure interaction has to be taken into account; especially for the benefit that soil flexibility can entail for vertical seismic excitations or vertical motions of the coupled (foundation + tank) system. Lastly, given the main drawback of standard isolators, i.e., the inherent high vertical stiffness, it is expected that the use of the investigated foundation for large structures characterized by rocking motion can reveal great innovative potential and undiscovered advantages.

Encouraged by the results presented in the second part of the thesis, the C-EDS method is suitable for being applied to an actual prototype plant in the laboratory.

Finally, in the last part of the thesis, given the limited number of leakage data of elbows and the two unmodeled pipelines connected to the LNG pump columns, both the effects of uncertainty in leakage thresholds and the correlation among damage levels of critical elbows on fragility functions deserve further investigation.

Bibliography

G. Abbiati, O.S. Bursi, O.S., P. Caperan, L. Di Sarno, F.J. Molina, F. Paolacci, P. Pegon, Hybrid simulation of a multi-span RC viaduct with plain bars and sliding bearings, *Earthquake Engineering & Structural Dynamics*, DOI: 10.1002/eqe.2580, 2015.

Abbiati G., Bursi O. S., Caracoglia L., di Filippo R., La Salandra V., 2016. Probabilistic Seismic Response of Coupled Tank-Piping Systems. Proceedings of the ASME 2016 Pressure Vessels & Piping Conference. PVP 2016, Vancouver, British Columbia, Canada, July 17-21, 2016.

Achaoui, Y., Ungureanu, B., Enoch, S., Brûlé, S., and Guenneau, S., (2016). Seismic waves damping with arrays of inertial resonators. *Extreme Mechanics Letters* 8, 30-37. <http://dx.doi.org/10.1016/j.eml.2016.02.004>

ANSYS Mechanical Software by ANSYS, Inc. 2015, Southpointe 2600 ANSYS Drive Canonsburg, PA 15317 USA

Antonioni G., Spadoni G., Cozzani V., 2007. A methodology for the quantitative risk assessment of major accidents triggered by seismic events. *Journal of Hazardous Materials* 147, 48–59.

ASME. Boiler and Pressure Vessel Code Section VIII. New York, USA: American Society for Mechanical Engineers; 2004.

ASME PCC-1-2010. Guidelines for pressure boundary bolted flange joint assembly, American Society of Mechanical Engineers.

Baesi S., Abdolhamidzadeh B., Hassan R., Hamid M. D., 2013. Application of a multi-plant QRA: A case study investigating the risk impact of the construction of a new plant on an existing chemical plant's risk levels *J. Loss Prev. Process Ind.*, 26 (5), 924-935.

Baker JW, 2015. Efficient Analytical Fragility Function Fitting Using Dynamic Structural Analysis. *Earthquake Spectra*. Vol. 31, No. 1, pp. 579-599.

Barka, A., (1999). The 17 August 1999 Izmit Earthquake. *Science* 285:5435, 1858-1859. doi: 10.1126/science.285.5435.1858

Barros da Cunha S., 2016. A review of quantitative risk assessment of onshore pipelines. *Journal of Loss Prevention in the Process Industries* 44, 282-298.

Belakroum, R., Kadja, M., Mai, T., and Maalouf, C., (2010). An efficient passive technique for reducing sloshing in rectangular tanks partially filled with liquid. *Mechanics Research Communications* 37:3, 341-349. doi: 10.1016/mechrescom.2010.02.003

Bernal, D. (1994). Viscous Damping in Inelastic Structural Response. *Journal of Structural Engineering*, 120(4), 1240–1254.

Bonelli, A., OS Bursi, Generalized-alpha Methods for Seismic Structural Testing, *Earthquake Engineering & Structural Dynamics*, 2004, 33, 1067-1102.

Brillouin, L., 1953. *Wave propagation in periodic structures*, 2nd ed.. new york: dover.

Brinnel V., Schaffrath S., Münstermann S., Feldmann M., 2016. Validation of a Concept for Burst Pressure Prediction by Damage Mechanics. Proceedings of the ASME 2016 Pressure Vessels & Piping Conference PVP. PVP2016, Vancouver, British Columbia, Canada, July 17-21, 2016.

Bursi O. S., Reza Md S., Abbiati G., Paolacci F., 2015a. Performance-based earthquake evaluation of a full-scale petrochemical piping system. *Journal of Loss Prevention in the Process Industries*, 33, pp. 10-22.

Bursi O. S. et al. 2015b, Report on seismic hazard for seismic input selection, Deliverable 1.2, INDUSE-2-SAFETY, Grant No. RFSR-CT-2014-00025.

Bursi et al., 2016a, Report on mechanical characterization of selected steel for cyclic loading and temperature sensitivity, Deliverable 4.1, INDUSE-2-SAFETY, Grant No. RFSR-CT-2014-00025.

Bursi, O. S., Reza S. et al., 2016b, "Component Fragility Evaluation, Seismic Safety Assessment and Design of Petrochemical Plants Under Design-Basis and Beyond-Design-Basis Accident Conditions", Mid-Term Report, INDUSE-2-SAFETY Project, Contr. No: RFS-PR-13056, Research Fund for Coal and Steel.

Bursi O.S. and D. J. Wagg, Eds. - *Modern Testing Techniques for Structural Systems Dynamics and Control* , CISM-Springer Wien NewYork 2008.

Bursi, O.S., Gonzalez-Buelga, A., Vulcan, L., Neild S.A. and Wagg, D. J., Novel coupling Rosenbrock-based algorithms for real-time dynamic substructure testing", *Earthquake Engineering and Structural Dynamics*, 37, 339-360, 2008.

Bursi, O.S., Abbiati, G., Cazzador, E., Pegon, P., Molina, F.J. "Nonlinear heterogeneous dynamic substructuring and partitioned FETI time integration for the development of low-discrepancy simulation models", *Int. J. for Numerical Methods in Eng.*, 2017, DOI: 10.1002/nme.5556.

Bursi, O.S., Abbiati, G., Reza M.S., A Novel Hybrid Testing Approach for Piping Systems of Industrial Plants. *Smart Structures and Systems*", Vol. 14, N. 6, 1-26, 2014.

Bursi, O.S., Ferrario, F., & Fontanari V. (2002). Non-linear analysis of the low-cycle fracture behaviour of isolated tee stub connections. *Computer & Structures*, 80, 2333-2360.

Bursi, O.S., Jia, C., Vulcan, L., Neild, S.A. and Wagg D.J. (2011), "Rosenbrock-based algorithms and 12 subcycling strategies for real-time nonlinear substructure testing", *Earthquake Engineering & Structural Dynamics*, 40, 1, 2011, 1-19.

Campedel M., Cozzani V., Garcia-Agreda A., Salzano E., 2008. Analysis of major industrial accidents triggered by natural events reported in the principal available chemical accident databases. JRC Scientific and Technical Reports, EUR 23391 EN -2008

Carta, G., Brun, M., and Movchan, A. B., (2014). Dynamic response and localization in strongly damaged waveguides. *Proceedings of the Royal Society A* 470:2167. doi: 10.1098/rspa.2014.0136

Carta, G., Movchan, A. B., Argani, L. P., and Bursi, O. S., (2016). Quasi-periodicity and multi-scale resonators for the reduction of seismic vibrations in fluid-solid systems. *International Journal of Engineering Science* 109, 216-239. doi: 10.1016/j.jengsci.2016.09.010

Cheng, Z., Yan, Y. Q., Menq, F.-Y., Mo, Y. L., Xiang, H.J., Shi, Z. F., and Kenneth, H. S., (2013). 3D Periodic Foundation-based Structural Vibration Isolation. *Proceedings of the World Congress on Engineering*, 3-5 July.

Cheng, Z. and Shi Z., (2017), Composite periodic foundation and its application for seismic isolation, *Earthquake Engineering Structural Dynamics*, 1 – 20.

Cheng, Z., and Zhifei, S., (2013). Novel composite periodic structures with attenuation zones. *Engineering Structures* 56, 1271-1282. <http://dx.doi.org/10.1016/j.engstruct.2013.07.003>

F. Chinesta, A., Leygue, F., Bordeu, J.V., Aguado, E. Cueto, D. Gonzalez, I. Alfaro, A., Ammar, A., Huerta, PGD-Based Computational Vademecum for Efficient Design, Optimization and Control, *Archives of Computational Methods in Engineering*, 2013, 20:31–59.

Cornell CA, Krawinkler H. 2000. Progress and challenges in seismic performance assessment. PEER Center News, <http://peer.berkeley.edu>.

Cornell, C.A, Jalayer, F, Hamburger, R.O, and Foutch, D.A. 2002. Probabilistic Basis for 2000 SAC Federal Emergency Management Agency Steel Moment Frame Guidelines. *ASCE Journal of Structural Engineering*, 128:4, 526-533.

Cozzani V, Antonioni G., Landucci G., Tugnoli A., Bonvicini S., Spadoni G., 2014. Quantitative assessment of domino and NaTech scenarios in complex industrial areas, *Journal of Loss Prevention in the Process Industries* 28, 10-22

A. Culla, W. D'Ambrogio, A. Fregolent, Parametric approaches for uncertainty propagation in SEA, *Mechanical Systems and Signal Processing*, Volume 25, Issue 1, January 2011, Pages 193-204

D'Ambrogio, W., & Fregolent, A., Direct hybrid formulation for substructure decoupling. In *Topics in Experimental Dynamics Substructuring and Wind Turbine Dynamics*, Volume 2, 2012 (pp. 89-107). Springer New York.

D'Ambrogio, W., A. Fregolent, Effect of uncertainties on substructure coupling: Modelling and reduction strategies, *Mechanical Systems and Signal Processing*, Volume 23, Issue 3, April 2009, Pages 588-605

D. de Klerk, D. Rixen, S. Voormeeren, General framework for dynamic substructuring: history, review and classification of techniques, *AIAA Journal* 46 (5), 1169–1181, 2008.

Ding, W. P., and Chen, H. L., (2001). A symmetrical finite element model for structure-acoustic coupling analysis of an elastic, thin-walled cavity. *Journal of Sound and Vibration* 243:3, 547-559. <https://doi.org/10.1006/jsvi.2000.3478>

Durbin, F. Numerical Inversion of Laplace Transforms: An Efficient Improvement to Dubner and Abate's Method. *The Computer Journal*, 1974, 17(4), 371–376.

Ebrahimian H., Jalayer F., Lucchini A., Mollaioli F., Manfredi G., 2015. Preliminary ranking of alternative scalar and vector intensity measures of ground shaking. *Bull Earthquake Eng* 13, 2805–2840.

ECCS TC1 TWG 1.3. (1986). Recommended testing procedure for assessing the behaviour of structural elements under cyclic loading. Brussels; European Convention for Constructional Steelwork.

EN 1092-1. (2007). Flanges and their joints – Circular flanges for pipes, valves, fittings and accessories, PN designated – Part 1: Steel flanges.

EN 1998-1. (2005). Eurocode 3: Design of steel structures – Part 1-8: Design of joints.

EN 1591-1. 2009. Flanges and their joints – Design rules for a gasketed circular flange connection – Part 1: Calculation method.

EN 1591-2. 2009. Flanges and their joints – Design rules for a gasketed circular flange connection – Part 2: Gasket parameters.

EN 1473. 2016. Installation and equipment for liquefied natural gas - Design of onshore installations.

EN 1990, Eurocode 0 – Basis of structural design

EN 1992-1-1, Eurocode 2: Design of concrete structures – Part 1-1: General rules and rules for buildings.

Fabbrocino, G., Irevolino, I., Orlando, F., and Salzano, E., (2005). Quantitative risk analysis of oil storage facilities in seismic areas. *Journal of hazardous Materials* 123, 61-69. <http://dx.doi.org/10.1016/j.jhazmat.2005.04.015>

C. Farhat, F. Roux, A method of finite element tearing and interconnecting and its parallel solution algorithm, *International Journal for Numerical Methods in Engineering*, Volume 32, Issue 6, October 1991, Pages 1205-1227.

Finocchio et al., (2018), Seismic isolation of buildings using composite foundations based on metamaterials, *Journal of Applied Physics* 123

Firoozabad E. S., Jeon, B. G., Choi, H. S., & Kim, N. S. 2015. Seismic fragility analysis of seismically isolated nuclear power plants piping system. *Nuclear Engineering and Design*, 284, 264-279. ^[1]_[SEP]

Gaofeng, J., and Zhifei, S., (2010). A new seismic isolation system and its feasibility study. *Earthquake Engineering and Engineering Vibration* 9, 75-82. doi: 10.1007/s11803-010-8159-8

GIE LNG Map, 2015, Gas Infrastructure Europe. www.gie.eu.

A. Gravouil, A. Combescure . Multi-time-step explicit – implicit method for non-linear structural dynamics, *International Journal for Numerical Methods in Engineering*, 2001, pp 199–225.

R. J. Guyan, Reduction of Stiffness and Mass Matrices, *AIAA Journal*, Vol. 3, February, 1965.

Ha, Y.-K., Kim, J.-E., Park, I.-W., and Lee, H. Y., (2002). Propagation of water waves through finite periodic arrays of vertical cylinders. *Applied Physics Letters* 81:7. doi: 10.1063/1.1499520

Huang, H.H., Sun, C.T., Huang, G.L., (2009). On the negative effective mass density in acoustic metamaterials. *International Journal of Engineering Science* 47:610-617. <https://doi.org/10.1016/j.ijengsci.2008.12.007>

Hoseyni, S.M., Yousefpour, S., Araei, A.A., Karimi, K., Hoseyni, S.M., 2014. Effects of soil-structure interaction on fragility and seismic risk; a case study of power plant containment. *Journal of Loss Prevention in the Process Industries*, 32, 276-285.

IAEA, 2009. Evaluation of Seismic Safety for Existing Nuclear Installation. IAEA Safety Guide NS-G-2.13. International Atomic Energy Agency, Vienna.

I Y.T., Cheng Te-Lung, 2008. The development of a 3D risk analysis method. *Journal of Hazardous Materials*, 153, 600–608.

Jalayer F, Cornell CA, 2009. Alternative non-linear demand estimation methods for probability-based seismic assessments. *Earthquake Engineering & Structural Dynamics*, 38(8), 951-972.

JNES-NUPEC, 2008. Seismic Analysis of Large-Scale Piping Systems for the JNES-NUPEC Ultimate Strength Piping Test Program.

Karamanos S., 2016. Mechanical Behavior of Steel Pipe Bends: An Overview. *J. Pressure Vessel Technology* 138(4), Paper No: PVT-15-1165; doi: 10.1115/1.4031940.

Kittel, C., 1962. *Elementary Solid State Physics: A Short Course*, 1st ed. New York: Wiley.

- Korndörfer J., Hoffmeister B., Feldmann M., 2016. Fragility Analysis of Horizontal Pressure Vessels in the Coupled and Uncoupled Case. Proceedings of the ASME 2016 Pressure Vessels & Piping Conference. PVP 2016, Vancouver, British Columbia, Canada, July 17-21, 2016.
- Krausmann, E., Cruz, A. M., & Affeltranger, B., 2010. The impact of the 12 May 2008 Wenchuan Earthquake on Industrial Facilities. *Journal of Loss Prevention in the Process Industries*, 23, 2, 242-248.
- La Salandra V.; di Filippo R.; Bursi O. S.; Paolacci F.; Alessandri S., 2016. Cyclic Response of Enhanced Bolted Flange Joints for Piping Systems. Proceedings of the ASME 2016 Pressure Vessels & Piping Conference PVP. PVP2016, Vancouver, British Columbia, Canada, July 17-21, 2016.
- C.P. Lamarche, A. Bonelli, OS Bursi, A Rosenbrock-W method for real-time dynamic substructuring and pseudo-dynamic testing, *Earthquake Engineering & Structural Dynamics*, 2009, 38 (9), 1071-1092.
- Lanzano G., de Magistris S. F., Fabbrocino G., Salzano E., 2015. Seismic damage to pipelines in the framework of Na-Tech risk assessment. *Journal of Loss Prevention in the Process Industries* 33 (2015) 159-172.
- Li X., Koseki H., Sam Mannan M., 2015. Case study: Assessment on large scale LPG BLEVEs in the 2011 Tohoku earthquakes. *Journal of Loss Prevention in the Process Industries*, 35, 257-266.
- Li H. and Mackenzie D., 2006. Characterising plastic collapse of pipe bend structures. *International Journal of Journal of Pressure Vessels and Piping* 83 (2006) 85–95.
- Liu, M., Gorman, D. G., (1995). Formulation of Rayleigh damping and its extensions. *Computers & Structures* 57:2, 277-285. [https://doi.org/10.1016/0045-7949\(94\)00611-6](https://doi.org/10.1016/0045-7949(94)00611-6)
- Liu, Z., Zhang, X., Mao, Y., Zhu, Y. Y., Yang, Z., Chan, C. T., and Sheng, P., (2000). Locally Resonant Sonic Materials. *Science* 289:5485, 1734-1736. doi: 10.1126/science.289.5485.1734
- Lomiento, G., Bonessio, N., & Benzoni, G. (2013). Friction Model for Sliding Bearings under Seismic Excitation. *Journal of Earthquake Engineering*, 17(8), 1162–1191. <http://doi.org/10.1080/13632469.2013.814611>
- Mackie K. and Stojadinović B., 2005. Comparison of Incremental Dynamic, Cloud, and Stripe Methods for Computing Probabilistic Seismic Demand Models. *Structures Congress 2005*: pp. 1-11.
- A. Maghareh, S.J. Dyke, A. Prakash, G. B. Bounting. Establishing a predictive performance indicator for real-time hybrid simulation, *Earthquake Engineering & Structural Dynamics*, 2014, 43, 2299-2448.

- Malhotra, K.P., Wenk, T., Wieland, M., (2000). Simple Procedure for Seismic Analysis of Liquid-Storage Tanks. *Structural Engineering International* 10:3, 197-201. <https://doi.org/10.2749/101686600780481509>
- MATLAB and Statistics Toolbox Release 2012b, The MathWorks, Inc., Natick, Massachusetts, United States.
- Molina, F. J., Magonette, G., Pegon, P., & Zapico, B. (2011). Monitoring Damping in Pseudo-Dynamic Tests. *Journal of Earthquake Engineering*, 15(6), 877–900.
- G. Mosqueda, B. Stojadinovic, S.A. Mahin, Real-Time Error Monitoring for Hybrid Simulation. Part I: Methodology and Experimental Verification, *Journal of Structural Engineering* 133 (8), 2007, 1100-1108.
- G. Mosqueda, B. Stojadinovic, S.A. Mahin, Real-Time Error Monitoring for Hybrid Simulation. Part II: Structural Response Modification Due to Errors, *Journal of Structural Engineering* 133 (8), 2007, 1109-1117.
- Mostaghel, N. (1999). “Analytical description of pinching, degrading hysteretic systems.” *J. Eng. Mech.*, 125(2), 216,224
- NM. Newmark, A method of computation for structural dynamics. *Journal of Engineering Mechanics*, ASCE, 1959, 85, pp 67–94.
- D. Neron, P. Ladeveze, Proper Generalized Decomposition for Multiscale and Multiphysics Problems”, *Archives of Computational Methods in Engineering*, 2010, 17, 351–372.
- Nie J., DeGrassi G., Hofmayer C., 2008. Seismic Analysis of Large-scale Piping Systems for the JNES-NUPEC Ultimate Strength Piping Test Program. U.S. NRC NUREG/CR-6983, BNL-NUREG-81548-2008.
- Norme Tecnica, 2008, “Norme Tecniche per le costruzioni,” DM Infrastrutture, 14 January 2008 (in Italian).
- Otani et al., 2017, Seismic Qualification Of Piping System By Detailed Inelastic Response Analysis Part 2. A Guideline For Piping Seismic Inelastic Response Analysis. Proceedings of the ASME 2017 Pressure Vessels & Piping Conference PVP. PVP2017, Waikoloa, Hawaii, United States, July 16-20, 2017.
- P. Pan, T. Wang, M. Nakashima, Development of Online Hybrid Testing - Theory and Applications to Structural Engineering, Butterworth Heinemann, Elsevier 2016.
- Peng L.C., 1989. Treatment of Support Friction in Pipe Stress Analysis. Design and Analysis of Piping and Components, Vol. 169., Truong, O.N., Goodling, E.C., Bulashak, JR. J. J., Widera, G.E.O., Editors, PVP, ASME.
- Park H.S., Lee T.H., 2015. Seismic Performance Evaluation of Boil-Off Gas Compressor in LNG Terminal. *The Open Civil Engineering Journal*, 2015, 9, 557-569.

K.C. Park, C. A. Felippa, U. A. Gumaste, A localized version of the method of Lagrange multipliers and its application, *Computational Mechanics* 24, 2000, 476-490.

PEER. Pacific Earthquake Engineering Research (PEER) Center, Ground Motion Database. <<http://ngawest2.berkeley.edu/site>>, May 24, 2016.

Phani, A. S., Woodhouse, J. & Fleck, N. A., 2006. Wave propagation in two-dimensional periodic lattices. *Acoustical Society of America*, April.

Raj, P. K., & Lemoff, T. (2009), "Risk analysis based LNG facility siting standard in NFPA 59A", *Journal of Loss Prevention in the Process Industries*, 22, 820-829.

Reza M.S., Bursi O.S., Paolacci F., Kumar A., 2014. Enhanced seismic performance of non-standard bolted flange joints for petrochemical piping systems. *Journal of Loss Prevention in the Process Industries*, pp. 124-136 (vol. 30).

RFS- PR-13056. INDUSE-2-SAFETY project.

D.J. Rixen, P.L.C. Van Der Valk, An Impulse Based Substructuring Approach for Impact Analysis and Load Case Simulations, *Journal of Sound and Vibration* 332 (26), 2013, 7174-7190.

Shi, Z. and Huang. J., (2013). Feasibility of reducing three-dimensional wave energy by introducing periodic foundations. *Soil Dynamics and Earthquake Engineering* 50, 204-212. <http://dx.doi.org/10.1016/j.soildyn.2013.03.009>

Shome N., Cornell C. A., 1999. Probabilistic seismic demand analysis of nonlinear structures. Reliability of marine structures no. RMS-35, Stanford University, Department of Civil and Environmental Engineering.

Sigalas, M., Kushwaha, M. S., Economou, E. N., Kafesaki, M., Psarobas, I. E., and Steurer, W., (2009). Classical vibration modes in phononic lattices: theory and experiment. *Zeitschrift für Kristallographie – Crystalline Materials* 220:9-10. <https://doi.org/10.1524/zkri.2005.220.9-10.765>

Singh P.K., Vaze K.K., Kushwaha H.S., Pukazhendi D.M., Seetharaman S., Murthy D.S.R., 2014. Experimental and Analytical Studies on Fatigue Crack Growth and Fracture Behaviour of Carbon Steel Elbows. 20th European Conference on Fracture, June-July 30-04, Trondheim-Norway.

W. Song, S. Dyke, Development of a cyber-physical experimental platform for real-time dynamic model updating, *Mechanical Systems and Signal Processing*, Volume 37, Issues 1–2, May–June 2013, 388-402

Stansberg C. T., Ormberg H., Oritsland O., Challenges in Deep Water Experiments: Hybrid Approach", *Transaction of the ASME*, 124, 143-154, 2002.

M.B. Tate and S.J. Rosenfeld, "Preliminary investigation of the loads carried by individual bolts in bolted joints", NACA TN 1051.

- Tondini N. and Stojadinovic B., 2012. Probabilistic seismic demand model for curved reinforced concrete bridges. *Bulletin of Earthquake Engineering*, 10(5):1455-1479, 2012, doi 10.1007/s10518-012-9362-y.
- Turso J.A., Edwards R.M., March-Leuba, J., "Hybrid Simulation of Boiling Water Reactor Dynamics Using a University Research Reactor", *Nuclear Technology*, 110, 1, 132-144, 1995.
- Vamvatsikos D, Cornell CA, 2004. Applied incremental dynamic analysis. *Earthquake Spectra*, 20(2), 523-553.
- P.L.C. Van der Valk, D.J. Rixen, "An Impulse Based Substructuring Method for Coupling Impulse Response Functions and Finite Element Models", *Computer Methods in Applied Mechanics and Engineering* 275, 2014, 113-137.
- Vathi M., Karamanos S. A., Kapogiannis I. A, Spiliopoulos K. V., 2015. Performance Criteria for Liquid Storage Tanks and Piping Systems Subjected to Seismic Loading, *Proceedings of the ASME 2015 Pressure Vessels & Piping Conference*. PVP 2015, Boston, Massachusetts, USA, July 19-23, 2015.
- Voormeeren, S.N., D. de Klerk, D.J. Rixen, "Uncertainty Quantification in Experimental Frequency Based Substructuring", *Mechanical Systems and Signal Processing* 24 (1), 2010, 106-118.
- Voormeeren, S.N., D.J. Rixen, "A family of substructure decoupling techniques based on a dual assembly approach", *Mechanical Systems and Signal Processing*, Volume 27, 2012, Pages 379-396.
- Voormeeren, S. N., & Rixen, D. J., "A family of substructure decoupling techniques based on a dual assembly approach". *Mechanical Systems and Signal Processing*, 2012, 27, 379–396.
- M. Wallace, "Stability analysis of real-time dynamic substructuring using delay differential equation models", *Earthquake Engineering & Structural Dynamics*, Volume 34, Issue 15, December 2005, 1817-1832
- YK Wen "Method for random vibration of hysteretic systems". *Journal of Engineering Mechanics*, ASCE, 1976, 102, 249 – 263.
- Wu, B., Wang. Z., Bursi, O.S., "Actuator dynamics compensation based on upper bound delay for real-time hybrid simulation", *Earthquake Engineering & Structural Dynamics*, 42,12, 2013, 1749-1765.
- Xie L. ,1998. The effect of multiple crack on the leak-before-break case of pipe. *Int. J. Pressure Vessels and Piping*. 75, 249-254. [11]
[SEP]

Yan, Y., Laskar, A., Cheng, Z., Menq, F., and Tang, Y., (2014). Seismic isolation of two dimensional periodic foundations. *Journal of Applied Physics* 116:044908. <http://dx.doi.org/10.1063/1.4891837>

TY Yang, J Moehle, B Stojadinovic, A Der Kiureghian. (2009). Seismic performance evaluation of facilities: methodology and implementation. *Journal of Structural Engineering*. 135,10, 1146-1154.

Young, S., Balluz, L., Malilay, J., 2005, Natural and technologic hazardous material releases during and after natural disasters: a review. *Sci. Total Environ.* 322, 3-20.

Zerres, H., & Guerout, Y., 2004. Present calculation methods dedicated to bolted flange connections. *International Journal of Pressure Vessels and Piping*, 81, 211216.



Contents on this book are licensed under a Creative Common Attribution
Non Commercial - No Derivatives
4.0 International License, excepts for the parts already published by other publishers.

University of Trento
Doctoral School in Civil, Environmental and Mechanical Engineering
<http://web.unitn.it/en/dricam>
Via Mesiano 77, I-38123 Trento
Tel. +39 0461 282670 / 2611 - dicamphd@unitn.it